Classified Index: TU317.1/TU311.3
U.D.C.: 624

Dissertation for the Doctoral Degree in Engineering

CONTROL AND TIME INTEGRATION ALGORITHMS FOR REAL-TIME HYBRID SIMULATION

Candidate:	WANG Zhen
Supervisor:	Prof. WU Bin
Co Supervisor:	Prof. BURSI O.S.
Academic Degree Applied for:	Doctor of Engineering
Specialty:	Disaster Prevention and Reduction Engineering and Protective Engineering
Affiliation:	School of Civil Engineering
Date of Defence:	May, 2012
Degree-Conferring-Institution:	Harbin Institute of Technology, China University of Trento, Italy

国内图书分类号：TU317.1/TU311.3　　学校代码：10213
国际图书分类号：624　　密级：公开

工学博士学位论文

实时混合试验的控制和时间积分算法

博士研究生：王贞
导　　师：吴斌教授
联合导师：Bursi O.S.教授
申请学位：工学博士
学　　科：防灾减灾工程及防护工程
所在单位：土木工程学院
答辩日期：2012 年 5 月
授予学位单位：哈尔滨工业大学（中国），特兰托大学（意大利）

Abstract

Seismic testing methodologies play a significant role in earthquake engineering due to complexities of engineering materials and ground motion. Among available testing methods, hybrid simulation is more appealing for its merits, e.g., evaluating dynamic responses of large scale structures at lower cost. As a novel member of hybrid simulation, Real-time Hybrid Simulations (RHS), since its conception in 1992, has shown its unique properties and capacity for testing complex structural components, especially rate-dependent ones.

RHS often partitions the emulated structure into portions, which are then either numerically or physically simulated in real-time according to our knowledge of them. In particular, the critical nonlinear and/or rate-dependent parts are often physically modeled within a realistic real-time test, while the remainder parts are simultaneously evaluated by solving differential equations. Evidently, the challenge of these methods is to enforce the coupling at the interface between portions via real-time loading and real-time computation.

Heretofore great development of RHS has been attained. This dissertation is devoted to developing RHS in two aspects, namely transfer system control and time integration algorithms. In detail, research work and findings are summarized as follows:

The dissertation initially focuses on the implementation of a model-based control strategy –internal model control (IMC) and its comparison with the classic PID/PI control on the lately conceived high performance test system - the TT1 test system. The control strategy of the electromagnetic actuators consists of three loops, namely one speed loop and two displacement loops. The outer displacement loop is regulated with IMC or PID/PI whilst the inner two loops with proportional control. In order to compare different control strategies, real tests with swept sinusoidal waves and numerical simulations concentrating on robustness were carried out. Analysis showed that IMC is preferable for its robustness and its ease of implementation and online tuning. Both IMC and PID work similarly and well on the actuator which can be simplified into a first-order system plus dead time. In addition, RHS was performed and showed the favorable state of the system.

In order to accurately compensate for a time-varying delay in RHS, online delay estimation methods were proposed and discussed based on a simplified actuator model.

The model consists of a static gain and dead time and result in nonlinear relationships of different displacements. The estimation based on the Taylor series expansion was further developed by introducing the recursive least square algorithm with a forgetting factor. Then this scheme was investigated and assessed in pure simulations and RHS via a comparison with two other methods. Finally, the proposed scheme was identified to be satisfactory in terms of its convergence speed, accuracy and repeatability and to be superior to other methods.

With the insight into the weakness of the available compensation schemes in mind, two polynomial delay compensation formulae considering the latest displacement and velocity targets were proposed. Assessment and comparisons of the formulae by means of frequency response functions and stability analysis were carried out. In order to facilitate delay compensation, another novel compensation scheme characterized by overcompensation and optimal feedback was conceived. Numerical simulations and realistic RHS was performed to examine the proposed schemes. The analysis revealed that the proposed polynomial formulae exhibit smaller prediction errors and the second-order scheme with the LSRT2 algorithm is endowed with a somewhat larger stability range. Moreover, the overcompensation scheme was concluded to have the ability of time-varying delay accommodation, error reduction and sometimes stability improvement.

With regard to time integration algorithms, this dissertation extends the equivalent force control (EFC) method which is a method of RHS with implicit integrators to RHSs on split mass systems. The EFC method for this problem was spectrally analyzed and was found more satisfactory stability than some explicit integrator. Then larger control errors due to quadartically interpolated EF commands were recognized and treated with a proposed displacement correction. In view of the inherent feature of RHSs –multiple quantities coupling at the interface, the correction was extended to simultaneously update displacement and acceleration. Spectral stability analysis and numerical simulations demonstrated that: (1) the correction can remove the constraint of zero-stability to the method and reduce algorithmic dissipation; (2) it also works well for MDOF.

Finally, an inter-field parallel algorithm for RHSs, namely IPLSRT2, was developed and analyzed. This method was based on the Rosenbrock (LSRT2) method and a prior inter-filed parallel integrator –PLSRT2. The LSRT2 with different stage sizes, velocity projection and modified Jacobian evaluation were introduced to the algorithm in order to avoid and/or weaken the disadvantages of the PLSRT2 method, such as inefficient computation, displacement and velocity drifts, and complicated starting procedure. Ac-

curacy analysis, spectral stability analysis, pure numerical simulations and realistic RHS was performed to investigate the properties of the IPLSRT2 method. Compared with the PLSRT2, this method exhibits pros and cons. In detail, the method loses the accuracy order due to the velocity projection applied at all time steps. However, it can provide more accurate displacement and velocity results in common applications where a little larger time step is required. In some cases, the proposed method exhibits smaller phase shifts and dissipation. Moreover, computation efficiency in Subdomain A is improved and its implementation in real-time applications is simplified.

Keywords: real-time hybrid simulation, control, delay, acceleration correction, inter-field parallel

摘　要

鉴于工程材料和地震动的复杂性，抗震试验方法在地震工程领域占有举足轻重的地位。在目前的多种抗震试验方法中，混合试验以其突出的优点更具魅力，比如能以较低的代价完成大型结构的动力响应分析。而实时混合试验方法作为混合试验方法家族的新成员，自从1992年提出以来展示了它独特的性质和分析复杂结构部件尤其是率相关部件的能力。

实时混合试验方法常把原型结构分成多个部分，然后根据对各部分的认知程度选择采用数值方法或者物理试验实时模拟。具体而言，关键、非线性部分或者率相关部分常采用真实的实时试验物理模拟，而其余部分通过求解微分方程同步分析。显而易见，该类方法的挑战在于通过实时加载和实时计算保证不同部分之间的界面耦合。

截至目前，实时混合试验领域已经取得了重要进展。本博士论文主要研究实时混合试验的传递系统控制和时间积分算。具体而言，本文的研究工作和主要成果总结如下：

本论文首先将基于模型的控制策略-内部模型控制应用于新近设计的高性能试验系统（TT1），并且与经典PID/PI控制方法相比较。本研究中电磁式作动器的控制由三个环组成，即转速环、内位移环和外位移环。外位移环采用内部模型控制或者PID/PI调节，其余两环均采用比例控制。为了比较不同的控制方法，分别完成了采用扫频位移信号的真实试验和检验方法鲁棒性能的数值模拟。分析表明，内部模型控制具有更好的鲁棒性能和方便的执行、在线调节特性。对于此类可以简化成一阶模型和纯延迟环节的作动器，内部模型控制和PID控制性能都较好且类似。另外，所完成的实时混合试验表明整个试验系统工作状态良好。

为了准确补偿实时混合试验中的时变时滞，提出并讨论了基于作动器简化模型的在线时滞估计方法。该模型由一个静态增益和纯延迟构成，从而可以导出不同位移量之间的非线性关系。通过引入考虑遗忘因子的递推最小二乘算法进一步发展了基于泰勒级数的估计方法。接着，在纯数值模拟和混合试验中，与另外两种在线估计方法进行了比较。研究表明，所提出的方法具有令人满意的收敛速度、估计精度和可重复性，优于其他两种现有方法。

在认识到现行时滞补偿方法缺点的基础上，我们提出了两种考虑最新位移和速度目标的多项式时滞补偿表达式，通过频响函数和稳定性分析了该类方法。为了降低时滞补偿的困难，设计了一种基于时滞过补偿和优化反馈恢

复力的新型时滞补偿方法，并完成了检验该方法的数值模拟和真实试验。析表明，所提出的多项式补偿表达式具有较小的位移预测误差，而二阶方与LSRT2积分算法结合具有略微较大的稳定界限。并且，时滞过补偿方法具容许时滞变化、减小同步误差和有时提高算法稳定性的能力，能降低时滞补的困难。

本论文在积分方法方面扩展了等效力控制方法以完成分离质量系统的时混合试验。等效力控制方法是一种基于隐式积分算法的实时混合试验方法谱分析表明，与显式积分算法相比，等效力控制方法具有更好的稳定性。认到二次插值的等效力命令可能导致更大的控制误差，提出了位移修正措施以低该误差的影响。鉴于实时混合试验内在的特征—界面上的多变量耦合，我把修正方法推广到同时更新位移和加速度的方法。谱稳定性分析和数值模表明：（1）同时修正位移和加速度的方法能解除零稳定性的约束和减小算法尼；（2）对于多自由度问题该修正方法仍然性能良好。

改进了一种实时混合试验的域间并行算法—IPLSRT2方法。该方法于Rosenbrock方法（LSRT2）和一个现有的域间并行算法—PLSRT2方法。为避免或弱化PLSRT2方法的缺点，比如较低的计算效率、位移和速度漂移以及杂的启动过程，引入了不等级步长的LSRT2方法、速度投影和修正的雅克比阵计算方法。为了检验该方法的性能，完成了精度分析、谱稳定性分析、纯值模拟和真实实时混合试验。与PLSRT2方法相比，该方法既有优点也有缺点比如，因为在所有积分点采用速度投影而降低了算法精度。然而，在通常的析应用中，因积分步长较大，它能提供更准确的位移和速度结果。并且，它少了A域的计算过程数，提高了A域的计算效率，降低了在实时应用中的执难度。

关键词： 实时混合试验；控制；时滞；加速度修正；域间并行

CONTENTS

LIST OF FIGURES

LIST OF TABLES

CHAPTER 1

INTRODUCTION

1.1 Context of the research

In the past decades, seismic design theory and practice were profoundly developed, especially in performance-based design (Priestley et al., 2007), structural vibration control (Soong and Costantinou, 1994) and health monitoring (Balageas et al., 2006). However, all of these developments are based on better understanding of excitations, material performance and nonlinear structural dynamic responses. Even though high performance computation provides effective tools to analyse structural responses, typically with finite element software, a great number of problems should be investigated and/or validated by means of physical experiments. These problems are often relevant to rate-dependent materials (e.g. magneto-rheological damper), strong nonlinearity performance or phenomenon (e.g. buckling-restrained brace and collapse), which are too complicated to be numerically modeled. In order to combine advantages of numerical simulations and physical experiments to meet the requirements, hybrid simulation has been developed.

Hybrid simulation is a large family of seismic testing, including pseudo-dynamic testing first proposed by Japanese researchers (Hakuno et al., 1969, in Japanese), real-time pseudo-dynamic testing proposed in 1992 (Nakashima et al., 1992), continuous pseudo-dynamic testing (Pegon and Magonette, 2002), distributed pseudo-dynamic testing (Mosqueda, 2003), hybrid simulation with a shaking table (Neild et al., 2005; Quéval et al., 2008) and so forth. Pseudo-Dynamic Testing (PDT) is the same

as numerical simulations of structures except that the restoring forces are measured from the specimen rather than calculated with a hysteretic model. In this way, assumption about the hysteretic model is cancelled and hence more accurate results are expected. Real-time pseudo-dynamic testing was developed based on PDT for evaluating dynamic responses of structures with a complicated velocity-dependent portion. Continuous pseudo-dynamic testing was proposed in order to reduce the effect of stress relaxation on test results in PDT. To take advantage of experimental facilities geographically distributed in different locations, distributed pseudo-dynamic testing was exploited. Shaking tables are viewed as a transfer system in hybrid simulation as well and this results in hybrid simulation with a shaking table. All them are characterized by combination of numerical computation and physical tests. The advantages of this philosophy are evident:

- Possible to test large-scale and complex structures in large or full scale;
- Reduce test costs and save time;
- Concentrate on critical portions of a structure.

However, there are always pros and cons. Taking the subject of this thesis, Real-time Hybrid Simulation (RHS), for example, it requires real-time computation of the numerical parts of the structure and real-time loading of the physical parts. In addition, data acquisition and information exchange should be rapidly completed. Therefore, knowledge of time step algorithms, transfer system control, signal processing and other related issues are prerequisites for conducting successful RHS.

1.2 Objective of the research

According to the discussion above, we can conclude challenges of RHS in detail as follows:

- High performance control of actuators in order to reduce amplitude and phase

errors between desired and actual displacement;

- Compensate for the system delay deriving from the phase lag of the actuators, filters and information exchange in the test;
- Develop integration algorithms or implement conventional algorithms in RHS considering test characteristics, such as explicit targets requirement, stability requirement and real-time implementation.

In view of these challenges, this thesis is devoted to develop techniques involved in RHS. The objectives can be mainly summarized as:

- Perform practical and advanced control schemes in RHS;
- Estimate and compensate for delay in the system;
- Implement RHS on split mass systems with an implicit algorithm;
- Implement the inter-field parallel integration schemes and improve the performance of the method.

1.3 Structure of the thesis

In order to achieve the objectives prescribed in the previous section, the thesis reviewed state-of-the-art and conducted related research work. Actuator control, delay estimation, delay compensation, the Equivalent Force Control (EFC) method for split-mass systems and inter-field parallel integration algorithms for the RHS were discussed, analysed and/or investigated. In detail, the thesis is organized as follows:

The review on the research work accomplished by other researchers related to the contents in this thesis is presented in Chapter 2. In particular, various structural seismic testing methods are summarized and commented on followed by the key topics involved in RHS. It includes integration algorithms, delay estimation and compensation, actuator control in conjunction with applications of RHS.

In Chapter 3, the internal model control is introduced and implemented in the T-T1 test rig and numerically and physically compared with PID control tuned by the CHR scheme. Primary tests of a SDOF system with the LSRT2 and IMC are also presented.

In the framework of adaptive delay compensation, two kinds of adaptive laws/delay estimation are proposed in Chapter 4 based on a simplified actuator model with the adoption of Newton's method and Taylor series. Taking real application problem into account, the least square algorithm is incorporated into the latter method. Numerical simulations and realistic RHSs are carried out to evaluate the method and to compare it with other schemes as well.

Chapter 5 describes two new delay compensation schemes. The first one considers latest displacement and velocity targets provided by some lately developed algorithms in RHS, e.g. the LSRT2 method. The second one consists of delay over-compensation and optimal force feedback.

Chapter 6 treats RHS with an implicit integration method, i.e. the α-method with the format of the Equivalent Force Control approach. Firstly, the advantages of the method are discussed in comparisons with the conventional iteration schemes. And then displacement correction and acceleration correction are proposed in order to improve the stability and accuracy of the methods. The performance of the method is numerically verified on a MDOF system.

The following chapter develops the inter-field parallel integration algorithm based on the LSRT2. The stability and accuracy are analysed. Numerical and real-time hybrid simulations are also carried out.

The main findings and conclusions of this research are summarized in Chapter 8 together with the prospectives of work.

CHAPTER 2

STATE-OF-THE-ART

2.1 Introduction

This chapter is devoted to introduce relevant previous research which is crucial for this thesis. To begin with, four kinds of seismic testing methodologies are introduced and reviewed. Then main topics of RHS are discussed, including integration algorithms, delay estimation and compensation, actuator control and applications of RHS. Many integration algorithms, classified into monolithic and partitioned, for RHS are discussed in Section 3. Section 4 presents different delay estimation and compensation methods applied in RHS nowadays. Issues related to transfer system control are discussed in Section 5 followed by applications of RHS in Section 6.

2.2 Seismic testing methodologies

Seismic testing plays a great role in earthquake engineering as a tool to validate theories and to discover new phenomena. This section briefly introduces and discusses various seismic testing methodologies, i.e., quasi-static testing, pseudo-dynamic testing, shaking table testing, effective force testing and real-time (or fast) hybrid simulation.

2.2.1 Quasi-static testing

Quasi-static testing is the extensively-applied testing method to evaluate performance of piers, connectors and so on by imposing specified displacement and/or force histories with servo hydraulic actuators. This testing method always provides force-displacement or moment-rotation relationships, which can be fitted to numerical hysteretic models used in numerical simulations for seismic assessments. These tests are characterized by its lower requirement to actuator performance and therefore, it is possible to test a larger specimen at lower expense. In addition, this method is easier to implement than pseudo-dynamic testing in that it needs no integration. However, it can not directly illustrate the performance of the specimen subjected to earthquake excitations without numerical simulations which may be dependent on the selected hysteretic model used to fit the test results. In addition, it cannot yield reliable performance of a rate-dependent device.

2.2.2 Pseudo-dynamic testing

Pseudo-Dynamic Testing (PDT) (Mahin and Shing, 1985; Mahin et al., 1989; Williams and Blakeborough, 2001) is the same as numerical simulations of structures except that the restoring forces are measured from the specimen rather than calculated with a hysteretic model. On the other hand, it is also similar to quasi-static testing in terms of actuator control except that the commands are generated by an integration scheme instead of being specified in advance. Basic procedures of PDT with an explicit integrator are shown in Figure 2.1.

PDT is appealing due to its low requirement to the transfer system and ability to assess structural responses subjected to earthquake records. However, due to its low loading rate, it is not suitable for a rate-dependent material which is common in structural control, such as fluid viscous dampers and tuned mass dampers. In order to meet this demand, Real-time Hybrid Simulation (RHS) is developed (at the beginning, one important member of RHS is referred to as real-time pseudo-dynamic testing (Nakashima et al., 1992), which implies the close relationship between two

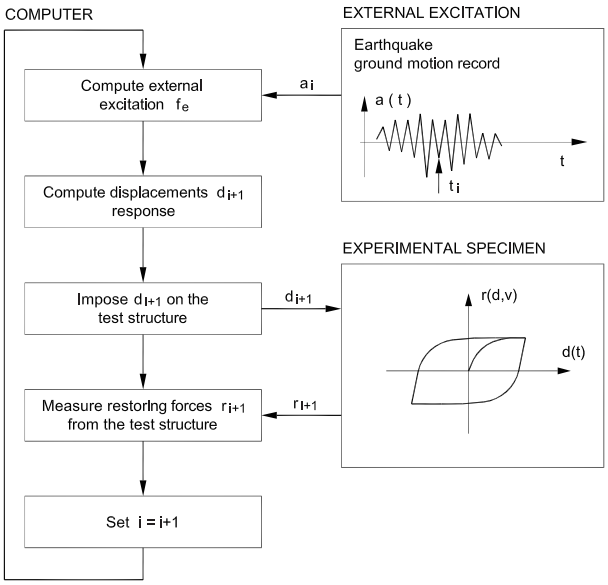

Figure 2.1: Schematic of PDT with explicit integrator (Bursi and Wagg, 2008, Page 9)

testing methodologies).

2.2.3 Shaking table testing

Shaking table testing is the most straightforward, and probably most effective technique to evaluate dynamic responses of a structure in a laboratory (Williams and Blakeborough, 2001). In this method, a structure or a structure model is equipped on a rigid platform excited by servo hydraulic actuators to replicate a specified ground motion. Therefore, shaking table testing can provides the realistic responses of the specimen by measuring in the tests, and then they can be extended to responses of the original structures with some assumption and the law of similarity. However, the disadvantages of this method are evident:

- expensive devices and sophisticated control are required to achieve the specified ground motion;
- tests are often conducted on a scaled model instead of the original structure due to the limited table area and load capacity of actuators, and there is often

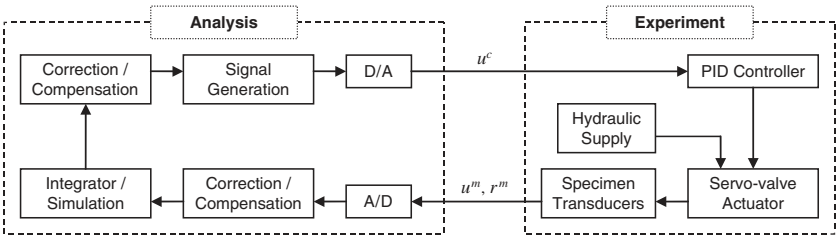

Figure 2.2: Block diagram of typical RHS(Ahmadizadeh et al., 2008)

a lack of confidence in the extrapolation of nonlinear dynamic responses to full scale;

- inspection of the failure mode of the structure is not as easy as that in PDT.

In order to extend the applications of shaking table, substructuring is introduced to shaking table testing and cause a new member of hybrid simulations(Neild et al., 2005; Quéval et al., 2008), which will be discussed further in the forthcoming sections.

2.2.4 Real-time hybrid simulation

Hybrid Simulation (Saouma and Sivaselvan, 2008) or heterogenous testing (Bursi and Wagg, 2008), stands for a big family of experimental methods capable of evaluating dynamic responses of substructured systems. In these methods, the emulated structure is torn into at least two portions, amongst which some parts called numerical subdomains or numerical substructure (NS) are computationally simulated while other parts called physical subdomains or physical substructures(PS) are modeled through actual tests in a laboratory. Pseudo-dynamic testing (Mahin et al., 1989), continuous pseudo-dynamic testing (Pegon and Magonette, 2002), fast hybrid testing (Jung et al., 2007), real-time substructure testing (Wu et al., 2005) and so on are methodologies developed within the hybrid simulation framework. In this thesis, we concentrate on real-time hybrid simulation, which includes real-time pseudo-dynamic testing, real-time dynamic substructure testing, shaking table hybrid testing and so forth.

The block diagram of typical RHS (Ahmadizadeh et al., 2008) is schematically

shown in Figure 2.2. One can see that the system consists of a transfer system, computation for the NS, correction/compensation modules and other blocks. Although it is employed to reduce convergence errors in PDT with an implicit integrator (Shing et al., 1991), correction schemes is not common in PDT. Conversely, correction or compensation for delay is inevitable in RHS, which is one of the key differences between two experimental methodologies. This results from the fact that in the latter approach the interaction between two substructures has to be achieved in real time. In other words, RHS is characterized by real-time computation of the NS and real-time loading of the PS. In particular, this technique involves integration, delay compensation and actuator control. This will be discussed in detail in the next sections.

2.2.5 Effective force testing

Effective Force Testing (EFT) was firstly conceptually proposed by Mahin et al. (Mahin and Shing, 1985; Mahin et al., 1989) in 1980s and then it was continuously discussed and investigated, among others, see (Dimig et al., 1999; Zhao, 2003). The philosophy of the method is to impose the effective force due to a specified ground motion to a structure by dynamic actuators in force control. Then structural responses can be measured directly from the specimen. Differently from PDT, direct integration algorithms are not necessary and the commands of the actuators can be determined in advance, which are the main advantages of the EFT method.

On the other hand, dynamically loading a force with a hydraulic actuator is the major challenge of the method for an lightly damped structure due to natural velocity feedback (Dyke et al., 1995). Investigations show that the frequency of the structure is corresponding to a zero of the system transfer function and hence the force related to this frequency cannot be effectively imposed on the structure. In order to overcome this problem, velocity feedback compensation (Zhao, 2003) is proposed for EFT on nonlinear SDOF systems. One weakness of the EFT method is that the emulated structure is totally physically modeled in a laboratory, rendering the methodology less economical and efficient. Recently, the hybrid EFT method (Chen, 2007) is proposed by introducing substructuring technique and is examined via numerical simulations and stability and accuracy analysis using the discrete transfer function approach.

However, real tests are required to validate the method and investigate influence of control errors and acceleration measurement errors on the test results.

2.3 Integration algorithms for RHS

Integration schemes are one key element for RHS, and up to now a good number of integrators has been developed and applied, such as the Central Difference (CD) method (Wu et al., 2005), the Newmark schemes (Bayer et al., 2005), the α-method (Jung et al., 2007), the Operator-Splitting (OS) method (Wu et al., 2006)and so forth. All of these methods are monolithic, which means that the whole problem is solved with a single scheme. However, requirement to information of the PS among these schemes are different. For example, the CD method and the LSRT2 method (Bursi et al., 2008) require only the restoring force of the PS and therefore the PS can be viewed as a black box. Conversely, the PS should be regarded as a gray box in tests with the CR method Chen and Ricles (2008a), where the initial stiffness and damping coefficient of the PS are necessary for the solution.

In fact, there is another type of integrators, called partitioned methods, which separate the overall dynamic problem into at least two dynamic sub-problems and conduct different integrators on each sub-problem. This kind of schemes is widely investigated for solving fluid-structure interaction A. et al. (2001). In hybrid simulations, more and more attention is paid to partitioned schemes because of their ability to evaluate responses of complex structures, among others, see (Pegon and Magonette, 2002). Although these schemes have not ever been applied in RHS, we introduce them herein since they play a great role in Chapter 7 of this thesis.

In this brief review, some typical schemes of both types are introduced. They are four monolithic schemes, namely, the central difference method, the LSRT2 method, the CR method and the Generalized α-method, and three partitioned schemes, namely, the GC method, the PM method and the inter-field parallel partitioned Rosenbrock method.

2.3.1 Monolithic algorithms

2.3.1.1 The central difference method

The Central Difference Method (CDM) is a well-known integrator in PDT for its ease to implement and its algorithmic properties, which read second-order accuracy and no algorithmic dissipation. However, it is identified implicit for RHS with a nonlinear velocity-dependant specimen in that velocity targets are not available until the restoring force (Note that this terminology is not precise here even it is commonly called) of the PS is measured (Wu et al., 2005). In other words, a nonlinear equation with respect to velocities is derived from the equation of motion and the acceleration and velocity approximations. This is the first time that distinctions of integrators for PDT and RHS have been recognized. In order to render the velocity explicit, a new velocity approximation firstly applied by Nakashima et al. (1992) is introduced for the PS, namely,

$$\dot{X}_{E,i+1} = \frac{X_{i+1} - X_i}{\Delta t} \tag{2.1}$$

Therefore, together with the other three equations, the CDM-RST can be formulated. Accuracy and stability of the CDM-RST is investigated and degradation is observed (Wu et al., 2005). Note that the target velocity in Eq. (2.1) complies with the interpolation to generate actuator commands in a fine step. Along this line, the CDM is extended for tests where the physical mass of the specimen can not be negligible by introducing an acceleration expression for the physical substructure in (Wu et al., 2009), i.e,

$$\ddot{X}_{E,i+1} = \frac{X_{i+1} - 2X_i + X_{i-1}}{\Delta t^2} = \ddot{X}_i \tag{2.2}$$

The paper by Wu et al. (2005) plays a significant role in development of RHS due to this insight and was followed by methods in order to render the velocity explicit, for instance, Wu et al. (2006); Bursi et al. (2008); Chen and Ricles (2008a). Unfortunately, there are two problems related to this treatment:

- no benefits obtained from this explicit velocity targets in tests: even though the velocity is explicit, it is not used in tests since as far as the author know, all tests are controlled in displacement;

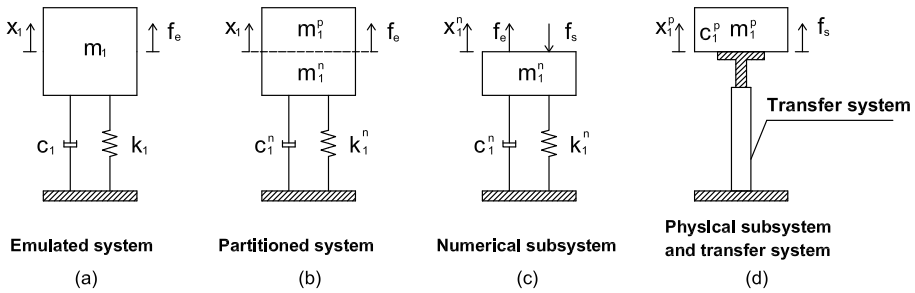

Figure 2.3: Schematic representation of a 2DOF structure with substructuring

- distinct assumptions in numerical analysis. In the paper, linear extrapolation is applied to generate displacement commands in a fine time step. Therefore, the achieved velocity is consistent with the target in Eq. (2.1) and the numerical analysis is reasonable. However, some other papers assume that the velocity target is achievable and applied in numerical analysis without any discussion on its possibility. This implies that test results may mismatch the theoretical analysis and numerical simulations.

Based on these insights, more investigations and works are needed relevant to the explicit targets. In Chapter 5 of this thesis, delay compensation schemes with the latest velocity targets are proposed and investigated.

2.3.1.2 The LSRT2 Method

Bursi et al. (2008) proposed to use of Rosenbrock-based integrators for RHS, namely the LSRT2 and LSRT3 methods for their accuracy, L-stability and ease of implementation. The LSRT2 scheme is in fact a variant of linearly semi-implicit Runge-Kutta methods, commonly referred to as Rosenbrock methods (Rosenbrock, 1963), therefore, at the beginning of each step, one Jacobian evaluation and decomposition are required. Herein the LSRT2 scheme is introduced by taking a substructured 2DOF system (Bursi et al., 2008), as shown in Figure 2.3. Then the state equation of the system can be expressed as

$$\dot{\mathbf{y}} = \mathbf{f}(\mathbf{y}, \mathbf{t}) = \left\{ \begin{array}{c} y_2 \\ \frac{1}{m^n}[f_e + f_s - c^n y_2 - k^n y_1] \end{array} \right\} \tag{2.3}$$

where $\mathbf{y} = \{x \ \ \dot{x}\}^T = \{y_1 \ \ y_2\}^T$ defines the state vector; m^n, c^n, k^n denote the mass, damping coefficient and stiffness of the numerical substructure, respectively; f_e and f_s are the external force on the numerical substructure and the coupling force between the two substructure. The LSRT2 method reads

$$\mathbf{y}_{i+1} = \mathbf{y}_i + b_1\mathbf{k}_1 + b_2\mathbf{k}_2 \tag{2.4}$$

with

$$\mathbf{k}_1 = [\mathbf{I} - \gamma\Delta t\mathbf{J}]^{-1}\,\mathbf{f}(t_i, \mathbf{y}_i)\Delta t \tag{2.5}$$

$$\mathbf{y}_{i+\alpha_{21}} = \mathbf{y}_i + \alpha_{21}\mathbf{k}_1 \tag{2.6}$$

$$\mathbf{k}_2 = [\mathbf{I} - \gamma\Delta t\mathbf{J}]^{-1}\left(\mathbf{f}\left(\mathbf{y}_{i+\alpha_{21}}, t_{i+\alpha_2}\right) + \mathbf{J}\gamma_{21}\mathbf{k}_1\right)\Delta t \tag{2.7}$$

where b_1, b_2, γ, $\gamma_{21}$and α_2 are algorithmic parameters, which are adjustable to obtain satisfactory numerical properties; $\mathbf{y}_{i+\alpha_{21}}$represents the estimate of the state vector at the time $t_{i+\alpha_2} = t_i + \alpha_2\Delta t$; $\mathbf{I}$ is the identity matrix; $\mathbf{J}$ is the Jacobian matrix, defined as

$$\mathbf{J}=\frac{\partial \mathbf{f}}{\partial \mathbf{y}} = \begin{bmatrix} 0 & 1 \\ -\frac{k^n}{m^n} & -\frac{c^n}{m^n} \end{bmatrix} \tag{2.8}$$

Algorithmic parameters can be determined in such a way to achieve second-order accuracy and L-stability for pure numerical simulations. The following values are recommended:

$$\gamma = 1 - \frac{\sqrt{2}}{2}, \quad \alpha_2 = \alpha_{21} = 1/2, \quad \gamma_{21} = -\gamma, \quad b_1 = 0, \quad b_2 = 1 \tag{2.9}$$

The hybrid test with the approach is summarized as follows:

① Compute the Jacobian matrix $\mathbf{J}$ by means of Eq. (2.8);

② Compute $\mathbf{k}_1$ from Eq. (2.5) and evaluate $\mathbf{y}_{i+\alpha_{21}}$ by means of Eq. (2.6);

③ Impose $\mathbf{y}_{i+\alpha_{21}}$ onto the PS, measure the coupling force $f_{s,i+\alpha_{21}}$ and evaluate $\mathbf{k}_2$ and $\mathbf{y}_{i+1}$ from Eq. (2.7) and Eq. (2.4);

④ Impose $\mathbf{y}_{i+1}$ upon the PS and measure the coupling force $f_{s,i+1}$;

⑤ Set $i = i + 1$ and go to 1.

From the aforementioned description, the integrator does not require the knowledge of the state y and the coupling force f_s ahead of the actual stage or at the end of the time step. This property is referred to as real-time compatibility (Gonzalez-Buelga et al., 2006). Furthermore, the integrator is based on a Runge-Kutta scheme and it is explicit for displacements and velocities, which is different from most schemes of Newmark family. Because of the explicit displacement and velocity, better control performance, such as rapid, accurate and stable responses, should be easily obtained. As the LSRT2 method is a linearly implicit method, it is more suitable to real-time test than most explicit integrators in terms of stability and accuracy. Moreover, its filtering capabilities beyond the Nyquist frequency $\Omega = \pi$ are favourable due to its L-stability. The method also works well for nonlinear RHS (Bursi et al., 2011).

However, it is worthwhile noting that the Jacobian matrix in Eq. (2.8) is calculated without any information of the PS. Therefore, the coupling force in Eq. (2.3) is reviewed as an external force and the PS a black box for this method. As can be anticipated, the properties of the RHS with this method will differ from the standard Rosenbrock method. The initial stiffness and damping coefficient of the PS is introduced to the Jacobian matrix by Lamarche et al. (2009). Nevertheless, the PS is converted to a gray box, similarly to that in PDT.

2.3.1.3 The CR Method

The CR method, proposed by Chen and Ricles (2008a), is a method based on second-order equations of motion and provides explicit displacements and velocities. It reads

$$\mathbf{M}\ddot{u}_{i+1} + \mathbf{r}_n(\mathbf{u}_{i+1}, \dot{\mathbf{u}}_{i+1}) = \mathbf{f}_{e,i+1} - \mathbf{f}_{s,i+1} \tag{2.10}$$

$$\dot{\mathbf{u}}_{i+1} = \dot{\mathbf{u}}_i + \alpha_1 \Delta t \ddot{\mathbf{u}}_i \tag{2.11}$$

$$\mathbf{u}_{i+1} = \mathbf{u}_i + \dot{\mathbf{u}}_i \Delta t + \alpha_2 \Delta t^2 \ddot{\mathbf{u}}_i \tag{2.12}$$

with

$$\alpha_1 = \alpha_2 = 4 \left(4\mathbf{M} + 2\Delta t \mathbf{C}_0 + \Delta t^2 \mathbf{K}_0\right)^{-1} \mathbf{M} \tag{2.13}$$

where $\mathbf{K}_0$ and $\mathbf{C}_0$ are the initial estimation of the stiffness and damping matrix corresponding to the emulated structure, defined as

$$\mathbf{K}_0 \approx (\frac{\partial \mathbf{r}_n}{\partial \mathbf{u}} + \frac{\partial \mathbf{r}_e}{\partial \mathbf{u}}) \tag{2.14}$$

$$\mathbf{C}_0 \approx (\frac{\partial \mathbf{r}_n}{\partial \dot{\mathbf{u}}} + \frac{\partial \mathbf{r}_e}{\partial \dot{\mathbf{u}}}) \tag{2.15}$$

One can observe that, similarly to the Chang method (Chang, 2002) but differently from Newmark method, the CR method is characterized by the algorithmic parameters which are relevant to structural properties. In addition, this approach is reported to be spectrally equivalent to the Newmark constant average acceleration scheme, with γ=1/2, β=1/4 and therefore be endowed with similar algorithmic properties, such as second-order accuracy, unconditional stability, non-dissipation and minor period distortion for monolithic problems.

The CR method was experimentally demonstrated to be stable and accurate for RHS. Chen et al. (Chen and Ricles, 2008a,b; Chen et al., 2009) investigated the stability of the scheme in both the linear and nonlinear regime and it was proven unconditionally stable as long as the system is of the softening type. This property is similar to that of the OSM-RST method (Wu et al., 2006). However, even through the velocity of the CR method is explicit, the velocity target is not used in the tests, and furthermore, the linear interpolation of displacement target should induce a velocity response different from the target. Then the unconditionally stability property may be destroyed in realistic RHSs. With this in mind, the OSM-RST developed by Wu et al. (2006) might perform better.

2.3.1.4 The Generalized α-Method

All methods reviewed above are explicit with respect to both displacement and velocity, which are attractive for RHS due to no iterations required. However, explicit methods often exhibit conditionally stable and this property often hampers their application to MDOF systems. In fact, aforementioned methods except the central difference method are spectrally unconditionally stable. Even so, algorithmic performance for a nonlinear system is not clear. In views of these, implicit methods may be an alternative choice for MDOF RHS. Herein we discuss the Generalized α-method (Chung and Hulbert, 1993), which includes a great family of integrators, such as the constant

average acceleration method, Newmark-β method and the α-method. This method is attractive for its user-defined dissipation which can limit higher frequency vibrations in responses and influence of measurement noises if applied in tests.

In order to introduce proper dissipation, the Generalized α-Method is based on an artificial equilibrium equation of motion. This philosophy can be interpreted as a filter Krenk and Hgsberg (2005). The equation of motion together with the same displacement and velocity approximation as Newmark-β method, the method reads

$$\mathbf{M}\ddot{\mathbf{u}}_{i+1-\alpha_m} + \mathbf{C}\dot{\mathbf{u}}_{i+1-\alpha_f} + \mathbf{r}_{i+1-\alpha_f} = \mathbf{f}_{e,i+1-\alpha_f} \tag{2.16}$$

$$\mathbf{u}_{i+1} = \mathbf{u}_i + \Delta t\dot{\mathbf{u}}_i + \Delta t^2 \left[\left(\frac{1}{2} - \beta \right) \ddot{\mathbf{u}}_i + \beta \ddot{\mathbf{u}}_{i+1} \right] \tag{2.17}$$

$$\dot{\mathbf{u}}_{i+1} = \dot{\mathbf{u}}_i + \Delta t \left[(1-\gamma)\ddot{\mathbf{u}}_i + \gamma \ddot{\mathbf{u}}_{i+1} \right] \tag{2.18}$$

in which

$$\mathbf{u}_{i+1-\alpha_f} = (1-\alpha_f)\mathbf{u}_{i+1} + \alpha_f \mathbf{u}_i \tag{2.19}$$

$$\dot{\mathbf{u}}_{i+1-\alpha_f} = (1-\alpha_f)\dot{\mathbf{u}}_{i+1} + \alpha_f \dot{\mathbf{u}}_i \tag{2.20}$$

$$\ddot{\mathbf{u}}_{i+1-\alpha_m} = (1-\alpha_m)\ddot{\mathbf{u}}_{i+1} + \alpha_m \ddot{\mathbf{u}}_i \tag{2.21}$$

In order to optimize the parameters, the following expressions are recommended:

$$\begin{aligned} &\beta = \tfrac{1}{(1+\rho_\infty)^2}, \gamma = \tfrac{1}{2}\tfrac{3-\rho_\infty}{1+\rho_\infty} \\ &\alpha_m = \tfrac{2\rho_\infty - 1}{1+\rho_\infty}, \alpha_f = \tfrac{2\rho_\infty}{1+\rho_\infty} \end{aligned} \tag{2.22}$$

where ρ_∞ denotes the spectral radius at infinity. $\rho_\infty = 0$ represents the case of asymptotic annihilation of the high-frequency response whereas $\rho_\infty = 1$ the case of no algorithmic dissipation, i.e., the constant average acceleration method.

The challenge to implement implicit integrators in RHS is to solve the nonlinear equation derived from the equation of motion and the algorithmic approximations. Conventional iterative methods often indicate that (1) the number of iterations varies amongst different time steps; and (2) the increment size decreases as the iteration converges and therefore, the actuator velocity changes greatly. In order to avoid these problems, an iteration procedure with a predetermined iteration number was proposed and combined with α-method for fast hybrid simulations (Jung et al., 2007). The equivalent force control method (Wu et al., 2007) is an alternative method which successfully converts the iteration process into force control and renders it possible to utilize control theory and implicit integration methods in RHS.

2.3.2 Partitioned algorithms

In this subsection, we discuss partitioned algorithms involved in structural analysis and hybrid simulations, including the GC method (Gravouil and Combescure, 2001), the PM method (Pegon and Magonette, 2002) and Rosenbrock-based methods (Jia, 2010; Jia et al., 2011). These methods are devised with the finite element tearing and interconnecting (FETI) method, in which a structure is firstly split into at least two subdomains and then continuity at the interface is ensured with Lagrange multipliers. Another coupling scheme is called the primal coupling method, where a primal valuable at the interface, either displacement or velocity, is enforced (Prakash, 2007). The methods discussed herein are very attractive for complex structural problems and fluid-structure coupling problems, since each subdomain can be separately solved with distinct integration algorithms and algorithmic parameters according to specific characteristics and requirements of the subdomain. Moreover, some methods can be incorporated into parallel computation and therefore computation cost can be effectively reduced. However, these methods always imply that equations of motion which are often ordinary differential equations(ODE) arising from the spatial discretization of the structure are converted to differential algebraic equations (DAE). The latter is more difficult to solve than the former (Petzold, 1982).

2.3.2.1 The GC method

Gravouil and Combescure (2001) proposed a multi-time-step explicit-implicit coupling method for nonlinear problems, labeled as the GC method, which is able to couple arbitrary Newmark family schemes with different time steps in different subdomains. The method is also proved stable by means of the global energy norm as long as each subdomain is stable. Moreover, the method is identified to be energy preserving for the case of the same time step applied in all the subdomains and dissipative at the interface for multi-time-step cases. The basic procedure of the method is depicted in Figure 2.4.

The GC method is very appealing for hybrid simulation and in particular for pseudo-dynamic testing (Pegon, 2008), since numerical and physical substructures can be

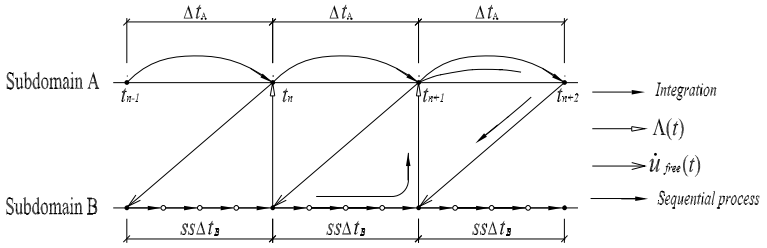

Figure 2.4: The solution procedure of the GC method (He, 2008, Page 35)

solved with different implicit/explicit Newmark schemes according to their complexity and characteristics. For the PS, the evaluation can be advanced with a finer time step in order to drive the actuator smoothly without any extrapolation/interpolation. Meanwhile, a course time step can be chosen for the NS considering the larger amount of DOFs and nonlinearity.

The GC method as can be observed in Figure 2.4, however, is inherently a sequential staggered algorithm, which means that the computation in different subdomains must be solved one by one instead of concurrently. This drawback may limit applications of the method to hybrid simulations, especially for RHS. In order to circumvent the problem, Pegon and Magonette (2002) developed and implemented an inter-field parallel algorithm based on the GC method, i.e., the PM method.

2.3.2.2 The PM Method

The PM method (Pegon and Magonette, 2002) is an extension of the GC method to advance all the domain simutaneously and continuously, as depicted in Figure 2.5. The method for advancing from t_{n-1} to t_{n+1} in Subdomain A and from t_n to t_{n+1} in Subdomain B can be summarized by the following pseudo-code:

① Solve the free problem in Subdomain A by using $2\Delta t_A$, thus advancing from t_{n-1} to t_{n+1};

② Start the loop on *ss* substeps in Subdomain B;

③ Solve the free problem in Subdomain B by using Δt_B, thus advancing from $t_{n+(j-1)/ss}$ to $t_{n+j/ss}$ with j=1,...,*ss*;

④ Linearly interpolate the free velocity $\dot{u}_{n+j/ss,f}$ in Subdomain A;

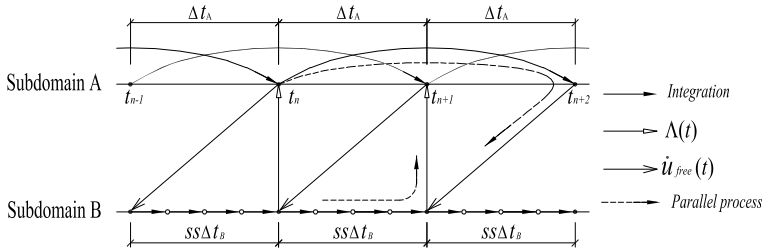

Figure 2.5: The inter-field parallel solution procedure of the PM method (He, 2008, Page 38)

⑤ Compute the Lagrange multipliers $\Lambda_{n+j/ss}$ by solving the condensed global problem;

⑥ Solve the link problem in Subdomain B at $t_{n+j/ss}$;

⑦ Compute kinematic quantities in Subdomain B at $t_{n+j/ss}$ by summing free and link quantities;

⑧ If *j*=*ss*, then end the loop in Subdomain B;

⑨ Solve the link problem in Subdomain A by using $2\Delta t_A$, from t_{n-1} to t_{n+1};

⑩ Compute kinematic quantities in Subdomain A at t_{n+1} by summing free and link quantities.

One can see from this procedure and Figure 2.5 that two subdomains can be concurrently advanced due to the actual time interval in Subdomain A which is $2\Delta t_A$. As a result, this method can be implemented not only for parallel simulations of numerical systems but also for hybrid simulations, such as continuous pseudo-dynamic testing (Bursi and Wagg, 2008).

The stability of the PM method was shown to be dependent on that of the explicit subdomain which is often conditionally stable. Bonelli et al. (2008) concluded that a rising of *ss* does not have any impact on the stability as soon as Δt_B satisfies the stability condition. With regard to the accuracy, the scheme is still second-order accurate when *ss* is equal to one, but first order accurate when *ss* is larger than one, a typical property for partitioned schemes. An explanation to the reason why *ss* affects the accuracy can be found in Jia (2010).

Bursi et al. (2010) and He (2008) extended the properties of the inter-field parallel PM method by introducing the Generalized-α method into it. In detail, the Generalized-α method (Chung and Hulbert, 1993) was incorporated into the partitioned scheme instead of the implicit Newmark method and thereby, some properties, for instance the controllable algorithmic dissipation of the Generalized-α method, is inherited in the combined scheme. It was numerically shown that the controllable numerical dissipation can be advantageous for suppressing the higher-frequency components in the responses.

2.3.2.3 The Inter-field Parallel Partitioned Rosenbrock Method

Jia et al. (2011) and Jia (2010) developed a series of partitioned methods based on the Rosenbrock method, including staggered and parallel procedures based on acceleration continuity, and parallel procedures based on a projection. For comparison in Chapter 7, the inter-field parallel procedure is introduced here.

Along the line of element partition (Prakash, 2007), the problem described in Eq. (2.16) can be separated into a set of non-overlapping subdomains constrained by acceleration continuity at the interface, namely

$$\begin{cases} \begin{bmatrix} \mathbf{I} & \mathbf{0} \\ \mathbf{0} & \mathbf{M}^i \end{bmatrix} \begin{Bmatrix} \dot{\mathbf{u}}^i \\ \ddot{\mathbf{u}}^i \end{Bmatrix} = \begin{Bmatrix} \dot{\mathbf{u}}^i \\ \mathbf{f}\left(\mathbf{u}^i, \dot{\mathbf{u}}^i, t\right) \end{Bmatrix} + \begin{bmatrix} \mathbf{0} \\ (\mathbf{G}^i)^T \end{bmatrix} \mathbf{\Lambda} \\ \sum_{i=1}^{S} \left[\mathbf{0}, \mathbf{G}^i\right] \begin{Bmatrix} \dot{\mathbf{u}}^i \\ \ddot{\mathbf{u}}^i \end{Bmatrix} = \mathbf{0} \end{cases} \quad i = 1, ..., S \tag{2.23}$$

or, in a more compact form,

$$\begin{cases} \mathbf{A}^i \dot{\mathbf{y}}^i = \mathbf{F}^i\left(\mathbf{y}^i, t\right) + (\mathbf{C}^i)^T \mathbf{\Lambda} \\ \sum_{i=1}^{S} \mathbf{C}^i \dot{\mathbf{y}}^i = \mathbf{0} \end{cases} \tag{2.24}$$

where i refers to the i-th subdomain. Both the state vector $\dot{\mathbf{y}}^i$ and the Lagrange multiplier vector $\mathbf{\Lambda}$ can be explicitly solved from Eq. (2.24), i.e.,

$$\dot{\mathbf{y}}^i = (\mathbf{A}^i)^{-1} \mathbf{F}^i\left(\mathbf{y}^i, t\right) + (\mathbf{A}^i)^{-1} (\mathbf{C}^i)^T \mathbf{\Lambda} \tag{2.25}$$

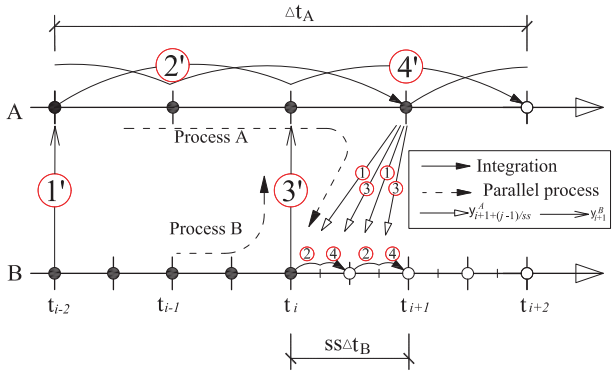

Figure 2.6: The inter-field parallel procedure based on the LSRT2 method with ss=2 (Jia et al., 2011, Page 1157).

$$\mathbf{\Lambda} = -\mathbf{H}^{-1} \sum_{i=1}^{S} \mathbf{C}^i (\mathbf{A}^i)^{-1} \mathbf{F}^i \left(\mathbf{y}^i, t\right) \tag{2.26}$$

with

$$\mathbf{H} = \sum_{i=1}^{S} \mathbf{C}^i (\mathbf{A}^i)^{-1} (\mathbf{C}^i)^T \tag{2.27}$$

Hence, each subdomain can be separately advanced with $\mathbf{\Lambda}$ calculated at the beginning of each step and the Jacobian matrix evaluated as

$$\mathbf{J}^i = \left(\mathbf{A}^i\right)^{-1} \frac{\partial \mathbf{F}_i \left(\mathbf{y}_i, t\right)}{\partial \mathbf{y}_i} \tag{2.28}$$

The proposed parallel procedure by Jia (2010), called the PLSRT2 method in Chapter 7, is presented in Figure 2.6. In the figure, Subdomain A is integrated with the coarse time step $\Delta t_A = 4\Delta t$ while Subdomain B with the fine time step $\Delta t_B = \Delta t / ss$, where $ss = 2$. Note that the solution procedure is highlighted in the figure with the numbering of the two processes and the subscript i referred to the time step Δt. In detail, the solution procedure for Subdomain A is as follows (Jia et al., 2011):

① evaluate $\mathbf{F}^A_{i-2}$ and $\mathbf{F}^B_{i-2}$ with the solutions $\mathbf{y}^A_{i-2}$ and $\mathbf{y}^B_{i-2}$, and then calculate the Lagrange multiplier $\mathbf{\Lambda}_{i-2}$,

$$\mathbf{\Lambda}_{i-2} = -\mathrm{H}^{-1} \left[\mathbf{C}^A \left(\mathbf{A}^A\right)^{-1} \mathbf{F}^A_{i-2} + \mathbf{C}^B \left(\mathbf{A}^B\right)^{-1} \mathbf{F}^B_{i-2}\right]. \tag{2.29}$$

② Compute $\mathbf{k}_1^A$ and advance the solution to $\mathbf{y}_i^A$,

$$\begin{aligned}\mathbf{k}_1^A &= \left[\mathbf{I} - 4\Delta t\gamma \mathbf{J}^A\right]^{-1} \left(\mathbf{A}^A\right)^{-1} \left(\mathbf{F}_{i-2}^A + \left(\mathbf{C}^A\right)^T \mathbf{\Lambda}_{i-2}\right) 4\Delta t,\\ \mathbf{y}_i^A &= \mathbf{y}_{i-2}^A + \frac{1}{2}\mathbf{k}_1^A.\end{aligned} \tag{2.30}$$

③ Evaluate $\mathbf{F}_i^A$ and $\mathbf{F}_i^B$, and then calculate $\mathbf{\Lambda}_i$,

$$\mathbf{\Lambda}_i = -\mathrm{H}^{-1}\left[\mathbf{C}^A \left(\mathbf{A}^A\right)^{-1} \mathbf{F}_i^A + \mathbf{C}^B \left(\mathbf{A}^B\right)^{-1} \mathbf{F}_i^B\right]. \tag{2.31}$$

④ Compute $\mathbf{k}_2^A$ and advance the solution to $\mathbf{y}_{i+2}^A$,

$$\begin{aligned}\mathbf{k}_2^A &= \left[\mathbf{I} - 4\Delta t\gamma \mathbf{J}^A\right]^{-1} \left(\left(\mathbf{A}^A\right)^{-1} \left(\mathbf{F}_i^A + \left(\mathbf{C}^A\right)^T \mathbf{\Lambda}_i\right) - \gamma \mathbf{J}^A \mathbf{k}_1^A\right) 4\Delta t,\\ \mathbf{y}_{i+2}^A &= \mathbf{y}_i^A + \mathbf{k}_2^A.\end{aligned} \tag{2.32}$$

⑤ Calculate $\mathbf{y}_{i+1+\frac{in}{2ss}}^A$ by means of the linear interpolation

$$\mathbf{y}_{i+1+\frac{in}{2ss}}^A = \left(1 - \frac{in}{2ss}\right)\mathbf{y}_{i+1}^A + \frac{in}{2ss}\mathbf{y}_{i+2}^A, (in = 1,\ 2,\ \cdots,\ 2ss). \tag{2.33}$$

Meanwhile, the advancement procedure for ($j = 1,\ \cdots,\ ss$) substeps in Subdomain B, e.g. from $\mathbf{y}_i^B$ to $\mathbf{y}_{i+1}^B$ reads (Jia et al., 2011):

① evaluate $\mathbf{F}_{i+\frac{j-1}{ss}}^A$ and $\mathbf{F}_{i+\frac{j-1}{ss}}^B$, and calculate $\mathbf{\Lambda}_{i+\frac{j-1}{ss}}$,

$$\mathbf{\Lambda}_{i+\frac{j-1}{ss}} = -\mathrm{H}^{-1}\left[\mathbf{C}^A \left(\mathbf{A}^A\right)^{-1} \mathbf{F}_{i+\frac{j-1}{ss}}^A + \mathbf{C}^B \left(\mathbf{A}^B\right)^{-1} \mathbf{F}_{i+\frac{j-1}{ss}}^B\right]. \tag{2.34}$$

② Calculate $\mathbf{k}_1^B$ and advance the solution to $\mathbf{y}_{i+\frac{2j-1}{ss}}^B$,

$$\begin{aligned}\mathbf{k}_1^B &= \left[\mathbf{I} - \frac{\Delta t}{ss}\gamma \mathbf{J}^B\right]^{-1} \left(\mathbf{A}^B\right)^{-1} \left(\mathbf{F}_{i+\frac{j-1}{ss}}^B + \left(\mathbf{C}^B\right)^T \mathbf{\Lambda}_{i+\frac{j-1}{ss}}\right) \frac{\Delta t}{ss},\\ \mathbf{y}_{i+\frac{2j-1}{ss}}^B &= \mathbf{y}_{i+\frac{j-1}{ss}}^B + \frac{1}{2}\mathbf{k}_1^B.\end{aligned} \tag{2.35}$$

③ Evaluate $\mathbf{F}_{i+\frac{2j-1}{2ss}}^A$ and $\mathbf{F}_{i+\frac{2j-1}{2ss}}^B$ and calculate $\mathbf{\Lambda}_{i+\frac{2j-1}{2ss}}$,

$$\mathbf{\Lambda}_{i+\frac{2j-1}{2ss}} = -\mathrm{H}^{-1}\left[\mathbf{C}^A \left(\mathbf{A}^A\right)^{-1} \mathbf{F}_{i+\frac{2j-1}{2ss}}^A + \mathbf{C}^B \left(\mathbf{A}^B\right)^{-1} \mathbf{F}_{i+\frac{2j-1}{2ss}}^B\right]. \tag{2.36}$$

④ Calculate $\mathbf{k}_2^B$ and advance the solution to $\mathbf{y}_{i+\frac{j+1}{ss}}^B$,

$$\begin{aligned}\mathbf{k}_2^B &= \left[\mathbf{I} - \frac{\Delta t}{ss}\gamma \mathbf{J}^B\right]^{-1} \left(\left(\mathbf{A}^B\right)^{-1} \left(\mathbf{F}_{i+\frac{2j-1}{2ss}}^B + \left(\mathbf{C}^B\right)^T \mathbf{\Lambda}_{i+\frac{2j-1}{2ss}}\right) - \gamma \mathbf{J}^B \mathbf{k}_1^B\right) \frac{\Delta t}{ss},\\ \mathbf{y}_{i+\frac{j}{ss}}^B &= \mathbf{y}_{i+\frac{j-1}{ss}}^B + \mathbf{k}_2^B.\end{aligned} \tag{2.37}$$

Note that, in order to start the procedure, three steps with a time step Δt should be evaluated by the LSRT2-based partitioned method with no subcycling (Jia et al., 2011) accounting for its second accuracy and parallelism.

This partitioned Rosenbrock method is appealing for its stability and second-order accuracy. In particular, most partitioned schemes are first-order accurate (See the GC method), while this one is second-order accurate. However, it exhibits some shortcoming in RHS, such as its drift-off effects. In order to circumvent these problems, research work is carried out and presented in Chapter 7.

2.4 Delay estimation and compensation in RHS

2.4.1 Delay effect in RHS

Delay in RHS has drawn a great number of attention since Horiuchi et al. (Horiuchi et al., 1999) analysed the effect of delay on RHS with a spring specimen. By means of energy approximation, the delay is proved to be equivalent to negative damping. When the negative damping exceeds the actual damping of the structure, the system is unstable. Following that, the same research group examined the effect of delay for RHS with a mass specimen and concluded that the delay is similar to positive damping in this case (Horiuchi et al., 2000). Some more investigations on delay influence and critical delay were carried out by other researchers, for instance, see Wallace et al. (2005a).

2.4.2 Delay estimation

In order to compensate for system delay in RHS, delay estimation becomes a crucial problem. Methods to measure delay can be classified into two types: online methods and off-line methods. In some cases, delay of transfer systems is variable due to

the stiffness change of the specimen (Darby et al., 2002). When adaptive control is applied to regulate the transfer system, control parameters can change and hence the delay of the system change as well. According to Bode plots of the system, it is evident that the delay also change with respect to the command frequency. Therefore, online delay estimation is necessary for these cases. However, it is worthy to note that in some other cases, the delay of the system can be simplified to a constant and hence, delay estimated based on preliminary tests may be accurate enough.

There are online estimation methods proposed or improved by Darby et al. (Darby et al., 2002), Ahmadizadeh et al. (2008) and (Bonnet, 2006, Page 67). They are not introduced here in that detailed discussions on them are presented in Chapter 4. With regard to off-line delay estimation, the method applied in Chapter 5 is recommended, which is to solve

$$\min_{\tau} \frac{1}{n} \sum_{i=1}^{n} |x_c(t_i) - x_m(t_i - \tau)|^2 \tag{2.38}$$

where τ is system delay and n the number of data points; x_c and x_m denote commanded and measured displacements, respectively.

2.4.3 Delay compensation

Numerous compensation schemes are available nowadays. These methods can be broadly classified into four types, namely, (1) compensation schemes based on polynomial extrapolation, (2) compensation schemes based on kinematic predictor, (3) compensation schemes based on control theory, and (4) compensation scheme based on measured forces. Some significant methods are introduced according to this category.

2.4.3.1 Compensation schemes based on polynomial extrapolation

Among all methods, one of the most essential methods is that proposed by Horiuchi et al. (Horiuchi et al., 1999) and improved by other researchers (Nakashima and Masaoka, 1999; Darby et al., 2002; Bonnet et al., 2007). Assumption behind this approach is that the transfer system can be simplified as a pure delay and additionally

the delay is a known constant, i.e. τ. Therefore, the delay can be compensated for by sending at time t the displacement response at $(t + \tau)$. As this displacement is not available at that instant, it has to be predicted by some schemes, e.g. polynomial extrapolation. In this sense, this compensation is nothing than a forward prediction with polynomial expressions. Along the line of Bonnet (Bonnet, 2006), the third-order one of this type is expressed as

$$\begin{aligned} x(t_i + \tau)' = &\left(1 + \tfrac{11}{6}\eta + \eta^2 + \tfrac{1}{6}\eta^3\right) x_i - \left(3\eta + \tfrac{5}{2}\eta^2 + \tfrac{1}{2}\eta^3\right) x_{i-1} \\ &+ \left(\tfrac{3}{2}\eta + 2\eta^2 + \tfrac{1}{2}\eta^3\right) x_{i-2} - \left(\tfrac{1}{3}\eta + \tfrac{1}{2}\eta^2 + \tfrac{1}{6}\eta^3\right) x_{i-3} \end{aligned} \tag{2.39}$$

with

$$\eta = \frac{\tau}{\Delta t} \tag{2.40}$$

where $x(t_i+\tau)'$ is predicted displacement at $(t_i+\tau)$ while x_i represents the displacement response at t_i; Δt denotes the time interval between two adjacent data points, and then it is often the time step used in a time stepping scheme. This method is being widely applied in RHS. The popularity and wide application lie in the simplicity and effectiveness of the method.

2.4.3.2 Compensation schemes based on kinematic predictor

Differently from the schemes in the last subsection which are derived from mathematical formula based on displacements, these schemes are formulated with displacements, velocities and accelerations. Therefore, they are anticipated more favorable since the differentiations of displacement are take into account. In addition, the same formula as the integration approximation may result in better numerical properties, such as stability and accuracy, for the RHS. Houriuchi et al. (Horiuchi and Konno, 2001) proposed a scheme based on the linear acceleration assumption, causing (Ahmadizadeh et al., 2008)

$$\begin{aligned} \ddot{x}(t_{i+1} + \tau)' &= \ddot{x}_i + \tfrac{\Delta t + \tau}{\Delta t}\left(\ddot{x}_i - \ddot{x}_{i-1}\right) = (2 + \eta)\,\ddot{x}_i - (1 + \eta)\,\ddot{x}_{i-1} \\ x(t_{i+1} + \tau)' &= x_i + (\Delta t + \tau)\,\dot{x}_i + \tfrac{1}{3}(\Delta t + \tau)^2\,\ddot{x}_i + \tfrac{1}{6}(\Delta t + \tau)^2\,\ddot{x}' \end{aligned} \tag{2.41}$$

where x_i, $\dot{x}_i$ and $\ddot{x}_i$ represent the displacement, velocity and acceleration provided by the integrator, respectively; $x(t_{i+1} + \tau)'$ means the predicted displacement at $t_{i+1} + \tau$ which is to send out at t_{i+1}; η is defined in Eq. (2.40). An expression based on

the displacement approximation in the explicit Newmark method was also studied in (Ahmadizadeh et al., 2008), which reads

$$x(t_{i+1} + \tau)' = x_i + (\Delta t + \tau)\dot{x}_i + \frac{1}{2}(\Delta t + \tau)^2 \ddot{x}_i. \tag{2.42}$$

2.4.3.3 Compensation schemes based on control theory

Theoretically, delay resulting from dynamics of the transfer system can be viewed as the phase lag divided by the corresponding frequency. In this sense, delay compensation aims to reduce or eliminate the phase lag. This objective can be totally or partly achieved with control theory, causing another kind of delay compensation schemes, schemes based on control theory. However, all these schemes can also be viewed as part of control system. They are regarded independent since they are always attached to the basic control loop of a transfer system. Numerous research works related to these compensation schemes were performed, see, among others, phase-lead network (Zhao et al., 2003), feed forward control (Jung and Shing, 2006), inverse control (Chen and Ricles, 2009) and outer loop control (Bonnet et al., 2007).

2.4.3.4 Compensation schemes based on measured forces

Evidently, all aforementioned methods achieve delay compensation by tackling displacement and control action. Then we can refer to them as pre-treatment methods. Conversely, a novel methodology to deal with measured forces (Ahmadizadeh et al., 2008) is proposed and investigated. In order to compensate for delay, this method predicts measured forces corresponding to the desired displacement rather than predicting the desired displacements.

One advantage of this method is to reduce control error. A new method is developed belonging to this kind in Chapter 5.

2.5 Transfer system control

To begin with, we focus on control mode of actuators. Most tests, including PDT and RHS, were carried out in displacement control. This benefits from integration methods which provide displacement commands for the actuators. However, it seems to be necessary to drive actuators in force control for EFT. In addition, force control is more advantageous for RHS when the specimen is stiff in order to reduce control errors. Therefore, for a specific applications, mixed version of displacement control and force control are possible. Combined control and switching control (Pan et al., 2005) were proposed for PDT on isolated structures. For real-time tests, one of the most significant limitations of force control with hydraulic actuators may be the natural velocity feedback, which greatly limits the ability of actuators to apply a force near the natural frequency of the structure (Dyke et al., 1995). In order to cope with this problem, velocity feedback compensation is devised for linear and nonlinear transfer system models. Sivaselvan et al. (2008) proposed a scheme to impose a displacement target upon stiff specimens by integrating a compliant element.

Another problem is associated with the control strategy. Nowadays most feedback loop control is operated with PI/PID control (Åström and Hägglund, 1995), the same case occurring in RHS except the widely investigated MCS method (Stoten and Gómez, 2001). In view of harsh requirements to control in RHS, basic control like PI/PID may be not satisfactory in some cases, such as dynamical physical substructures and coupling between actuators. With this in mind, one model based strategy - internal model control, is carried out in this research.

2.6 Applications of RHS

Wu et al. (2011a) employed RHS to investigate vibration reduction of a Magneto-

Rheological (MR) fluid damper incorporated in the JZ20-2NW offshore platform subjected to ice and seismic loads. The central difference method (Wu et al., 2005) was applied to evaluate the governing equation of motion with the time step Δt = 10ms. In view of the stability limit of the method, only the first three modes of the offshore platform were considered. From the simulations, significant vibration reduction was observed for both types of excitations.

RHS were conducted by Christenson and Lin (2008) for investigating the performance of a seismically excited structure with multiple large-scale MR fluid dampers. In simulations, the 3-story structure was chosen as the NS while 3 MR dampers as the PS. In order to solve the governing equation of motion of the structure, the α-method was carried out together with a fixed number iteration. The system delay was identified to vary from 3ms to 6ms and was compensated for by an unique scheme called virtual coupling. The RHS results documented that the MR damper effectively reduces peak interstory drifts of the first floor and maximum absolute accelerations of the top floor. The comparison between test results and pure numerical simulations with a prior prediction of the MR fluid damper illustrated the effectiveness of RHS as a cost-effective tool to experimentally assess some critical components in structural engineering.

2.7 Summary

This brief review provides the context of this thesis research. First of all, various seismic experimental methods are introduced and commented on, including the well-established methods, i.e., quasi-static testing, pseudo-dynamic testing and shaking table testing, as well as the methods under development, i.e., the effective force testing and real-time hybrid simulation. Successively main topics in real-time hybrid simulations are discussed, which are concerned with integration methods, delay estimation and compensation, transfer system control and applications of RHS.

CHAPTER 3

THE INTERNAL MODEL CONTROL FOR REAL-TIME HYBRID SIMULATION WITH THE TT1 TEST SYSTEM

3.1 Introduction

In Real-time Hybrid Simulation (RHS), transfer systems are required to rapidly and accurately respond to the reference input in order to enforce the coupling between the two substructures. If the specimen is loaded by several transfer systems - typically actuators, disturbance rejection performance of each control system should be considered to decline the coupling influence amongst transfer systems. In the research (Bonnet et al., 2007), unacceptable displacement errors are observed when actuators are strongly coupled with each other. Even though state space control (Stoten and Gómez, 2001) is an alternative solution to this problem, a simple and practical control strategy is more desirable. Another control problem encountered in research is that the controller has to be tuned again once the specimen changes, which can be circumvented by the disturbance rejection performance of control as well. Due to its favorable disturbance rejection and performance of tracing reference inputs, the Internal Model Control (IMC) (Morari and Zariou, 1989; William, 2011) is carried out in this research.

This chapter concentrates on the control issue in RHS with a novel test rig in the University of Trento, Italy. In particular, IMC and the novel test system for the Type Test 1 (TT1) in the SERIES project supported by the European Communitys Seventh Framework Programme are initially introduced. And then the speed loop and inner

displacement loop for the electromagnetic actuators are discussed. Successively, IMC is implemented on the test rig as well as the conventional PID/PI control. Both controllers are compared in the frequency domain with swept commands and in the time domain with step change inputs, respectively. Lastly, a preliminary hybrid test on a SDOF system performed with the LSRT2 method are presented.

3.2 Brief introduction to IMC

As indicated by the terminology, IMC is a control strategy where the plant model is explicitly an internal part of the controller (William, 2011). Since formally proposed by Garcia et al in 1982 (Garcia and Morari, 1982), IMC has been rapidly developed for decades and combined with many other control strategies, including adaptive control, model predictive control, and widely used in chemical industries (Vijaya et al., 2006). The popularity of the method lies in its characteristics, such as the simple structure, fewer parameters to be online tuned, trade-off between performance and robustness and so on.

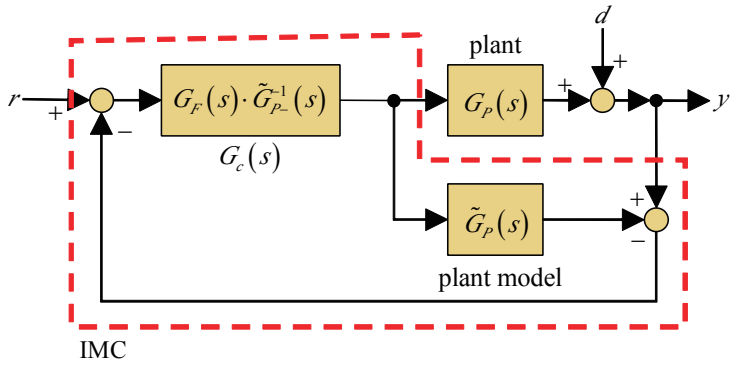

Figure 3.1: Block diagram of IMC.

The block diagram of IMC is depicted in Figure 3.1, where r, d and y denote reference inputs, disturbances and outputs, respectively; $G_p(s)$ and $\tilde{G}_p(s)$ represent the

transfer functions of the plant and plant model while $G_F(s)$ a low-pass filter. $G_{p-}(s)$ is the transfer function of the minimum phase part of the plant model. As shown in the figure, if the plant model can perfectly represent the plant, setpoint tracing control is an open loop and the closed-loop can reject a disturbance. If the plant model is not perfect, the closed loop can suppress the discrepancy between the plant output and the model output. Therefore, IMC can rapidly respond to the setpoints and can provide accurate control performance, in that it combines the advantages of both open loop and closed-loop. These insights can also be revealed by the transfer functions from the disturbance and setpoint to the plant output, namely

$$y(s) = \frac{G_p(s)G_c(s)}{1 + (G_p(s) - \tilde{G}_p(s))G_c(s)} r(s) \tag{3.1}$$

$$y(s) = \frac{1 - \tilde{G}_p(s)G_c(s)}{1 + (G_p(s) - \tilde{G}_p(s))G_c(s)} d(s) \tag{3.2}$$

In Eq. (3.1) , if $G_p(s)G_c(s) = 1$ and $\tilde{G}_p(s) = G_p(s)$, we obtain $y(s) = r(s)$, which means perfect setpoint tracing performance. Moreover, in Eq. (3.2), we attain $y(s) = 0$, which means perfect disturbance rejection, if $\tilde{G}_p(s)G_c(s) = 1$, no matter whether $\tilde{G}_p(s) = G_p(s)$. Therefore, the final objectives of control, i.e., tracing setpoint and rejecting disturbance, can be theoretically realized if $\tilde{G}_p(s) = G_p(s)$ and $\tilde{G}_p(s)G_c(s) = 1$. In practice, it is easier for IMC to compromise between two objectives than for the conventional feedback control, even perfect control may be impossible(Morari and Zariou, 1989). Furthermore, the trade-off between two objectives can be eliminated if the two-degree of freedom IMC is implemented, as shown in Figure 3.2. In the structure of the two-degree of freedom IMC, two independent controllers are devised with one for setpoint tracing (i.e. $G_{cr}(s)$) and the other for disturbance rejection (i.e. $G_{cd}(s)$). This property of IMC renders it favorable for control of coupling actuators in RHS.

IMC is an open control scheme and many concepts, such as robustness, adaptive control, can be incorporated into it. Let's consider model reference adaptive control (MRAC) (loannou and Fidan, 2006) as an example, which is extensively-used adaptive control. Figure 3.3 shows the block diagram of model reference adaptive inverse control (MRAIC) system (Widrow and Walach, 2008), which is the combination of two-degree of freedom IMC and MRAC. In view of this combination, MRAIC can cancel plant noise and disturbance.

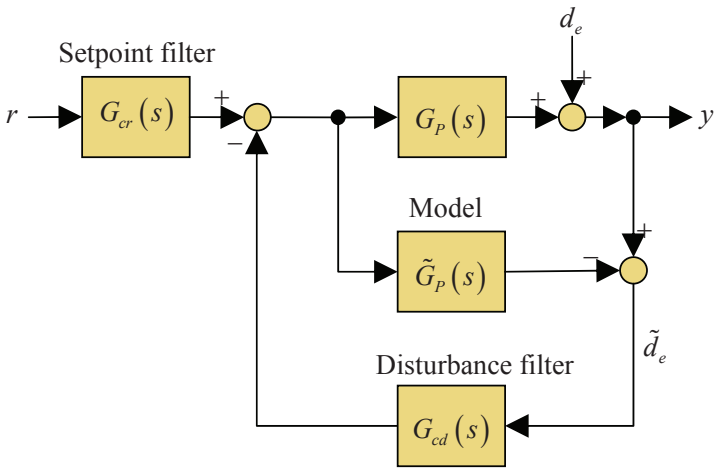

Figure 3.2: Two-degree of freedom IMC.

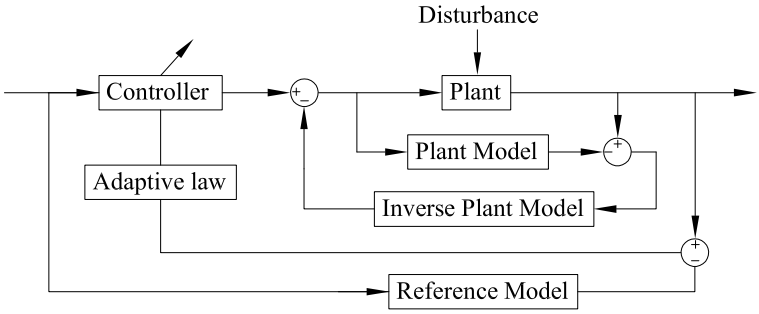

Figure 3.3: Model reference adaptive inverse control system.

With regard to the design procedure of IMC, it is straightforward for a stable plant, summarized as follows (Li et al., 2009; Vijaya et al., 2006):

① Factorize the plant model $\tilde{G}_p(s)$ into invertible element $\tilde{G}_{p-}(s)$ and noninvertible element $\tilde{G}_{p+}(s)$, namely

$$\tilde{G}_p(s) = \tilde{G}_{p-}(s)\tilde{G}_{p+}(s) \tag{3.3}$$

where $\tilde{G}_{p-}(s)$ is the transfer function of the minimum phase part while $\tilde{G}_{p+}(s)$ contains the non-minimum phase part and dead time;

② IMC controller can be expressed

$$G_c(s) = \tilde{G}_{p-}^{-1}(s)G_F(s) \tag{3.4}$$

where $G_F(s)$ indicates a low-pass filter devised to render $G_c(s)$ proper. In addition, it can detune the tracking performance and improve robustness of the system. It can be written as

$$G_F(s) = \frac{1}{(1 + Ts)^n} \tag{3.5}$$

where T and n are the time constant and the order difference between the denominator and numerator of $\tilde{G}_{p-}(s)$.

Evidently, the only parameter for this scheme to tune is the time constant T. By tuning this parameter, trade-off between tracking performance and robustness performance can be achieved. Software for design and simulations of IMC is also available (Brosilow and Joseph, 2002).

3.3 The TT1 test system

The novel test system for the Type Test 1 (TT1) in the project called SEISMIC ENGINEERING RESEARCH INFRASTRUCTURES FOR EUROPEAN SYNERGIES (SERIES) is conceived to evaluate high-performance control and assess errors in RHS.

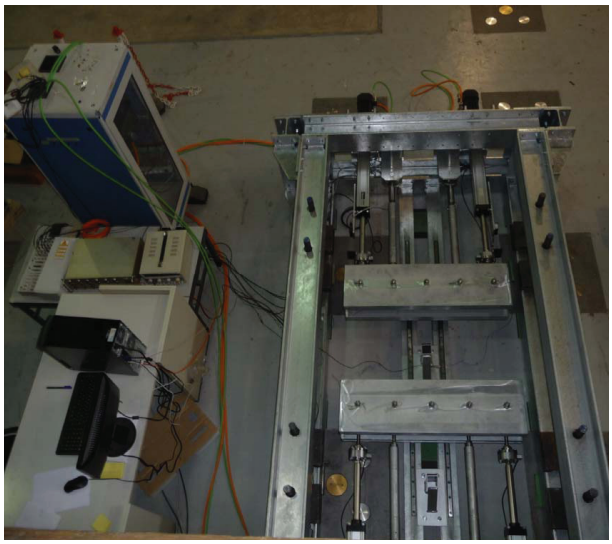

Figure 3.4: The plan view of the TT1 test system.

As demonstrated in Figure 3.4 and Figure 3.5, it consists of four electro-magnetic actuators, a dSpace DS1103 control board, two masses, two dampers, a series of springs, various sensors and other accessories. With this hardware, various specimens from single components to a four-DOF system can be configured and tested. Moreover, the system can replicate geometric nonlinearities by allowing the rotation of masses and discontinuous supports by configuring the coil springs and the connectors. With regard to various configurations of the physical substructure(s)(PS) and numerical substructure(s)(NS) involved in the test system, more information can be found in Jia (2010).

In order to ensure the compatibility and force equilibrium between the PS and the NS in RHS, electro-magnetic actuators manufactured by Parker are employed. Characteristics of the motors (S.B.C., 2009) and actuators (Hannifin, 2008) are presented in Table 3.1 and Table 3.2. In fact, the motors are of permanent magnets synchronous brushless machines and operated by a three-phase voltage of an amplitude between 0 to 400V and a frequency 0 to 200Hz. The voltage is generated and controlled by the AC890 system, including Paker 890 common bus supply (890CS) and 890 common bus drives (890CD) (Drives, 2007), both of which are designed for speed control of standard AC three-phase motors. In our case, one 890CS and four 890CD are

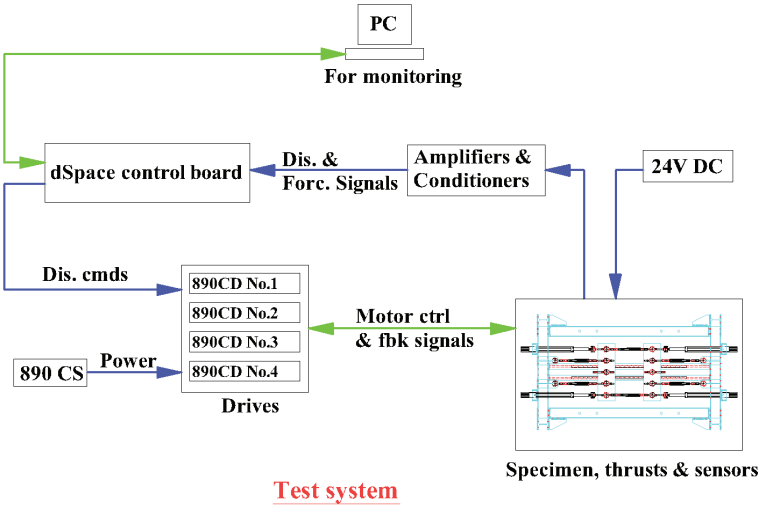

Figure 3.5: The schematic representation of the TT1 test system.

adopted. In addition, electronics devices, like inductors, toroids and an EMC filter, are also installed to reduce ambient electromagnetic noises, as shown in Figure 3.6.

Table 3.1: Characteristics of the motors

Items	Values
Code	MBAV1053004519S2D65M
Nominal voltage	322 V rms
Maximum speed	314 rad/s
Maximum torque	4.00Nm
Nominal power	1.1kW
Momentum mass	0.403 g$\times$m^2
Torque constant	1.65Nm/A rms
Resistance	6.9Ω
Inductance	24.8mH

Table 3.2: Characteristics of the actuators

Items	Values
Type	ETB80M10LA77DM500A
Screw lead	10mm
Screw diameter	25mm
Stroke	500mm
Max speed	540mm/s
Max. acceleration	6m/s^2
Max. thrust force	8300N

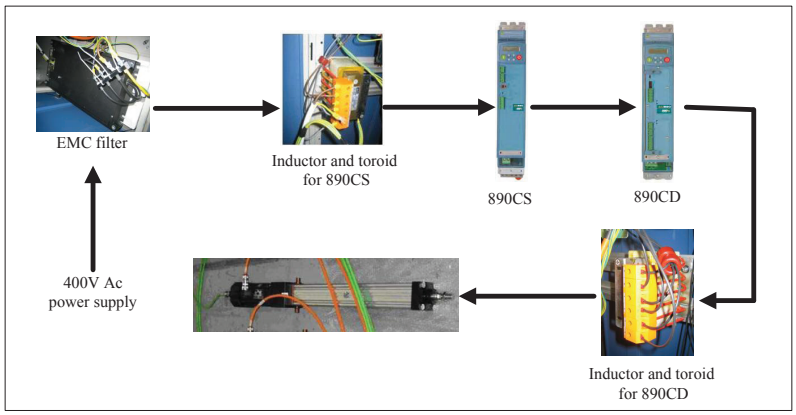

Figure 3.6: Schemes to reduce noises.

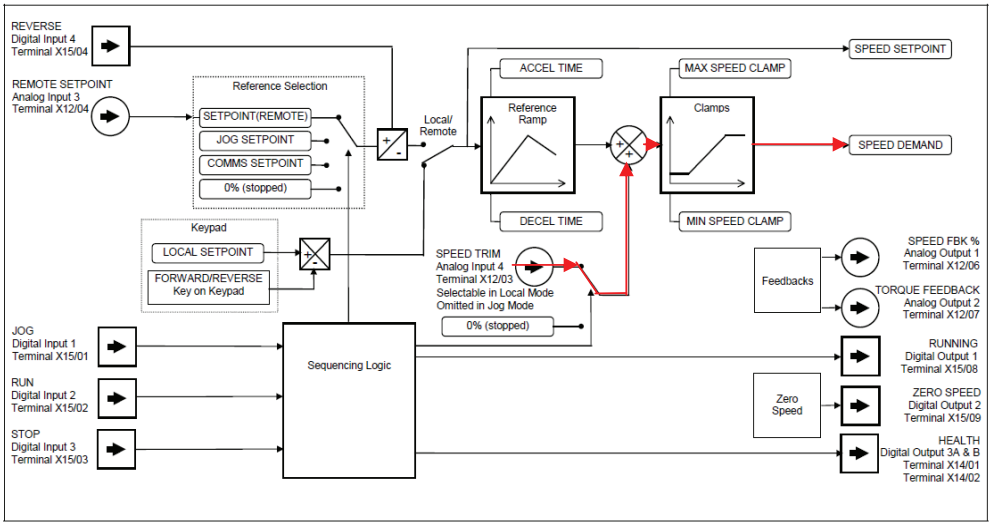

Figure 3.7: Different manners to generate speed demands.

3.4 Control in the speed loop and the inner displacement loop

Electromagnetic motors are often operated in speed with a PI controller. The controller produces drive signals to the drive circuits which output the required voltage and frequency for a particular motor speed. According to the engineering reference (Drives, 2008), Permanent Magnetic Alternating Current (PMAC) is adopted as a control mode here. This control set-up is expected to exhibit higher performance, since the resolver for speed feedback signals is used. However, displacements are more straightforward and easier to operate for a linear movement. Therefore, displacement control is often attached to the speed loop to obtain better performance of translational displacement responses. One speed loop and two displacement loops are adopted in our cases. In this section, we introduce the speed loop and inner displacement loop control followed by the outer displacement loop control in the next section.

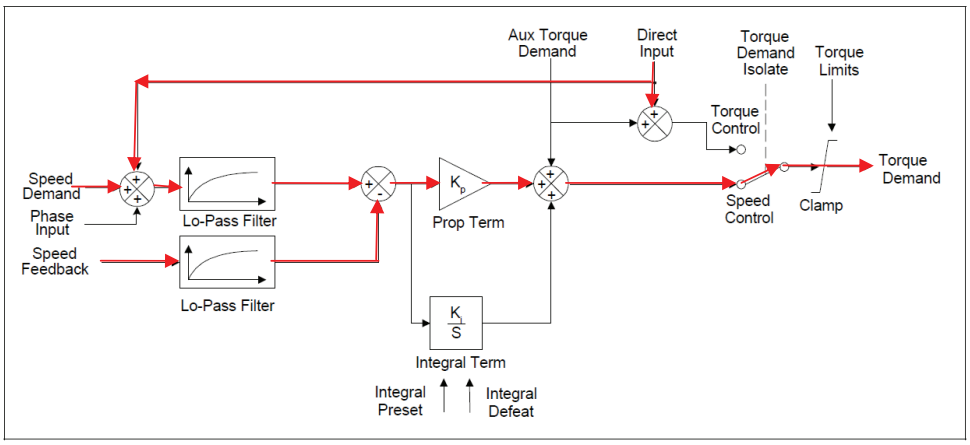

Figure 3.8: The PI control in the speed loop.

3.4.1 Control in the speed loop

In order to accommodate different cases, two different manners to generate speed demands are designed by Parker(Drives, 2008), as shown in Figure 3.7. The difference between them is whether the Reference Ramp block is employed or not, which restricts the change speed of demands. In RHS, one crucial requirement to the actuator is to respond rapidly and accurately. Thereby, in our cases, the reference speed is directly transferred to the port of SPEED TRIM Analog Input 4 of the 890CD from the dSpace output channel, as highlighted in red in Figure 3.7. In this way, the speed demand becomes the same as the reference and the response speed of the system to the reference can be improved at the expense of likely unsmooth demands.

On the other hand, Direct Input, see Figure 3.8, is also adopted. According to Drives (2008), the direct input to the speed loop is an analog input which is sampled synchronously with the speed loop. This ensures that the speed loop always has the most up-to-date value of the input, allowing it to respond faster. Another function of the Direct Input is to avoid the saturation of the speed reference.

Generally speaking, proportional-integral (PI) and proportional-integral-derivative (PID) control should be superior to proportional (P) control in terms of the response speed and accuracy. However, both of them increase the order of the system due

to the integral term and derivative term and increase the complexity of the control in the outer loop. In addition, (Åström and Hägglund, 1995, Page 280) pointed out that it is not necessary to introduce integral action in the speed loop and derivative action in the displacement loop due to the inherent integration from the speed to displacement. In view of this fact, proportional control, which can render it easier to design a displacement controller, is devised as speed controller instead of PI or PID here. Therefore, drive configuration settings are made via Parker software Drive System Explorer Lite (DSE Lite). Table 3.3 presents parameters which are different from default ones for PMAC control for the motors used in our case.

With this configuration, we can derive the transfer function of the speed. In fact, a permanent magnetic synchronous motor operated with field oriented control can be modeled like a DC motor, which means the electric torque is dependent of the motor current, namely

$$T_e = K_t i_q \tag{3.6}$$

where T_e and i_q represent the electric torque and the motor current, respectively; K_t is a gain related to the number of pole pairs, d-axis mutual inductance and equivalent d-axis magnetizing current of the motor Enrique (2006); Lin et al. (1998). Then the mechanical torque equation for the motor reads

$$T_e = T_L + B\omega_m + J_m \frac{d\omega_m}{dt} \tag{3.7}$$

where T_L and ω_m is the load torque and the actual motor speed; B and J_m are the damping coefficient and the moment of inertia of the motor, respectively. In addition, two gains, i.e. the maximum torque T_m and the inverse of the gain K_t, are set to convert the physical quantities from speed to current. Therefore, we obtain the block diagram of the speed loop, as shown in Figure 3.9. The the transfer function from the speed reference to speed response with proportional control but not any load torque is

$$G_\omega(s) = \frac{K_{p,\omega} T_m}{J_m s + B + K_{p,\omega} T_m} \tag{3.8}$$

which means that the speed loop is of first-order.

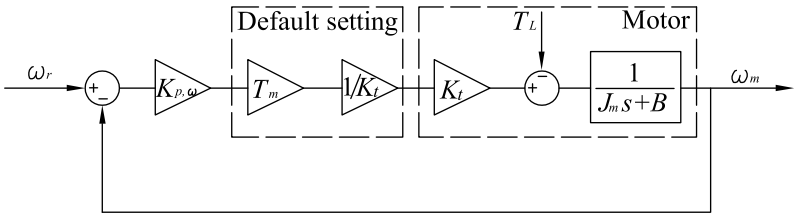

Figure 3.9: Block diagram of the speed loop

3.4.2 The inner displacement loop control

For the purpose of operating the actuators with displacement references and implementing the internal model control, two displacement loops are designed, as shown in Figure 3.10. Note that R in the figure is a conversion ratio of rotational-to-linear motion, which is $R = l/(2\pi)$, where l denotes the ballscrew lead (Kim and Chung, 2005). Broadly speaking, the inner displacement loop may be not necessary in common applications, whereas it is helpful in our practical operation. First of all, any small speed control error leads to a linearly-increasing displacement response, which may create problems when identifying the plant model from speed command to displacement responses for control design. Secondly, the inner displacement loop is useful when accidental operations occur in the outer displacement loop. Without the inner displacement loop, actuators may keep on moving before some collisions, since it is operated in speed. In our case, actuators can stay stationary when it may achieve the inner loop reference. Another reason to apply the inner displacement loop is to convert the integrating process to a normal process. Research (Hashimoto et al., 2007) shows that the integration in the process causes a response offset when disturbance exists in some cases controlled by the IMC strategy and a disturbance observer can resolve this problem. In our application, the inner displacement loop was applied and hence, the plant of the outer displacement loop is a normal process instead of an integrating one. Lastly, the inner displacement loop does not increase the order and control complexity of the system since only proportional control is carried out. The proportional gain $K_{p,1d}$=0.015 (MaxSpeed/mm) is set here. Since performance of the system is determined by the outer displacement controller, this gain in the inner dis-

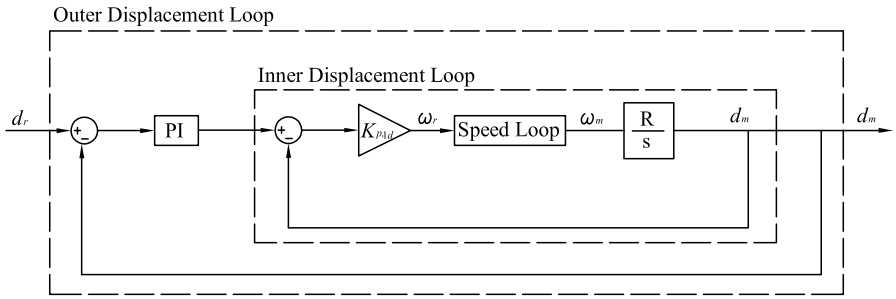

Figure 3.10: Two displacement loops of actuator control

Table 3.3: Parameters in the speed loop

Displayed Name	Value	Description
Seed prop gain	50	Proportional gain in the speed loop
Int defeat	True	Eliminate the integral term in the speed loop controller
Direct ratio	1	Ratio of direct input
Speed dmd filter	1ms	Time constant of low-pass filter for speed demand
Speed fbk filter	1ms	Time constant of low-pass filter for speed feedback

placement loop has less influence and can be chosen any value in a large range. Notice that the unit of the speed command is MaxSpeed, and therefore, the command of 1 indicates the desired movement of 314rad/s for the motor or 540mm/s for the actuator, see Table 3.1 and Table 3.2.

In order to devise the controller for the outer displacement loop, the numerical model of the inner displacement loop was identified with swept sinusoidal waves. With the transfer function in Eq. (3.8), the transfer function of the inner displacement loop can be obtained, namely

$$G_{1,d}(s) = \frac{K_{p,1d}K_{p,\omega}T_mR}{J_ms^2 + (B + K_{p,\omega}T_m)s + K_{p,1d}K_{p,\omega}T_mR} \tag{3.9}$$

Therefore, the inner displacement loop is second-order. Considering delay introduced by acquiring systems and output filters, the second-order system with dead-time is chosen as the model structure, namely

$$G_m(s) = \frac{K_m}{(T_{1m}s + 1)(T_{2m}s + 1)}e^{-\delta t_m \times s} \tag{3.10}$$

where δt_m indicates the dead-time of the system while T_{1m} and T_{2m} denote the time constants, respectively; K_m represents the static gain. Tests were conducted with displacement reference of swept sinusoidal waves with the frequency from 0.1Hz to 20Hz and the amplitude of 10mm. Then the numerical model was identified using the Matlab command: pem, which is designed to estimate model parameters using iterative prediction-error minimization method. The resulting model reads

$$G_m(s) = \frac{0.9868}{(5.397 \times 10^{-2}s + 1)(5.014 \times 10^{-3}s + 1)} e^{-9.331 \times 10^{-3}s} \tag{3.11}$$

The model is validated by comparing the simulated results with the measured displacement in the frequency domain, as shown in Figure 3.11. One can observe the excellent fitness of the measured and simulated Bode plots. In addition, as demonstrated in Eq. (3.11), the time constants of two terms in the denominator are so different that the smaller one can be negligible. Therefore, for this specific issue, the inner displacement loop can be almost reduced to a first-order system plus dead time. It is worthwhile to mention that the reason why swept sinusoidal waves were applied instead of a step change is to limit the influence of measurement noises, electromagnetic noises and mechanical gaps on the identification results.

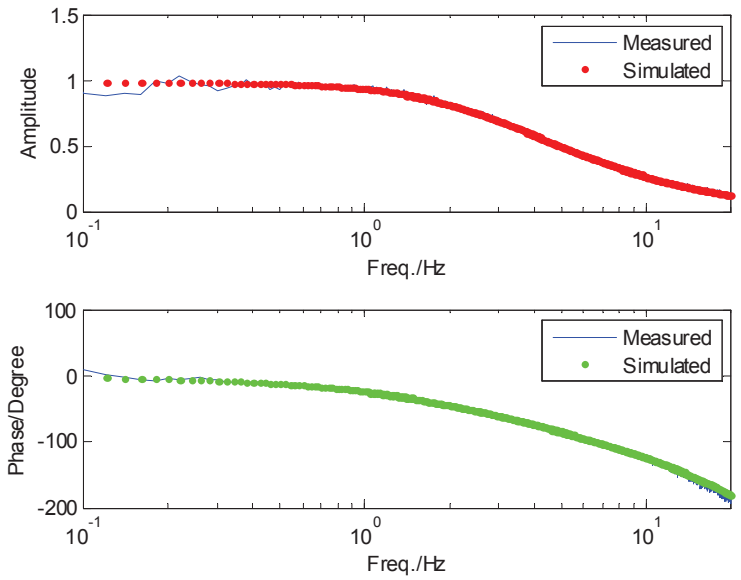

Figure 3.11: Model identification and validation of the inner displacement loop.

3.5 PID/PI and IMC implementations in the outer displacement loop

3.5.1 PID/PI and its implementation on the TT1 test system

PID control and PI control are the most widely used nowadays for its simplicity and effectiveness (Åström and Hägglund, 1995), and this is the reason why we compared the IMC with them. With the identified plant model, PID and PI controllers were designed herein using the CHR tuning scheme for 0.0% overshoot step response, as tabulated in Table 3.4. The CHR tuning scheme (Åström and Hägglund, 1995) is hoped to achieve quickest response with a specified overshoot for setpoint response or disturbance rejection performance. In the table, T indicates the time constant of the plant while a and L define a two-parameter model of the plant, both of which are also employed in the well-known PID tuning method - the Ziegler-Nichols method (Åström and Hägglund, 1995). In our case, these parameters are calculated with the identified model in Eq. (3.11). The designed controller parameters read

$$K = 3.320 \quad T_i = 0.05899 \quad T_d = 0.006305 \tag{3.12}$$

for PID control expressed as

$$G_{PID}(s) = K\left(1 + \frac{1}{T_i s} + T_d s\right) \tag{3.13}$$

and

$$K = 1.937 \quad T_i = 0.07079 \tag{3.14}$$

for PI control expressed as

$$G_{PI}(s) = K\left(1 + \frac{1}{T_i s}\right). \tag{3.15}$$

Then the controllers are discritized with zero-order holder and implemented in the dSpace control board.

Table 3.4: CHR-PID setpoint response method with 0.0% overshoot.

Controller	K	T_i	T_d
PI	$0.35/a$	$1.2T$	/
PID	$0.6/a$	T	$0.5L$

3.5.2 IMC implementation on the TT1 test system

As mentioned above, the TT1 test rig are very flexible and it is possible to configure specimens endowed with various characteristics. On the other hand, if the controller designed for the actuator is strongly dependent on the specimen, the numerical model of the system should be identified once the new configuration is performed. Therefore, we would like to view the specimen as a disturbance to the control loop and design the controller only for the actuator. Figure 3.12 shows the block diagram of the inner displacement loop with a dynamic specimen. In the figure, η is efficiency of the force transmission mechanisms. K_{eq} means the equivalent stiffness of the mechanisms. Generally speaking, K_{eq} is larger; otherwise, there is a considerable deformation of the mechanisms and this can render control of the system difficult and inaccurate. Therefore, we can, in common cases, replace the measured displacement of the specimen with the displacement referred to as d' in the figure. With this explanation, the new diagram of the inner displacement loop is shown in Figure 3.13. One can see that the difference of the inner displacement loop in Figure 3.10 and Figure 3.13 is the disturbance. In the former one, there is no disturbance for the loop while in the latter one the load torque is the disturbance. In view of the disturbance rejection performance of IMC, we can neglect the specimen. This means that the controller designed without any specimen can be applied with a specimen if the specimen is not too strong.

Following the procedure in Section 3.2, the IMC was designed. First of all, we obtain the invertible part of the model, namely

$$G_{p-}(s) = \frac{0.9868}{(5.397 \times 10^{-2}s + 1)(5.014 \times 10^{-3}s + 1)} \tag{3.16}$$

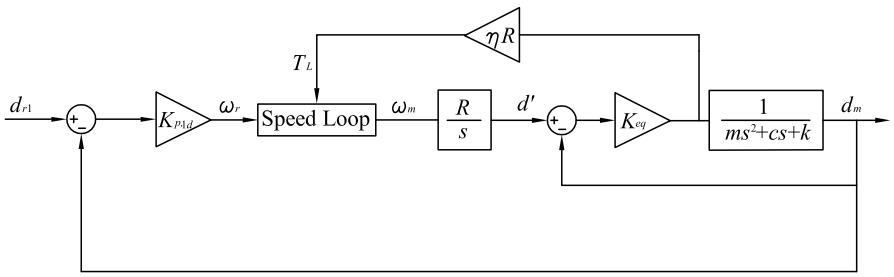

Figure 3.12: Block diagram of the inner displacement loop with specimen

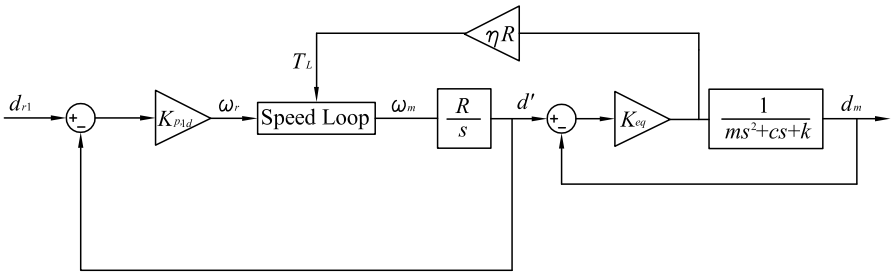

Figure 3.13: Block diagram of the inner displacement loop with disturbance

Then the controller can be expressed as

$$G_c(s) = G_{p-}G_F(s) = \frac{(5.397 \times 10^{-2}s + 1)(5.014 \times 10^{-3}s + 1)}{0.9868(Ts + 1)^2} \tag{3.17}$$

where T is the time constant of the filter, which is to be tuned later.

3.5.3 Comparative tests and numerical simulations with PID/PI and IMC

To begin with, tests were conducted with a swept wave characterized by the frequency range from 0.1Hz to 20Hz without any specimen considered. The time histories of response displacements of actuators controlled by different strategies are presented in Figure 3.14. It is evident that the PI control is not satisfactory due to the considerable amplitude errors and the phase errors. Conversely, both the PID control and the IMC control exhibit better performance than the PI control. In order to compare the PID control and the IMC control, Bode plots of two strategies were carried out and presented in Figure 3.15 where IMC-6 denotes the IMC controller with a time constant $T = 6ms$. One can observe that both controllers are similar and favorable in the frequency range from 0.1Hz to 10Hz in terms of the amplitude responses. On the other hand, the IMC control exhibits somewhat larger delay in the frequency range of [5 10]Hz for this specific time constant of the filter. As demonstrated in the next tests, the delay can be effectively reduced by decreasing the time constant.

Then tests were carried out on a spring-mass-damper oscillator shown in Figure 3.20 and results are presented in Figure 3.16. As shown in Figure 3.12, the inner displacement loop contains the specimen, different from the case in Figure 3.10. However, we implement the same controller by neglecting the specimen. One can see that both controllers perform similarly in terms of amplitude response whilst the IMC exhibit a slight phase lag. In order to reduce the phase lag of the IMC control, the time constant $T = 5ms$ were chosen and results are also depicted in the figure. Clearly, the IMC-5 is almost identical to the PID control. Therefore, it is pretty easy to improve the response speed of the IMC controller by reducing the only parameter -the time constant of the filter.

In order to further investigate the robustness of both controllers, numerical simulations were carried out taking into account the parameter uncertainties and distur-

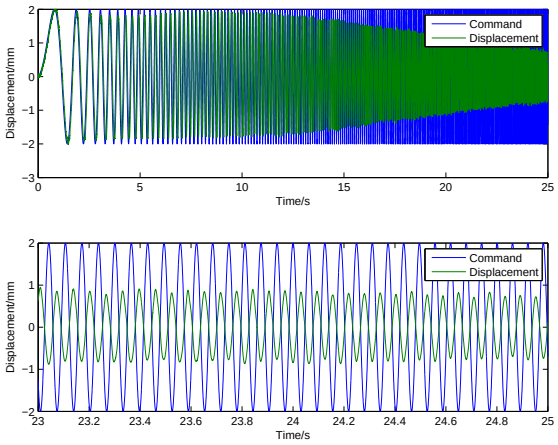

(a) PI

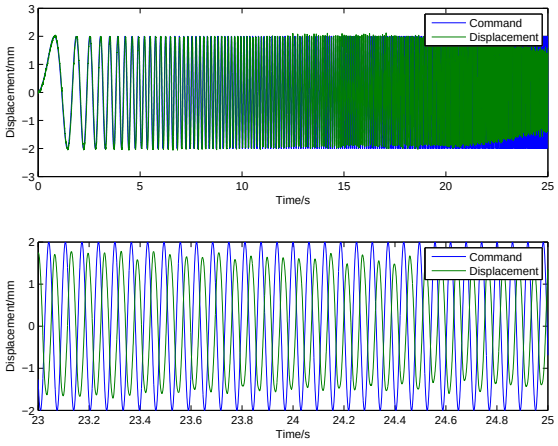

(b) PID

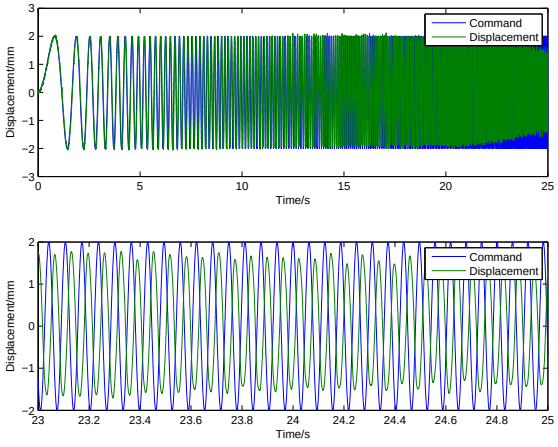

(c) IMC(T=0.006)

Figure 3.14: Time histories of displacements with different control strategies.

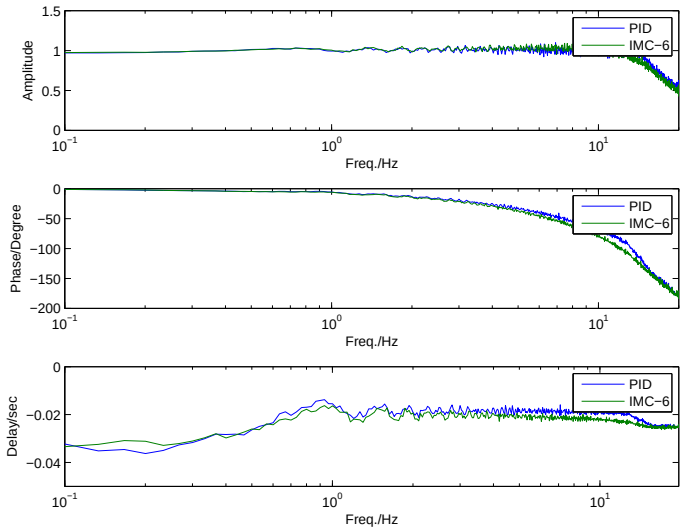

Figure 3.15: Comparisons in the frequency domain of the two control strategies.

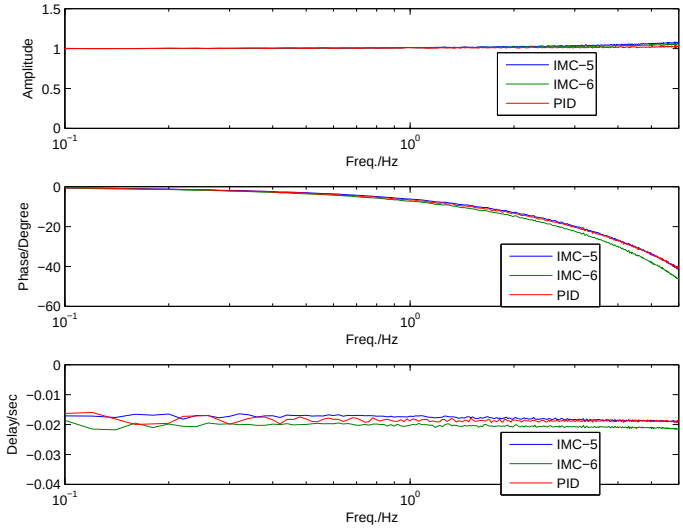

Figure 3.16: Comparisons of test results with the specimen in the frequency domain.

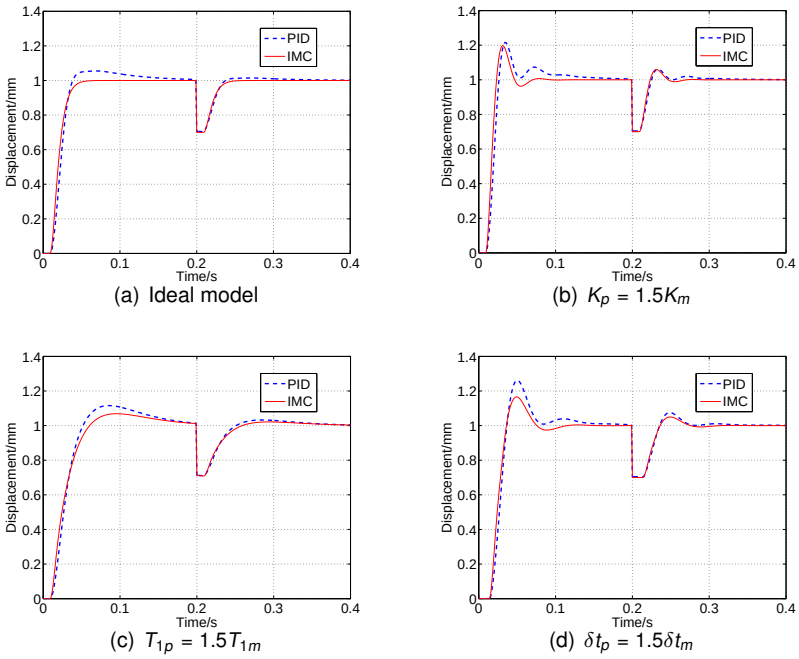

Figure 3.17: Simulations considering different uncertainties.

bance. In Figure 3.17(a), the identified model in Eq. (3.11) is used as the plant and plant model. Note that suberscripts of p and m mean 'Plant' and 'Model', respectively. In 3.17(b), (c) and (d), parameters uncertainties are considered by introducing 50% variation to a specific parameter in the plant. In addition, step change is applied at $t = 0$ while disturbance $d = -0.3$ at $t = 0.2s$. One can observe that (1) IMC exhibits faster and more accurate responses for setpoint changes; (2) both controllers can reject disturbance but IMC exhibits more favorable performance.

In this research, the actuator is dominated by a first-order model plus dead time. Therefore, numerical simulations in the time domain are carried out again in order to investigate performance of the IMC method for hydraulic servo actuators which often exhibit higher-order properties. The actuator herein is modeled by a second-order system (Wu et al., 2007), namely,

$$G_A(s) = \frac{K_A \omega_A^2 e^{-\tau_A s}}{s^2 + 2\xi_A \omega_A s + \omega_A^2} \tag{3.18}$$

in which ω_A and ξ_A denote the circular frequency and equivalent damping ratio, respectively; τ_A and s indicate the dead time of the system and the Laplace variable; K_A

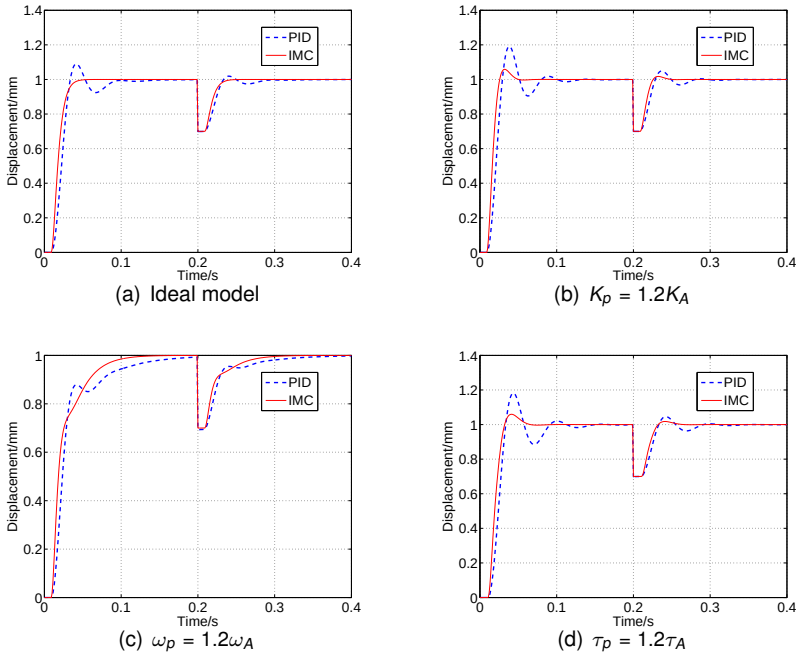

Figure 3.18: Simulations considering a second-order model and different uncertainties.

represents the static gain. In the simulations, ω_A = 80rad/s, ξ_A = 0.80, τ_A= 9ms and K_A =1 are set. Similarly to Figure 3.17, the CHR-PID is also designed for comparison in conjunction with step changes, step disturbance and parameter uncertainties. The results are depicted in Figure 3.18, from which one can observe that the IMC is more desirable than the CHR-PID. The time constant of the filter in the IMC is chosen as 5ms.

In summary, We draw the main conclusions before we move on to the next section:

① IMC is favorable in terms of the simple structure, the easier manner to achieve the trade-off between control objectives and so on;

② For the electromagnetic actuator control in the TT1 test rig, the IMC control and the PID tuned via the CHR method perform similarly;

③ When robustness is considered, the IMC control is superior to the PID control in terms of setpoint tracing and disturbance rejection, especially for a higher-order system.

3.6 Preliminary real-time hybrid simulation

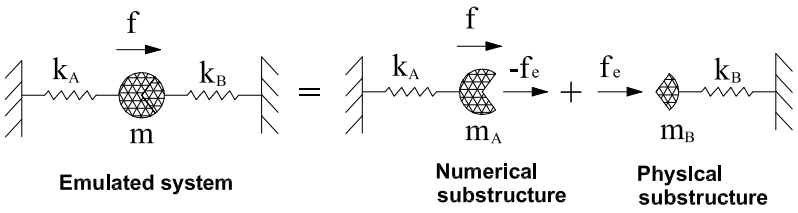

Figure 3.19: The emulated and split structures

RHS on a split mass system were carried out and are presented in this section. The emulated structure and substructures are schematically depicted in Figure 3.19, whilst the test rig is shown in Figure 3.20. For the sake of brevity, we consider only

Figure 3.20: The test rig of the real-time hybrid tests

Table 3.5: Characteristics of the NS and the PS

M_N	K_N	C_N	M_P	K_P	C_P
2989kg	426kN/m	3.57kNs/m	298.9kg	42.6 kN/m	5.3kNs/m

the translational movement of the specimen and therefore, the same commands were sent out to both actuators and the sum of the forces measured by the attached load cells to the actuators were fed back to the numerical substructure(NS). The structural parameters of the NS were chosen in such a way that the mass ratio and stiffness ratio of two substructures are 10 and the damping ratio of the NS is 5%, as illustrated in Table 3.5. A swept wave with the frequency from 0.1Hz to 5Hz and the amplitude 1406N was adopted to excite the emulated structure. The dynamic responses of the NS was evaluated by the LSRT2 method (Bursi et al., 2008) with the time step 9.7656ms. The IMC controller designed in the last section and the polynomial extrapolation scheme proposed by (Nakashima and Masaoka, 1999) were utilized to compensate for the dynamics and phase lag of the system.

The effectiveness of the delay compensation is illustrated in Figure 3.21. Loops between the command displacement and measured displacement are observed in Figure 3.21(a), which shows the phase discrepancy between two displacements. Clearly, if on compensation is implemented, the command is identical to the desired displacement and hence the same phase discrepancy between the desired displace-

ment and the measured displacement exists. This discrepancy implies delay which can lead to instability of the test. On the other hand, loops are almost eliminated between the desired and measured displacements, as shown in Figure 3.21(b), because of the delay compensation. Therefore, the compensation is successfully carried out and measured and desired displacements are almost synchronous. The time history of the displacement is illustrated in Figure 3.22 together with the numerically simulated result considering a linear specimen model. The agreement of the tested and simulated result in the figure shows that the test results are reliable.

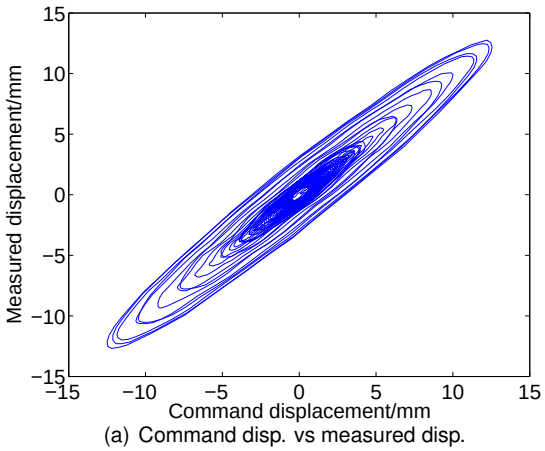

(a) Command disp. vs measured disp.

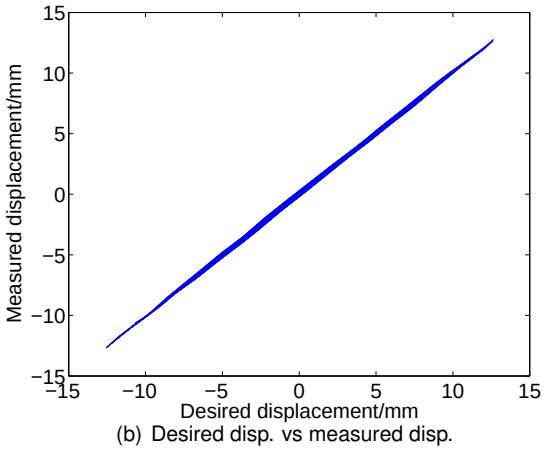

(b) Desired disp. vs measured disp.

Figure 3.21: Effectiveness of the delay compensation

3.7 Summaries and conclusions

The PID/PI control and the internal model control (IMC) are discussed and compared with the TT1 test system in this chapter accompanied by preliminary RHS on a split mass system. In detail, advantages and the design procedure of IMC are firstly introduced. The software for the speed loop of the electromagnetic motors is configured and the inner displacement loop is designed and identified. Then IMC and PID (sometimes as well as PI contol) for the outer displacement loop are implemented and compared in the frequency domain with swept sinusoidal waves and in the time domain with a step change. In addition, a preliminary RHS on a split mass system are conducted with the TT1 test system regulated by IMC. Analysis shows that IMC is preferable for its performance considering robustness and its ease to implementation. Numerical simulations of the test confirm that the test results are reliable and the system works well.

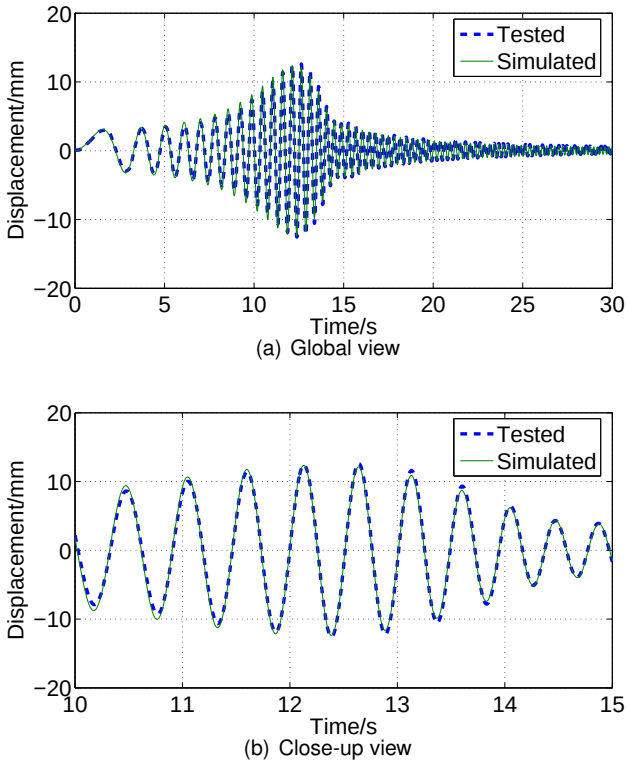

Figure 3.22: Tested and simulated time histories of displacement responses

CHAPTER 4

ONLINE DELAY ESTIMATION BASED ON SIMPLIFIED ACTUATOR MODELS FOR REAL-TIME HYBRID SIMULATION

4.1 Introduction

One of the most significant challenges involved in Real-time Hybrid Simulation(RHS) is delay effects and delay compensation. Since first identified in 1999 (Horiuchi et al., 1999), issues relevant to delay effects and compensation have been focused on in this field due to possible negative influence of system delay on test results. Delay herein is defined as the time from the displacement command being sent to the actuator and the actuator reaching the required position (Darby et al., 2002), resulting from the actuator inherent dynamics and information exchanges and hence inherently inevitable. Horiuchi et al. (1999) investigated the effect of delay in RHS and found that the delay is equivalent to negative damping to the structure when a stiffness specimen is taken as the physical substructure. If the negative damping is more than the actual damping of the structure, experiments will lose stability. In order to circumvent this problem, delay compensation in RHS was widely investigated and numerous compensation schemes were proposed, as reviewed in Chapter 2. Unfortunately, most schemes of them require delay information of the testing system, which should be identified in a prior test.

Further studies revealed that the system delay changes according to the specimen stiffness (Darby et al., 2002) and other possible causes, such as command frequencies and amplitude, and adaptive controllers. Therefore, online delay estimate

is essential for complex and large scale problems in order to obtain reliable experimental results. Some methods to online measure delay were developed by Darby et al. (2002) and Ahmadizadeh et al. (2008) and other researchers. These online estimation approaches and compensation methods constitutes adaptive delay compensation schemes. Wallace et al. (2005b) and Chen and Ricles (2009) proposed adaptive compensation scheme, respectively.

This chapter is dedicated to adaptive delay compensation based on a simplified actuator model. To some extent, actuators can be simplified to a pure delay multiplied by a gain representing amplitude errors. Along this line, nonlinear relationships among desired, commanded and measured displacements are established. In order to obtain the delay information, two classic techniques, namely Newton's method and the Taylor series expansion, are employed, resulting in two types of estimation schemes or adaptive laws in the framework of adaptive control. As the focus, the latter one is developed further by introducing the recursive least square algorithm with a forgetting factor to online estimate the delay of the system. The control amplitude error of the system can also be identified within this method. Successively, numerical simulations and realistic RHS with a stiffness specimen are carried out in order to examine the ability of this method to estimate and compensate for delay.

4.2 Adaptive delay compensation

Model reference adaptive control and self-tuning adaptive control are two most significant types of adaptive control. Here we concentrate on the latter for compensating for system delay in RHS. In RHS, delay can be measured with commanded and measured displacements, or with desired and measured displacements; and hence two varieties of adaptive control can be conceived, as shown in Figure 4.1. Clearly, the difference between two schemes is the adaptive law, which determines how to obtain/estimate the system delay according to the displacement time histories. So the next section focuses on the adaptive law based on a simplified actuator model. Note

that sometimes the adaptive law herein is called delay estimation since it aims to measure the system delay.

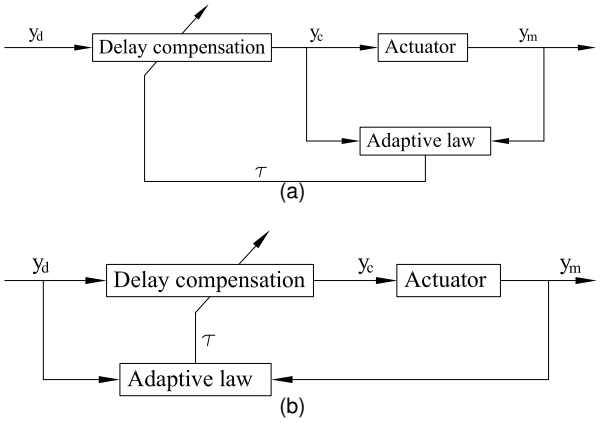

Figure 4.1: Adaptive delay compensation with different adaptive laws: (a) Based on commanded and measured displacements; (b) Based on desired and measured displacements.

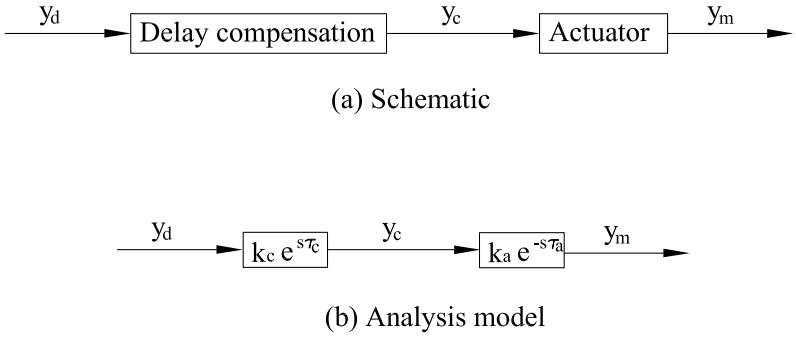

Figure 4.2: Schematic and analysis model of delay-compensated system.

4.3 Delay estimation based on simplified actuator model

The delay-compensated system is schematically depicted in Figure 4.2(a). Firstly, the command y_c is generated by applying a compensation scheme to the desired (analysed) displacement y_d with a constant delay. In order to smoothly drive the actuator, interpolation is frequently conducted (Nakashima and Masaoka, 1999) but not included in the figure. Then at the specified instant, the achieved displacement y_m of actuators is measured. As shown in Figure 4.2(b), the delay compensation and actuators are modeled by a pure delay times a gain reflecting the amplitude errors, which was justified by the research of Bonnet (2006). In Figure 4.2(b), τ_c denotes the estimated delay while τ_a the actual delay of the actuator. Therefore, we can formulate relationships between various displacements, i.e.

$$y_c(t_i - \tau_c) = k_c y_d(t_i) \tag{4.1}$$

$$y_m(t_i) = k_a y_c(t_i - \tau_a) \tag{4.2}$$

where gains k_a and k_c are referred to as amplitude factors. Eq. (4.2) shows that the measured displacement $y_m(t_i)$ is dependent on time and system delay. For simplicity, however, it is denoted by a function of time herein, namely $y_m(t_i)$. Inserting Eq. (4.1) into Eq.(4.2) yields

$$y_m(t_i) = k_a k_c y_d(t_i + \tau_c - \tau_a) \tag{4.3}$$

Evidently, if $\tau_c = \tau_a$, perfect delay compensation, with which there is neither any phase lag nor phase lead between the desired and measured displacements, can be achieved.

4.3.1 Use of Newton's method

4.3.1.1 Delay estimation between commanded and measured displacements

Eq. (4.2) can be regarded as a fixed point problem with an unknown τ_a and a constant $y_m(t_i)$. Therefore, Newton's method (Isaacson and Keller, 1994, Page 97) can be

applied to obtain the delay, i.e.

$$\tau_{a,i}^{(j+1)} = \tau_{a,i}^{(j)} - \frac{y_m(t_i) - k_a y_c(t_i - \tau_{a,i}^{(j)})}{k_a \dot{y}_c(t_i - \tau_{a,i}^{(j)})} \tag{4.4}$$

where $\tau_{a,i}^{(j+1)}$ represents the $j+1$-th iterate in the i-th time step; $y_c(t_i - \tau_{a,i}^{(j)})$ and $\dot{y}_c(t_i - \tau_{a,i}^{(j)})$ denote commanded displacement and velocity at the instant $(t_i - \tau_{a,i}^{(j)})$. They are available since $\tau_{a,i}^{(j)}$ is theoretically larger than zero. Note that Eq. (4.4) implies that there may be many iteration steps in one time step.

For a common nonlinear equation, Eq.(4.4) can be applied until convergence is achieved. However, in real-time tests, the iteration may be not convergent because of the limited time range before the estimated delay is required for compensation in the next step. Taking this into account, real-time iteration, which conducts single iteration in one time instant, is a more realistic solution. This method has been ever used for nonlinear optimization in optimal feedback control (Diehl et al., 2005). It is expressed as

$$\tau_{a,i+1} = \tau_{a,i} - \frac{y_m(t_i) - k_a y_c(t_i - \tau_{a,i})}{k_a \dot{y}_c(t_i - \tau_{a,i})} \tag{4.5}$$

Compared with Eq. (4.4), the superscript j is negected here since it is always zero. Appendix A of this dissertation provides a sufficient condition for convergence of this iteration. In this way, we attain the delay measure or an adaptive law based on the simplified system model with the commanded and measured displacements.

4.3.1.2 Delay estimation between desired and measured displacements

The purpose of delay estimation is to use it to compensate for delay. So the delay can be used as an intermediate variable in a closed-loop delay compensation scheme. Apparently, the delay should be adapted in order that the measured matches desired displacement as close as possible. To investigate the theoretic foundation of the adaptive law of the estimated delay τ_c, we take the actual system delay τ_a as an unknown parameter in this subsection rather than an unknown variable as determined by iteration in last subsection. Note that τ_a is not explicitly required to get τ_c in the actual test, since τ_a is inherently included in the actual actuator system and the target of adapting τ_c is to let the measured track the desired. If the dynamics can be represented by pure delay, then τ_c theoretically is equal to the system delay τ_a for

perfect compensation. From this analysis, the estimated delay τ_c should be so chosen that the realized or measured displacement matches the desired or calculated one, *i.e.*, τ_c should satisfy

$$y_m(t_i) = k_a k_c y_d(t_i + \tau_c - \tau_a) = y_d(t_i) \tag{4.6}$$

Note that Eq. (4.3) is substituted into this equation. Therefore, similarly to Eq. (4.5), τ_c can be obtained through real-time iteration as

$$\tau_{c,i+1} = \tau_{c,i} + \frac{y_d(t_i) - y_m(t_i)}{\dot{y}_m(t_i)} \tag{4.7}$$

Note that in implementation, y_m can not be replaced by $k_a k_c y_d$, since τ_a is unknown.

It is interesting to point out that this formula is similar to the method proposed by Ahmadizadeh et al. (2008), which reads

$$\tau_{a,i} = \tau_{a,i-1} + 2G\Delta t \frac{y^a_{d,i} - y^a_{m,i}}{y_{m,i} - y_{m,i-2}} \tag{4.8}$$

$$y^a_{d,i} = \frac{y_{d,i} + y_{d,i-1} + y_{d,i-2}}{3} \tag{4.9}$$

$$y^a_{m,i} = \frac{y_{m,i} + y_{m,i-1} + y_{m,i-2}}{3} \tag{4.10}$$

where G is a learning gain and the superscript a denotes the average of displacements in the last three steps. Rearranging Eq.(4.8) yields

$$\tau_{a,i} = \tau_{a,i-1} + G \frac{y^a_{d,i} - y^a_{m,i}}{v^a_{m,i-1}} \tag{4.11}$$

with the average velocity

$$v^a_{m,i-1} = \frac{y_{m,i} - y_{m,i-2}}{2\Delta t} \tag{4.12}$$

Eq. (4.7) will be reduced to Eq. (4.8) if a learning gain is introduced and Eq. (4.12) is applied to evaluate the measured velocity.

4.3.2 Use of Taylor series expansion

If $y_c(t_i - \tau_a)$ in Eq. (4.2) is expanded with the Taylor series expansion, we obtain

$$y_m(t_i) = k_a y_c(t_i) - k_a \dot{y}_c(t_i) \times \tau_a + k_a \frac{\ddot{y}_c(t_i)}{2!} \times \tau_a^2 - k_a \frac{\dddot{y}_c(t_i)}{3!} \times \tau_a^3 + ... \tag{4.13}$$

Thus $y_m(t_i)$ can be approximated by the first two terms in the right-hand side of Eq. (4.13), i.e.,

$$y_m(t_i) = k_a y_c(t_i) - k_a \dot{y}_c(t_i) \times \tau_a \tag{4.14}$$

Rearranging this formula gives

$$\tau_a = \frac{k_a y_c(t_i) - y_m(t_i)}{k_a \dot{y}_c(t_i)} \tag{4.15}$$

which indicates that the delay can be approximately evaluated once measured displacement, commanded displacement and velocity and amplitude gain k_a of the actuator are available.

As a by-product, Eq. (4.14) indicates the effect of delay in RHS. If the physical substructure is a stiffness specimen, the restoring force is

$$F(t_i) = k_E y_m(t_i) = k_E k_a y_c(t_i) - k_E k_a \dot{y}_c(t_i) \tau_a \tag{4.16}$$

where k_E is the stiffness of the specimen. If $k_a = 1$, Eq. (4.16) means that the physical substructure is of a spring and a viscous damper with a negative damping coefficient $-k_E \tau_a$. The conclusion is in agreement with Horiuchi et al. (1999) and Wallace et al. (2005a). Moreover, this analysis indicates that the conclusion that delay introduces negative energy is based on the assumption that higher-order differentiations are neglected. As a consequence, this conclusion may be not accurate when delay is relatively large. In the similar way, delay effects on mass and/or damper specimens can be investigated as well.

4.3.3 Pros and cons of the proposed methods

Newton's method is second-order convergent when the derivative of the function with respect to the variable is not equal to zero, whereas linearly convergent when it is zero. Hence, adaptive laws based on Newton's method are favourable for its usually rapid convergence and its convergence even at displacement peaks. As a practical application, however, there are some problems to be resolved. Pros and cons of these schemes are as follows:

① Eq.s(4.4) and (4.5) are favourable when amplitude errors due to control is negligible, namely, $k_a \approx 1$. Otherwise, k_a should be firstly estimated even though it may be not easy;

② Convergence of Eq. (4.7) does not imply that the ultimate aim expressed in Eq. (4.6) can be achieved for the case with $k_a k_c \neq 1$. This is because the solution τ_c^* does not exist. In other words, any τ_c can not satisfy Eq. (4.6) when $k_a k_c \neq 1$. Therefore, the gains must be identified if they are not equal to unity;

③ The velocity of the actuator is required in Eq. (4.7) and hence, it should be either numerically evaluated or physically measured in tests, and noise effects in velocity evaluation need to be reduced;

④ The case when the velocity at the denominator of the formulae is close or equal to zero should be cautiously considered in order to avoid sharp increments of estimated delay, since any minor error, e.g., measurement noise, can cause larger estimation errors or even instability.

Likewise, pros and cons of the adaptive law based on the Taylor series expansion are summarized as follows:

① This method is attractive for its ease of acceptance and of implementation;

② The scheme is based on a first-order approximation, which is a shortcoming. However, this may be acceptable since the delay in RHS is in the order of 0.01s, meaning the displacement error is about $0.5 \times 10^{(}-5)\ddot{y}_c$;

③ The estimated value is relevant to k_a and hence, it should be estimated if possible. In addition, measurement noise and zero velocity induce sharp increments and special treatment is required.

In order to improve the accuracy of Eq.(4.14), Padè approximation (Chi et al., 2010) may be a choice applied to expand the pure delay, rather than the Taylor series expansion in this chapter. This approximation results in the following formula instead of Eq. (4.14),

$$y_m(t_i) + \dot{y}_m(t_i) \times \frac{\tau_a}{2} = \mu y_c(t_i) - \mu \dot{y}_c(t_i) \times \frac{\tau_a}{2} \tag{4.17}$$

which means that the achieved velocity is required. Therefore, if velocity of the physical substructure is available, the framework of this paper can be employed with this approximation.

From these comments, we can see that they can not perform well in RHS until special treatments are applied. As an example, in the following parts of this chapter, we propose to apply the least square algorithm for the adaptive law based on the Taylor series expansion. In fact, it should be also possible to deal with these problems for the other schemes.

4.4 Online delay estimation with the Taylor series expansion and the least square algorithm

Eq. (4.14) means that the nonlinear relationship between commanded and measured displacements is linearized at t_i. Along this line, the relationship at different time instants can be represented by a series of this kind of linearized equations, though the delay and the amplitude error may be time-varying in RHS. Suppose the system changes slowly, online estimation approaches for linear time-varying systems can be applied to attain the system delay. In this equation, $\dot{y}_c(t_i)$ can be approximately expressed by backward differentiation, it is to say

$$\dot{y}_c(t_i) = \frac{y_c(t_i) - y_c(t_{i-1})}{\Delta t} \tag{4.18}$$

Note that $\dot{y}_c(t_i)$ can also be replaced by predicted velocities obtained by conducting extrapolation polynomials on desired velocities. Substituting Eq. (4.18) into Eq. (4.14), one attains

$$y_m(t_i) = \widehat{\theta}\mathbf{\Psi_i} \tag{4.19}$$

with

$$\widehat{\theta} = \begin{bmatrix} \theta_1 & \theta_2 \end{bmatrix} = \begin{bmatrix} k_a - \frac{k_a \tau_a}{\Delta t} & \frac{k_a \tau_a}{\Delta t} \end{bmatrix} \tag{4.20}$$

$$\boldsymbol{\Psi_i} = \begin{bmatrix} y_c(t_i) & y_c(t_{i-1}) \end{bmatrix}^{\mathbf{T}} \tag{4.21}$$

If there are two groups of $y_m(t_i)$ and $\boldsymbol{\Psi_i}$, the gain k_a and the delay τ_a can be solved from the above linear equations, namely

$$k_a = \theta_1 + \theta_2 \tag{4.22}$$

$$\tau_a = \frac{\Delta t \theta_2}{\theta_1 + \theta_2} \tag{4.23}$$

In view of displacement errors in RHS, it is advisable to apply the least square algorithm to estimate them. In essence, the gain k_a and the delay τ_a in RHS are time-varying as aforementioned; and hence the recursive least-square algorithm with a forgetting factor (Söderström and Stoica, 1989, Page 324) is a good candidate. This algorithm is suitable to online estimation for time-varying parameters because of its small storage size and low calculation efforts. The recursive formulae of the method are

$$\widehat{\theta}_i = \widehat{\theta}_{i-1} + \frac{\mathbf{P}_{i-1}\boldsymbol{\Psi}_i}{\boldsymbol{\Psi}_i^T \mathbf{P}_{i-1}\boldsymbol{\Psi}_i + \rho}[y_m(t_i) - \boldsymbol{\Psi}_i^T \widehat{\theta}_{i-1}] \tag{4.24}$$

$$\mathbf{P}_i = \frac{1}{\rho}\left[\mathbf{P}_{i-1} - \frac{\mathbf{P}_{i-1}\boldsymbol{\Psi}_i\boldsymbol{\Psi}_i^T\mathbf{P}_{i-1}}{\boldsymbol{\Psi}_i^T\mathbf{P}_{i-1}\boldsymbol{\Psi}_i + \rho}\right] \tag{4.25}$$

where ρ is the forgetting factor, $0<\rho\leq 1$. The greater the forgetting factor ρ is, the greater effect on the current estimated delay the previous data has. When ρ=1, the algorithm degenerates to the recursive least-square algorithm. As to the initial values for the recursive procedure, the standard least-square algorithm is recommended, which reads

$$\boldsymbol{\Psi}_1 = (\boldsymbol{\Psi}_1\boldsymbol{\Psi}_1^T)^{-1} \tag{4.26}$$

$$\widehat{\theta}_1 = \left(\boldsymbol{\Phi}^T\boldsymbol{\Phi}\right)^{-1}\boldsymbol{\Phi}^T\mathbf{Y} \tag{4.27}$$

$$\boldsymbol{\Phi} = \begin{bmatrix} \boldsymbol{\Psi}_1^T & \boldsymbol{\Psi}_2^T & \ldots & \boldsymbol{\Psi}_p^T \end{bmatrix}^T \tag{4.28}$$

$$\mathbf{Y} = \begin{bmatrix} y_m(t_1) & y_m(t_2) & \ldots & y_m(t_p) \end{bmatrix}^{\mathbf{T}} \tag{4.29}$$

where p means the group number of the data. Since the standard least-square algorithm was utilized to estimate the initial value for the recursive procedure, the first estimation obtains the current delay. Even though the desired displacement is small and the measured displacement is contaminated by measurement noises in real

tests, the method can rapidly and accurately converge since the estimated value is originated from overdetermined systems. If the matrix form is expanded, it needs not to calculate the inverse matrix and the calculation efforts are limited. In this sense, the proposed method is expected to be favourable. However, note that the estimated value is based on a first-order approximation and the estimated value cannot converge to the actual one.

4.5 Numerical simulations

This section carries out two types of numerical simulations, namely estimation of time-invariant and time-varying delays with the proposed method and simulations of RHS considering a second-order actuator model in conjunction with delay estimation and compensation. The latter implements adaptive delay compensation as shown in Figure 4.1, respectively.

4.5.1 Delay estimation with the proposed method

4.5.1.1 Time-invariant delay

Suppose that actuator commands are sinusoidal waves with the amplitude 1mm and the frequency 1Hz and that the actuator can be simplified to a pure delay with the dead time 10ms. In order to simulate random measurement noises, a random variable expressed as

$$w_i = \frac{X - 0.5}{50} y_{r,i} \tag{4.30}$$

is added to the actuator response to attain the measured displacement, i.e.,

$$y_{m,i} = w_i + y_{r,i} \tag{4.31}$$

where X denotes a random variable uniformly distributed in the set (0 1). Eq. (4.30) indicates that the noise amplitude is about 1% of the actuator response amplitude.

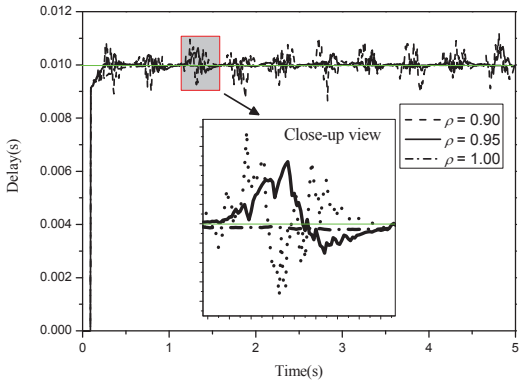

Figure 4.3: Time histories of the estimated delay of a time-invariant delay with the proposed method.

The method proposed herein was applied with the time interval 5 ms and $p = 20$. The estimated delay is illustrated in Figure 4.3. One can observe that the estimated delay of the standard least-square algorithm is about 90% of the final value. The following estimation is based on this result and therefore, the method exhibits favourable convergence speed. In addition, the estimated delay varies around the actual delay and the oscillation is affected by the forgetting factor. A larger factor renders the oscillation amplitude smaller. In summary, the proposed method exhibits good convergence speed and accuracy for constant system delay even though the method is based on an approximate expression, i.e., Eq. (4.14).

4.5.1.2 Time-varying delay

Herein we assume that the delay can be formulated as

$$\tau_a = 0.01 + 0.01 \times \sin(0.2\pi t) \tag{4.32}$$

In addition, the proportional gain 1.1 is adopted to simulate amplitude control errors of the actuator. All other parameters and conditions not especially stated here are employed with the same values as those in the last subsection. The estimated delay with different parameters is depicted in Figure 4.4. Clearly, the closer to 1 the forgetting factor is, the smoother the estimated delay history is. As an extreme case, it approaches the constant 0.01 when the forgetting factor equals 1. This indicates

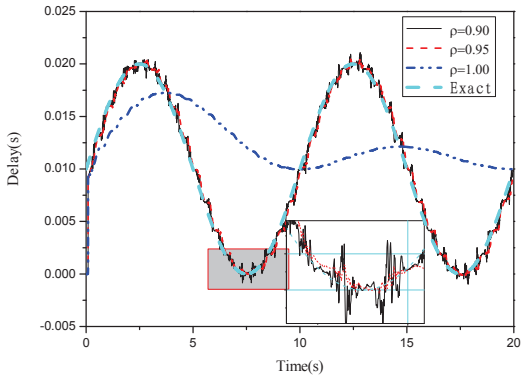

Figure 4.4: Time histories of the estimated delay of a time-varying delay with the proposed method.

that the estimated value cannot trace the actual change of the time varying parameter when ρ = 1, which is called data saturation phenomenon derived from summation of the effect with the same weight of all data on the estimated value(C. and D., 1988, Pages 159-160). In view of the accuracy and the oscillation, ρ = 0.95 may be a better choice. This simulation shows that the proposed method can trace the delay change even the noise and amplitude control errors exist in the system.

4.5.2 Numerical simulations of RHS with adaptive delay compensation

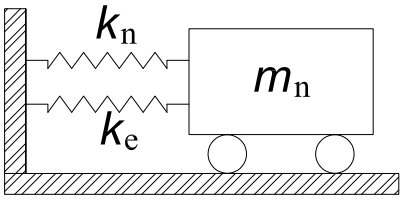

Figure 4.5: Computation schematic of the emulated structure in RHS.

The structural parameters are chosen in such a way that the natural period of the emulated structure is 0.5s and damping ratio 5%. The Tabas earthquake record (Ahmadizadeh et al., 2008) in Iran in 1978 with the peak acceleration 0.852g was utilized to excite the structure. In the analysis, mass and damping are simulated in the

numerical substructure and the spring is modelled as a specimen, as schematically depicted in Figure 4.5. In addition, the actuator is modeled by a second-order system, namely,

$$T_A(s) = \frac{\omega_A^2 e^{-\tau_A s}}{s^2 + 2\xi_A \omega_A s + \omega_A^2} \tag{4.33}$$

in which ω_A and ξ_A denote the circular frequency and equivalent damping ratio, respectively; τ_A and s indicate the dead time of the system and the Laplace variable. In the simulations, ω_A = 100rad/s, ξ_A = 0.80 and τ_A= 0 are set. It should be known that τ_A= 0 implies that the dead time of the system is zero but it does not mean that the delay of the system in RHS is zero. According to the fact that the delay is identical to the ratio of phase lag with respect to the corresponding frequency, the delay corresponding to the structural natural frequency, about 16.01ms, is viewed as the reference in the following simulations. Moreover, the Central Difference Method is used to evaluate the response of the structure with the time interval 10ms. Delay of the actuator is compensated for by means of the polynomial extrapolation proposed by Horiuchi et al. (1999) and developed by Nakashima and Masaoka (1999), expressed as

$$y_c(t_{i+1}) = \sum_{j=0}^{3} a_j y_a(t_{i+1-j}) \tag{4.34}$$

in which the factor $a_j$are calculated via Lagrange formulas.

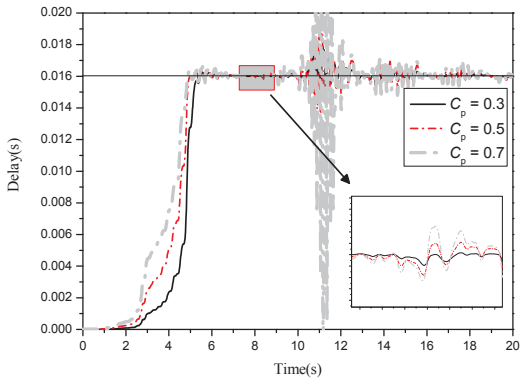

Figure 4.6: Time histories of the estimated delay with Darby's method.

Time histories of the estimated delay of Darby's method are shown in Figure 4.6. From the figure, larger parameters can cause fast convergence speeds and larger

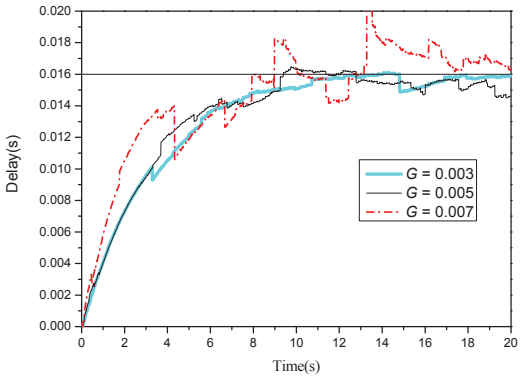

Figure 4.7: Time histories of the estimated delay with Ahmadizadeh's method.

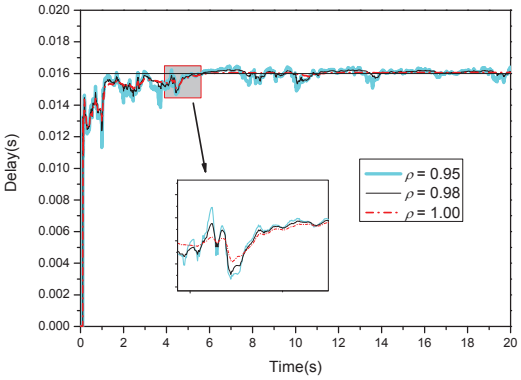

Figure 4.8: Time histories of the estimated delay with the proposed method.

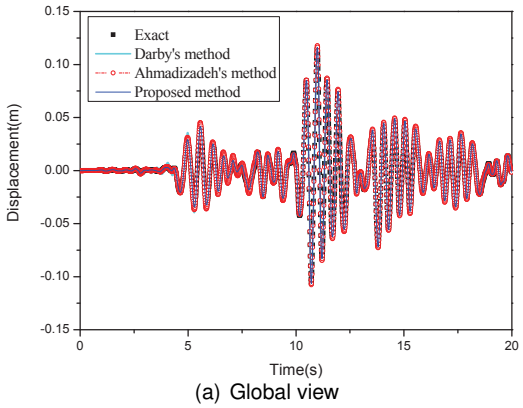

(a) Global view

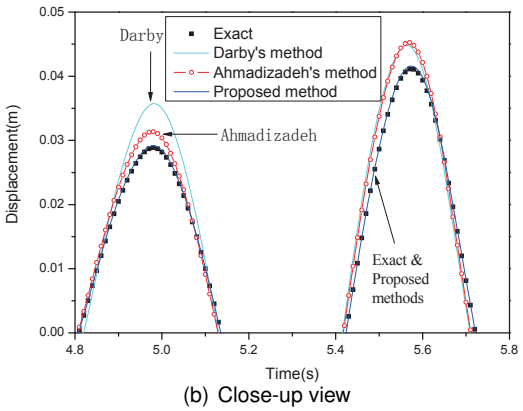

(b) Close-up view

Figure 4.9: Time histories of displacements in RTSs with different delay estimation approaches.

oscillations. Nonetheless, in the first five seconds, the estimated values are much less than the reference whatever the parameter is. This is due to the fact that the method responds slowly if the relative position errors are small, as aforementioned. The estimated value may oscillate dramatically or even be unstable at the peak of the relative position errors if the parameter is not suitable. Therefore, the parameter value is limited by this peak. For the sake of stability, only smaller parameters are feasible even though it may mean slow response speeds. Meanwhile, time histories of the estimated delay of Ahmadizadeh's method are illustrated in Figure 4.7. Similarly, the estimated values are smoother with respect to time when the parameter is smaller. However, sharp changes are observed if increasing the parameters.

Time histories of the estimated delay provided by the proposed method with the forgetting factor 0.95, 0.98 and 1.00 are plotted in Figure 4.8. Obviously, smaller forgetting factors result in larger oscillations of the estimated values. When ρ = 1.00, the method are favourable in terms of the accuracy and response speed, which is in agreement with results in the previous section. However, commands in these simulations are complex and consists of a series of frequency components. This implies that the variation of the delay in this specific problem is small.

Time histories of displacement responses with three estimation methods and parameters C_p = 0.3, G = 0.003, ρ = 1.00 are plotted in Figure 4.9. For Darby's method, the error in the first five seconds are a little larger followed by smaller error in the next 15 seconds. Ahmadizadeh's method causes larger response amplitudes due to smaller estimated-delay than the reference delay. Conversely, the displacement responses with the proposed estimation method match the exact results best.

From these simulations, the following conclusions are drawn:

① Darby's method converges slowly due to the feasible but smaller parameter determined by the peak of relative position errors;

② Ahmadizadeh's method exhibits almost random sharp changes even without noise and is sensitive to the learning gain;

③ The proposed method exhibits comparative advantages, such as suitable to online estimation and to treat noise-contaminated data, ease to determine the parameter and favourable convergence speeds and accuracy.

Validation tests were carried out at the Mechanical and Structural Testing Center of the Harbin Institute of Technology. The schematic diagram of the overall emulated structure is shown in Figure 4.5. A buckling-restrained brace (BRB), on which further information can be found in (Li, 2007, in Chinese), was regarded as the experimental substructure. A photograph of the experimental substructure installed on the MTS servo-hydraulic actuator is illustrated in Figure 4.10. In the tests, computation of the time-discretized equation of motion, delay estimation and delay compensation were performed in Calculation Editor of the control system of MTS servo-hydraulic actuator, i.e. Flex Test GT (MTS) (Corporation, 2001). Calculation Editor provides an easy way to online process signals by programming.

Figure 4.10: Photograph of test set-up for RHS.

The initial stiffness of the physical substructure was assumed 144×10^6N/m while the stiffness of the numerical substructure was chosen as half of that, i.e., K_N = 72×10^6N/m. The mass of the system was chosen in such a way that the circular

frequency of the overall structure was $2\pi s^{-1}$ for all test cases if the BRB is linear. The damping of the numerical substructure was assumed zero. The Central Difference Method was used to solve the equation of motion with the integration time interval 4.902ms. The third-order polynomial extrapolation was carried out to compensate for the system delay. In view of the delay about 18ms which was about three times of the integration time interval, the following equation was employed

$$y_c(t_{i+1}) = \sum_{j=0}^{3} a_j y_a(t_{i+1-2j}) \tag{4.35}$$

The factor a_j are calculated by Lagrange formula. In addition, the whole structure was subjected to El Centro (1940, NS) earthquake.

4.6.1 Linear specimens

In order to let the specimen behave linearly, the peak acceleration of the excitation was tuned to 16 m/s2. Figure 4.11 and Figure 4.12 show the estimated delay histories and displacement histories when Ahmadizadeh's method was applied. Tests with the learning gain G= 0.001 were repeated for twice in order to investigate its repeatability. When G is 0.0005, the estimated delay is smaller than the reference delay, about 18ms, estimated in a prior study. When the learning gain G increases to 0.001, the estimated delay histories exhibits sharp changes which happen almost randomly. Owing to the sharp changes, the estimated delay in the first test with G=0.001 is greater than the reference delay while the second in the same time range is less than that. From the figure, the estimated delay in the first three seconds with G=0.0005 is zero. In fact, the estimated delay is negative due to sharp changes, and it is set to be zero to stabilize the test. Therefore, these results show that the approach not only is a little sensitive to the parameter but also exhibits unsatisfactory repeatability.

According to Figure 4.15, the actual initial stiffness of the BRB is around 148.07×10^6 N/m. Then the response of the structure is evaluated considering this value, which is denoted by "simulated" in Figure 4.12. Compared with the simulated response of the structure, tested displacements are either greater or smaller, in agreement with the estimated delay histories in Figure 4.11 considering negative damping introduced by a delay for a stiffness specimen.

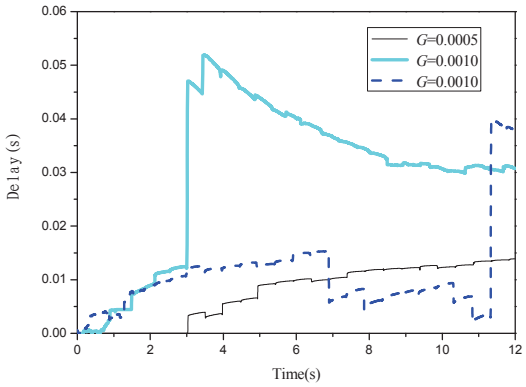

Figure 4.11: Time histories of the estimated delay with Ahmadizadeh's method in linear tests.

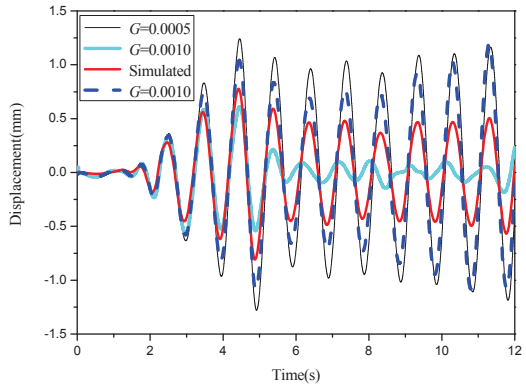

Figure 4.12: Time histories of displacement responses with Ahmadizadeh's method in linear tests.

It should be mentioned that the sharp change of estimated delay also happens in Ahmadizadeh et al. [2008], but increments are smaller. The increments may be related to structural responses, the integration time interval, the actuator dynamics, the excitation and other parameters and conditions. The increment of the estimated delay expressed in Eq. (4.8) may be greater in this case, since the integration time interval and the structure response is smaller, which means the value of $(y_{m,i} - y_{m,i-2})$ is smaller. Different displacement noises of two cases also result in the discrepancy of the increments.

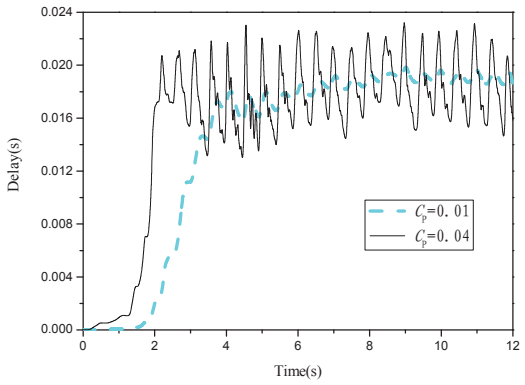

Figure 4.13: Time histories of the estimated delay with Darby's method in linear tests.

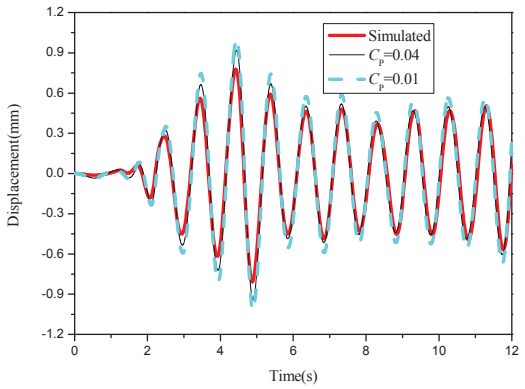

Figure 4.14: Time histories of displacement responses with Darby's method in linear tests.

The estimated delay histories with Darby's method are plotted in Figure 4.13. It takes around four seconds for the estimated delay to reach the final value for the first

time when C_p=0.01 is utilized while the rising time is about two seconds with C_p=0.04 applied. Meanwhile, the amplitudes of oscillations increase. Therefore, for Darby's method, it is inconsistent to increase convergence speed with declining the oscillation amplitude of the estimated delay. The algorithm is a little sensitive to the parameter since the oscillations increase much when the parameter increase from 0.01 to 0.04. Moreover, the parameters in previous numerical simulations and in Darby et al. [2002] are different from the parameters in this test, and hence in every test there are few helpful experiences to establish the parameter, and the only thing to do is to tune the parameter through real tests for the specific cases. In this sense, it is not convenient to apply Darby's method when the specimen is easy to damage.

Figure 4.14 shows the desired displacements in two tests and the numerically predicted response of the structure. In the figure, the solid line matches the simulated response better than the dashed line, which indicates that the estimated delay with C_p=0.04 is more accurate. It is worth noting that although the oscillation does not induce instability, we are not confident that the test is stable when the parameter keeps increasing. An algorithm that is endowed with rapid convergence speed and limited oscillations of estimated-delay is desired. Figure 4.15 depicts the force-displacement relationship of the specimen obtained in the test with C_p=0.04. The fitted solid line indicates the stiffness 148.07$\times 10^6$N/m.

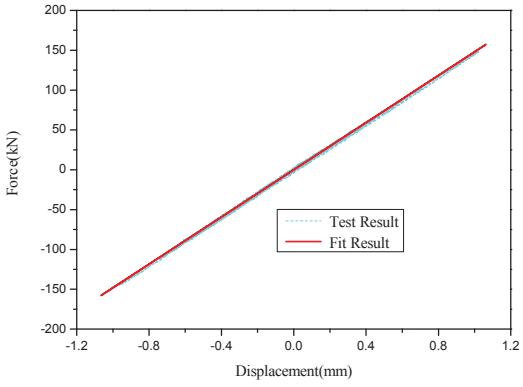

Figure 4.15: Force-displacement relationship of the specimen in a linear test.

Figure 4.16 presents the estimated delay of the proposed method with the forgetting factor ρ=0.98 and ρ=0.99 compared with that provided by Darby's method.

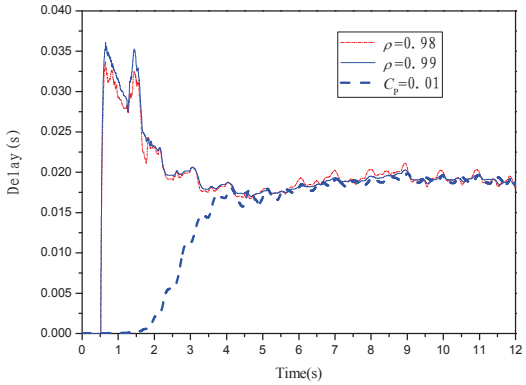

Figure 4.16: Comparisons of the estimated delay between the proposed method and Darby's method in linear tests.

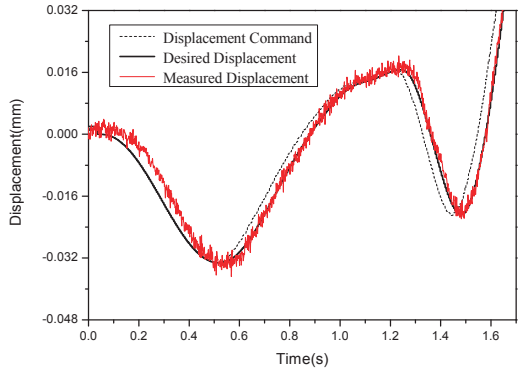

Figure 4.17: Close-up view of the displacement histories with the proposed method (ρ = 0.99).

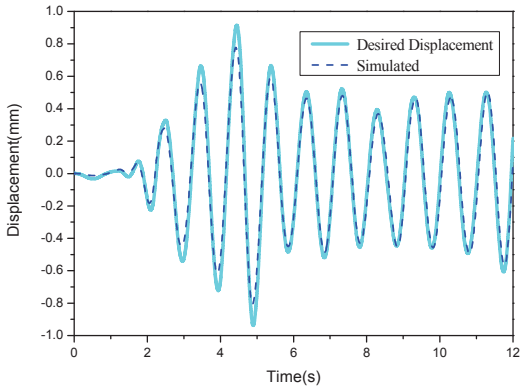

Figure 4.18: Displacement time history with the proposed method in linear tests (ρ = 0.98).

Evidently, the two tests of the proposed method provide similar delay histories and gives similar estimated values to Darby's method after the first four seconds. In the first four seconds, the estimated values by the proposed method are much greater than those provided by Darby's method. However, as shown in Figure 4.17, the delay is not over-compensated for in the beginning of the test and therefore the estimated delay of Darby's method is less than the actual delay. In fact, it is likely that the delay is greater in this stage since the loading system has to start to move. In addition, the tested displacement provided in the simulation with ρ=0.98 matches the predicted displacement well, as shown in Figure 4.18.

4.6.2 Nonlinear specimen

In this section, the peak acceleration of the earthquake record is tuned to 120m/s2. Because of its weakness, Ahmadizadeh's method was not utilized to conduct the RHS in this section. Figure 4.19 shows the estimated delay histories with Darby's method, which exhibits some oscillations. The desired displacement obtained in the test with C_p=0.01 and the displacement response of the structure without delay compensation are plotted in Figure 4.20, which shows that they are not greatly different. This is because the hysteretic dissipation of the specimen is so strong that the equivalent

negative damping due to the delay affect less results. The hysteretic curve of the specimen obtained in the test with C_p=0.01 is shown in Figure 4.21 and the maximum displacement about 4mm and the maximum restoring force 400kN are observed.

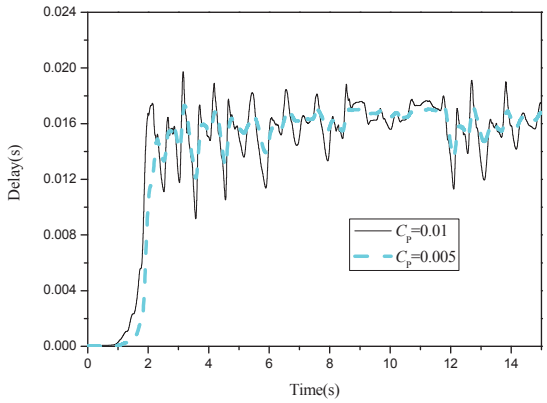

Figure 4.19: Time histories of the estimated delay with Darby's method in nonlinear tests.

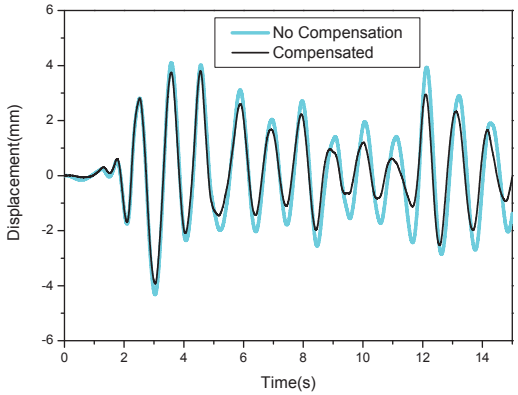

Figure 4.20: Time histories of displacement responses with and without delay compensation.

Figure 4.22 and Figure 4.23 plot the estimated delay histories and the desired displacement with the proposed method, respectively. In order to investigate the repeatability, each test was carried out for twice. Figure 4.22 also illustrates the similar characteristics as described above. However, the delay oscillation is smaller. In fact,

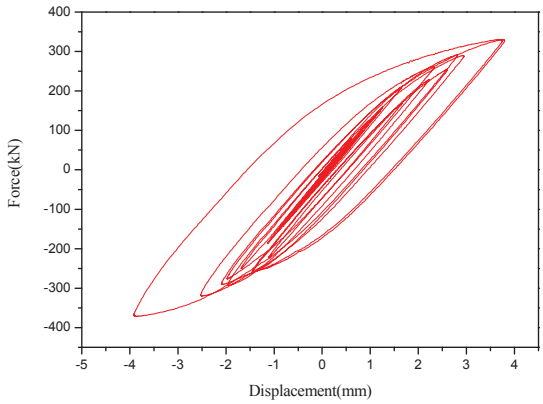

Figure 4.21: Hysteresis curve of the specimen in nonlinear ranges.

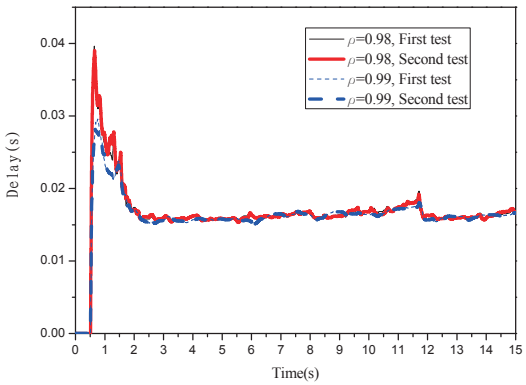

Figure 4.22: Time histories of the estimated delay with the proposed method in nonlinear tests.

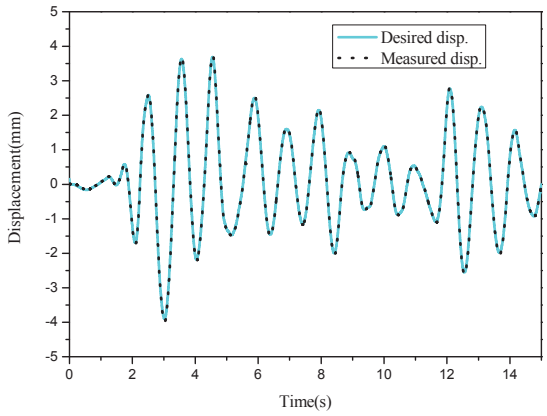

Figure 4.23: Desired displacement and measured displacement in RHS with the proposed method (ρ = 0.98, second test) in nonlinear tests

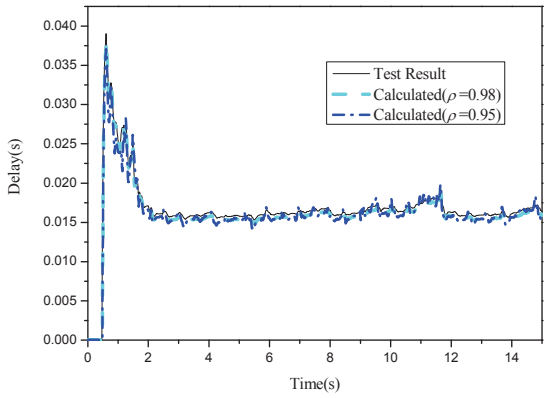

Figure 4.24: Comparisons of online and off line estimated delays with the proposed method.

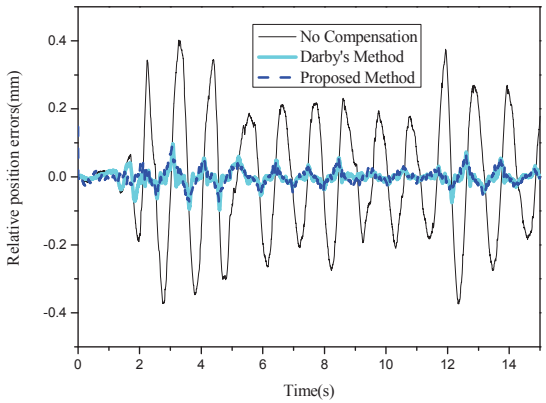

Figure 4.25: Comparisons of relative position errors.

the proposed method measures the system delay with the displacement command and measured displacement, therefore the delay could be measured off line, different from the Ahmadizadeh's and Darby's methods. With different parameters, the estimated delay histories are plotted in Figure 4.24. The figure shows the off line estimated-delay histories with ρ = 0.95 and ρ = 0.98 are almost the same as the on-line measured results. As discussed before, the algorithm can effectively trace time-varying delay with ρ=0.95, and hence the delay in the nonlinear test may not change greatly. Actually, the MTS facility has a loading capacity of 2500kN, around 6.3 times more than the maximum restoring force and thus in the test the non-linearity of the actuator is not apparent. Therefore, the delay does not greatly vary in the simulations.

Figure 4.25 shows the relative position errors, which are almost the same after the first five seconds even though the estimated delay histories are different. In the first five seconds, the error is a little larger in the tests with Darby's method due to the estimated delay smaller than the actual one.

4.7 Summaries and conclusions

In this chapter, two types of delay estimation approaches, also known as adaptive laws in the framework of adaptive control, are conceived based on a simplified actuator model with Newton's method and the Taylor series expansion. The recursive least square algorithm is then incorporated into the one relevant to the Taylor series expansion in order to circumvent application problems, such as measurement noises and amplitude errors due to actuator control, resulting in a practical estimation method. Numerical simulations and realistic RHS are carried out to examine the ability of this method for estimating and/or compensating for system delay. From this research, we can conclude that: (i) the proposed method can treat estimation problems of time-invariant and time-varying delays even with amplitude control errors and measurement noises; and (ii) this method is preferable in terms of its convergence speed and accuracy in linear and nonlinear RHS.

CHAPTER 5

TWO NOVEL DELAY COMPENSATION SCHEMES IN REAL-TIME HYBRID SIMULATION

5.1 Introduction

Real-time Hybrid Simulation (RHS) (Nakashima et al., 1992; Saouma and Sivaselvan, 2008; Bursi and Wagg, 2008; Wu et al., 2009; Bursi et al., 2008), as a novel technique for evaluating dynamic responses of structures, draws much attention in the past two decades. Up to now, much literature is available in this field on integration algorithms (Bonnet et al., 2008; Chen and Ricles, 2008a; Lamarche et al., 2009), delay compensation (Ahmadizadeh et al., 2008; Wallace et al., 2005b), control strategies (Neild et al., 2005; Zhao et al., 2003) and its applications (Wu et al., 2011b; Lamarche et al., 2010; Lee et al., 2007). However, it appears to be not ready for multiple DOF (MDOF) applications due to computation burdens, delay compensation for higher frequency signals, as well as control for larger loads and complex signals. In this chapter, we treat the delay compensation and error reduction for this kind of applications.

Delay compensation is often evaluated by frequency response function (Ahmadizadeh et al., 2008; Nakashima and Masaoka, 1999). However, this seems to be not enough, in that the delay compensation is only one portion of RHS among delay estimation, integration and transfer system control. From the view point of the integration, movement quantities of the Numerical/Computational Substructure (NS) obey different formulae from the corresponding quantities of the Physical/Experimental Sub-

structure (PS) due to delay compensation. Moreover, even they have the same formula, different step intervals result in different errors compared with exact ones. As a consequence, the conditions for the integrations, including the equations of motion and the approximation expressions, are often violated in RHS due to delay compensation. Hence, numerical properties of an integrator in RHS often degrades. Integration methods exhibit worse properties in RHS (Wu et al., 2009, 2005; Bursi et al., 2011) due to a similar violation between the PS and the NS. With this in mind, the performance of delay compensation should be analysed together with the integrators. As it will be shown, better performance according to the frequency response function of a delay compensation method does not indicate better performance of the RHS.

Another problem related to delay compensation is that the latest velocity target is often neglected. Wu et al. (2005) firstly recognized that in RHS conventional explicit integrators for pseudo-dynamic tests may reduce to implicit methods and analysed the stability of the central difference method (Wu et al., 2005) and the operator splitting method (Wu et al., 2006) with linearly-interpolated commands. Following that, integrators, which are explicit for both displacement and velocity, are proposed and applied, among others, see Chen and Ricles (2008a); Lamarche et al. (2009). However, even thought it is declared explicit, the velocity target is often neglected in tests. Furthermore, sometimes the latest displacement is not utilized in delay compensation either, since the velocity and acceleration at the same instant are not available. For example, the delay compensations based on displacement approximations of the explicit Newmark method (Ahmadizadeh et al., 2008) and the linear acceleration method (Ahmadizadeh et al., 2008; Horiuchi and Konno, 2001) are of this type. Note that the achieved velocity of an ideal actuator yields to the velocity target in Wu et al. (2005, 2006), indicating that the numerical analysis may match well with real tests. Nonetheless, this is not the fact for some other aforementioned papers, since the velocity target may be not achievable with the specified interpolation to generate actuator commands.

One natural question following these two problems is how to improve the performance of the tests. And it is clear that this can not be solved by improving the numerical integration methods and the delay compensation separately. Here we propose a strategy to determine the feedback force from the PS to enhance the test perfor-

mance. Nowadays the digital control is overwhelming in RHS and the measured force is always fed back to the NS according to the system timer. We refer to this strategy as time-stepped force feedback. Conversely, a new strategy characterized by delay overcompensation and optimal feedback is proposed and examined herein by simulations and real tests. Not only for delay compensation helpful is the strategy, but also for data post-processing and control.

The reminder parts of this chapter are organized as follows. In Section 2, assessment of delay compensation via spectral stability analysis is highlighted, illustrating influence of delay compensation on the stability of the method. Following that, in Section 3, a new delay compensation considering the latest displacement and velocity targets is conceived and analysed in terms of the frequency response function and the stability in conjunction with the Rosenbrock-based L-stable real-time compatible two stage (LSRT2) method (Bursi et al., 2008). The newly-developed force feedback aforementioned is described in detail in Section 4 even though the essence is straightforward. Numerical simulations are performed in Section 5 to show the effectiveness of the proposed strategy. Section 6 presents three tests designed and carried out to verify the analysis and the effectiveness of the force feedback strategy. Finally, conclusions are drawn in Section 7 followed by a discussion on future work.

5.2 Assessment of delay compensation via spectral stability analysis

Delay in RHS is believed to be inevitable, since its sources are the phase lag of the transfer system and time required for information exchange. In this sense, the delay compensation is also inevitable. In available literature, delay compensation approaches can be classified into two types: i) to reduce the system delay via inverse control (Carrion et al., 2009), outer loop control (Bonnet et al., 2007) and other control techniques (Jung and Shing, 2006); ii) to predict the desired displacement or modify the measured force (Ahmadizadeh et al., 2008). Among them, displacement prediction based delay compensation, especially the polynomial compensation approaches, are

extensively applied due to its ease of implementation and effectiveness. Therefore, we focus on polynomial compensation approaches, schematically illustrated in Figure 5.1. From the figure, we can see that the method firstly evaluates the structural responses at t_{i+1} (denoted by Step ① in the figure), and then predicts the structural responses at $(t_{i+1} + \tau_c)$ (Step ②), which is used to generate commands during the subsequent interval and will be immediately sent out at t_{i+1} (Step ③). Therefore, the essence of the method is to shift the time axis of the command by the system delay τ to eliminate discrepancies between desired and actual displacements. In addition, when the shift time τ_c is greater than the system delay τ, overcompensation is achieved, which is the case we will discuss further in Section 4. The polynomial is only a method to predict the structural response and to render the shift possible. Unfortunately, the predicted responses are theoretically different from the ones evaluated by the integrator, therefore, the conditions of the approximation of the integrator are violated. Literature confirms that violations due to measures to render the algorithm explicit and subcycling (Wu et al., 2009, 2005; Bursi et al., 2011) can degrade the numerical performance. Along this line, we anticipate that delay compensation also worsens stability and accuracy of an algorithm.

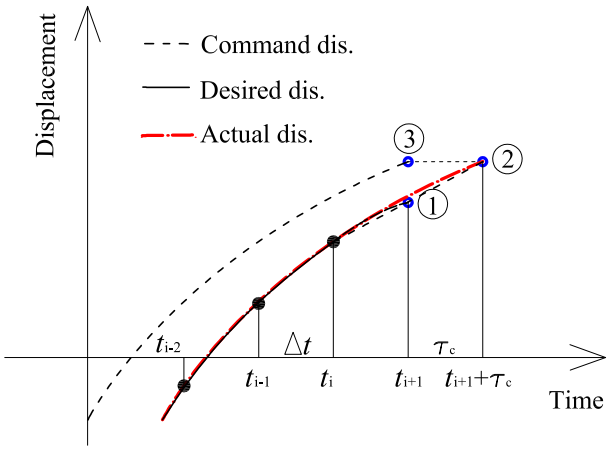

Figure 5.1: Schematic of the polynomial delay compensation.

As mentioned in Section 1, assessment of delay compensation via frequency response function is not satisfactory, since it just shows the prediction properties rather than properties of RHS. For further investigating different delay compensation meth-

ods, spectral stability analysis on a single-DOF system is carried out herein provided a known constant delay. The specimen is assumed to be a spring not only to simplify the problem but also to demonstrate the worst case, since the delay equivalently introduces negative dissipation to RHS with a spring specimen.

The equation of motion of the entire structure in RHS is descritized by the explicit Newmark method herein, i.e.

$$m_n\ddot{x}_{i+1} + c_n\dot{x}_{i+1} + r_{n,i+1} + r_{e,i+1} = f_{i+1} \tag{5.1}$$

$$x_{i+1} = x_i + \Delta t\dot{x}_i + \frac{1}{2}\Delta t^2\ddot{x}_i \tag{5.2}$$

$$\dot{x}_{i+1} = \dot{x}_i + \frac{1}{2}\Delta t(\ddot{x}_i + \ddot{x}_{i+1}) \tag{5.3}$$

where m, c and r indicate the mass, damping coefficient and restoring force, respectively; subscripts n and e denote the NS and PS; Δt is the time interval; the restoring force $r_{e,i+1} = m_e\ddot{x}_{e,i+1} + c_e\dot{x}_{e,i+1} + k_e x_{e,i+1}$. This method is conditionally stable for monolithic problems and the stability condition is

$$\Omega \leq 2 \tag{5.4}$$

Even though it does not offer the explicit velocity and acceleration, this method was applied to RHS for a system up to 50 degrees of freedom (Bonnet et al., 2008).

In order to compensate for the delay, two polynomial methods based on approximations of integrators are employed herein, i.e. the explicit Newmark method (Ahmadizadeh et al., 2008) and the linear acceleration method (Ahmadizadeh et al., 2008; Horiuchi and Konno, 2001). The former one (called as the explicit Newmark method herein) can be expressed as

$$x(t_{i+1} + \tau)' = x_i + (\Delta t + \tau)\dot{x}_i + \frac{1}{2}(\Delta t + \tau)^2\ddot{x}_i \tag{5.5}$$

while the latter (referred to as the linear acceleration method) reads

$$\begin{aligned} \ddot{x}(t_{i+1} + \tau)' &= \ddot{x}_i + \tfrac{\Delta t+\tau}{\Delta t}\left(\ddot{x}_i - \ddot{x}_{i-1}\right) = (2+\eta)\,\ddot{x}_i - (1+\eta)\,\ddot{x}_{i-1} \\ x(t_{i+1} + \tau)' &= x_i + (\Delta t + \tau)\,\dot{x}_i + \tfrac{1}{3}\,(\Delta t + \tau)^2\,\ddot{x}_i + \tfrac{1}{6}\,(\Delta t + \tau)^2\,\ddot{x}' \end{aligned} \tag{5.6}$$

with

$$\eta = \frac{\tau}{\Delta t} \tag{5.7}$$

where $x(t_{i+1}+\tau)'$ denotes the predicted displacement response of the emulated structure at $(t_{i+1}+\tau)$. The former method and the latter one are of second-order and third-order, respectively. In addition, the former one performs the same expression as the integration displacement approximation while the latter does not. In order to compensate for the delay τ, $x(t_{i+1}+\tau)'$ should be sent out to actuators at t_{i+1}, and therefore the actual displacement response of actuators at t_{i+1} is $x(t_{i+1})'$ provided that the actual delay is τ. A closer look at these schemes shows that the displacement of the NS at t_{i+1} expressed in Eq. (5.2) is not used since velocity and acceleration at t_{i+1} are not available. This means that the delay compensation is not implemented with the latest information even though the explicit displacement targets are available. Meanwhile, integrators providing explicit displacement and velocity are lately developed and applied. With these in mind, two compensation schemes considering latest velocity and displacement targets are proposed in the subsequent section.

With the assumption of a perfectly-estimated constant delay $\tau = \Delta t$ and perfect control, the restoring force of a linear spring specimen reads

$$r_{e,i+1} = k_e x_{e,i+1} = k_e x(t_{i+1})' \tag{5.8}$$

In practice, $x_{e,i+1}$ is not necessarily identical to x_{i+1} due to delay estimation, delay compensation and transfer system control. Effects of this violation are assessed by means of spectral analysis. In detail, RHS with either Eq. (5.5) or Eq. (5.6) yield the recurrence expression

$$\mathbf{X}_{i+1} = \mathbf{A}\mathbf{X}_i \tag{5.9}$$

in which $\mathbf{X}$ denotes the state vector and $\mathbf{A}$ the amplification matrix. For the explicit Newmark compensation, both of them are defined as

$$\mathbf{X}_i = [x_i \;\; \Delta t\dot{x}_i \;\; \Delta t^2\ddot{x}_i \;\; x(t_{i+1})']^T \tag{5.10}$$

and

$$\mathbf{A} = \begin{bmatrix} 1 & 1 & 1/2 & 0 \\ -\Omega_N^2/2 & 1-\Omega_N^2/2 & 1/2-\Omega_N^2/4 & -\Omega_E^2/2 \\ -\Omega_N^2 & -\Omega_N^2 & -\Omega_N^2/2 & -\Omega_E^2 \\ 1 & 2 & 2 & 0 \end{bmatrix}. \tag{5.11}$$

while for the linear acceleration compensation as

$$\mathbf{X}_i = [x_i \;\; \Delta t\dot{x}_i \;\; \Delta t^2\ddot{x}_i \;\; \Delta t^2\ddot{x}_{i-1} \;\; x(t_{i+1})']^T \tag{5.12}$$

and

$$\mathbf{A} = \begin{bmatrix} 1 & 1 & 1/2 & 0 & 0 \\ -\Omega_N^2/2 & 1-\Omega_N^2/2 & 1/2-\Omega_N^2/4 & 0 & -\Omega_E^2/2 \\ -\Omega_N^2 & -\Omega_N^2 & -\Omega_N^2/2 & 0 & -\Omega_E^2 \\ 0 & 0 & 1 & 0 & 0 \\ 1 & 2 & 10/3 & -4/3 & 0 \end{bmatrix} \tag{5.13}$$

where $\Omega_N^2 = \Delta t^2 k_n/m$ and $\Omega_E^2 = \Delta t^2 k_e/m$. Then the stability can be investigated by examining the eignvalues of the amplification matrix, as plotted in Figure 5.2 provided that $k_e = k_n$, $c_e = 0$, $m_e = 0$ and

$$\Omega = \sqrt{\frac{k_n + k_e}{m_n}}\Delta t. \tag{5.14}$$

In the figure, dissipation and stability limit reduction are observed for the first mixed method while the second one is not stable in a small range of Ω close to zero. This implies that the structural circular frequency ω can not be higher than 82.5 rad/s in RHS with Δt=0.01s and τ=0.01s when the first method is applied. On the other hand, if Δt=τ=0.02, then the condition is $\omega < 41.25$ rad/s. Sometimes in order to obtain stable and more accurate results, the time interval is reduced. However, this is not suitable for the second method due to its instability. One may argue that the maximum eigenvalue is very close to 1 even though greater than 1. In fact, taking Δt=0.005s and Ω=0.2828 (equivalently ω= 56.56 rad/s) for example, the amplitude increases from 1 to 2.2 in 25s, which is unacceptable. Therefore, when these methods are employed for MDOF, problems of accuracy and stability should be carefully examined.

On the other hand, these figures show that it is not enough only to evaluate the frequency response function of a delay compensation method. The linear acceleration polynomial exhibits better accuracy and phase overcompensation, as shown in Ahmadizadeh et al. (2008), also in the next section, however, this does not necessarily mean that it can provide better results in RHS for MDOF systems. More examinations should be carried out taking into account the integrations before real tests, instead of examining only the compensation methods (Ahmadizadeh et al., 2008; Nakashima and Masaoka, 1999; Horiuchi et al., 1999).

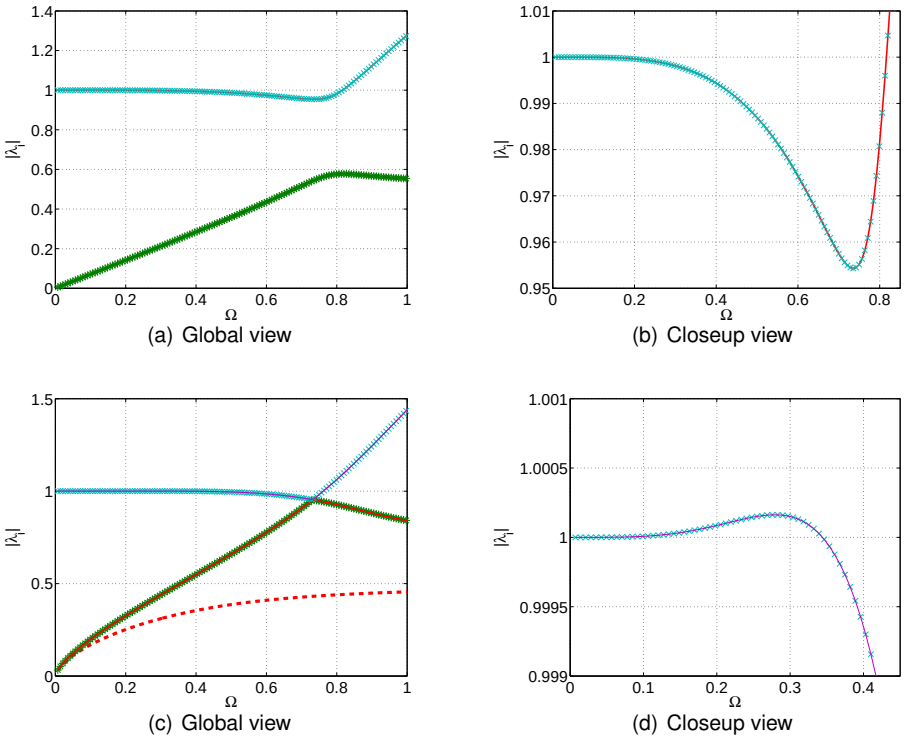

Figure 5.2: Absolute values of eigenvalues of RHS with different delay compensation methods:(a) and (b): the explicit Newmark method; (c) and (d): the linear acceleration method.

5.3 Delay compensation considering latest displacement and velocity targets

As mentioned above, in this section we first derive the formulae for delay compensation taking into account the latest displacement and velocity targets. Then they are assessed through frequency transfer functions. Finally, spectral stability of RHS on a mass-spring oscillator is analysed with the LSRT2 (Bursi et al., 2008) and the new delay compensation methods.

5.3.1 Formulation of the scheme

We choose second-order and third-order polynomials to fit the displacement time history, expressed by

$$x(t) = \sum_{j=0}^{n} \gamma_j t^j \tag{5.15}$$

where γ_j denotes the factors and n the order of the polynomial extrapolations. The predicted displacement for delay compensation is

$$x(t_{i+1} + \tau)' = x[(i+1)\Delta t + \tau] = \sum_{j=0}^{n} \gamma_j [(i+1)\Delta t + \tau]^j \tag{5.16}$$

In order to determine the factors, $(n+1)$ conditions are required. As discussed above, displacement and velocity targets at t_i and t_{i+1} are available. Hence, conditions are obtained:

$$\begin{cases} x_{i+1} = \sum_{j=0}^{3} \gamma_j [(i+1)\Delta t + \tau]^j \\ x_i = \sum_{j=0}^{3} \gamma_j [(k-1)\Delta t]^j \\ \dot{x}_{i+1} = \sum_{j=0}^{3} j\gamma_j [(i+1)\Delta t + \tau]^{j-1} \end{cases} \tag{5.17}$$

for $n = 2$ and

$$\begin{cases} x_{i+1} = \sum_{j=0}^{3} \gamma_j [(i+1)\Delta t + \tau]^j \\ x_i = \sum_{j=0}^{3} \gamma_j [i\Delta t + \tau]^j \\ \dot{x}_{i+1} = \sum_{j=0}^{3} j\gamma_j [(i+1)\Delta t + \tau]^{j-1} \\ \dot{x}_i = \sum_{j=0}^{3} j\gamma_j [i\Delta t + \tau]^{j-1} \end{cases} \tag{5.18}$$

for $n = 3$. Solving these linear equations with respect to γ_j and substituting them to Eq. (5.16) give the expression of the delay compensation, namely

$$x(t_{i+1} + \tau)' = \left(1 - \eta^2\right) x_{i+1} + \eta^2 x_i + \left(\eta + \eta^2\right) \Delta t \dot{x}_{i+1} \tag{5.19}$$

as a second-order method and

$$x(t_{i+1} + \tau)' = \left(1 - 3\eta^2 - 2\eta^3\right) x_{i+1} + \left(3\eta^2 + 2\eta^3\right) x_i + \left(\eta + 2\eta^2 + \eta^3\right) \Delta t \dot{x}_{i+1} + \left(\eta^2 + \eta^3\right) \Delta t \dot{x}_i$$

(5.20)

as a third-order method. It is evident that the discrepancy between these two expressions is whether the velocity condition at t_i is applied. Compared with other methods, the two formulae are characterized by applying the latest displacement and velocity at t_{i+1}, and hence better performance is expected. Note that Eqs (5.17) and (5.18) are two special cases of Hermite interpolation, instead of Lagrange interpolation.

5.3.2 Performance comparisons by means of frequency response function

In order to assess the compensation procedures, similar approaches to examine the ability of the procedures to predict a harmonic signal employed in Ahmadizadeh et al. (2008) and Nakashima and Masaoka (1999) are carried out. Suppose the displacement response of the structure can be expressed by

$$x(t) = A\sin(\omega t) \tag{5.21}$$

in which ω and A denote the circular frequency and amplitude of the sinusoidal wave, respectively. The corresponding velocity and acceleration can be expressed by the first-order and second-order derivatives, namely,

$$\dot{x}(t) = A\omega\cos(\omega t) \tag{5.22}$$

$$\ddot{x}(t) = -A\omega^2\sin(\omega t) \tag{5.23}$$

In addition, according to the above discussion, displacement and velocity responses at t_i and t_{i+1} are available. So are the accelerations at t_i t_{i-1}, but not at t_{i+1}. Then the predicted displacement for delay compensation can be expressed as

$$\begin{aligned} x(t_{i+1}+\tau)' &= \alpha A\sin(\omega t_p) + A\beta\cos(\omega t_p) \\ &= \sqrt{\alpha^2+\beta^2}A\sin(\omega t_p+\theta) \\ \theta &= \tan^{-1}\left(\frac{\beta}{\alpha}\right) \end{aligned} \tag{5.24}$$

where α and β are dependent on the compensation procedure; the subscript p varies among methods, i.e.

$$p = \begin{cases} i+1 & \textit{for the proposed formulae} \\ i & \textit{for the other two methods} \end{cases} \tag{5.25}$$

Taking the proposed second-order method for example, we obtain

$$\begin{aligned} \alpha &= \left(1-\eta^2\right)+\eta^2\cos(\omega\Delta t) \\ \beta &= \left(\eta+\eta^2\right)\omega\Delta t-\sin(\omega\Delta t) \end{aligned} \tag{5.26}$$

On the other hand, the exact displacement at $[(i+1)\Delta t+\tau]$ is

$$x(t_{i+1}+\tau) = A\sin\{\omega[(i+1)\Delta t+\tau]\} \tag{5.27}$$

Therefore the amplitude magnification and phase shift due to the compensation procedure can be expressed as

$$\begin{aligned} m &= \sqrt{\alpha^2+\beta^2} \\ \varphi &= \theta-\omega\Delta t \end{aligned} \tag{5.28}$$

Both quantities are depicted with respect to $\Omega=\omega\Delta t$ for various procedures in Figure 5.3 provided that $\Delta t = 0.01$ and $\tau = 0.01$. Note that, for breviety, the proposed formulae are denoted by "2nd-order with velocity" and "3rd-order with velocity", respectively.

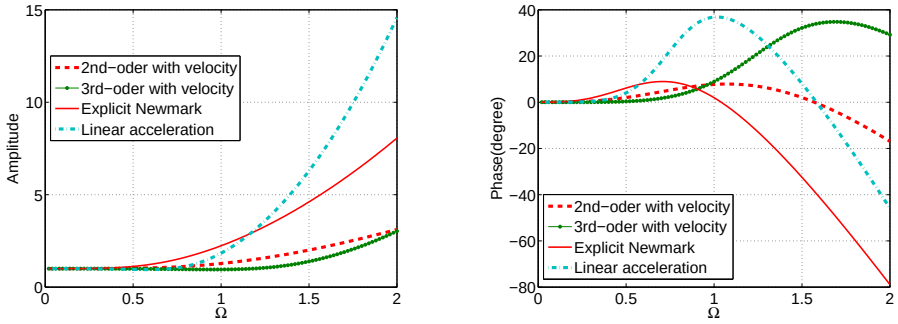

(a) Amplitude vs frequency (b) Phase vs frequency

Figure 5.3: Frequency response functions of different delay compensation methods.

As shown in Figure 5.3(a), the proposed formulae are endowed with smaller magnification when $\Omega < 2$ and slower increase speed of the amplitude magnification with increasing Ω. With regard to the phase shift, we hope that it is greater than zero to introduce possible dissipation to stabilize the method, and that it is closer to zero to limit the introduced dissipation. In this sense the proposed formulae are more favorable than the same order other method. In addition, the proposed methods show a similar property to that of the other methods: the third order formula exhibits smaller amplitude errors and a larger frequency range in which the phase shift $\varphi > 0$

than the second-order method. In summary, we can conclude from the frequency response function that the proposed formulae result in smaller prediction errors and overcompensation in larger frequency ranges. Note that the curves for the other two methods are very similar to those presented in Ahmadizadeh et al. (2008) considering $\tau = 0.9\Delta t$.

5.3.3 Stability analysis

Stability analysis of RHS is carried out on a spring specimen with the LSRT2 method and different compensation schemes. Parameters are defined in the same way as those in Section 2. In each step, compensation is applied for two times because the LSRT2 method is a two stage method. Symbolic math toolbox in Matlab was applied to obtain the amplification matrix **A** due to its complexity. Figure 5.4 shows that the proposed second-order formula exhibits the best stability while the third-order one is unconditionally unstable. Even through in Figure 5.2 RHS with the linear acceleration compensation is unstable in a small range of Ω, it is stable here as long as $\Omega < 0.8$. The stability limit of RHS with the explicit Newmark compensation is also larger than that in Figure 5.2. From these simulations and analysis, we can see that: i) the stability of RHS is related to the integration methods and compensation methods; ii) better performance of compensation methods concluded from frequency response functions does not indicate better performance of RHS; iii) second-order compensation methods may be better choices than third-order methods in terms of stability of RHS. Therefore, more attention should be paid to RHS including compensation and integration rather than only to compensation schemes; iv) the proposed second-order formula exhibits satisfactory prediction accuracy and better stability.

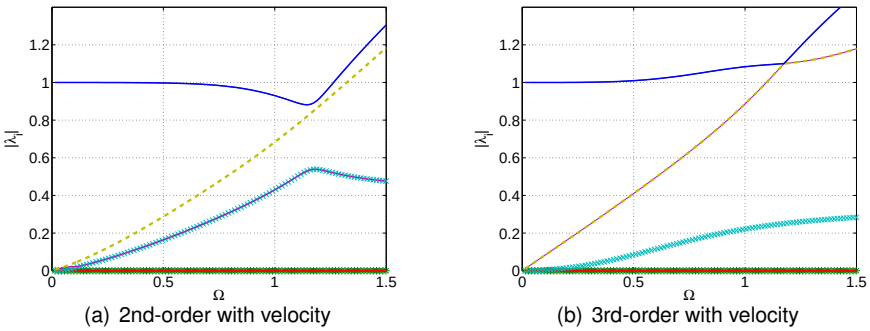

(a) 2nd-order with velocity

(b) 3rd-order with velocity

(c) Explicit Newmark

(d) Linear acceleration

Figure 5.4: Absolute values of eigenvalues of RHS with the LSRT2 and different compensation methods.

5.4 Delay Overcompensation and optimal feedback

5.4.1 The principle of the delay overcompensation scheme

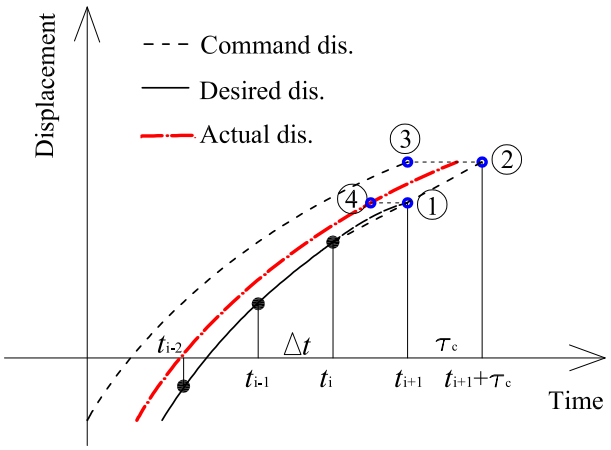

Figure 5.5: RHS with the proposed scheme.

From analyses conducted in the two previous sections, we can identify difficulty in delay compensation for RHS of MDOF. The stability of RHS is illustrated to be related to the integration method and the delay compensation. Meanwhile, even the newly-developed compensation schemes exhibits dissipation, conditional stability or unconditional instability. Moreover, the known constant delay is assumed in the analysis while in real tests, the delay may be variable and has to be identified online (Darby et al., 2002) because of its change according to the specimen stiffness, controller and the signal frequency. This analysis also assumes that the transfer system can be simply modeled as a dead time and hence no control error exists. Actual transfer systems are much more complicated and disturbance and interaction also affect control performance. Consequently, measures are required to improve properties of delay compensation and control in RHS.

On the other hand, nowadays the force of the physical substructure is fed back to the integration according to a system clock. For example, the force measured at t_i

is viewed as the force $r_{e,i}$, related to $x_{e,i}$. This kind of scheme is referred to as time-stepped force feedback. This operation is based on the assumption that the desired displacements are achieved in real-time, which implies that: i) the desired displacements are perfectly predicted, i.e. the desired displacement is successfully predicted ahead by the amount of the system delay τ; ii) the transfer system is perfectly controlled. Unfortunately, this is not the fact due to uncertainties of the structure and the transfer system. Firstly, the nonlinearity of the structure, including the physical and numerical parts, result in the difficulty to predict the structural responses in order to compensate for the system delay. Meanwhile, it is difficult to predict responses of higher frequency. In addition, uncertainties in the system, such as disturbance and non-linearities of the actuators and noises render the perfect control and perfect delay estimation complicated, if possible.

In order to facilitate delay compensation and avoid the assumptions, we propose a new scheme to treat the delay, which is characterized by overcompensation and minimization. Due to its overcompensation, we call it the overcompensation method hereafter. As shown in Figure 5.5, the procedure of RHS with this scheme can be described as follows: i) evaluate the structural responses at t_{i+1} (denoted by Step ① in the figure); ii) predict the response at $t_{i+1} + \tau_c$ (denoted by Step ②) where τ_c is larger than the actual delay τ of the system to overcompensate for the system delay; iii) send the predicted response out at t_{i+1} (denoted by Step ③); iv) search for the optimal measured displacement and feedback the corresponding measured forces to the numerical integration (referred to as Step ④).

Evidently, as long as the measured displacement is found at ④, perfect delay compensation is achieved, which means that the measured force is related to the desired displacement x_{i+1} without any errors due to polynomial prediction and actuator control. As a result, satisfactory properties, such as error reduction and stability improvement, can be anticipated. It is this merit that encourages us to further investigate this methodology.

5.4.2 The compensated delay

One key problem related to this overcompensation scheme is how to determine the compensated delay τ_c. Theoretically, any delay larger than the actual one τ is sufficient to accomplish overcompensation. On the other hand, the error due to polynomial prediction increase with the increasing compensated delay. Therefore, it is the best choice to set

$$\tau_c = \tau_{max} \equiv \max_t \tau \quad t \in [0 \quad T] \tag{5.29}$$

where T denotes the duration of the test. When τ_{max} is not available, the compensated delay can be defined in the subsequent way. Firstly, we separate the system delay as

$$\tau = \tau_m + \Delta\tau \tag{5.30}$$

where τ_m and $\Delta\tau$ are the main part and variable part of the system delay, respectively. The former one is easy to estimate a priori while the latter one needs to be identified online. Then the overcompensated delay can be determined by means of

$$\tau_c = \tau_m + (\mu - 1) * \tau_m \tag{5.31}$$

where μ is a constant larger than 1 which causes that τ_c is not less than the maximum value of the system delay in the test, i.e., $\tau_c \geq \tau_{max}$. In this case, the maximum acceptable variation of the delay is $(\mu-1)\tau_m$. As an example, the maximum acceptable variation of the delay is $\kappa\Delta t$ when we choose

$$\tau_c = \tau_m + \kappa\Delta t. \tag{5.32}$$

When $\kappa = 1/2$, this definition causes the achievement of the desired displacement around the middle of each time step.

5.4.3 The optimal instant of feedback quantities

Another key problem is how to optimally select the force feedback or the restoring force, and the displacement feedback. As schematically shown in Figure 5.5 provided

the compensated delay τ_c and the system delay τ defined as Eq. (5.32) and Eq. (5.30), the time instant $t_{op,i+1}$ (called the optimal instant hereafter) when the desired displacement x_{i+1} is achieved can be formulated as

$$t_{op,i+1} = t_{i+1} - (\tau_m + \kappa\Delta t) + (\tau_m + \Delta\tau) = t_{i+1} - \kappa\Delta t + \Delta\tau \tag{5.33}$$

Clearly, $t_{op,i+1}$ is in the time range $(t_{i+1} - 2\kappa\Delta t \quad t_{i+1})$. Then we can search for it in this time range by solving the problem

$$\textit{Sought } t_{op,i+1} \textit{ in } (t_{i+1} - 2\kappa\Delta t \quad t_{i+1}) \textit{ such that } |x_e(t_{op,i+1}) - x_{i+1}| \leq |x_e(t) - x_{i+1}| \tag{5.34}$$

The solution can be expressed as

$$t_{op,i+1} = \arg \min_t |x_e(t) - x_{i+1}| \quad t \in (t_{i+1} - 2\kappa\Delta t \quad t_{i+1}) \tag{5.35}$$

Then the optimal restoring force and displacement feedback are those measured at $t_{op,i+1}$. Unfortunately, the desired displacement may be not achieved during the interval due to the extrapolation and control errors. Consequently, we redefine the optimal instant as

$$t_{op,i+1} = \arg \min_t |x_c(t) - x_{i+1}| \quad t \in [t_{i+1} - 2\kappa\Delta t \quad t_{i+1}] \tag{5.36}$$

Therefore, Eq. (5.36) implies that $t_{op,i+1}$ is either t_i or t_{i+1} when the desired displacement is not achieved during the interval. Another alternative is to view t_{i+1} as $t_{op,i+1}$ and hence overcompensation at the current step is realized. In this case, the optimal instant yields

$$t_{op,i+1} = \begin{cases} \arg \min_t |x_e(t) - x_{i+1}| & x_{i+1} \in [\min x_e(t) \quad \max x_e(t)], t \in (t_{i+1} - 2\kappa\Delta t \quad t_{i+1}) \\ t_{i+1} & \textit{others} \end{cases} \tag{5.37}$$

This treatment is beneficial since overcompensation at these steps may introduce limited dissipation. This will be reconfirmed in numerical simulations.

These two strategies are easy to implement in RHS for their fixed time ranges. However, the method to determine the optimal instant in the varying time range defined as from the last optimal instant to the current instant t_{i+1} may be preferable.

This method can ensure that the subsequent optimal instant is always later than the previous one, which is helpful to treat the cases when the desired displacement is around its trajectory peak, see Figure 5.6. In addition, the storage size of the feedback quantities with this method is relatively small. Nevertheless, programming for this method is somewhat complex for the time-varying length of the interval. Similarly to Eqs (5.36) and (5.37), the expressions with this method can be formulated.

It is interesting to note that only limited computational burdens are required by all these optimal schemes, since no iteration process is involved. Meanwhile, noise in tests introduces less problems to the overcompensation scheme. When the measured quantities are strongly contaminated by noise, it is advisable to design a filter to reduce the influence of the noise. Devising a filter for tests with the overcompensation scheme should be easier for its delay variation accommodation than tests without this scheme. In the latter scenario, the phase shift due to the filter needs to be tackled. Even no filter is performed in both cases, tests with the overcompensation scheme would not exhibit drawbacks related to the noise comparing to the other case.

5.4.4 Pros and cons

For the purpose of clearly describing the testing procedure with the overcompensation scheme, it is summarized in detail in Table 5.1. Note that in order to compensate for delay and ensure the smooth movement of the transfer systems, extrapolation and interpolation procedures in Nakashima and Masaoka (1999) are employed. In addition, we can see that this overcompensation scheme is different from the those in Wallace et al. (2005a) and Li and Tso (1999) due to its implementation during the whole test and the minimization.

We explain further this overcompensation scheme taking into account the compensated delay and the optimal instant. Here suppose the compensated delay is determined according to Eq. (5.32) and then the overcompensated delay is $\kappa\Delta t$ if $\Delta\tau = 0$. To begin with, let's focus on the ideal case, indicating that both perfect prediction and control are accomplished. Then the desired and measured displacements are shown in Figure 5.6. Evidently, one measured displacement which is identical to the desired one can be always found in common cases, for example, the measured

Table 5.1: Procedure of RHS with the overcompensation scheme

Step	Description
1	Initialize the test parameters: structural parameters, integral time interval Δt, step number i, main part of the actuator delay and other parameters;
2	Evaluate x_{i+1} and $\dot{x}_{i+1}$ through the specified integrator;
3	Predict the structural responses according to Eq. (5.32) and either Eq. (5.19) or Eq. (5.20);
4	Interpolate the predicted displacement to generate the commands in a fine step;
5	Send out the commands to the transfer system and acquire the achieved displacement and force every sampling time until time approaches t_{i+1};
6	Evaluate $t_{op,i+1}$ by means of either Eq. (5.36) or Eq. (5.37);
7	Find the optimal feedbacks and save them;
8	Set $i = i + 1$ and go back to Step 2 until the test ends.

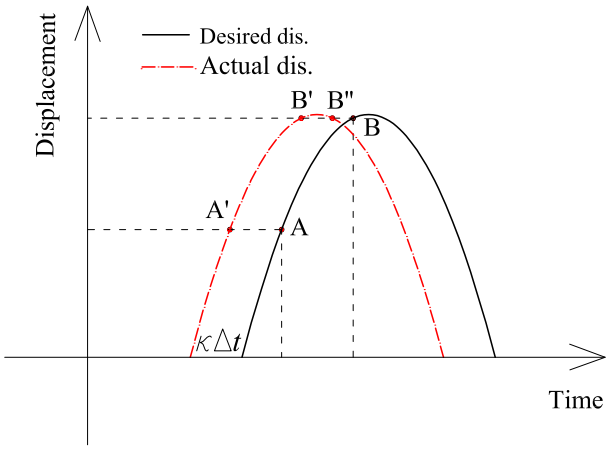

Figure 5.6: The overcompensation scheme in an ideal case.

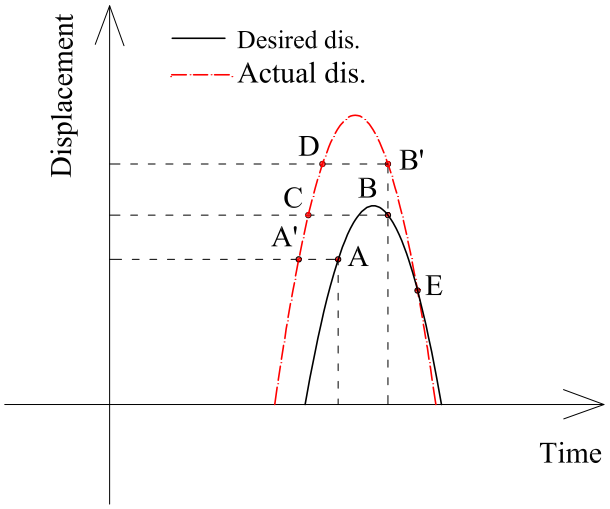

Figure 5.7: The overcompensation scheme with *ka* = 1.05.

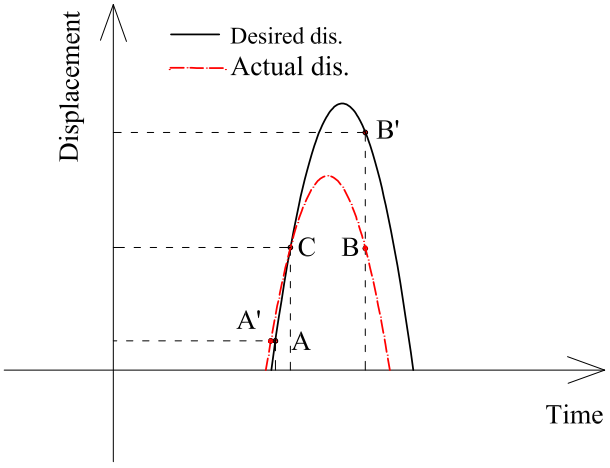

Figure 5.8: The overcompensation scheme with *ka* = 0.95.

displacement A' is corresponding to the desired displacement A. With regard to the desired displacement around its trajectory peak, two equal measured displacements may be found according to either Eq. (5.36) or Eq. (5.37), denoted by B' and B'' as an example in the figure. Conversely, only B' is identified if the optimal strategy with a time-varying length of the interval. The corresponding measured displacement can be also found with special treatment to these two points. As a result, the optimal measured displacement can be always obtained in the tests. In addition, we assume that the delay is overcompensated for by $\kappa\Delta t$ herein. If the system delay varies a little, the phase shift between two displacements changes. However, the measured displacement corresponding to the desired one can be always identified as long as the delay variation is less than $\kappa\Delta t$. Consequently, this overcompensation scheme can accommodate delay change and results in favorable delay compensation.

Then we move on to cases with an amplitude amplification factor *ka* which is resulted from polynomial prediction and/or actuator control, and is defined as the ratio of the measured-displacement amplitude to the desired-displacement amplitude. Figures 5.7 and Figure 5.8 plot the cases with $ka = 1.05$ and $ka = 0.95$. Similarly, the optimal measured displacement exists in common cases in both figures. This means that errors can be reduced to the level of measurement noise in these cases. In Figure 5.7, the corresponding measured displacement to B is dependent on the overcompensated delay $\kappa\Delta t$, the optimal strategy and time discrepancy t_{BC} between C and B. Firstly, C may be out of the time range $(t_{i+1} - 2\kappa\Delta t \quad t_{i+1})$ and this therefore results in that C is not found according to Eq. (5.35) when t_{BC} is larger than $2\kappa\Delta t$. This condition may be satisfied when *ka* is larger or the overcompensated delay $\kappa\Delta t$ is smaller. Secondly, if the length of the time range $2\kappa\Delta t$ is less than $t_{B'D}$, B' is viewed as the closest point to the desired displacement B according to either Eq. (5.36) or Eq. (5.37). At this moment, the proposed overcompensation scheme is reduced to the overcompensation applied in Wallace et al. (2005a), in that the measured quantities at t_B are directly fed back to the integration. In addition, this case also happens in the time range $[t_B \quad t_E]$. However, the two optimal strategies lead to different results when $t_{B'D} < 2\kappa\Delta t < t_{BC}$. In this case, Eq. (5.37) still regards B' as the desired point while Eq. (5.36) yields one measured displacement between C and D corresponding to the time t_i. The former one is characterized by overcompensation at the current

step whereas the latter one by the smallest error. In summary, the overcompensation method should be better than the proper compensation in terms of error reduction and stability. Likewise, the same summary can be also attained from Figure 5.8.

From this qualitatively analysis, we can see that i) in the most cases the overcompensation can result in perfect compensation meaning that the feedback force is corresponding to the desired displacement even amplitude errors due to the polynomial extrapolation and actuator control exist; ii) the different optimal strategies result in different feedback around peaks of the desired displacement, however, the overcompensation should exhibit better performance than proper compensation schemes.

Advantages of the overcompensated scheme can be concluded as follows. Initially, it can accommodate delay variation and hence exact delay estimation is not necessary as long as $\Delta\tau < \kappa\Delta t$ when τ_c is determined according to Eq. (5.32). Secondly, the minimization can reduce the error originating from control and delay compensation. Especially for the case in Eq. (5.35), the discrepancy between the displacements of the NS and PS can be reduced to noise level in an authentic test. The effectiveness of the proposed overcompensation scheme can be also qualitatively assessed according to the energy introduced to the structure owing to the test Mosqueda et al. (2007). Clearly, this scheme can effectively reduce the displacement discrepancy between the desired displacement and the feedback displacement and hence reduce the energy error. Another advantage of the scheme is to apply the overcompensation scheme which may introduce positive dissipation to the system and stabilize the simulations.

These advantages are at the expense of delay compensation for a larger delay and storing the quantities measured in the past $\kappa\Delta t$ in memory, which implies disadvantages of the overcompensation scheme. Firstly, compensation for a larger delay can cause larger prediction errors, as illustrated in Figure 5.3. Therefore, it is advisable to implement the method considering the latest displacement and velocity. Secondly, tests may diverge in some cases due to this compensation. However, the stability limit is different from that presented in Figure 5.4 due to the minimization. One example to illustrate the effect of the optimal strategies on the stability is presented in Section 4. Unconditional stable compensation is also desirable for the overcompensation scheme. Another disadvantage of the overcompensation is to store the measured

quantities for a while in memory before the optimal feedback is determined. However, these disadvantages are acceptable in routine applications considering the advantages of this scheme.

5.5 Numerical simulations

This section presents two numerical simulations with the proposed second-order and third-order compensation formulae on a SDOF system shown in Figure 5.9, as well as the overcompensation and optimal feedback.

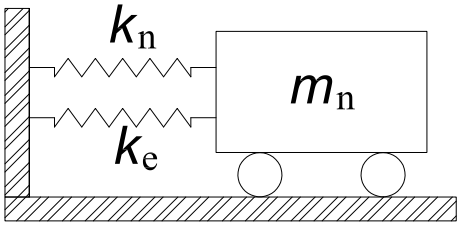

Figure 5.9: Computation schematic of the SDOF system.

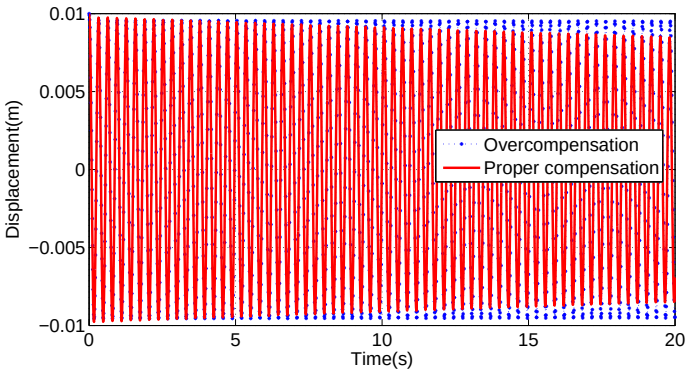

Figure 5.10: Numerical simulations with the proposed 2nd-order compensation scheme.

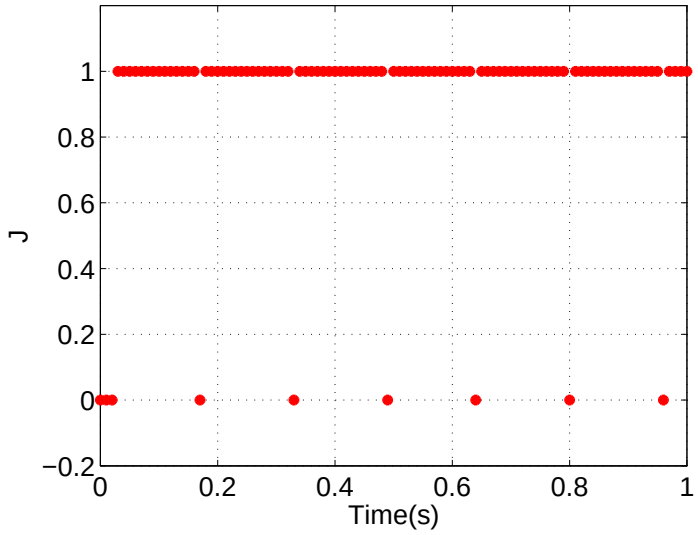

Figure 5.11: The indicator J.

5.5.1 The second-order compensation scheme

Figure 5.10 presents the simulation result of free vibration with the initial displacement $d_0 = 0.01$m integrated by the LSRT2 with $\Delta t = 0.01$s. The mass of the structure model is set 1kg while the stiffness is chosen in such a way that $\Omega = 0.2$. Therefore, $k_n = k_e = 200$N/m. Delay is assumed to be equal to Δt. In the figure, the line denoted by 'Proper compensation' means that the compensated delay is equal to the actual delay, i.e. $\tau_c = \tau$, while 'Proposed scheme' means that the overcompensation for the delay $1.5\Delta t$ and the optimal feedback are applied. Clearly, the proper compensation results in dissipation, in agreement with the spectral analysis shown in Figure 5.4(a). Conversely, the proposed scheme effectively reduces the dissipation and provides more accurate results, consistent with analysis in Section 4.

Before we finish this subsection, let's remark that the proposed scheme can realize perfect compensation in the most points of the time history. In order to examine this comment, an indicator J is defined as

$$J = \begin{cases} 1 & \textit{perfect compensation} \\ 0 & \textit{others} \end{cases} \tag{5.38}$$

The indicator related to the simulation in Figure 5.10 is depicted in Figure 5.11. It is evident that the result matches well with the comment.

5.5.2 The third-order compensation scheme

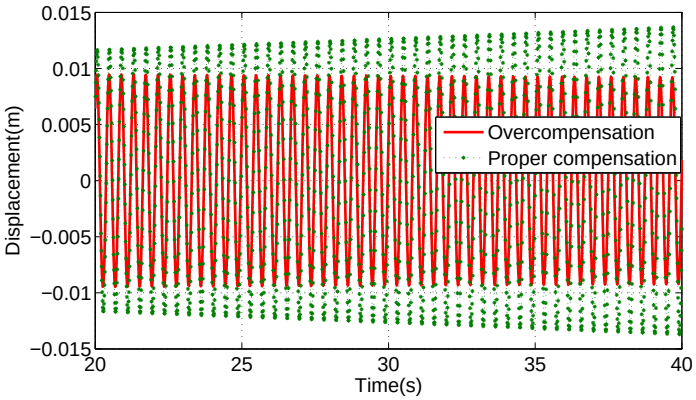

Figure 5.12: Numerical simulations with the proposed 3rd-order compensation scheme.

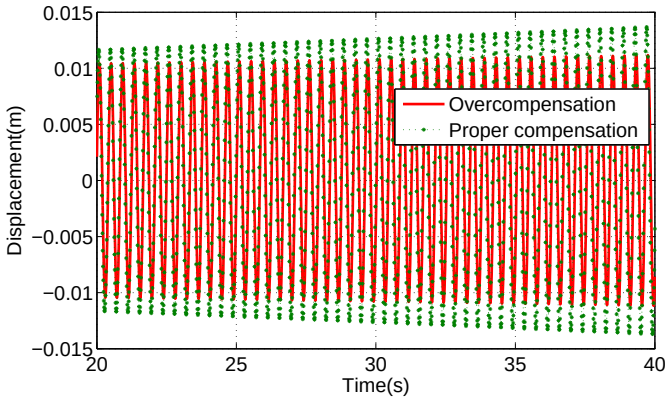

Figure 5.13: Numerical simulation with Eq.(5.36).

Figures 5.12 and 5.13 present simulation results when the proposed third-order compensation scheme is applied. All parameters defined in the last subsection are employed again except $\Omega = 0.15$. In the figures, only responses from 20s to 40s are

depicted. Clearly, the proper compensation provides unstable responses, in agreement with spectral analysisshown in Figure 5.4(b). On the other hand, the proposed overcompensation scheme with the optimal feedback determined according to Eq. (5.37) cause stable results as shown in Figure 5.12. This confirms that the overcompensation at some peaks of the displacement trajectory introduce dissipation. Nonetheless, the alternative to determine the optimal instant in Eq. (5.36) does not stabilize the results, even though it effectively reduces the error compared with proper compensation.

5.6 Test validation

In this section, three types of tests for performance assessment of the delay compensation and the proposed overcompensation scheme were conducted, i.e. loading assessment, RHS on SDOF and RHS on MDOF.

5.6.1 Test rig

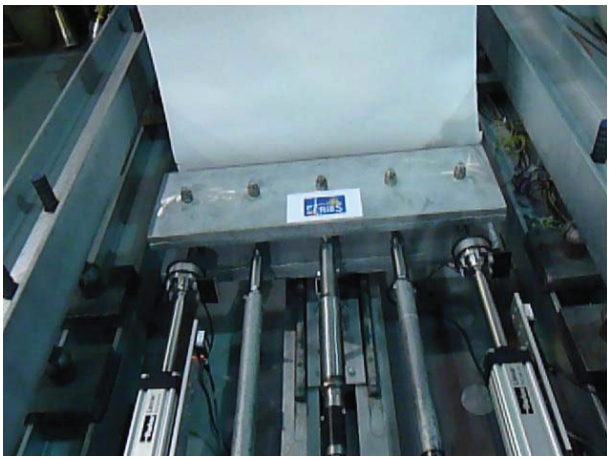

Figure 5.14: Photo of the test rig.

A versatile system was conceived and installed for examining control techniques and assessing reliability of results in RHS for linear/nonlinear MDOF structures at the University of Trento, Italy. The system consists of four actuators, one dSpace DS1103 control board and other high performance devices. The test rig is flexible and specimens endowed with different characteristics can be configured with springs, dampers and masses, as demonstrated in Figure 5.14. For the RHS considered here, the actuators were operated with a PID controller tuned with the Chien, Hrones and Reswick (CHR) scheme for 0.0% overshoot step response Åström and Hägglund (1995). In detail, this scheme is expected to achieve the quickest response with a specified overshoot as well as disturbance rejection. In addition, electromagnetic noise was reduced by an elliptic filter Mitra (2005) with a pass frequency and a stop frequency of 20Hz and 30Hz, respectively. The sampling frequency of both control and measurements were set equal to 1024Hz.

5.6.2 System delay and open-loop test

First of all, tests were performed with the sinusoidal commands to attain the system delay defined as the difference between the time when the commands are sent out and the time when the actuator achieve the targets. The commands (here equal to the desired displacement) in *mm* read

$$x_c(t) = 10\sin(2\pi t) \tag{5.39}$$

In order to evaluate the delay, the following problem was solved

$$\min_{\tau} \frac{1}{n}\sum_{t_i=0}^{25} \left|x_c(t_i) - x_m(t_i-\tau)\right|^2 \tag{5.40}$$

where $x_m(\bullet)$ denotes the measured displacements while n indicates the length of the time histories. The solution shows that the delay of the system is around 16.6 ms. Then this delay was compensated for by the proposed third-order polynomial approach with the assumption that the system delay was constant when the actuator was excited by commands containing three frequency components, expressed as

$$x(t) = 5\sin(2\pi t) + 3\sin(4\pi t) + 2\sin(8\pi t) \tag{5.41}$$

Both proper-compensation and overcompensation were carried out. For the overcompensation, the displacements endowed with the smallest discrepancy to the desired displacement were recorded.

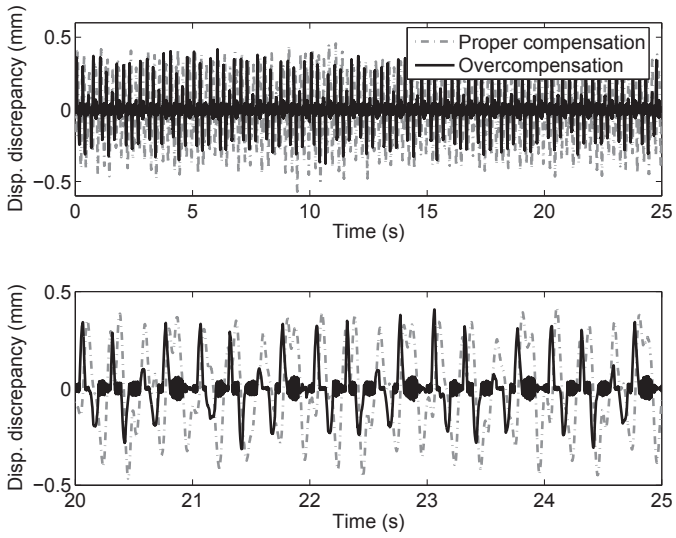

Figure 5.15: Global and close-up views of the synchronization errors with sinusoidal commands.

The proposed overcompensation scheme was compared with the proper compensation by means of the synchronization errors defined as the discrepancy of the desired displacement and the actual displacement in both the time domain and the frequency domain, as shown in Figures 5.15 and 5.16. In Figure 5.15, the error sometimes is reduced to the noise level when the proposed scheme is adopted. In the frequency domain, the error at the frequency 4Hz is reduced by half due to the proposed overcompensation scheme. Theoretically, the discrepancy can be eliminated for a pure delay system and with the assumption of a perfect predictor. Here the amplitude error may result from amplitude errors of actuator control, as shown in Figure 5.17, where phase error is not evident while amplitude errors are observed. With these test results in mind, RHS with the proposed scheme were anticipated to exhibit better accuracy.

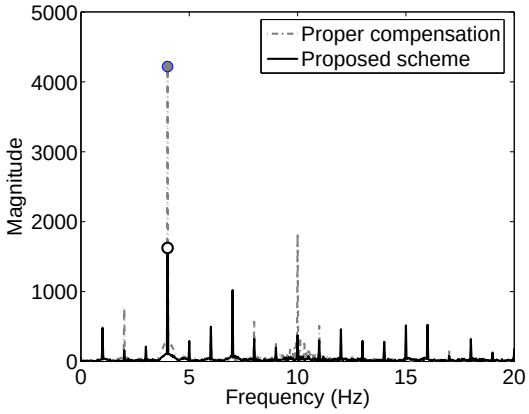

Figure 5.16: Frequency components of the synchronization errors with sinusoidal commands.

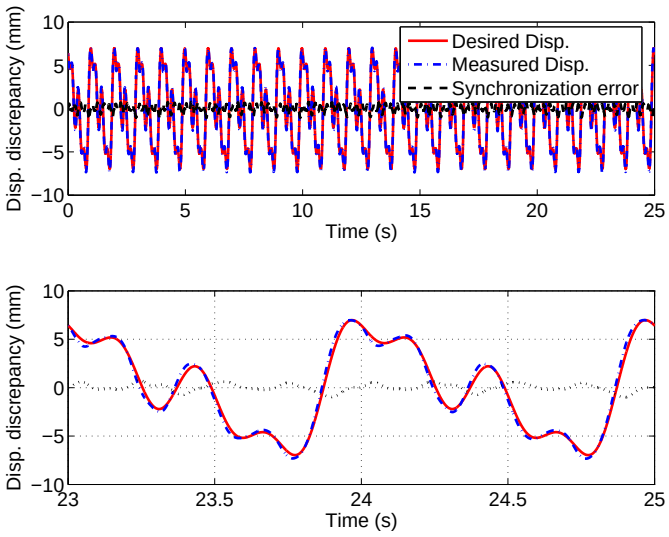

Figure 5.17: Global and close-up views of displacement time histories with proper compensation.

Table 5.2: Structural characteristics of the SDOF system

m_n(kg)	k_n(kN/m)	c_n(kNs/m)	k_e(kN/m)	c_e(kNs/m)
1.52×10^3	20	0	≈ 40	0

Note: friction exists.

5.6.3 RHS on a SDOF system with a spring specimen

RHS of a SDOF system with a spring specimen were conceived to investigate the method. The structure model is depicted in Figure 5.9 and structural characteristics are presented in Table 5.2. In order to excite the structure, a sinusoidal wave with the frequency 1.3Hz and the amplitude 300N was applied on the structure. In addition, multitasking strategy was employed for integration and control with the time intervals 10ms and 1ms, respectively, even though the structure is simple, since the objective of this development is to conduct RHS for large-scale and complex structures. Three cases, including proper-compensation, under-compensation (i.e. τ_c = 15$ms < \tau$) and the proposed overcompensation method, were carried out. The desired displacements are presented in Figure 5.18 as well as the simulated results considering the specimen stiffness and Coulomb's Friction, i.e.,

$$F = k_e x + F_0 sign(\dot{x}) \tag{5.42}$$

with the sign function

$$sign(\dot{x}) = \begin{cases} 1 & \dot{x} >= 0 \\ -1 & \dot{x} < 0 \end{cases} \tag{5.43}$$

where F_0 = 50N. Figure 5.18, where τ_c denotes the compensated delay, shows the similarity of four time histories. In fact, this is due to the friction in the specimen, which makes the test less sensitive to the delay. However, Figure 5.19 shows the different synchronization error in the frequency domain. Clearly, the synchronization error increases much if the error of the estimated delay or the delay variation of the system is 1ms. Conversely, it will not change if the proposed overcompensation scheme is applied. This means that this method is effective to treat delay-varying systems.

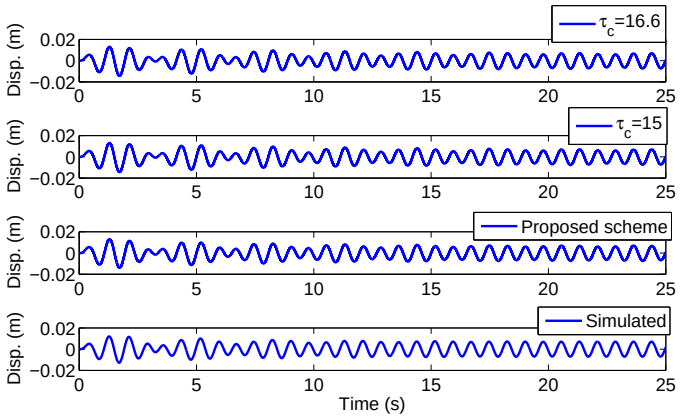

Figure 5.18: Displacement time histories of the SDOF system.

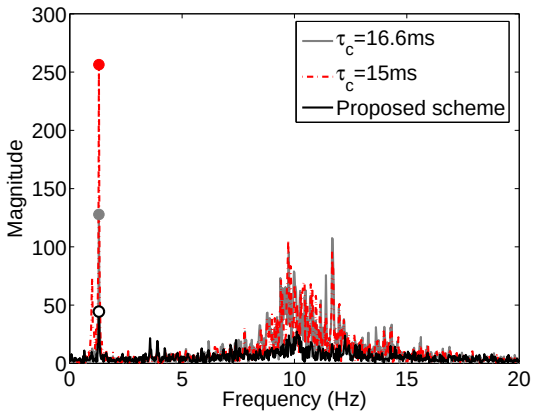

Figure 5.19: Comparisons of displacement synchronization errors in frequency domain.

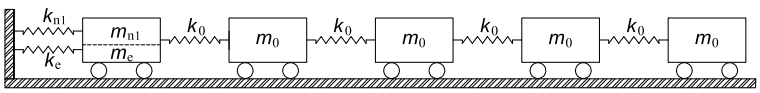

Figure 5.20: Computation schematic of the 5DOF system.

5.6.4 RHS on a five DOF system considering specimen mass

These tests are characterized in two aspects, five DOFs and a dynamic physical substructure. The structure model is schematically depicted in Figure 5.20, where k_0 = 200kN/m, m_0 = 900kg, $k_e \approx$ 40kN/m, $m_e \approx$ 298kg, causing the natural frequencies 0.68Hz, 1.97Hz, 3.11Hz, 3.99Hz and 4.55Hz. Figure 5.14 shows the test rig, in which a mass, two springs as well as a damper can be observed. However, the damper was disconnected in the tests due to its too strong behavior. To begin with, the proposed third-order method was attempted to be used. Unfortunately, vibration which might be induced by the force noise and delay compensation pushes us to discard it. Then the tests were conducted with the second order method. The time histories of desired displacements and simulated displacements are presented in Figure 5.21. These figures indicate that the test results are reliable. In addition, the frequency components of the displacement synchronization errors are illustrated in Figure 5.22, which reconfirms the effectiveness of the proposed method in terms of treatment to delay-varying systems and, to some extent, control errors.

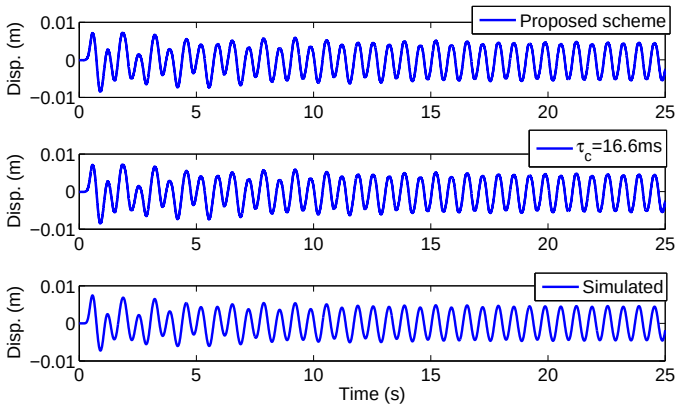

Figure 5.21: Time histories of displacement responses at the interface of the 5DOF system.

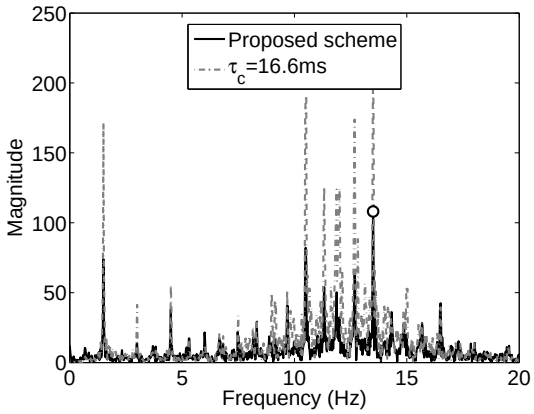

Figure 5.22: Comparisons of displacement synchronization errors in frequency domain.

5.7 Conclusions

In this chapter, two polynomial delay compensation formulae considering the latest displacement and velocity targets and a new scheme consisting of overcompensation and optimal feedback were proposed. In particular, the two delay compensation formulae are formulated in the format of polynomial schemes with the latest velocity and displacement targets provided by integrators explicit for displacement and velocity. Then the methods are evaluated by the frequency response function and the analysis shows its advantages over other schemes in terms of its smaller amplitude error and phase overcompensation in a larger frequency range. However, the stability analysis shows that the frequency response function is not enough for a successful test. In order to improve the test results, a overcompensation scheme is conceived. Different from the widely used time based force feedback scheme, this scheme is characterized by overcompensation and optimal feedback quantities. It exhibits advantages, such as error reduction and sometimes stability improvement, in numerical simulations and real tests for single and multiple DOF structures.

The main contribution of this chapter might be applied to RHS with implicit integrators, which exhibits more favorable performance than explicit methods in terms

of stability and error propagation (Wu et al., 2007; Shing and Manivannan, 1990; Mosqueda and Ahmadizadeh, 2007). Implicit integrators are not welcomed in RHS for possible undesired loading and unloading cycles and variable convergence speed resulting from iteration solution procedures to nonlinear equations. With the proposed overcompensation scheme, a table can be established between the measured displacement and forces. Therefore, in the iteration, when the restoring forces are required, the only thing to do is to search in the table. In this way, the two weaknesses due to the iteration can be avoided. In summary, this chapter may result in a possible approach to implement RHS with implicit integrators.

CHAPTER 6

THE EQUIVALENT FORCE CONTROL METHOD FOR REAL-TIME HYBRID SIMULATION ON SPLIT MASS SYSTEMS

6.1 Introduction

The equivalent force control (EFC) method (Wu et al., 2007) was devised to solve the derived nonlinear equations in Real-time Hybrid Simulation (RHS) using an implicit integrator without conventional iteration schemes. The objective is achieved by means of a force feedback loop. Relevant research work numerically and/or experimentally illustrated the ability of the method for RHS in terms of its accuracy and stability when the physical substructure was displacement- or velocity- dependent. However, in practice, specimens are sometimes acceleration-dependent, for example tuned mass dampers and tuned liquid dampers (Iemura, 1994). Moreover, specimens in RHS are always found acceleration-dependent when the coupling between two substructures is replicated by a shaking table. In Xu (2009), numerical simulations of the EFC method for dynamic specimens were carried out. This chapter is devoted to some crucial issues encountered to extend the EFC method to the tests on split mass systems. In these tests, one mass of the emulated system is separated and simulated in both substructure, among others, see Bursi et al. (2008) and Deng (2011).

In this chapter, we first focus on the similarity of the EFC method and conventional iteration schemes and conclude the advantages of the method. Successively, command interpolation approaches and stability of the EFC method for this variety of tests are numerically and spectrally analyzed. Then procedures for improving the perfor-

mance of the method are developed. In particular, displacement and acceleration corrections are proposed and investigated. Especially for the acceleration correction, stability analysis and numerical simulations are performed. RHS on a MDOF split-mass system are also numerically carried out and presented.

6.2 Formulations of the EFC method

The EFC method was proposed and formulated based on the constant average acceleration method in Wu et al. (2007). However, we prefer the α method of Hilber et al. (1977) here, since the method, in addition to the second-order accuracy, exhibits the property of user-defined numerical damping. In RHS, algorithmic damping is desirable to limit the effect of under-compensated delay and measurement noise in the acquired displacement and force. The equation of motion for hybrid simulations and displacement and velocity approximations of the α method read

$$\begin{aligned} M_N a_{i+1} + (1+\alpha) C_N v_{i+1} - \alpha C_N v_i + (1+\alpha) r_{N,i+1} - \alpha r_{N,i} + (1+\alpha) R_{E,i+1} \\ -\alpha R_{E,i} = (1+\alpha) f_{i+1} - \alpha f_i \end{aligned} \tag{6.1}$$

$$d_{i+1} = d_i + \Delta t v_i + \Delta t^2 [(\frac{1}{2} - \beta) a_i + \beta a_{i+1}] \tag{6.2}$$

$$v_{i+1} = v_i + \Delta t [(1-\gamma) a_i + \gamma a_{i+1}] \tag{6.3}$$

where a, v and d denote acceleration, velocity and displacement responses, respectively; M_N, C_N and r_N are lumped mass, damping coefficient and restoring force of the NS; $R_{E,i+1}$ indicates the coupling force at the interface, namely $R_{E,i+1} = M_E a_{E,i+1} + C_E v_{E,i+1} + r_{E,i+1}$. α, β and γ are algorithmic parameters. From the results of the Generalized-α (Chung and Hulbert, 1993), it is more favorable to use different factors for the spring force, damping force and inertial force. However, during the test, we can not recognize them and hence, the same parameters are employed for all forces of the physical substructure, as shown in Eq. (6.1). Note that, for simplicity, we still call the algorithm exploited herein the α method even though this is correct only

if $M_E = 0$. Substituting Eq.s (6.2) and (6.3) into Eq. (6.1) gives

$$K_{PD} d_{i+1} + (1+\alpha) r_{N,i+1} + (1+\alpha) R_{E,i+1} = F_{EQ,i+1} \tag{6.4}$$

with

$$F_{EQ,i+1} = (1+\alpha) f_{i+1} - \alpha f_i + K_{PD} d_i + C_{PD} v_i + M_{PD} a_i + \alpha r_{N,i} + \alpha R_{E,i} \tag{6.5}$$

$$K_{PD} = \frac{M_N}{\Delta t^2 \beta} + \frac{(1+\alpha)\gamma C_N}{\Delta t \beta} \tag{6.6}$$

$$C_{PD} = \frac{M_N}{\Delta t \beta} + \frac{(1+\alpha)\gamma C_N}{\beta} - C_N \tag{6.7}$$

$$M_{PD} = (\frac{1}{2} - \beta)\frac{M_N}{\beta} + (1+\alpha)(\frac{\gamma}{2\beta} - 1)\Delta t C_N \tag{6.8}$$

where $F_{EQ,i+1}$ is referred to as the equivalent force (EF) relevant to the external force, the characteristics and movement quantities of the NS and algorithmic parameters; K_{PD} is called the pseudo stiffness. Note that Δt^2 is in the denominator in Eq. (6.6) and thereby, the force contributed by K_{PD} is often much larger than other terms on the left-hand side of Eq. (6.4).

In order to advance the time from t_i to t_{i+1}, Eq. (6.4) needs to be solved. In fact, it is a standard fixed-point problem if the restoring force is just related to the displacement. In this case, it is often numerically solved with an iteration scheme, such as Newton's method (Isaacson and Keller, 1994). In hybrid simulations, it was solved with a modified Newton iteration, amongst others, see Shing et al. (1991),

$$d^{j+1} = d^j + \theta \frac{1}{K}(F_{EQ,i+1} - F_{fb}^j) \tag{6.9}$$

where θ and K denote the reduction factor and the derivative of the expression on the right-hand side of Eq. (6.4) with respect to displacement. Note that this formula is expressed via the symbols of this dissertation and some mathematical manipulation is necessary to obtain this expression from those in Shing et al. (1991). With this iteration, referred to as the traditional iteration in this chapter, we do not know the required number of iterations to render the unbalanced force or the displacement increment small enough, i.e., convergent. We can bear this in pseudo dynamic tests (PDT) whilst this is not allowed in fast hybrid tests or RHS because the iterations must be completed in a time range dependent on the time interval and time scale. Jung and Shing (2006) adopts a new iteration scheme characterized by fixed iteration

numbers in an integration step and command generation by means of a quadratic interpolation, which is further analyzed by Chen and Ricles (2011) in terms of its stability and accuracy for linear elastic, nonlinear softening and nonlinear hardening structures.

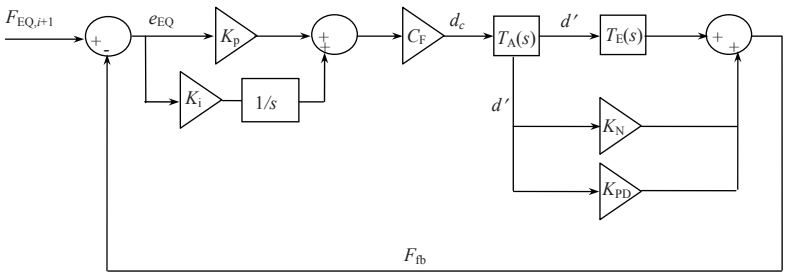

Figure 6.1: Block diagram of the EFC method with PI control

In Wu et al. (2007), the left-hand side of Eq. (6.4) is viewed as three elements in parallel. Therefore, the objective to solve the equation is to impose the equivalent force onto them, and the final displacement of elements is the solution of the equation. Hence, the EF is implemented in force control on the hybrid system. In order to operate the actuator in displacement control, a converter, acting in the like way of a Jacobian matrix, is inserted into the loop. This treatment is beneficial in understanding the scheme even theoretically this converter is not necessary as it can be contained in the EF controller. Then we obtain the basic block diagram of the EFC method as shown in Figure 6.1. This scheme heretofore has been employed with proportional-derivative control, proportional-integral control and sliding mode control to perform tests on springs, MR dampers, and BRBs, which demonstrated that the EFC method exhibits desirable stability and accuracy. Encouraged by this achievement, we concentrate on RHS on split mass systems in this chapter.

6.3 A closer look at the EFC method

As stated in (Wu et al., 2007), the EFC method is attractive in that conventional iterations is not required by performing force control. However, the relationship between the conventional iteration method and the EFC method is not clear. Moreover, the comparative advantages of the method should be drawn. This section is dedicated to analyzing the EFC method by comparing with the conventional iteration.

6.3.1 Explanation of the EFC method in the iterative background

To begin with, we focus on the EFC method with a stiffness specimen. As shown in Figure 6.1, the control action of the digital proportional-integral controller can be expressed as follows

$$CA^{j+1} = K_p(F_c^{j+1} - F_{fb}^{j}) + K_i \sum_{k=0}^{j} (F_c^{k+1} - F_{fb}^{k})\delta t \tag{6.10}$$

where K_p and K_i are the proportional and integral gains of the EF controller, respectively; F_c^{j+1} and F_{fb}^{j} denote the EF command and EF feedback; δt is the sampling time of the control loop. For simplicity, the integration in control is approximated by the area sum of a series of rectangles rather than trapezoids. Then the actuator command reads

$$d_c^{j+1} = CA^{j+1}C_F = K_p C_F(F_c^{j+1} - F_{fb}^{j}) + K_i C_F \sum_{k=0}^{j} (F_c^{k+1} - F_{fb}^{k})\delta t \tag{6.11}$$

in which C_F is the force-displacement converter. Here we choose

$$C_F = \frac{1}{K_{N,ini} + K_{PD} + K_{E,ini}} \tag{6.12}$$

where $K_{N,ini}$ and $K_{E,ini}$ denote the initial stiffness of the NS and the PS, respectively. In addition, the command at the previous sampling instant is

$$d_c^{j} = CA_j C_F = K_p C_F(F_c^{j} - F_{fb}^{j-1}) + K_i C_F \sum_{k=0}^{j-1} (F_c^{k+1} - F_{fb}^{k})\delta t \tag{6.13}$$

Subtracting the above two equations gives

$$d_c^{j+1} = d_c^j + K_p C_F (F_c^{j+1} - F_c^j) + K_p C_F (F_{fb}^{j-1} - F_{fb}^j) + K_i C_F (F_c^{j+1} - F_{fb}^j)\delta t \tag{6.14}$$

Therefore, if $K_p = 0$, this equation is reduced to

$$d_c^{j+1} = d_c^j + K_i C_F (F_c^{j+1} - F_{fb}^j)\delta t \tag{6.15}$$

This equation has the same format as the traditional Newton-type iteration scheme expressed in Eq. (6.9) as long as the EF commands are held as a constant. In addition, it is reduced to Eq. (6.9) if we define $K_i \delta t = \theta$. This suggests that the EFC method with integral control for conventional PDT is equivalent to the traditional iteration except the fixed iteration number. If the EF commands change in a time interval, a series of nonlinear equations at different time instants need to be solved, namely

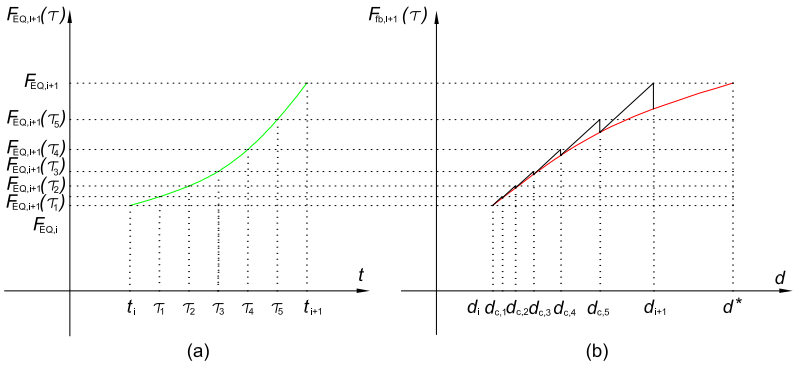

Figure 6.2: Schematic representation of the EFC method with interpolated EF commands:(a)EF interpolation; (b)Solution of equations.

$$K_{PD} d_{i+1}(\tau_j) + (1+\alpha) r_{N,i+1}(\tau_j) + (1+\alpha) R_{E,i+1}(\tau_j) = F_{EQ,i+1}(\tau_j) \qquad \tau_j \in (t_i \quad t_{i+1}] \tag{6.16}$$

in which $F_{EQ,i+1}(\tau_j)$ denotes the EF command at the time instant τ_j, which is sampled every δt; $R_{E,i+1}(t)$ is the restoring force time history of the PS, which is corresponding to the EF command. Clearly, Eq. (6.4) is only the last one in this equation group. In order to solve these equations at different instants, we can carry out the traditional iteration with each equation. In real-time implementation, the iteration should be

completed in a short time. Therefore, we often conduct only one step iteration for each equation with the results of the last equation as the initial value. This process is called real-time iteration Diehl et al. (2005). In fact, Eq. (6.15) also describes this process. As schematically depicted in Figure 6.2, the EF commands between t_i and t_{i+1} are initially interpolated via some functions with respect to time; then for the EF command at some time, one iteration is conducted with the previous step results as the initial value. Therefore, the EFC method is the real-time iteration as long as the EF command is interpolated and the integral control is applied.

In other cases, the specimen contains some dampers and/or masses, which cause Eq. (6.16) to be an ordinary differential equation (ODE) with respect to the actuator displacement due to the continuity of the physical word. Then it is somewhat confusing to solve an ODE with the EFC method or the iteration presented in Eq. (6.9). In fact, the EFC method is still reasonable to perform RHS on a mass and/or a damper. If the damping force and/or the inertia force are known, they could be moved to the right-hand side of Eq. (6.16)and the ODE is reduced to a nonlinear problem. In reality, the velocity and/or acceleration solutions related to the damping force and/or inertia force are not available until the end of the time step. However, we can achieve some velocity and/or acceleration targets during the iteration process and remove the corresponding force from the EF, since velocity and/or acceleration targets, as the derivative or double derivative of the displacement, are faster to achieve than a displacement. As an extreme example, accelerations of a structure can be excited before its displacement varies if an external force is imposed on it. Wu et al. (2007) came to a similar conclusion with a numerical simulation. Consequently, the damping force and/or inertia force can be subtracted from the equations before the actuator finally achieves the displacement solution, causing Eq. (6.4) to be approximately solved.

This analysis implies that we can extend the results for the spring specimen, such as the stability and accuracy properties, and relationship between the EFC method to the traditional iteration, to those for a damping and/or mass specimen with the assumption: the interpolation induces correct velocity and acceleration responses. In practice, this never happens, since the correct velocity and the correct acceleration at the current step can not be exactly predicted at the beginning of this step.

Nonetheless, it suggests the importance of the interpolation and the ideal results of the method. Fortunately, if the integration step is smaller, the shape of the EF force is similar to that of the displacement response, thus the EF commands can be interpolated to achieve some velocity or acceleration. In order to re-obtain the equilibrium, it is essential to conduct corrections. Interpolation schemes and movement quantity corrections are discussed further in the forthcoming sections.

6.3.2 Advantages of the EFC method

From the above description, the EFC method with simple controllers to some extent acts like traditional iterations or very real-time iterations. However, it is often preferable. Initially, if Kp is not equal to zero in Eq. (6.15), the change of the EF commands are considered to evaluate the actuator commands. Nevertheless, control parameters should be cautiously designed; otherwise, some unintended properties, for instance oscillation and overshoot, may occur. From the numerical analysis, it may be difficult to design parameters for this iteration. Conversely, with the help of control theory, it is convenient to establish the parameters for a specific problem. Therefore, the EFC method provides a framework to design a real-time iteration with control theory.

In addition, the EFC method is not only a type of iteration but also a compensation for the dynamics of actuators from the control viewpoint. The terms on the right-hand side of Eq. (6.15) are related to the actual responses and commands of the actuator, and hence the actuator is implicitly considered. The compensation to the dynamics of the actuator is similar to outer loop control schemes, amongst others, see Bonnet et al. (2007). Shi (2011) concluded that the EFC method can effectively compensate for the system dynamics and dead time and hence, specific delay compensation is not necessary. In this sense, the EFC method considers the actuator and the iteration simultaneously. Jung et al. (2007) employed an iteration scheme based on the actual responses and the system delay was directly compensated for with other schemes.

In sum, the EFC method is mathematically similar to some iteration schemes, but it is more convenient to design the parameters with the help of the control theory. For a simple controller, we can convert the EFC method into a real-time iteration easily, but for more complicated controllers, it is difficult or even impossible to finish that.

Another advantage is the compensation of the force feedback loop to the dynamics of the actuator, which is so favorable that sometime the delay compensation for the actuator can be neglected even in real-time tests.

6.4 Interpolations for the EF commands

As discussed above, for a specimen containing mass, the equivalent force commands should be quadratically interpolated to achieve some acceleration responses, namely

$$F_{EQ,i+1}(\tau) = \alpha_2\tau^2 + \alpha_1\tau + \alpha_0 \tag{6.17}$$

where α_1, α_2 and α_3 are factors and $F_{EQ,i+1}(\tau)$ the equivalent force command at τ in the $(i+1)$-th step. In order to establish the factors, three conditions are needed. Two schemes have been applied based on different conditions and herein they are compared by means of numerical simulations to choose a better one for the following analysis. The first scheme considered, referred to as "Interpolation 1" in Figure 6.4, is based on three equivalent forces (Xu, 2009), i.e.,

$$\begin{cases} F_{EQ,i+1}(-\Delta t) = F_{EQ,i-1} \\ F_{EQ,i+1}(0) = F_{EQ,i} \\ F_{EQ,i+1}(\Delta t) = F_{EQ,i+1} \end{cases} \tag{6.18}$$

and the factors of the interpolation function can be solved as

$$\begin{cases} \alpha_0 = F_{EQ,i} \\ \alpha_1 = \dfrac{F_{EQ,i+1} - F_{EQ,i-1}}{2\Delta t} \\ \alpha_2 = \dfrac{F_{EQ,i+1} + F_{EQ,i-1} - 2F_{EQ,i}}{2\Delta t^2} \end{cases} \tag{6.19}$$

For the first step, the following formula is utilized

$$F_{EQ,1}(\tau) = \frac{\tau^2}{\Delta t^2}F_{EQ,1} + (1 - \frac{\tau^2}{\Delta t^2})F_{EQ,0} \tag{6.20}$$

where

$$F_{EQ,0} = K_{PD} d_0 + (1+\alpha) r_{N,0} + (1+\alpha) R_{E,0} \tag{6.21}$$

Wang and Wu (2008) exploited a scheme based on the constant average acceleration approximation of the Newmark-β method, named 'Interpolation 2' in Figure 6.4. With the constant acceleration assumption, the displacement response can be expressed as

$$d_{i+1}(\tau) = d_i + v_i \times \tau + \frac{1}{2} \tilde{a}_{i+1} \times \tau^2 \tag{6.22}$$

where the acceleration $\tilde{a}_{N,i+1}$ is unknown. According to Eq. (6.4) the equivalent force feedback, if the NS is linear, should be

$$\begin{aligned} F_{EQ,i+1}(\tau) = {} & [(1+\alpha)K_N + K_{PD}] d_i + [(1+\alpha)K_N + K_{PD}] v_i \tau \\ & + \frac{[(1+\alpha)K_N + K_{PD}] \tilde{a}_{i+1} \tau^2}{2} + R_{E,i+1}(\tau) \end{aligned} \tag{6.23}$$

The measured force $R_{E,i+1}(\tau)$ can be approximated by $R_{E,i}$, since it is very small compared with the other terms. Considering the continuity at the t_{i+1}, the factors of the interpolation function read

$$\begin{cases} \alpha_0 = F_{EQ,i} \\ \alpha_1 = [(1+\alpha)K_N + K_{PD}] v_i \\ \alpha_2 = \dfrac{F_{EQ,i+1} - F_{EQ,i} - [(1+\alpha)K_N + K_{PD}] v_i}{\Delta t^2} \end{cases} \tag{6.24}$$

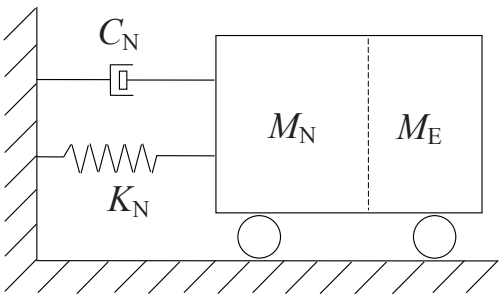

Figure 6.3: Schematic representation of the structure in RHS with a pure inertia specimen

In order to choose the preferable interpolation, numerical simulations are conducted on a split mass system. As discussed in the last section, the displacement error

can be reduced through more iteration or more carefully designed controller parameters. Here we just concentrate on the influence of the interpolation on acceleration responses. Consequently, the split mass system, shown in Figure 6.3 is chosen Wu et al. (2009), where the physical substructure only contains a mass. In addition, the steady state acceleration responses in Eq. (6.30) are assumed to be achieved. Parameters in RHS are defined as

$$\begin{aligned} &\alpha = 0 \quad \Delta t = 10\text{ms} \quad \delta\text{t} = 1\text{ms} \quad \text{f} = 10\sin(4\pi\text{t}) \\ &K_N = 3600\text{N/m} \quad \text{M}_\text{N} = 100\text{kg} \quad \text{M}_\text{E} = 50\text{kg} \end{aligned} \tag{6.25}$$

where f indicates the external force. The simulated displacements together with reference displacements are depicted in Figure 6.4, which shows that both interpolations introduce damping, and the second one is relatively accurate. The damping can be explained as the effect of the delay in the acceleration responses due to the predicted acceleration error (Horiuchi et al., 2000). The second method utilizes the right information at the i-th and $(i+1)$-th steps, while the other method uses information from the $(i-1)$-th step to the $(i+1)$-th step. The older the information is, the greater the delay and the delay-induced damping are. In view of this, the second method is a better choice, which will be adopted in the next sections.

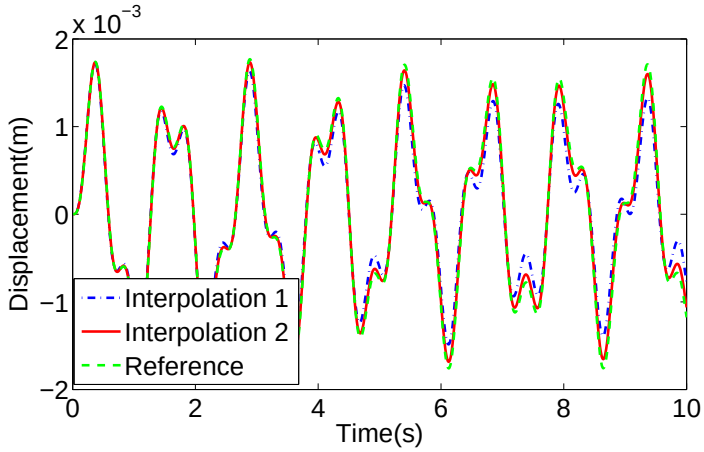

Figure 6.4: Comparisons of displacement time histories obtained with different interpolations

As demonstrated in the last section, numerical properties of time integration algorithms deteriorate when applied in RHS. Similar results were presented in Wu et al. (2005, 2009). In order to examine the change of the numerical properties in a wider range, the stability analysis of the EFC method is performed on the structure as shown in Figure 6.5. The structural parameters are assumed to be

$$\frac{M_E}{M_N} = \frac{K_N}{K_E} = \frac{C_E}{C_N} = \frac{1}{b} \tag{6.26}$$

where b is a parameter indicating the ratio of the frequencies of the PS and the NS. Wang and Wu (Wang and Wu, 2009, in Chinese) conducted stability analysis of the

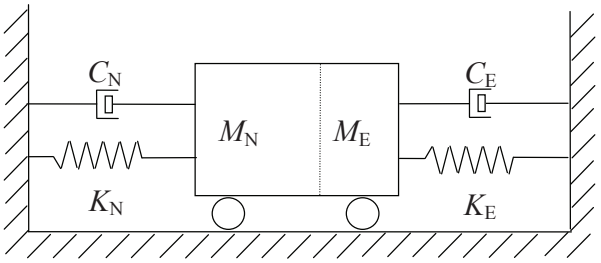

Figure 6.5: Computation schematic of structure in RHS with dynamic specimen

EFC method with a dynamic specimen taking into account a second-order model of actuators. The results are helpful for testing, however, are affected by the actuator model. In order to focus on the stability of the method, we neglect the actuator models by introducing some assumption. Wu et al. (2007) analyzed the stability of the EFC method with a linear EF interpolation on a linear SDOF system containing a physical damper under the assumption that the steady state velocity is achieved at the end of each integration step. This assumption is based on the fact that a velocity target is easier to achieve than a displacement target and the response speed of the EF control system can be tuned through the EF controller. In this chapter, a similar assumption is made, which is that the steady state acceleration due to the quadratic EF commands is achieved at the end of each step. Another assumption is $d_{E,i+1}(\tau)$

= $d_{N,i+1}(\tau)$, where τ is defined in Eq. (6.16). Therefore, the derivative and double derivative of the acceleration approach zero, which means the following equations hold

$$K_{PD}a_{E,i+1} + (1+\alpha)K_N a_{E,i+1} + (1+\alpha)K_E a_{E,i+1} = 2\alpha_2 \tag{6.27}$$

$$K_{PD}v_{E,i+1} + (1+\alpha)K_N v_{E,i+1} + (1+\alpha)K_E v_{E,i+1} + (1+\alpha)C_E a_{E,i+1} = 2\alpha_2\Delta t + \alpha_1 \tag{6.28}$$

Eq. (6.4) can be rewritten as

$$K_{PD}d_{E,i+1}+(1+\alpha)K_N d_{E,i+1}+(1+\alpha)K_E d_{E,i+1}+(1+\alpha)C_E v_{E,i+1}+(1+\alpha)M_E a_{E,i+1} = F_{EQ,i+1} \tag{6.29}$$

From the above three equations, the responses can be solved, viz.

$$a_{E,i+1} = \frac{2\alpha_2}{K_{PD} + (1+\alpha)K_N + (1+\alpha)K_E} \tag{6.30}$$

$$v_{E,i+1} = \frac{2\alpha_2\Delta t + \alpha_1 - (1+\alpha)C_E a_{E,i+1}}{K_{PD} + (1+\alpha)K_N + (1+\alpha)K_E} \tag{6.31}$$

$$d_{E,i+1} = \frac{F_{EQ,i+1} - (1+\alpha)C_E v_{E,i+1} - (1+\alpha)M_E a_{E,i+1}}{K_{PD} + (1+\alpha)K_N + (1+\alpha)K_E} \tag{6.32}$$

The velocity can also be expressed as

$$v_{E,i+1} = \frac{2\alpha_2\Delta t + \alpha_1}{K_{PD}v_{E,i+1} + (1+\alpha)K_N v_{E,i+1} + (1+\alpha)K_E} - \frac{2\alpha_2(1+\alpha)C_E}{[K_{PD} + (1+\alpha)K_N + (1+\alpha)K_E]^2} \tag{6.33}$$

In the above equations, the physical stiffness is the actual stiffness at the instant, not the initial stiffness. From the acceleration expression, one can see that the E-FC method equivalently introduces an explicit acceleration predictor for the physical substructure if K_E is a constant while the velocity and displacement are implicit due to the dependence on the physical damping ratio and physical mass. If K_E is not a constant, the method is totally implicit for a nonlinear physical substructure. However, the movement quantities can not be exactly identical to those of the NS. It is to say, the interpolation deteriorate the methods. To analyze the effects, the stability is considered.

Then the structure responses can be updated according to the responses of the physical substructure. Even though different corrections can be adopted to update, as discussed in the next sections, they make no difference for the numerical substructure responses in this ideal case due to the assumptions. Then the following recursive equation is obtained

$$\mathbf{X}_{i+1} = \mathbf{A}\mathbf{X}_i \tag{6.34}$$

where $\mathbf{X}_{i+1} = [d_{i+1} \quad v_{i+1}\Delta t \quad a_{i+1}\Delta t^2 \quad F_{EQ,i}]^T$. The spectral radius of the matrix $\mathbf{A}$ indicates the stability of the method.

6.5.1 Zero Stability analysis

The zero stability is nothing more than the stability of an integrator when the time step approaches zero. It is a necessary condition of convergence for an integrator. With the help of numerical analysis software, the limit of the amplification matrix can be obtained when $\Omega = \omega_{Overall}\Delta t$ tends to zero. For $\alpha = 0$, the amplification matrix reads

$$\mathbf{A}_0 = \begin{bmatrix} \frac{2b-1}{2b} & 1 & \frac{2b-1}{8b} & \frac{1}{8b} \\ -\frac{1}{b} & 1 & \frac{2b-1}{4b} & \frac{1}{4b} \\ -\frac{2}{b} & 0 & -\frac{1}{2b} & \frac{1}{2b} \\ 4 & 4 & 1 & 0 \end{bmatrix} \tag{6.35}$$

The corresponding eigenvalues of the amplification matrix are

$$\lambda_1 = 0, \ \lambda_{2,3} = 1, \ \lambda_4 = -\frac{1}{b} \tag{6.36}$$

Therefore, the spectral radius is

$$\rho(\mathbf{A}_0) = \max(1, \frac{1}{b}) \tag{6.37}$$

which means that if the ratio b is smaller than one, the method is unstable even the integration step approaches zero. In addition, the results show that the damping in the structure has no effect on the zero-stability. Other researchers have drawn similar conclusions that the physical mass should be less than the corresponding numerical part, see Bursi et al. (2008).

Figure 6.6 depicts the cases when $\alpha \neq 0$ and shows that the only condition for the zero-stability is $b \geq 1$ even α belongs to [-1/3 0], which is an optimal interval for the α method. Note that weak instability (Hughes, 1983) due to eigenvalues which are of multiplicity greater than one and equal to one in modulus is viewed to be stable here. Meanwhile, it can also be observed that the approach is zero-stable with a careful selection of the parameter if $b < 1$. However, this case is neglected since it is not convenient to search for suitable parameters in applications.

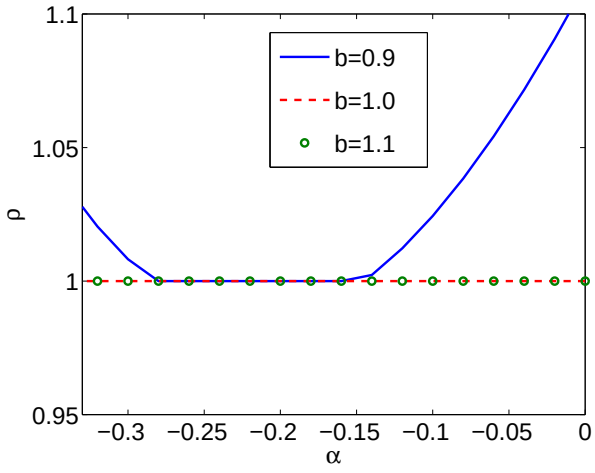

Figure 6.6: Zero stability analysis

6.5.2 Spectral stability analysis

Figure 6.7 plots spectral radius curves for α = 0. One can observe that the dissipative property of the EFC method, which matches the simulation in Figure 6.4 and is inconsistent with the standard α method. The dissipation goes up with the reduction of the parameter *b*, which means the physical substructure has a smaller frequency and a larger mass. This can be viewed as the effect of the acceleration delay as well. Sometimes we hope the integrator can decay the high frequency noise and oscillation, which can be achieved through the introduction of α. Figure 6.8 presents the spectral radii of the EFC method with *b* = 10 and different values of the parameter α. For the sake of comparison, the spectral radii of the α method for the overall emulated structure are illustrated as well. It is evident that the EFC method exhibits very similar dissipation to the standard α method when Ω is large enough. Meanwhile, the undesired dissipation at low frequency is also observed. However, the EFC method shows more favorable stability than the explicit method - the central difference method for real-time hybrid simulations with a dynamic specimen presented in (Wu et al., 2009).

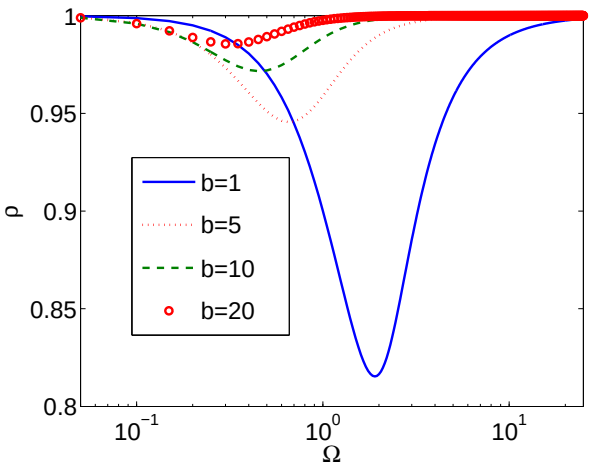

Figure 6.7: Spectra radii corresponding to different values of the parameter *b*

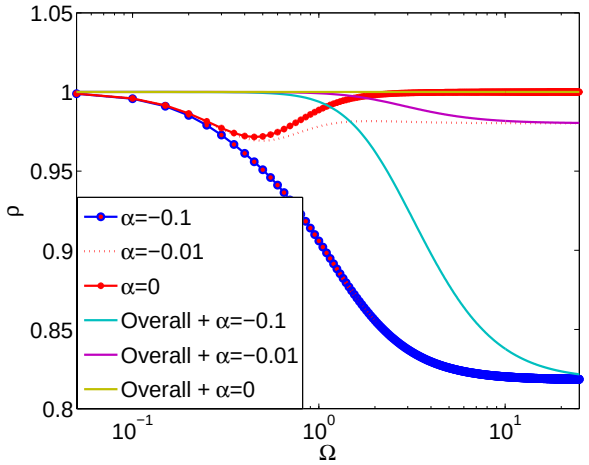

Figure 6.8: Spectra radii corresponding to different values of the parameter α

Before we move on to next sections, this section is concluded as follows:

① The condition of the zero-stability of the EFC method with a dynamic specimen is $b \geq 1$;

② The EFC method with a dynamic specimen is unconditionally stable if $b \geq 1$, however, undesired dissipation at low frequency is observed;

③ The EFC method with a dynamic specimen exhibits similar high-frequency dissipation to the standard α method.

6.6 Necessity of movement quantity correction and displacement correction

6.6.1 Necessity of movement quantity correction

We have heretofore discussed the important role of the EF command interpolation and derived the steady state acceleration under some assumptions. Xu (2009) showed that the command interpolation can reduce overshoot and hence avoid some unintended loading/unloading cycles. In order to examine the steady state acceleration and investigate the influence of interpolation, we analyze the steady state response and steady state errors from viewpoints of control theory.

The closed-loop transfer function from the EF commands to the acceleration response corresponding to the block diagram as shown in Figure 6.1 with a PI controller reads

$$\begin{aligned} T_{CLA} &= \frac{(K_p + K_i/s)C_F T_A s^2}{1 + (K_p + K_i/s)C_F T_A (K_N + K_{PD} + K_E + C_E s + M_E s^2)} \\ &= \frac{(K_p s + K_i)C_F T_A s^2}{s + (K_p s + K_i)C_F T_A (K_N + K_{PD} + K_E + C_E s + M_E s^2)} \end{aligned} \tag{6.38}$$

where T_A denotes the transfer function of the actuator. With the EF reference in Eq. (6.17), the steady state acceleration response according to the final value theorem

(Burns, 2001, Page 38) is

$$\lim_{s\to 0} s(\frac{2\alpha_2}{s^3}+\frac{\alpha_1}{s^2}+\frac{\alpha_0}{s})T_{CLA} = 2\alpha_2 \times \lim_{s\to 0}\frac{(K_p s+K_i)C_F T_A}{s+(K_p s+K_i)C_F T_A(K_N+K_{PD}+K_E+C_E s+M_E s^2)}$$
$$= \frac{2\alpha_2}{K_N+K_{PD}+K_E} \tag{6.39}$$

which reconfirms Eq. (6.30).

For a feedback control system, we analyze the steady state error by means of the *type* of the system. The type of a system (Burns, 2001, Page 168) is defined as the number of pure integrations in the open-loop transfer function. If the open-loop transfer function can be expressed as

$$G(s) = \frac{num(s)}{s^n den(s)} \tag{6.40}$$

then the system will be of Type n. For an actuator control system, it is at least Type I to eliminate the steady state error, i.e. $n \geqslant 1$. The closed loop transfer function of the actuator is

$$T_A(s) = \frac{\frac{num(s)}{s^n den(s)}}{1+\frac{num(s)}{s^n den(s)}} = \frac{num(s)}{s^n den(s)+num(s)} \tag{6.41}$$

In our case, the open-loop transfer function from the EF commands to the EF feedback with a PI controller reads

$$\begin{aligned} T_{OLEF} &= (K_p+\frac{K_i}{s})C_F T_A(K_N+K_{PD}+K_E+C_E s+M_E s^2) \\ &= (K_p+\frac{K_i}{s})C_F\frac{\frac{num(s)}{s^n den(s)}}{1+\frac{num(s)}{s^n den(s)}}(K_N+K_{PD}+K_E+C_E s+M_E s^2) \\ &= \frac{num(s)}{s[s^n den(s)+num(s)]}(K_p s+K_i)C_F(K_N+K_{PD}+K_E+C_E s+M_E s^2) \end{aligned} \tag{6.42}$$

Therefore, it is at most a Type I system. According to properties of a Type I system, there is no steady state error between the EF command and the EF feedback if the EF commands are sent to the loop as a step. Meanwhile, the steady state EF error is a constant if they are given with a linear interpolation. This implies that the derivative of the EF commands and feedback are the same, causing that the velocity target can be achieved. If the EF commands are quadratic interpolated, the steady state EF

errors are infinity and the error of derivatives of the EF commands and EF feedback is a constant, and the double-derivative of them are the same. It means that the acceleration target can be achieved while the errors exist between the targets and the achieved counterparts of the velocity and displacement. This analysis shows that the EF error may be greater at the end of an integration step for a quadratic EF interpolation than a step or linear interpolation.

To reduce the control errors, it is a good choice to improve the type of the system with a feed forward control for the reference. If the transfer function $G(s)$ can be rewritten into

$$G(s) = \frac{a_m s^m + a_{m-1} s^{m-1} + \cdots + a_1 s + a_0}{s(b_m s^n + b_{m-1} s^{n-1} + \cdots + b_1 s + b_0)} \tag{6.43}$$

Then the feed forward controller can be designed as

$$G_f(s) = \mu_1 s + \mu_0 \tag{6.44}$$

with

$$\begin{aligned} \mu_0 &= \frac{b_0}{a_0} \\ \mu_1 &= \frac{b_1 - \mu_0 a_1}{a_0} \end{aligned} \tag{6.45}$$

in which μ_0 and μ_1 are dependent on the actuator and the specimen. On the other hand, the actuator and the specimen are usually time-varying and nonlinear. Consequently, it is not easy to improve the system to Type III. In addition, the control systems in operation are often Type I and Type II. Hence it is a good choice to design some schemes to update the displacement with the error in mind, which will be discussed in the next section.

6.6.2 Displacement corrections

In hybrid simulations, error accumulation may result in instability and several researchers proposed different updating schemes to cope with them (Peek and Yi, 1990a,b; Shing et al., 1991; Shing and Vannan, 1991). In fact, larger errors exist in RHS based on an implicit integrator than in implicit PDT due to real-time loading and the real-time iteration in the former, which imply larger control errors and convergence

errors. Therefore, suitable correction methods must be used to contain the propagation of the errors. The EFC method (Wu et al., 2007) adopted the scheme proposed by Peek and Yi (1990a) (referred to as Peek's correction herein), while Jung et al. (2007) used another scheme originated from the method proposed by Shing (Shing and Vannan, 1991). Shing et al. proved that the iteration and correction based on the initial stiffness is energy-dissipative for a softening structure (Shing and Vannan, 1991) and has a smaller error propagation amplification factor (Shing et al., 1991). Their simulations showed that sometimes Peek's correction is unstable. The reason why Peek's correction is unstable is analyzed for hybrid tests on a spring specimen hereafter.

In Peek's correction the updated displacement reads

$$d_{i+1} = \frac{F_{EQ,i+1} - (1+\alpha)R_{E,i+1}}{K_{PD} + (1+\alpha)K_{N,ini}} \tag{6.46}$$

Then the equations can be obtained for the method:

$$K_{PD}d_{i+1}^{EX} + (1+\alpha)K_N d_{i+1}^{EX} + (1+\alpha)K_E d_{i+1}^{EX} = F_{EQ,i+1} \tag{6.47}$$

$$K_{PD}d_{i+1} + (1+\alpha)K_N d_{i+1} + (1+\alpha)K_E d_{E,i+1} = F_{EQ,i+1} \tag{6.48}$$

where d_{i+1}^{EX} and d_{i+1} denote the exact and updated displacement, respectively. Subtracting them one gets

$$[K_{PD} + (1+\alpha)K_N](d_{i+1}^{EX} - d_{i+1}) = -(1+\alpha)K_E(d_{i+1}^{EX} - d_{E,i+1}) \tag{6.49}$$

Therefore, we can obtain the relationship between signs of $(d_{i+1}^{EX} - d_{i+1})$ and $(d_{i+1} - d_{E,i+1})$, namely,

$$sign(d_{i+1}^{EX} - d_{i+1}) = -sign(d_{i+1}^{EX} - d_{E,i+1}) \tag{6.50}$$

which means that the correction renders the updated displacement greater than the exact solution when $d_{i+1}^{EX} > d_{E,i+1}$. As a result, for PDT, where undershoot often happens, the correction would amplify the response, causing instability. Fortunately, it takes a long time to accumulate the error since the error at one step is greatly reduced due to $[K_{PD} + (1+\alpha)K_N] \gg (1+\alpha)K_E$.

In real-time tests with the EFC method, both of the overshoot and undershoot may take place although in PDT test only undershoot happens. Here overshoot and undershoot are used to define the relationship between the exact solution to Eq. (6.4) and

the measured displacement of the actuator. Firstly, delay compensation approaches, which can introduce prediction errors, can lead to overshoot or undershoot. Secondly, sometimes control parameters result in overshoot in the EFC method. In addition, if the physical stiffness is not taken into account or the structure is a stiffness-strengthening system, overshoot may happen. As a result, some correction considering overshoot and undershoot is desired in the EFC method. However, Shing's correction (Shing and Vannan, 1991; Jung et al., 2007) can not be directly used in the EFC method although their correction works well in their research. As pointed out in the previous section, the EFC method combines the iteration and the compensation to the dynamics of the actuator together. It means that the actuator commands associated with the EF controller and the actuator and are not the solution to Eq. (6.4).

The following correction is proposed to deal with this problem:

$$d_{i+1} = \begin{cases} d_{E,i+1} + \dfrac{\Delta R}{K_{PD} + (1+\alpha)K_{N,ini} + (1+\alpha)K_{E,ini}} & \textit{undershoot} \\ \dfrac{F_{EQ,i+1} - (1+\alpha)R_{E,i+1}}{K_{PD} + (1+\alpha)K_{N,ini}} & \textit{overshoot} \end{cases} \tag{6.51}$$

The principle is that: if the loading overshoots, the correction makes the updated displacement go back; if it undershoots, the correction makes the displacement closer to the exact results. But it needs to determine whether the EF feedback overshoots or not. The following relationship can be used to check:

$$\begin{cases} \textit{undershoot} & \Delta R \times \Delta F > 0 \\ \textit{overshoot} & \Delta R \times \Delta F < 0 \end{cases} \tag{6.52}$$

with

$$\begin{aligned} \Delta R &= F_{EQ,i+1} - F_{FB,i+1} \\ \Delta F &= F_{EQ,i+1} - F_{EQ,i} \end{aligned} \tag{6.53}$$

For the split mass shown in Figure 6.5, simulations are carried out to investigate the effectiveness of the displacement corrections, presented in Figures 6.9 and 6.10. In simulations, the following set of parameters is chosen

$$\begin{aligned} &\alpha = 0 \quad \Delta t = 10ms \quad \delta t = 1ms \\ &K_N = 3600N/m \quad M_N = 100kg \quad C_N = 0 \\ &M_E = 0 \quad K_E = 3600N/m \quad C_E = 0 \quad f = 10sin(2\pi t) \end{aligned} \tag{6.54}$$

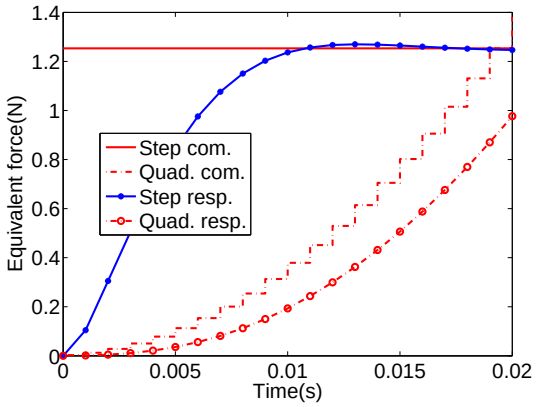

Figure 6.9: Comparisons of EF responses with step commands and quadratic interpolation commands

In addition, a second-order model of actuators (Wu et al., 2007) is employed, i.e.,

$$T_A(s) = \frac{\omega_A^2}{s^2 + 2\zeta_A\omega_A s + \omega_A^2} e^{-\tau_A s} \tag{6.55}$$

where ω_A and ζ_A denote the circular frequency and equivalent damping ratio, respectively; τ_A and s indicate the dead time of the system and the Laplace variable. In the simulations, ω_A= 100rad/s, ζ_A = 0.9 and τ_A= 0 are set.

In Figure 6.9, the same EF controller and actuator model are applied with different EF commands. For the step EF commands, the EF response achieves steady states in 20ms and the error between commands and feedback approaches zero. Conversely, for the quadratic commands, that error increases with respect to time, in agreement with the analysis in the last subsection. Therefore, the correction to reduce the impact of the control error on the test results is more necessary for the quadratic commands than for the step commands. In Figure 6.10, the legend "Step" and "Quad." denote the manner to send out the EF commands, step change or quadratic interpolation, respectively. Meanwhile, "Peek" and "Prop." indicates the correction method proposed by Peek et al. and that in this chapter. For the purpose of comparisons, the results evaluated with the α method with α = 0 for the overall structure are also presented, referred to as Reference. Clearly, the results with the quadratic interpolation and Peek's correction are unstable while the other two cases match the reference well. This sim-

ulation confirms the analysis in the previous section and verifies the performance of the proposed correction.

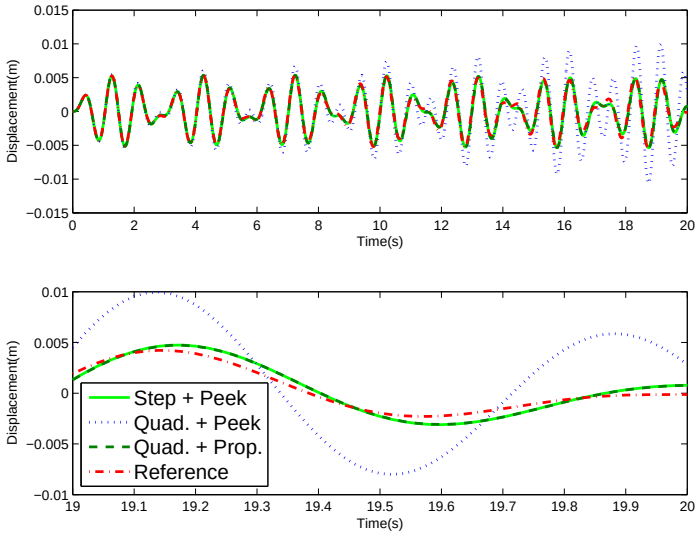

Figure 6.10: Comparisons of time histories with different EF commands and corrections

6.7 Acceleration correction approach

As shown in the previous section, the discrepancy between the steady state acceleration and accelerations of the NS introduces dissipation to the EFC method. Even though the positive dissipation is beneficial to stabilize the tests, we hope to reduce or eliminate it to improve the accuracy. Hereafter, a correction that considers its displacement and acceleration responses is presented and its effectiveness is illustrated by stability analysis with the use of the spectral radius technique.

6.7.1 The proposed acceleration correction scheme

To begin with, we look back at the first formula of the displacement correction in Eq. (6.51), which can be re-written as

$$[K_{PD} + (1+\alpha)K_{N,ini}]d_{i+1} = F_{EQ,i+1} - (1+\alpha)\times R_{E,i+1} - (1+\alpha)K_{E,ini}(d_{i+1} - d_{E,i+1}) \quad (6.56)$$

where $K_{N,ini}$ and $K_{E,ini}$ denote the initial stiffnesses of the NS and PS, respectively. Compared with Eq. (6.4), $(d_{i+1} - d_{E,i+1})$, which should be zero for an ideal case, can be thought as the displacement correction increment of the PS, whilst the restoring force of PS is corrected by the increment of $K_{E,ini}(d_{i+1} - d_{E,i+1})$. Hence, Eq. (6.56) may be called the corrected equilibrium equation. It is clear that the correction leads to the same results as the standard integrator for a linear system. Therefore, to reduce the effects of the displacement error in PS, the possible method is to add the predicted error of the reaction force of the PS into the equilibrium equation. With this in mind, the inertia force correction for RHS can be $M_{E,ini}(a_{i+1} - a_{E,i+1})$, in which $M_{E,ini}$ indicates the initial mass of the PS, and for the split mass system, the corrected equilibrium equation reads

$$\begin{aligned}[K_{PD} + (1+\alpha)K_{N,ini}]d_{i+1} &= F_{EQ,i+1} - (1+\alpha)\times R_{E,i+1} \\ &-(1+\alpha)K_{E,ini}(d_{i+1} - d_{E,i+1}) - (1+\alpha)M_{E,ini}(a_{i+1} - a_{E,i+1})\end{aligned} \quad (6.57)$$

Two variables, displacement and acceleration responses, exist in this equation, which can be solved from the following system:

$$\begin{cases} [K_{PD} + (1+\alpha)K_{N,ini}]d_{i+1} = F_{EQ,i+1} - (1+\alpha)\times R_{E,i+1} \\ \quad -(1+\alpha)K_{E,ini}(d_{i+1} - d_{E,i+1}) - (1+\alpha)M_{E,ini}(a_{i+1} - a_{E,i+1}) \\ d_{i+1} = d_i + \Delta t v_i + \Delta t^2[(\frac{1}{2} - \beta)a_i + \beta a_{i+1}] \end{cases} \quad (6.58)$$

This is a linear system of equations, and thus it increases little computational effort. After displacement and acceleration responses solved, the velocity can be updated using the velocity approximation, and the time of the test is advanced to the next step. From Eq. (6.58), one can observe that this correction provides the same results as the standard numerical method for an undamped linear physical system. In addition, the method corrects two variables at the same time, which is different from the correction in PDT, for example Eq. (6.51), and reflects one inherent nature of RHS-multiple

variable coupling between two substructures. Note that the method is called acceleration correction to highlight the acceleration as the displacement is always corrected in the EFC method.

In RHS, interface conditions should be met to obtain a desirable test result. In practice, it is difficult, if possible, to achieve the conditions owing to i) complexities of real-time control for multiple targets; ii) the fact that velocity and/or acceleration targets are not available for most integrators. Therefore, the aforementioned correction is a good candidate for a stronger coupling. First, it simultaneously improves the displacement coupling and acceleration coupling. Secondly, it can be adopted with most of the currently-used integrations. The idea presented here is also suitable for explicit integrators when Eq. (6.58) is recognized to be a variation of the equilibrium equation. Lastly, little computation effort is required.

Two practical problems encountered by this strategy may be how to conduct the strategy for a distributed-mass system and how to code with the measurement acceleration noise. For the former problem, one equivalent lumped mass can be assumed. For the latter one, a well-designed filter or Kalman filter can reduce the influence of the noise. In fact, to some extent the acceleration noise can be converted to the mass prediction error, and the following analysis will show that the influence is not so bad. It is interesting to mention that with Kalman filter and the measured displacement and acceleration, the velocity response can be observed and a three-state correction can be easily conducted with the frame of this correction. It is worth pointing out that the method presented here can also be used for substructure shaking table tests (Neild et al., 2005).

6.7.2 The performance of the proposed scheme

In order to examine the performance of the correction, stability analysis similar to the cases in the previous sections and numerical simulations are conducted on the structure model in Figure 6.5. In the stability analysis, the reaction force and the displacement and acceleration responses of the PS expressed in Eq.s (6.30) and (6.32) are substituted into the corrected equilibrium equation, and then the displacement and acceleration are solved and the velocity is updated by means of the correspond-

ing approximation, i.e., Eq. (6.3). Finally, the following recursive equation is obtained for each case

$$\mathbf{X}_{i+1} = \mathbf{A}\mathbf{X}_i \tag{6.59}$$

where $\mathbf{X}_{i+1} = [d_{i+1} \quad v_{i+1}\Delta t \quad a_{i+1}\Delta t^2 \quad F_{EQ,i}]^T$. The spectral radius of the matrix $\mathbf{A}$ is used to check the stability of the method.

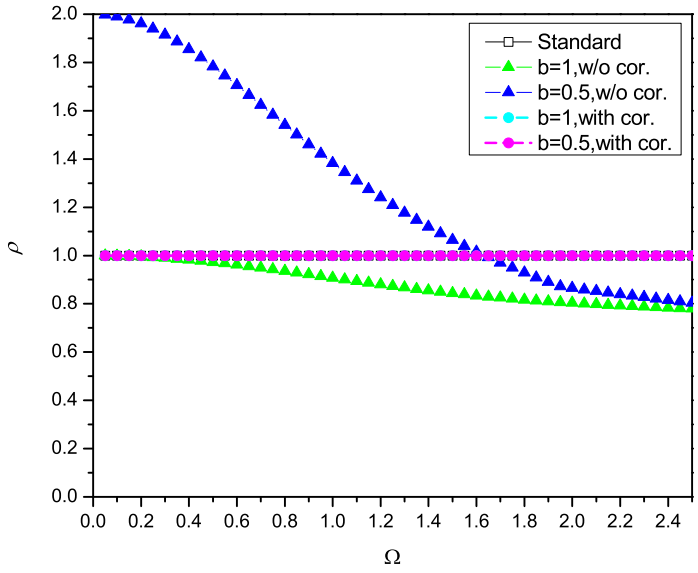

Figure 6.11: Spectral radii comparisons of the standard α-method, the EFC method without and with the acceleration correction when $\alpha = 0$ and $\gamma_m = 1$.

Three cases with $\alpha = 0$ and

$$\gamma_m = \frac{M_{E,ini}}{M_E} = 1 \tag{6.60}$$

are compared in Figure 6.11, which are i) the EFC method with the acceleration correction; ii) the EFC method without acceleration correction, namely the case in Section 6.5; iii) the standard α method (Hilber et al., 1977). One can observe that, the EFC method with the acceleration correction exhibits the same spectral behavior as the standard method. This indicates that the acceleration correction results in the

EFC method to be the standard method when α = 0 and γ_m = 1, and that the mass ratio of the physical mass to the numerical mass is no more a constraint for RHS. This can also be concluded from Eq. (6.57), which shows that in this specific case the EFC with acceleration correction is reduced to the standard method.

In practice, the correction cannot be perfect owing to mass prediction errors and acceleration measurement errors. Figure 6.12 shows the effects of the mass prediction error by means of the spectral radius. When γ_m is greater than unity, the method is unconditionally unstable whatever the value of *b* is. When γ_m is less than unity, the method is stable and dissipation exists. Therefore, in a real test, the predicted mass should be a little smaller than the exact. It is interesting to mention that the predicted stiffness in the correction is often larger than the exact stiffness for unidirectional convergence.

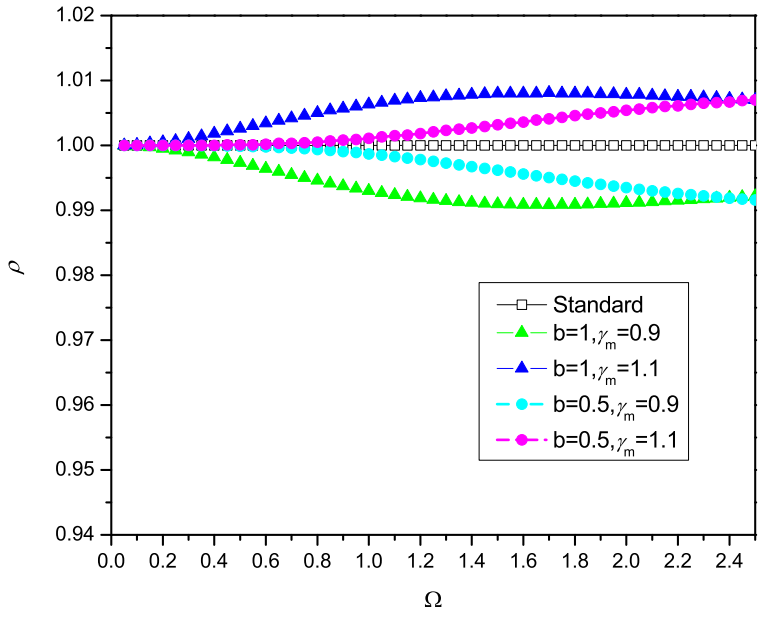

Figure 6.12: Effects of the ratio γ_m between the predicted mass and the actual mass.

Notice that the EFC method with correction can not exhibit the same properties as the α method until α is equal to zero, since the same factor α is also adopted for the inertia force of the PS. Figure 6.13 depicts the spectral radii of the α method and of the EFC method with the correction for different values of α. It apparently shows that the EFC method, with an even exactly-predicted mass, introduces damping compared

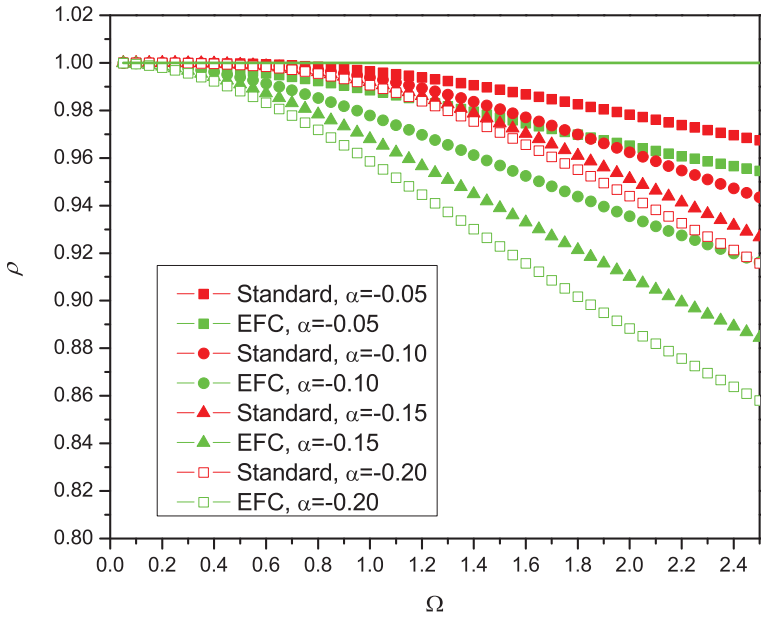

Figure 6.13: Spectral radii when $\alpha \neq 0$.

with the standard method. Unfortunately, this happens in the low frequency range. Therefore, the reasonable range of α may be [0 -0.1] for accuracy consideration.

To verify the spectral stability analysis and assumptions in Eq.s (6.30) $\sim$ (6.32), numerical simulations are conducted considering the linear second-order actuator model presented in Eq. (6.55). Parameters in the simulations are as follows: α = 0, b = 1, Δt = 0.05, Ω = 0.3. The initial condition of the structure is d_0 = 10mm. In Figure 6.14, "EFC" stands for the results of the EFC method considering the acceleration correction while "A" represents the time history analysis with the actuator model considered instead of the stead state assumptions. One can observe that displacements are unstable when γ_m= 1.05, whilst stable when γ_m = 0.95. This agrees with the analysis in Figure 6.13. Although small differences in different time histories exist, the time histories have the same trend. This indicates that the assumption of the steady state acceleration is reasonable, and the stability analysis is suitable.

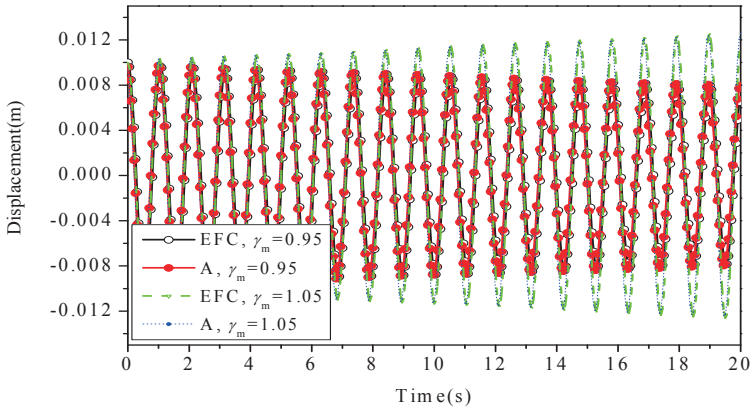

(a) Global view

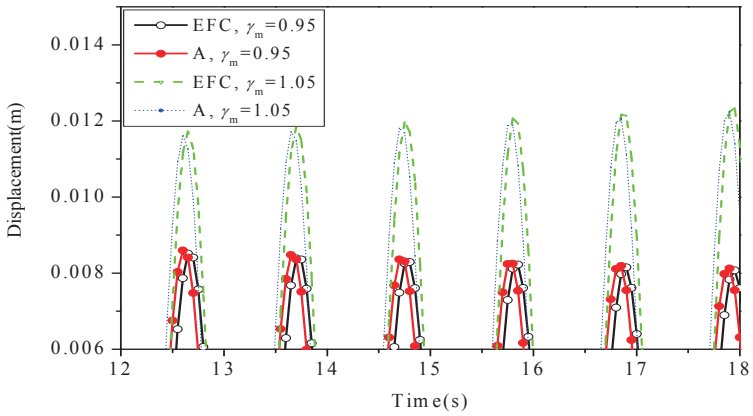

(b) Close-up view

Figure 6.14: Displacement time histories obtained with different methods.

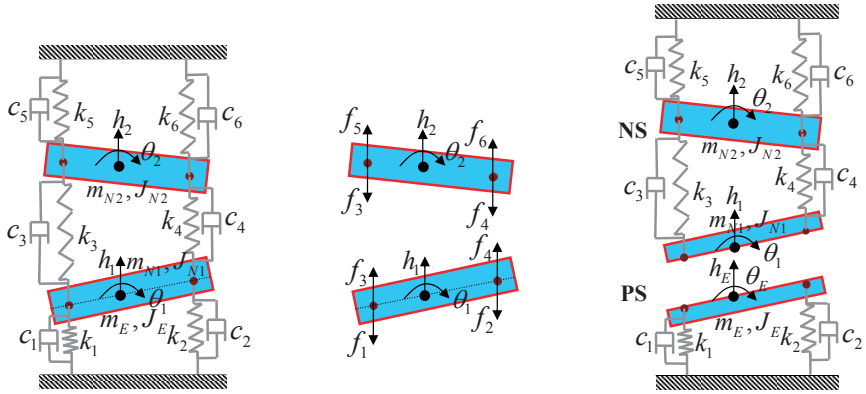

(a) Emulated structure (b) Internal forces (c) Substructure partition

Figure 6.15: Schematic representation of the 4 DOF system.

6.8 Simulations on Multiple DOF system

Simulations are performed to investigate the effectiveness of the acceleration correction for multiple DOF systems. The emulated structure and the partition are presented in Figure 6.15. Evidently, the emulated structure is a 4DOF system, including two translational and two rotational DOF. Meanwhile, the NS contains 4DOF while the PS 2DOF. Thereby, geometric nonlinearity is involved in both substructures.

To begin with, we establish the governing equations of motion of the emulated structure, i.e.,

$$\begin{cases} (m_{N1}+m_E)\ddot{h}_1 + f_1 + f_2 - f_3 - f_4 = F_1 \\ (J_{N1}+J_E)\ddot{\theta}_1 + (f_1 e_1 - f_2 e_2)\cos\theta_1 + (f_4 e_4 - f_3 e_3)\cos\theta_1 = F_{\theta 1} \\ m_{N2}\ddot{h}_2 + f_3 + f_4 - f_5 - f_6 = F_2 \\ J_{N2}\ddot{\theta}_2 + (f_3 e_3 - f_4 e_4 - f_5 e_5 + f_6 e_6)\cos\theta_2 = F_{\theta 2} \end{cases} \tag{6.61}$$

where m and J denote inertia mass and inertia moment, respectively, while $F_\bullet$ ($\bullet$ = 1 or 2) and $F_{\theta\bullet}$ mean external forces in translational and rotational directions; $h_\bullet$ and $\theta_\bullet$ are the primary movement quantities of mass centers, i.e., the translational displacements and rotational angles; $e_\bullet$ indicates the distance from the action point of each spring to the corresponding mass center. Meanwhile, $f_\bullet$ represents internal

forces, for instance,

$$\begin{cases} f_1 = k_1(h_1 + e_1 \sin\theta) + c_1(\dot{h}_1 + e_1\dot{\theta}\cos\theta) \\ f_2 = k_2(h_1 - e_2 \sin\theta) + c_2(\dot{h}_1 - e_2\dot{\theta}\cos\theta) \end{cases} \tag{6.62}$$

Likewise, we can derive the governing equations of motion of the NS, which read

$$\begin{cases} m_{N1}\ddot{h}_1 - f_3 - f_4 + F_c = F_1 \\ J_{N1}\ddot{\theta}_1 + (f_4 e_4 - f_3 e_3)\cos\theta_1 + F_{c\theta} = F_{\theta 1} \\ m_{N2}\ddot{h}_2 + f_3 + f_4 - f_5 - f_6 = F_2 \\ J_{N2}\ddot{\theta}_2 + (f_3 e_3 - f_4 e_4 - f_5 e_5 + f_6 e_6)\cos\theta_2 = F_{\theta 2} \end{cases} \tag{6.63}$$

with the coupling forces at the interface

$$\begin{cases} F_c = m_E\ddot{h}_E + f_1 + f_2 \\ F_{c\theta} = J_E\ddot{\theta}_E + (f_1 e_1 - f_2 e_2)\cos\theta_1 \end{cases} \tag{6.64}$$

In order to replicate the movement of the NS by linear actuators, the translational displacement and rotational angle must be converted into those in actuator coordinates. The following equation can be formulated

$$\begin{cases} d_1 = h_E + e_{1A}\sin\theta_E \\ d_2 = h_E - e_{2A}\sin\theta_E \end{cases} \tag{6.65}$$

where e_{1A} and e_{2A} denote the distances from the action point of each actuator to the mass center When the actual displacements of actuators are measured and the primary movement quantities are required in the NS, the inverse transformation of Eq. (6.65) are needed.

In the implementation of the EFC method with acceleration correction expressed in Eq. (6.58), the initial stiffness of two substructures are required. As a result, they are derived from Eq. (6.62) and other internal force expressions at the equilibrium point

Table 6.1: Main parameters in simulations

Items	Description
$\alpha = 0$	Algorithmic parameter
δt = 1ms Δt = 5ms	Sampling time for control/integration
$F_1 = F_2 = 200sin(2\pi t)$ $F_{\theta 1} = F_{\theta 2} = 400sin(1.5\pi t)$	External forces in N and Nm
$e_1 = e_2 = e_3 = e_4 = e_5 = e_6 = 0.5$m	Eccentricity
$c_1 = c_2 = c_3 = c_4 = c_5 = c_6 = 0$	Damping coefficient
$k_1 = 14800$ $k_2 = 0.8k_1$ $k_3 = k_4 = k_5 = k_6 = 0.6k_1$	Stiffness in N/m
$m_E = 59.25$, $m_{N1} = 2m_E$, $m_{N2} = 3m_E$	Mass in kg
$J_E = 5.3819$, $J_{N1} = 2J_E$, $J_{N2} = 3J_E$	Inertia moment in kgm^2

and expressed as follows

$$\mathbf{K}_{N,ini} = \begin{bmatrix} k_3+k_4 & k_3e_3-k_4e_4 & -k_3-k_4 & -k_3e_3+k_4e_4 \\ k_3e_3-k_4e_4 & k_3e_3^2+k_4e_4^2 & -k_3e_3+k_4e_4 & -k_3e_3^2-k_4e_4^2 \\ -k_3-k_4 & -k_3e_3+k_4e_4 & k_3+k_4+k_5+k_6 & k_3e_3-k_4e_4+k_5e_5-k_6e_6 \\ -k_3e_3+k_4e_4 & -k_3e_3^2-k_4e_4^2 & k_3e_3-k_4e_4+k_5e_5-k_6e_6 & k_3e_3^2+k_4e_4^2+k_5e_5^2+k_6e_6^2 \end{bmatrix}$$

$$\mathbf{K}_{E,ini} = \begin{bmatrix} k_1+k_2 & k_1e_1-k_2e_2 & 0 & 0 \\ k_1e_1-k_2e_2 & k_1e_1^2+k_2e_2^2 & 0 & 0 \\ 0 & 0 & 0 & 0 \\ 0 & 0 & 0 & 0 \end{bmatrix} \tag{6.66}$$

In simulations, we suppose that the actuator is ideal, i.e., $G(s) = 1$, and then velocities and accelerations of the PS are evaluated by difference equations. Parameters applied in simulations are listed in Table 6.1, which cause the translational frequencies 1.6066Hz and 2.3880Hz, and the rotational frequencies 2.7527Hz and 4.1970Hz of the system at the equilibrium state. Two cases of simulations are performed: one with Peek's correction and the other with the proposed acceleration correction. Displacement and angle time histories are presented in Figure 6.16 together with the reference provided by the embedded command ode45 in Matlab for the overall struc-

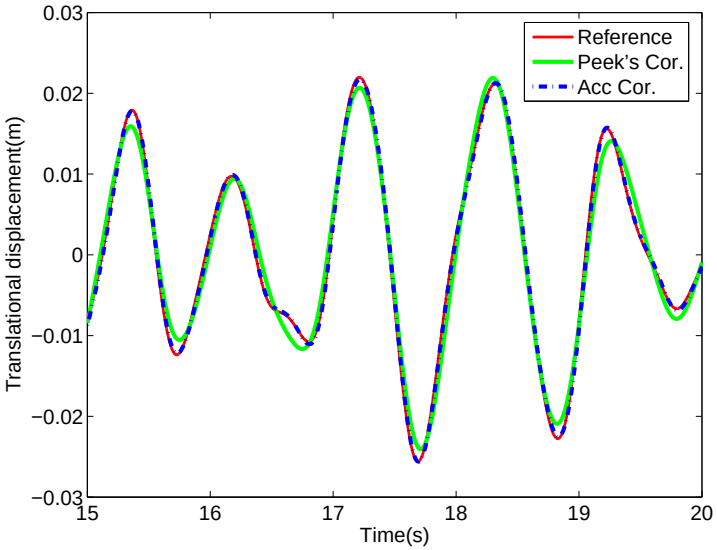

(a) Translational displacement

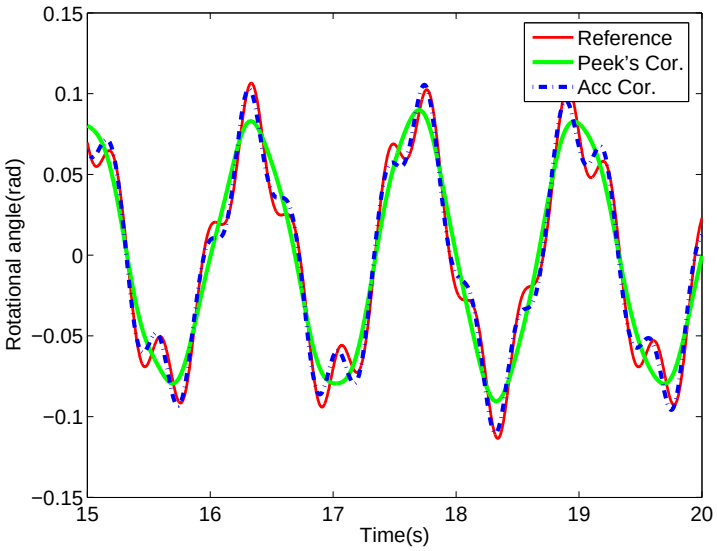

(b) Rotational angle

Figure 6.16: Response time histories of No.1 mass.

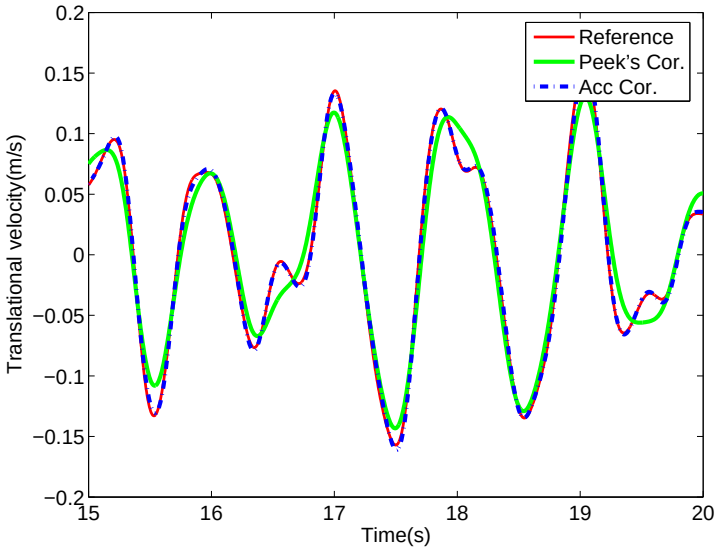

(a) Translational velocity

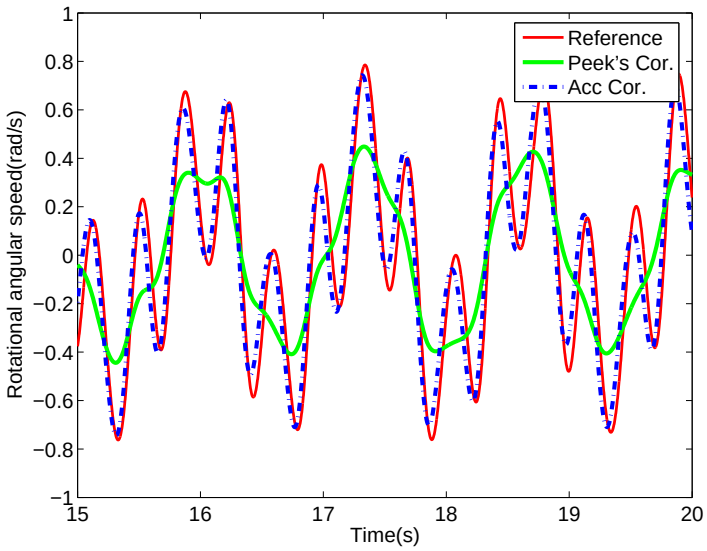

(b) Rotational angular speed

Figure 6.17: Response time histories of No.1 mass.

ture. In addition, corresponding velocity and angular speed time histories are depicted in Figure 6.17. Clearly, these figures show that all responses provided by the proposed acceleration correction are in excellent agreement with the corresponding references. Conversely, considerable discrepancies between those provided by the Peek's correction and the references are observed, especially for the rotational angular speed in Figure 6.17(b). These errors can be attributed to the dissipation, which is resulting from acceleration delay and can damp out low-frequency vibration. In summary, these two figures show the comparative advantages of the proposed correction.

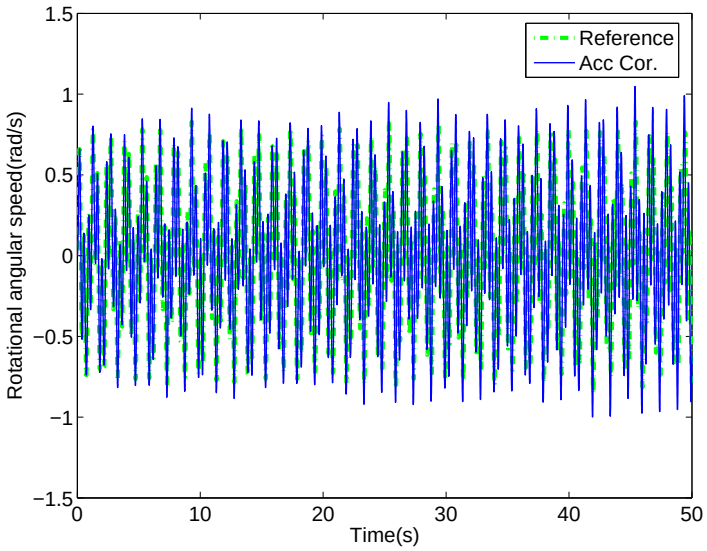

Figure 6.18: Rotational angular speed of No.1 mass with γ_m = 1.05.

In order to verify the influence of the mass ratio γ_m in Eq. (6.60) on the stability, γ_m = 1.05 is chosen rather than γ_m = 0.95 in the previous two figures. Rotational angular speeds presented in Figure 6.18 illustrate the instability, in agreement with stability analysis in Figure 6.12. This implies that insights revealed in the stability analysis can be extended to MDOF systems.

6.9 Conclusions

This chapter discusses the EFC method for RHS on split-mass systems and analyses relevant crucial issues. To begin with, the EFC method was compared with the traditional iteration and advantages of the method were concluded. Then two interpolations for EF commands in RHS with dynamic specimens were employed in simulations and the one based on the constant average acceleration approximation was chosen in the forthcoming sections for its better accuracy. Following that, the stability of the EFC method on a split mass system was analysed and a displacement correction was proposed and examined by numerical simulations. Moreover, a correction for both displacement and acceleration was devised and investigated for RHS as well. Stability analysis showed the improvements of the acceleration correction in the stability limits and algorithmic dissipation, while the numerical simulations confirmed its effectiveness for nonlinear MDOF systems.

CHAPTER 7

AN IMPROVED INTER-FIELD PARALLEL PARTITIONED ALGORITHM BASED ON THE ROSENBROCK METHOD

7.1 Introduction

So far some monolithic integration algorithms (Bursi et al., 2008; Lamarche et al., 2009), which are endowed with favorable numerical properties, such as A-stability and user-defined damping, have been designed and applied in real-time hybrid simulation(RHS). However, these methods may be inefficient for large-scale and complex problems in RHS considering the computation capacity of computers. In addition, different time steps are always required for integration of the NS and control of the PS in RHS. On one hand, commands for the transfer system should be generated in a very fast manner for the purpose of obtaining smoother physical movements. On the other hand, larger time steps are required for the computational portion due to the limited computational capacity. In view of these two requirements, parallel partitioned methods, which can first separate the structure into several coupled subdomains and then independently conduct integrations in each domain with different algorithms and/or different time steps, might be an preferable candidate. The parallelism of parallel partitioned methods makes it possible to conduct RHS of large-scale and complex structures. With this in mind, this chapter focuses on parallel partitioned methods based on the Rosenbrock method and its implementation in RHS.

Various partitioned methods based on acceleration continuity and the Rosenbrock method (Rosenbrock, 1963), including staggered and inter-field parallel methods, are

proposed by Jia (Jia, 2010). Moreover, partitioned methods based on projection to eliminate drift are presented as well. Among them, the inter-field parallel method is regarded promising for structural problems and RHS in terms of the multi-rate properties, parallelism and the second-order accuracy. However, it exhibits some disadvantages which may limit its applications in RHS. First of all, four parallel integration procedures are required in Subdomain A (also referred to as the NS), which implies the inefficient computation. Secondly, the basic parallel method based on the Rosenbrock method, recommended for starting the procedure, increases the difficulty of information exchange and hence, it is complicated to conduct the real-time application. Additionally, displacement drifts sometimes are in the unacceptable range even for common cases.

Here the research aims to simplify the implementation procedure and reduce the drift. In order to achieve this objective, a group of parameters for the LSRT2 are designed firstly and then employed with the inter-field parallel thoughts. Velocity projection based on mass matrices is performed to indirectly reduce the displacement drift. Even though the algorithm exhibits some pros and cons, as expected, a better trade-off is realized and it seems to be improved in terms of actual accuracy and stability.

7.2 The LSRT2 with different stage sizes

The LSRT methods proposed by Bursi et al. (2008) for RHS based on the Rosenbrock method have favourable performance, such as L-stable and suitable for stiff problems, real-time compatible, user-defined dissipation via parameter choices. In fact, the abbreviation LSRT denotes L-Stable Real-Time compatible and originates from the properties. Here we just discuss the case with two stages, namely, the LSRT2. For structural problems in Euler-Lagrange format, i.e.,

$$\dot{\mathbf{y}} = \mathbf{f}(\mathbf{y}, t), \text{ with } \mathbf{y} = \begin{Bmatrix} \mathbf{u} \\ \dot{\mathbf{u}} \end{Bmatrix}, \ \mathbf{f}(\mathbf{y}, t) = \begin{Bmatrix} \dot{\mathbf{u}} \\ \mathbf{r}(\mathbf{u}, \dot{\mathbf{u}}, t) \end{Bmatrix} \tag{7.1}$$

the LSRT2 method reads

$$\mathbf{k}_1 = [\mathbf{I} - \gamma\Delta t\mathbf{J}]^{-1}\,\mathbf{f}\,(\mathbf{y}_i, t_i)\,\Delta t,\ \mathbf{y}_{i+\alpha_{21}} = \mathbf{y}_i + \alpha_{21}\mathbf{k}_1, \tag{7.2}$$

$$\mathbf{k}_2 = [\mathbf{I} - \gamma\Delta t\mathbf{J}]^{-1}\left(\mathbf{f}\left(\mathbf{y}_{i+\alpha_{21}}, t_{i+\alpha_2}\right) + \gamma_{21}\mathbf{J}\mathbf{k}_1\right)\Delta t,\ \mathbf{y}_{i+1} = \mathbf{y}_i + b_1\mathbf{k}_1 + b_2\mathbf{k}_2. \tag{7.3}$$

The conditions of L-stability and second-order accuracy can be expressed as

$$\begin{cases} b_1 = 1 - b_2, \alpha_{21} = \alpha_2, \\ \alpha_2 = \frac{1}{2b_2}, \gamma_{21} = -\frac{\gamma}{b_2}, \gamma = 1 \pm \frac{\sqrt{2}}{2}. \end{cases} \tag{7.4}$$

The recommended parameters for structural problems in (Bursi et al., 2008) are

$$\begin{cases} b_1 = 0, b_2 = 1, \alpha_{21} = \alpha_2 = 0.5, \\ \gamma = 1 \pm \frac{\sqrt{2}}{2}, \gamma_{21} = -\gamma. \end{cases} \tag{7.5}$$

Clearly, this set of parameters meets the conditions in Eq. (7.4) and hence yields L-stable and second-order accurate results. Note that the different value of the parameter γ can result in different dissipation performance. In our case, in order to simplify the integration processes in Subdomain A, we choose

$$\begin{cases} b_1 = -1, b_2 = 2, \alpha_{21} = \alpha_2 = 0.25, \\ \gamma = 1 \pm \frac{\sqrt{2}}{2}, \gamma_{21} = -\frac{\gamma}{2}. \end{cases} \tag{7.6}$$

Similarly to Eq. (7.5), this group of parameters also yields L-stable and second-order accurate results. As shown in Eq. (7.2) and Eq. (7.3), α_2 and α_{21} define the time at which the restoring force is required. Therefore, $\alpha_2 = \alpha_{21} = 0.25$ indicates that the first stage results are at $1/4\Delta t$. These different stage time sizes are schematically shown in Figure 7.1 compared with those of the same time step sizes. In view of the performance, we just analyze the linear case here. Expanding the expression of $\mathbf{y}_{k+1}$ in Eq. (7.3) with Eq. (7.2) and Eq. (7.4) gives

$$\begin{aligned} \mathbf{y}_{i+1} &= \mathbf{y}_i + b_1\mathbf{k}_1 + b_2\,[\mathbf{I} - \gamma\Delta t\mathbf{J}]^{-1}\left(\mathbf{f}\left(\mathbf{y}_{i+\alpha_{21}}, t_{i+\alpha_2}\right) + \gamma_{21}\mathbf{J}\mathbf{k}_1\right)\Delta t \\ &= \mathbf{y}_i + b_1\mathbf{k}_1 + b_2\,[\mathbf{I} - \gamma\Delta t\mathbf{J}]^{-1}\left(\mathbf{J}\mathbf{y}_i + \alpha_{21}\mathbf{J}\mathbf{k}_1 + \gamma_{21}\mathbf{J}\mathbf{k}_1\right)\Delta t \\ &= \mathbf{y}_i + b_1\mathbf{k}_1 + b_2\Delta t\,[\mathbf{I} - \gamma\Delta t\mathbf{J}]^{-1}\,\mathbf{J}\mathbf{y}_i + b_2\,(\alpha_{21} + \gamma_{21})\,\Delta t\,[\mathbf{I} - \gamma\Delta t\mathbf{J}]^{-1}\,\mathbf{J}\mathbf{k}_1 \\ &= \mathbf{y}_i + \mathbf{k}_1 + b_2\,[\mathbf{I} - \gamma\Delta t\mathbf{J}]^{-1}\,\mathbf{J}\mathbf{k}_1\left(\frac{1}{2b_2} - \frac{\gamma}{b_2}\right)\Delta t \\ &= \mathbf{y}_i + \mathbf{k}_1 + [\mathbf{I} - \gamma\Delta t\mathbf{J}]^{-1}\,\mathbf{J}\mathbf{k}_1\left(\frac{1}{2} - \gamma\right)\Delta t \end{aligned} \tag{7.7}$$

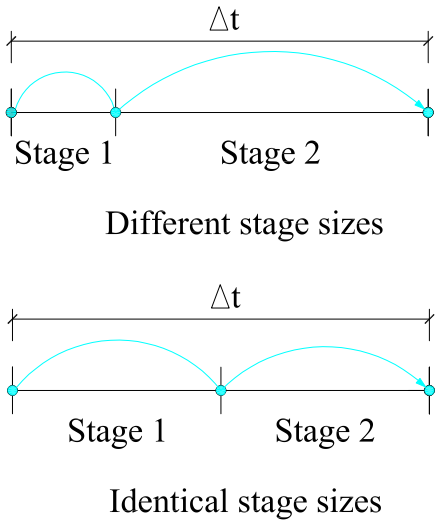

Figure 7.1: Schematic representation of the LSRT2 algorithm with different parameters.

Therefore, the responses are just relevant to the parameter γ instead of α_2 and α_{21} if the parameters satisfy the conditions of L-stability and second-order accuracy. This means that the performance of the LSRT2 does not change for solving linear problems between two sets of parameters.

7.3 Drift-off effects and velocity projection

Drift-off effects are a common phenomenon for solving constrained dynamic problems, i.e. differential algebraic equations (DAE). Continuous problems are constrained on displacement, velocity and acceleration levels while discretized models just meet some constraint to reduce the *Index* of the problem, for example acceleration constraint in the underlying case. Therefore errors exist between the unconstrained corresponding movement quantities. Moreover, these errors linearly or quadratically accumulate during the analysis and hence errors are introduced to movement quan-

tities, which is referred to as DRIFT. In order to reduce the drift and stabilize the numerical results, since the first stabilization method proposed by Burgermeister et al. (2006), numerous methods have been developed and available nowadays (Bauchau and L., 2008). Among others, the projection method based on minimization problems (Orden and Aguilera, 2011; Burgermeister et al., 2006) is popular and can be embedded into any integrators for DAEs. Furthermore, researchers illustrated that velocity projection is more efficient for stabilizing numerical integration than displacement projection. Orden and Aguilera (2011) proved that velocity projection performed with the mass matrix introduces non-negative dissipation to the system. As demonstrated later on, the displacement drift is effectively reduced to an acceptable level in some cases by this velocity projection and energy dissipation is also observed.

When employing velocity projection with the mass matrix, the following problem is solved

$$\min_{\dot{\mathbf{u}} \in R^l} \left\| \dot{\mathbf{u}} - \tilde{\dot{\mathbf{u}}} \right\|_{\mathrm{M}} \text{ with } \mathbf{G}\dot{\mathbf{u}} = \mathbf{0}. \tag{7.8}$$

where $\dot{\mathbf{u}}$ and $\tilde{\dot{\mathbf{u}}}$ denote velocity vectors after and before the projection, respectively. $\mathbf{M}$ indicates the positive definite mass matrix and the M-norm is defined as

$$\left\| \dot{\mathbf{u}} - \tilde{\dot{\mathbf{u}}} \right\|_{\mathrm{M}} = \frac{1}{2} \left(\dot{\mathbf{u}} - \tilde{\dot{\mathbf{u}}} \right)^T \mathbf{M} \left(\dot{\mathbf{u}} - \tilde{\dot{\mathbf{u}}} \right). \tag{7.9}$$

Additionally, $\mathbf{G}\dot{\mathbf{u}} = \mathbf{0}$ describes the velocity constraint, which is the first-order derivative of the displacement constraint. Therefore the velocity projection implies that the stabilized velocity is the point on the velocity constraint surface which is the closest point to the integrated results. With regard to the solution of the minimization problem, though several methods can be conducted, we exploit the Lagrange multiplier method. Coupling the target function and the constraint function with the Lagrange parameters and then performing derivatives with respect to the unknowns yield the necessary conditions, i.e.

$$\begin{cases} \mathbf{M}(\dot{\mathbf{u}} - \tilde{\dot{\mathbf{u}}}) + \mathbf{G}^T \mu = \mathbf{0} \\ \qquad \mathbf{G}\dot{\mathbf{u}} = \mathbf{0}. \end{cases} \tag{7.10}$$

This is a system of linear equations with respect to projected velocity and Lagrange multiplier and can be exactly solved without any iteration, i.e.

$$\dot{\mathbf{u}} = \mathbf{P}(\tilde{\dot{\mathbf{u}}}) \tag{7.11}$$

where **P** is a linear operator.

7.4 The inter-field parallel (PLSRT2) method based on the LSRT2 method

In order to solve the DAE arising from the partitioned governing equations in RHS, an inter-field parallel methods based on acceleration constraint with different time steps in different subdomains were proposed by Jia (Jia, 2010; Jia et al., 2011). Along the line of Jia, a system, separated into S non-overlapping subdomains, together with acceleration continuity at the interface, can be expressed as

$$\begin{cases} \begin{bmatrix} \mathbf{I} & \mathbf{0} \\ \mathbf{0} & \mathbf{M}^i \end{bmatrix} \begin{Bmatrix} \dot{\mathbf{u}}^i \\ \ddot{\mathbf{u}}^i \end{Bmatrix} = \begin{Bmatrix} \dot{\mathbf{u}}^i \\ \mathbf{f}\left(\mathbf{u}^i, \dot{\mathbf{u}}^i, t\right) \end{Bmatrix} + \begin{bmatrix} \mathbf{0} \\ (\mathbf{G}^i)^T \end{bmatrix} \Lambda \\ \sum_{i=1}^{S} \left[\mathbf{0}, \mathbf{G}^i\right] \begin{Bmatrix} \dot{\mathbf{u}}^i \\ \ddot{\mathbf{u}}^i \end{Bmatrix} = \mathbf{0} \end{cases} \quad i = 1, ..., S. \tag{7.12}$$

where $\mathbf{M}^i$ denotes the mass matrix of the i^{th} subdomains; $\mathbf{G}^i$ represents the constraint matrix which expresses the linear relationship at the interface. In fact, this is an Index One system, which is defined as the minimum number of differentiations needed to transform a system of DAE into a system of ODE. With the notation $\mathbf{y} = \left\{\mathbf{u}^T \quad \dot{\mathbf{u}}^T\right\}^T$, one obtains

$$\begin{cases} \mathbf{A}^i \dot{\mathbf{y}}^i = \mathbf{F}^i\left(\mathbf{y}^i, t\right) + (\mathbf{C}^i)^T \mathbf{\Lambda} \\ \sum_{i=1}^{S} \mathbf{C}^i \dot{\mathbf{y}}^i = \mathbf{0} \end{cases} \tag{7.13}$$

For ease of notation, both matrices $\mathbf{A}^i$ and $\mathbf{C}^i$ refer to the i-th subdomain. Substituting Eq. (7.13)(a) into Eq. (7.13)(b) to eliminate the acceleration yields the expression of the Lagrange multiplier

$$\mathbf{\Lambda} = -\mathbf{H}^{-1} \sum_{i=1}^{S} \mathbf{C}^i (\mathbf{A}^i)^{-1} \mathbf{F}^i\left(\mathbf{y}^i, t\right) \tag{7.14}$$

$$\mathbf{H} = \sum_{i=1}^{S} \mathbf{C}^i (\mathbf{A}^i)^{-1} (\mathbf{C}^i)^T \tag{7.15}$$

Clearly, the Lagrange multiplier is explicitly expressed by the state vectors and no nonlinear equation needs to be solved. In detail, the Lagrange multiplier can be exactly evaluated using the given state vectors provided by the integrator, e.g. the LSRT2. This is the reason why the acceleration constraint is exploited here. Subsequently, Eq. (7.13) can be re-cast as

$$\dot{\mathbf{y}} = \mathbf{A}^{-1}\mathbf{F}(\mathbf{y}, t) - \mathbf{A}^{-1}\mathbf{C}^T \left[\mathbf{C}\mathbf{A}^{-1}\mathbf{C}^T\right]^{-1} \mathbf{C}\mathbf{A}^{-1}\mathbf{F}(\mathbf{y}, t) \tag{7.16}$$

where

$$\begin{aligned} &\mathbf{y} = \left\{(\mathbf{y}^1)^T \quad ... \quad (\mathbf{y}^S)^T\right\}^T, \quad \mathbf{A} = \text{Blockdiagonal}[\mathbf{A}^1 \quad ... \quad \mathbf{A}^S] \\ &\mathbf{F}(\mathbf{y}, t) = \left\{\left[\mathbf{F}^1\left(\mathbf{y}^1, t\right)\right]^T \quad ... \quad \left[\mathbf{F}^S\left(\mathbf{y}^S, t\right)\right]^T\right\}^T, \ \mathbf{C} = [\mathbf{C}^1 \quad ... \quad \mathbf{C}^S] \end{aligned} \tag{7.17}$$

This is the ODE arising from the DAE. The Jacobian matrix of the ODE is given by

$$\mathbf{J} = \left(\mathbf{A}^{-1} - \mathbf{Q}\right) \frac{\partial \mathbf{F}(\mathbf{y}, t)}{\partial \mathbf{y}} \tag{7.18}$$

with $\mathbf{Q} = \mathbf{A}^{-1}\mathbf{C}^T \left[\mathbf{C}\mathbf{A}^{-1}\mathbf{C}^T\right]^{-1} \mathbf{C}$. Actually, this matrix is not diagonal. In partitioned methods, we prefer less information exchange to reduce the communication burdens and hence we neglect the upper-right and down-left blocks even loosing the coupling, leading to the Jacobian matrices

$$\mathbf{J}^A = \left(\left(\mathbf{A}^A\right)^{-1} - \mathbf{Q}^A\right) \frac{\partial \mathbf{F}^A\left(\mathbf{y}^A, t\right)}{\partial \mathbf{y}^A} \tag{7.19}$$

$$\mathbf{J}^B = \left(\left(\mathbf{A}^B\right)^{-1} - \mathbf{Q}^B\right) \frac{\partial \mathbf{F}^B\left(\mathbf{y}^B, t\right)}{\partial \mathbf{y}^B} \tag{7.20}$$

It is interesting to mention that the Jacobian matrices used in (Jia, 2010) are

$$\mathbf{J}^A = \left(\mathbf{A}^A\right)^{-1} \frac{\partial \mathbf{F}^A\left(\mathbf{y}^A, t\right)}{\partial \mathbf{y}^A} \tag{7.21}$$

$$\mathbf{J}^B = \left(\mathbf{A}^B\right)^{-1} \frac{\partial \mathbf{F}^B\left(\mathbf{y}^B, t\right)}{\partial \mathbf{y}^B} \tag{7.22}$$

which imply that the Lagrange multipliers are regarded as external forces rather than functions with respect to the state vectors. More accurate simulation results are expected when Eq. (7.19) and Eq. (7.20) are utilized because they are closer to the

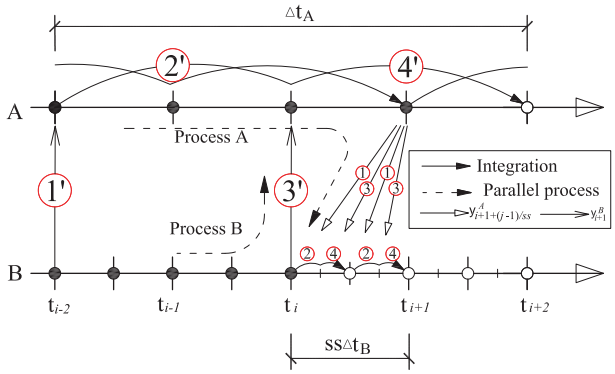

Figure 7.2: The inter-field parallel integration method based on the LSRT2 (PLSRT2).

actual ones expressed in Eq. (7.18). This is validated via simulations and accuracy analysis in the following parts.

The schematic representation of the algorithm developed in the inter-field parallel framework based on the LSRT2 for solving the problem expressed in Eq. (7.13), is depicted in Figure 7.2, in which Subdomain A is integrated with a course time step $\Delta t_A = 4\Delta t$ and Subdomain B with a fine time step $\Delta t_B = \Delta t/ss$. Additionally, the time scale is numbered every Δt which, called the equivalent time step, is defined as the time in which two stages of the LSRT2 have to be finished.

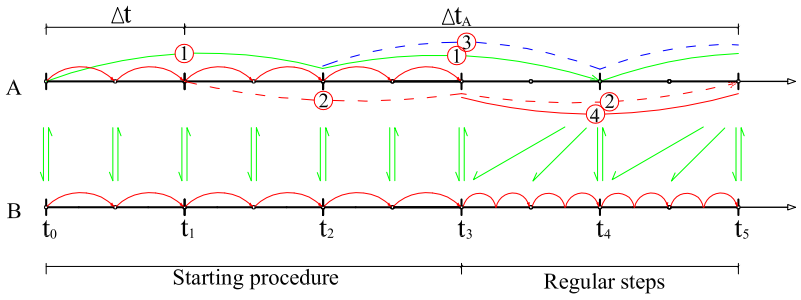

Figure 7.3: The first five steps of the PLSRT2 method.

The PLSRT2 is not a method which can self-start and the parallel method based on the LSRT2 without subcycling is recommended to start the method due to the similarity of two methods and its second-order accuracy. Figure 7.3 depicts the first five steps of the PLSRT2 including the starting procedure. It is evident that in Subdomain A four independent integration processes starting at different times with time step $4\Delta t$

are required. This results in the burden to complete two stages in the time interval Δt for real-time applications. Therefore, the integration is not very efficient and a higher requirement to the computation capacity are imposed for a real-time application. Another problem shown in Figure is relevant to the several different utilized time steps. As a consequence, at least three routines have to be designed and information exchange among them is complicated. The third shortcoming, probably of greater importance, is the drift-off effect of displacement responses that is discussed in the forthcoming sections. This displacement drift may render to reduce the time step or to re-design the partitioning scheme. In fact, both them might be determined by available experimental facilities and actual problems. From the view of this disadvantages, applications of the method may be limited.

7.5 The improved inter-field parallel (IPLSRT2) method based on the LSRT2 method

For the purposes of improving the computational efficiency and reducing drift in displacement responses, a new integration procedure is developed herein, as shown in Figure 7.4.

Taking the advancement in Subdomain A from time t_{i+2} to t_{i+4} and simutanously in Subdomain B from time t_i to t_{i+2} for example, the solution procedure in Subdomain A of this method reads,

(1) Evaluate internal forces $\mathbf{F}_i^A\left(\mathbf{y}_i^A\right)$ and $\mathbf{F}_i^B\left(\mathbf{y}_i^B\right)$ and compute the Lagrange multiplier by

$$\mathbf{\Lambda}_i = -\mathbf{H}^{-1}\left[\mathbf{C}^A(\mathbf{A}^A)^{-1}\mathbf{F}_i^A + \mathbf{C}^B(\mathbf{A}^B)^{-1}\mathbf{F}_i^B\right]. \tag{7.23}$$

(2) Compute $\mathbf{k}_1^A$ and $\mathbf{y}_{i+1}^{A,h}$ and evaluate the intermediate step solutions,

$$\mathbf{k}_1^A = \left[\mathbf{I} - 4\gamma\Delta t\mathbf{J}^A\right]^{-1}(\mathbf{A}^A)^{-1}\left[\mathbf{F}_i^A + (C^A)^{-1}\mathbf{\Lambda}_i\right]4\Delta t, \tag{7.24}$$

$$\mathbf{y}_{i+1}^{A,h} = \mathbf{y}_i^A + \frac{1}{4}\mathbf{k}_1^A. \tag{7.25}$$

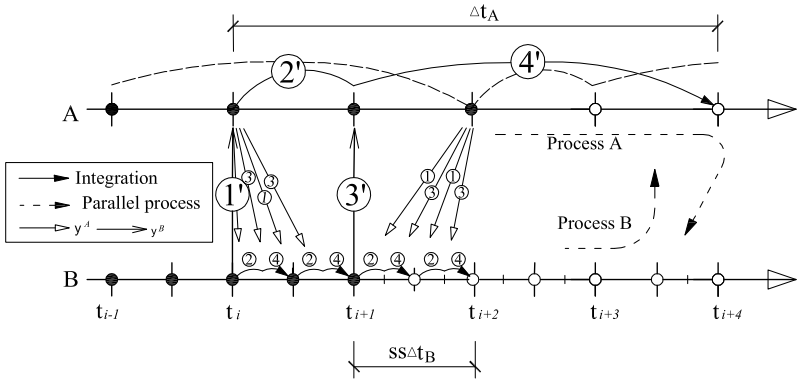

Figure 7.4: The inter-field parallel integration method based on the LSRT2 with different stage sizes.

(3) When the state of Subdomain B is available at t_{i+1} (after the velocity projection), evaluate internal forces $\mathbf{F}_{i+1}^{A,h}\left(\mathbf{y}_{i+1}^{A,h}\right)$ and $\mathbf{F}_{i+1}^{B}\left(\mathbf{y}_{i+1}^{B}\right)$ and compute the Lagrange multiplier

$$\mathbf{\Lambda}_{i+1} = -\mathbf{H}^{-1}\left[\mathbf{C}^{A}(\mathbf{A}^{A})^{-1}\mathbf{F}_{i+1}^{A,h} + \mathbf{C}^{B}(\mathbf{A}^{B})^{-1}\mathbf{F}_{i+1}^{B}\right]. \tag{7.26}$$

(4)Compute $\mathbf{k}_2^A$ and advance the solution to $\mathbf{y}_{i+4}^A$ in Subdomains A,

$$\mathbf{k}_2^A = \left[\mathbf{I} - \gamma\Delta t\mathbf{J}^A\right]^{-1}(\mathbf{A}^i)^{-1}\left[\mathbf{F}_{i+1}^{A,h} + (C^A)^{-1}\mathbf{\Lambda}_{i+1} - \gamma\mathbf{J}^A\mathbf{k}_1^A\right]4\Delta t, \tag{7.27}$$

$$\mathbf{y}_{i+4}^A = \mathbf{y}_i^A - \mathbf{k}_1^A + 2\mathbf{k}_2^A. \tag{7.28}$$

Simultaneously, computations in Subdomain B are performed as follows:

(1) Interpolate the responses of Subdomain A between t_i to t_{i+2} with

$$\mathbf{y}_{i+\frac{j}{2ss}}^A = \mathbf{y}_i^A + \frac{j}{4ss}\left(\mathbf{y}_{i+2}^A - \mathbf{y}_i^A\right), \quad (j = 0, ..., 4ss-1). \tag{7.29}$$

(2) Set j=0;

(3) Evaluate the internal forces $\mathbf{F}_{i+\frac{j}{2ss}}^A\left(\mathbf{y}_{i+\frac{j}{2ss}}^A\right)$ and $\mathbf{F}_{i+\frac{j}{2ss}}^B\left(\mathbf{y}_{i+\frac{j}{2ss}}^B\right)$and calculate the Lagrange multiplier,

$$\mathbf{\Lambda}_{i+\frac{j}{2ss}} = -\mathbf{H}^{-1}\left[\mathbf{C}^{A}(\mathbf{A}^{A})^{-1}\mathbf{F}_{i+\frac{j}{2ss}}^{A} + \mathbf{C}^{B}(\mathbf{A}^{B})^{-1}\mathbf{F}_{i+\frac{j}{2ss}}^{B}\right]. \tag{7.30}$$

(4) Compute $\mathbf{k}_1^B$ and evaluate the intermediate step solutions $\mathbf{y}_{i+\frac{j}{2ss}}^{B,h}$,

$$\mathbf{k}_1^B = \left[\mathbf{I} - \gamma\frac{\Delta t}{ss}\mathbf{J}^B\right]^{-1}(\mathbf{A}^B)^{-1}\left[\mathbf{F}_{i+\frac{j}{2ss}}^B + (C^B)^{-1}\mathbf{\Lambda}_{i+\frac{j}{2ss}}\right]\frac{\Delta t}{ss}, \tag{7.31}$$

$$\mathbf{y}^B_{i+\frac{j+1}{2ss}} = \mathbf{y}^B_{i+\frac{j}{2ss}} + \frac{1}{2}\mathbf{k}^B_1. \tag{7.32}$$

(5) Evaluate the internal forces $\mathbf{F}^A_{i+\frac{j+1}{2ss}}\left(\mathbf{y}^A_{i+\frac{j+1}{2ss}}\right)$ and $\mathbf{F}^{B,h}_{i+\frac{j+1}{2ss}}\left(\mathbf{y}^{B,h}_{i+\frac{j+1}{2ss}}\right)$ and calculate the Lagrange multiplier,

$$\mathbf{\Lambda}_{i+\frac{j+1}{2ss}} = -\mathbf{H}^{-1}\left[\mathbf{C}^A(\mathbf{A}^A)^{-1}\mathbf{F}^A_{i+\frac{j+1}{2ss}} + \mathbf{C}^B(\mathbf{A}^B)^{-1}\mathbf{F}^{B,h}_{i+\frac{j+1}{2ss}}\right]. \tag{7.33}$$

(6) Compute $\mathbf{k}^B_2$ and advance the solution to $\mathbf{y}^{B,h}_{i+\frac{j+2}{2ss}}$ at time $\left(t_i + \Delta t/ss\right)$ in Subdomains B,

$$\mathbf{k}^B_2 = \left[\mathbf{I} - \gamma\frac{\Delta t}{ss}\mathbf{J}^B\right]^{-1}(\mathbf{A}^B)^{-1}\left[\mathbf{F}^{B,h}_{i+\frac{j+1}{2ss}} + (C^A)^{-1}\mathbf{\Lambda}_{i+\frac{j+1}{2ss}} - \gamma\mathbf{J}^A\mathbf{k}^B_1\right]\frac{\Delta t}{ss}, \tag{7.34}$$

$$\mathbf{y}^{B,h}_{i+\frac{j+2}{2ss}} = \mathbf{y}^B_i + \mathbf{k}^B_2. \tag{7.35}$$

(7) Set $j = j + 1$ and go back to (3) and repeat this procedure to reach t_{i+1};

(8) Perform velocity projection as follows

$$\begin{bmatrix} \dot{\mathbf{u}}^A_{i+1} \\ \dot{\mathbf{u}}^B_{i+1} \end{bmatrix} = \mathbf{P}\left(\begin{bmatrix} \dot{\mathbf{u}}^A_{i+1} \\ \dot{\mathbf{u}}^B_{i+1} \end{bmatrix}\right). \tag{7.36}$$

(9) Set $j = j + 1$ and go back to (3) and repeat this procedure for Subdomain B in order to advance to t_{i+2}.

Hence, the solutions are advanced by $2\Delta t$ in both subdomains. Replacing i with $i + 2$ and repeating this procedure yield solutions of two domains in expected time ranges. As can be seen, in order to reduce displacement drifts, the velocity projection is conducted every Δt. In addition, interpolation is required to obtain results at odd steps in Subdomain A for conducting projection.

As shown in the procedure, the responses of Subdomain A at t_i and t_{i+2} should be known before performing this procedure and therefore this method can not self-start. Here the CR method Chen et al. (2009) based on the entire structure is suggested starting the proposed method, since it provides explicit displacement and velocity responses like the LSRT2 and is second-order accurate. The CR method with the time step $2\Delta t$ is expressed as

$$\begin{aligned} \mathbf{u}_2 &= \mathbf{u}_0 + 2\Delta t \times \dot{\mathbf{u}}_0 + \alpha_1\Delta t^2 \times \dot{\mathbf{u}}_0 \\ \dot{\mathbf{u}}_2 &= \dot{\mathbf{u}}_0 + \alpha_2\Delta t \times \ddot{\mathbf{u}}_0 \end{aligned} \tag{7.37}$$

where

$$\alpha_1 = \alpha_2 = 4[4\mathbf{M} + 2\Delta t\mathbf{C}_0 + \Delta t^2\mathbf{K}_0]^{-1}\mathbf{M} \tag{7.38}$$

in which $\mathbf{C}_0$ and $\mathbf{K}_0$ denote the damping ratio matrix and stiffness matrix of the whole structure.

7.6 Zero-stability analysis

As displayed in the following sections, this method is only conditionally stable to solve constrained dynamic problems, similarly to the PLSRT2. Therefore examination of zero stability is necessary to ensure the method stable when the time step is vanishing to zero. Zero stability, the stability when the time step tends to zero, is one necessary condition of convergence for any integrators. As an L-stable algorithm, zero stability of the LSRT2 can be immediately proved since $\mathbf{k}_1$ and $\mathbf{k}_2$ approach zero and consequently the responses are exactly the same as the initial conditions when the time step tends to zero, i.e.

$$\mathbf{y}_{i+1} = \mathbf{y}_i = \mathbf{y}_0 \qquad \Delta t \to 0 \tag{7.39}$$

In view of the zero stability of partitioned algorithms, Kubler and Achiehlen (2004) concluded that it just depends on the coupling of the algorithms if the integration approaches adopted in each domain are zero stable. Nonetheless, the algorithm treated herein is complicated due to the two-stage property of the integrations and the subcycling strategy and hence, we conduct the zero stability analysis step by step.

To begin with, the CR method, applied for starting the procedure, results in the time-invariant state vector because of its zero stability, it is to say,

$$\mathbf{y}_2^A = \mathbf{y}_0 \tag{7.40}$$

Therefore, interpolating the state vector of Subdomain A gives the identical results. On the other hand, the LSRT2 on Subdomain B leads to the same results in the forthcoming two steps as the initial condition of Subdomain B when the time step

approaches zero. The following projection operation at time t_1 also gives the same results provided that initial conditions of two subdomains are compatible at the interface. The same case happens to Subdomain A, as well, in that the LSRT2 is conducted there. The projection at t_2, as expected, leads to the same state vector. The analysis shows that the state of the system is the same after the starting and one loop evaluation. Repeat this analysis and we can draw the conclusion: the partitioned method is zero stable if the initial conditions of two subdomains are compatible. This analysis not only shows the zero stability of the partitioned method but also attaches significance to the initial condition for the algorithms convergence. Moreover, this analysis implies that all partitioned algorithms based on the LSRT2 may be zero stable, in that the time step Δt in the expressions of $\mathbf{k}_1$ and $\mathbf{k}_2$ isolates integration processes in two subdomains.

7.7 Stability and accuracy analysis on a split mass system

In order to investigate numerical performance of the proposed algorithm, stability analysis and accuracy analysis are carried out in this section. The underlying emulated structure is a linear Single-DOF system, and then separated into two subdomains, denoted by Subdomain A and B as described above. This system, as shown in previous chapters and re-depicted in Figure 7.5 for convenience, was widely exploited to examine performance of partitioned algorithms, among others, see Pegon (Pegon and Magonette, 2002). In order to concentrate on the stability of the method, we neglect external forces and damping forces in the system and therefore, the structural characteristics are defined by $m = m_A + m_B = 1$ and $k_A + k_B = 1$. Broadly speaking, another two conditions of mass and stiffness ratios are required to determine the separate subdomains. For brevity, the frequency ratio of two subdomains is defined, which can be expressed by means of

$$b_0 = \frac{\omega_B}{\omega_A} = \frac{m_A}{m_B} = \frac{k_B}{k_A}. \tag{7.41}$$

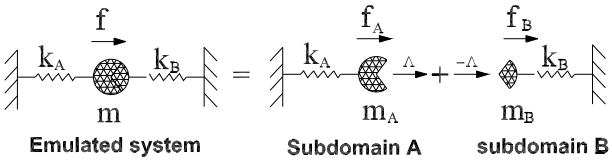

Figure 7.5: A split mass system.

7.7.1 Stability analysis on the split mass system

Spectral stability analysis are performed by examining eigenvalues of the amplification matrix **R** of the algorithm, which is indicated in the recursive formula, namely,

$$\mathbf{X}_{i+1} = \mathbf{R}\mathbf{X}_i + \mathbf{L}\mathbf{F} \tag{7.42}$$

where **X** is the sate containing all quantities required to advance the algorithm step by step. Once the amplification matrix is established, the spectral radius resulting from eigenvalues determines the stability.

With regard to the developed method, the necessary state of two subdomains is

$$\mathbf{X}_i = \left[\left(\mathbf{y}_i^A\right)^T \quad \left(\mathbf{y}_i^B\right)^T \quad \left(\mathbf{y}_{i+2}^B\right)^T \right]^T. \tag{7.43}$$

Clearly, with $\mathbf{X}_i$ as the initial condition, one can advance the analysis by following the solution procedure in Section 7.5 and finally obtain the new state $\mathbf{X}_{i+1}$. To reduce the computational burdens, it is suggested that the vector

$$\mathbf{X}_i^l = \left[0_{1\times(l-1)} \quad 1 \quad 0_{1\times(6-l)} \right]^T \quad l \in \left[1 \quad 6 \right] \tag{7.44}$$

be practically used as the initial condition to obtain the l-th row of the amplification matrix and then the amplification matrix is assembled.

To begin with, we consider the influence of the substep number *ss* in Subdomain B. The exact Jacobian matrix is not available in tests considering the nonlinearity and other uncertainties of the specimen. Therefore, multirate or subcycling may be desired. Global and close-up views of the eigenvalues with respect to Ω defined as $\Omega = \omega \Delta t_A$ are plotted in Figure 7.6. Clearly, they are very similar in shape and the stability limits vary a bit according to *ss*. This results are similar to that obtained by Jia (Jia, 2010). Due to the similarity of the eigenvalues for different *ss*, we just analyze the case with $ss = 2$ in the following analysis.

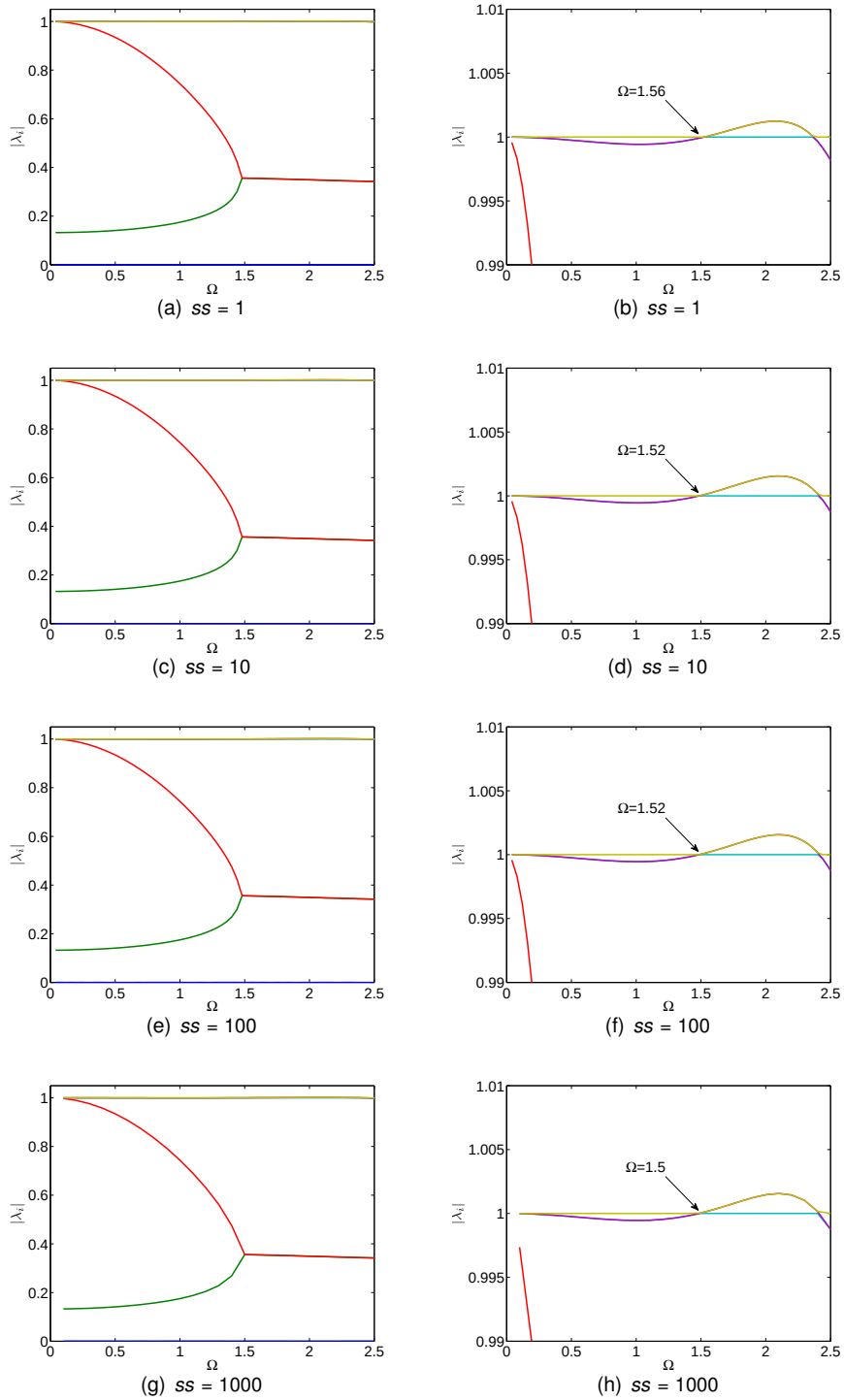

Figure 7.6: Spectral stability analysis with $\gamma = 1 - \sqrt{2}/2$ for both subdomains and: (a) and (b) *ss* = 1; (c) and (d) *ss* = 10; (e) and (f) *ss* = 100; (g) and (h) *ss* = 1000.

The influence of the Jacobian modification and velocity projection on the stability of the underlying method is analysed in Figure 7.7 when b_0 = 0.1 and b_0 = 2, respectively. We can observer that when b_0 = 0.1, the Jacobian modification reduces the stability limit while the velocity projection can stabilize the method. When b_0 = 2, the Jacobian modification exhibits less influence on the stability limit while the velocity projection greatly increase the stability limit. As mentioned in Section 7.3, the velocity projection introduce somewhat dissipation to the method and hence the fact it stabilizes the method is expected. Taking into account the stability and accuracy, we conduct both them.

The stability analysis results with different b_0 are illustrated in Figure 7.8. When b_0 increases from 0.1 to 2.0, the stability range declines from $\Omega < 1.52$ to $\Omega < 0.68$. From Eq. (7.41) we can see that the frequency of Subdomain B goes up with the increase in b_0 and therefore it is concluded that the algorithm exhibits a bit difficulty to be stable for a relative stiff Subdomain B. This analysis shows a different property of partitioned methods from the monolithic ones, that the numerical performance of partitioned schemes are dependent on the test problems. In fact, this can be attributed to the complexity of the partitioned method, which resulting in that it is impossible to select some parameters not directly related to the test problems as independent variables of the amplification matrix eigenvalues. Nonetheless, for the monolithic method it is not complicated.

In the analysis above, for simplicity, the same value γ for both subdomains are performed: $\gamma_A = \gamma_B = 1 - \sqrt{2}/2$. Herein we introduce more algorithmic damping by conducting $\gamma_A = \gamma_B = 1 + \sqrt{2}/2$. From Figure 7.9, broadly speaking, the stability limits decrease with increasing the frequency ratio and an exception occurs when b_0 = 0.5. Compared with analysis above, the dissipation introduced by the algorithm parameters enlarges the stability range.

Before we move on to the next section, let's just make a brief summary on the stability analysis. First of all, the algorithm is often conditionally stable, and the stability limits are dependent on the structural parameter and the algorithm parameters. Secondly, the algorithm dissipation, as expected, can enlarge the stability range. Therefore, for practical applications, all these factors may be considered to obtain stable results.

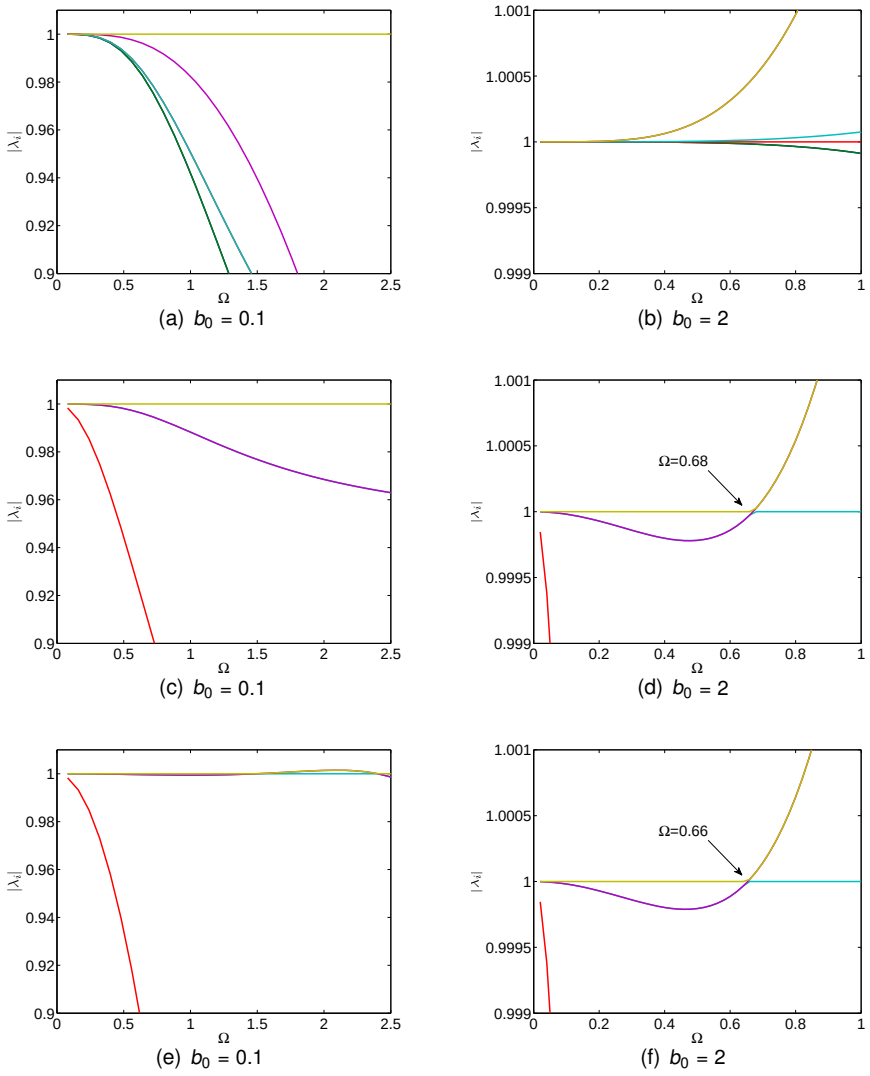

Figure 7.7: Influence of the Jacobian modification and velocity projection on stability: (a),(b) without the modification and velocity projection; (c) and (d) with velocity projection;(e) and (f) with modification and the velocity projection.

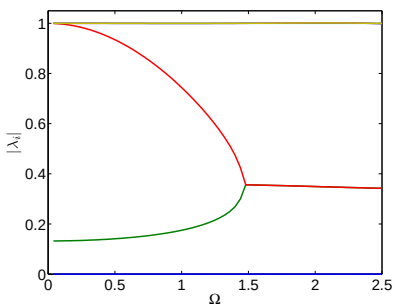

(a) Global view with $b_0 = 0.1$

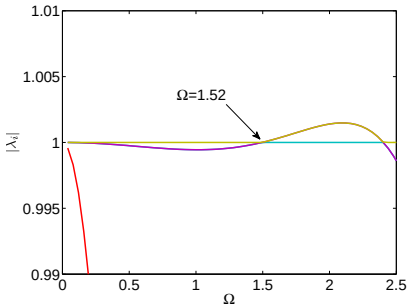

(b) Close-up view with $b_0 = 0.1$

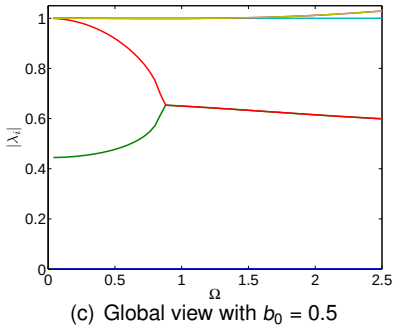

(c) Global view with $b_0 = 0.5$

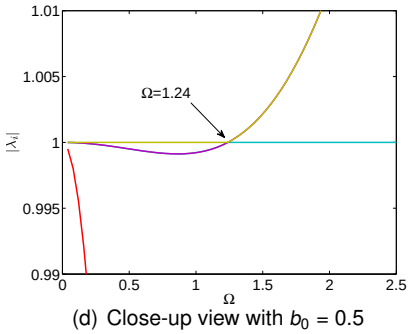

(d) Close-up view with $b_0 = 0.5$

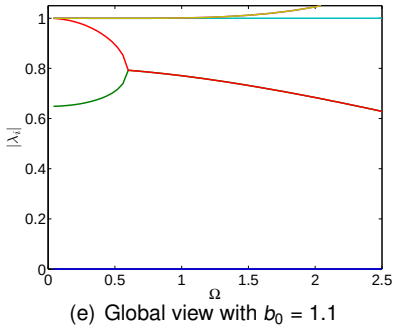

(e) Global view with $b_0 = 1.1$

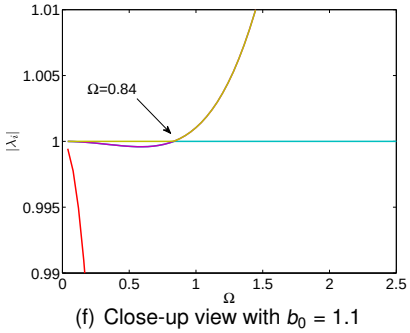

(f) Close-up view with $b_0 = 1.1$

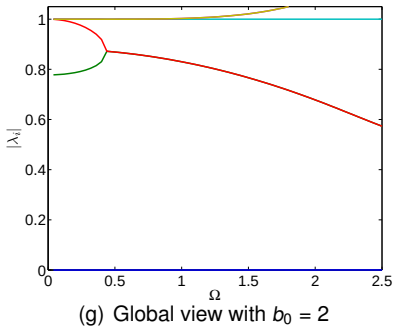

(g) Global view with $b_0 = 2$

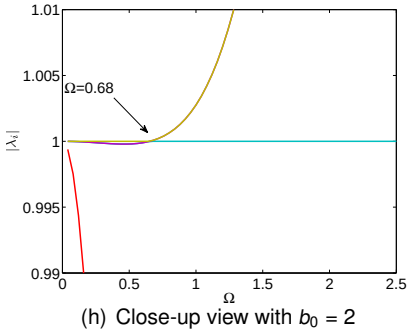

(h) Close-up view with $b_0 = 2$

Figure 7.8: Spectral stability analysis with $\gamma = 1 - \sqrt{2}/2$ for both subdomains, *ss* = 2.

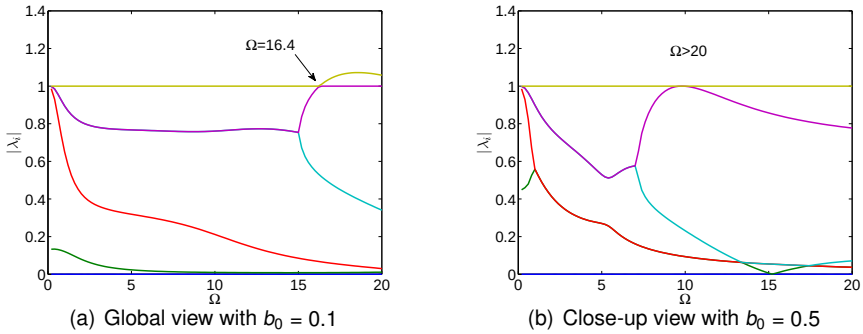

(a) Global view with $b_0 = 0.1$ (b) Close-up view with $b_0 = 0.5$

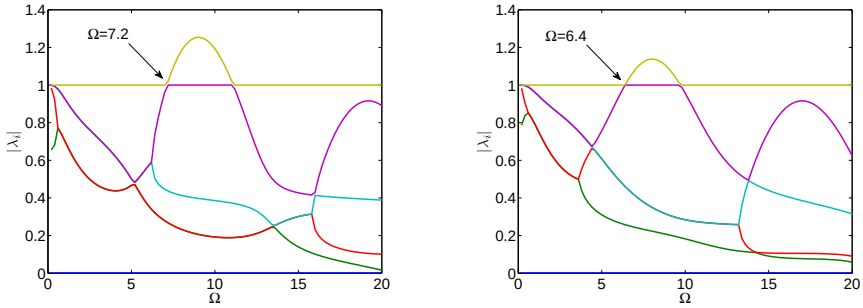

(c) Global view with $b_0 = 1.1$ (d) Close-up view with $b_0 = 2$

Figure 7.9: Spectral stability analysis with $\gamma = 1 + \sqrt{2}/2$ for both subdomains, $ss = 2$.

7.7.2 Accuracy analysis on the split mass system

In order to investigate the convergence of the underlying inter-field parallel algorithm, simulations on the split mass system depicted in Figure 7.5 are carried out with different sets of parameters. Unless specially stated, the set of parameters is utilized: $u_0 = 0.01$, $\dot{u}_0 = 0.0$, $\gamma_A = \gamma_B = 1 - \sqrt{2}/2$. The initial conditions $u_0 = 0.01$ and $\dot{u}_0 = 0.0$ are performed and the displacement and velocity responses at $t = 0.8s$ are compared with the analytical results to examine the global errors.

First of all, the effectiveness of the Jacobian modification and velocity projection are illustrated in Figure 7.10. Clearly, without any operations, including Jacobian modification and the velocity projection, the method is second-order accurate, as shown in Figure 7.10(a) and (b). The drift-off effects in displacement and velocity responses of two subdomains, defined as the differences between corresponding responses of two subdomains, however, are observed. Both of the Jacobian modification and velocity projection are effective to reduce the drift. In detail, the Jacobian modification makes sense to reduce the displacement drift while the velocity projection works well for velocity drift reduction. Unfortunately, drift reduction is at the expense of loosing absolute accuracy. By comparing Figure 7.10(a) and (c), Figure 7.10(b) and (d), respectively, it is evident that the velocity projection reduces the accuracy. The reason of this will be discussed in Section 7.10. While all monolithic methods exploited in RHS are second-order accurate, the parallel partitioned methods may be first-order accurate, such as the PM method (Pegon and Magonette, 2002) with $ss > 1$ and the inter-field parallel method based on the α method (He, 2008). In fact, errors in RHS arise from control errors, measurement errors and numerical integrations. Amongst them, the main source is the control error. With this view in mind, the first-order accurate method may be acceptable. Therefore, in our case, we conduct both of the projection and Jacobian modification to obtain better properties, as shown in Figure 7.10(e) and (f). For more widely investigating the effectiveness, discussions are performed based on numerical simulations in the next section.

As illustrated in Figure 7.11, the accuracy of the IPLSRT2 method varies amongst different scenarios. First of all, when $\gamma = 1 - \sqrt{2}/2$, the closer to zero b_0 is, the closer to second-order accuracy the method is. Additionally, the dissipation introduced by

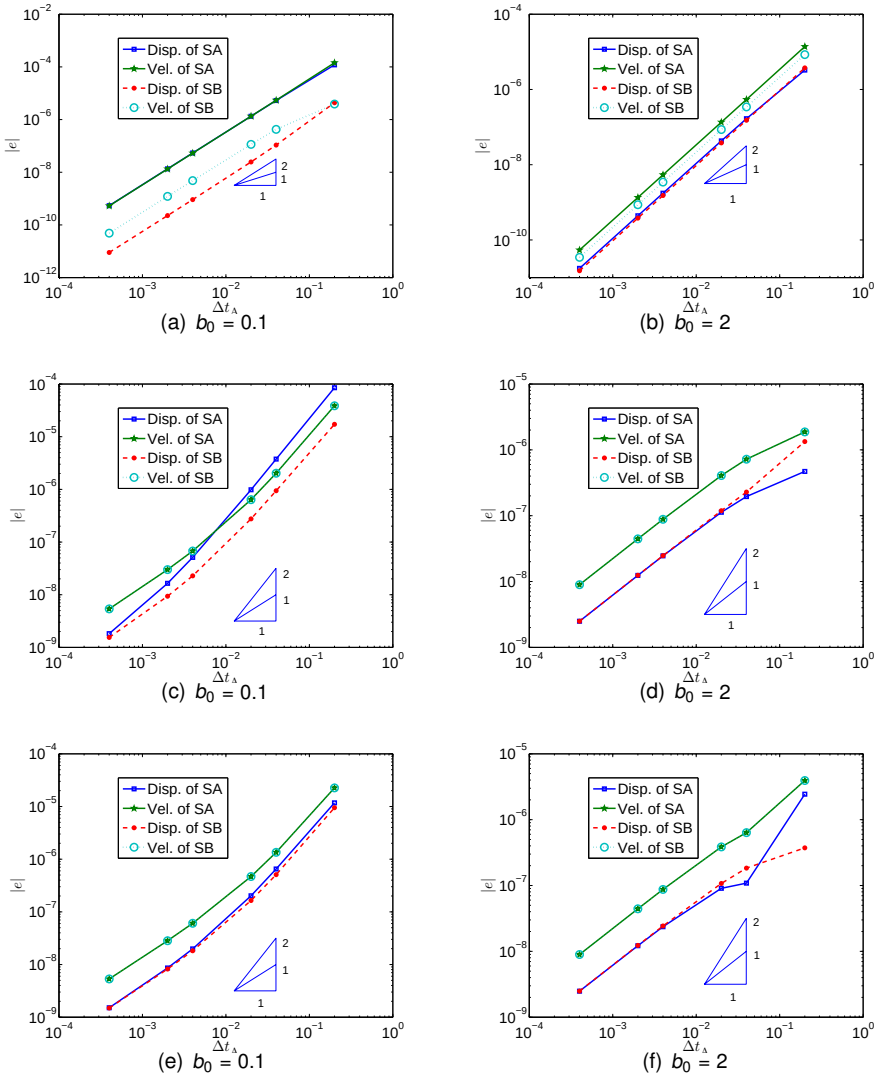

Figure 7.10: Influence of the Jacobian modification and velocity projection on convergence : (a),(b) without the modification and velocity projection; (c) and (d) with velocity projection;(e) and (f) with modification and the velocity projection.

the parameter γ worsens the accuracy. Compared with the accuracy results with only the Jacobian modification, it is evident that the velocity projection reduces the accuracy. However, the accuracy is always higher than first-order. Accuracy analysis of the PLSRT2 method and the IPLSRT2 method under the same conditions on the split mass system are presented in Figure 7.12. Clearly, it is not necessary for the PLSRT2 to exhibit better accuracy even though it is second-order accurate for a little larger time step. Consequently, for the common real-time applications, the developed method is preferable to the PLSRT2 in terms of its accuracy even though it is not second order.

7.8 Representative numerical simulations

In order to validate the effectiveness of the developed algorithm for real-time simulations, a series of numerical simulations and tests are conducted. In this section, we present three types of numerical simulations, i.e. simulations on the single-DOF split mass system, two-DOF split mass system and 4DOF split mass system. In addition, all results are compared with those provided by the progenitor method, the PLSRT2.

7.8.1 Numerical simulations on Single-DOF split mass system

To start with, simulations on the Single-DOF split mass system in Figure 7.5 are carried out. The structural parameter is assumed to be m=1 and $k = 6.28 \times 6.28$, which results in the natural frequency 1Hz. The integration time step is chosen δt = 10ms. First, we take into account the case of free vibrations with the initial conditions u_0 = 0.0m, $\dot{u}_0$ = 0.01m/s and the parameter b_0 = 0.1. Simulations with both methods are presented in Figure 7.13 as well as the results provided by the IPLSRT2 but without the Jacobian modification. One can observer and summarize that (1) the PLSRT2 is not satisfactory due to the larger displacement drift and velocity phase dis-

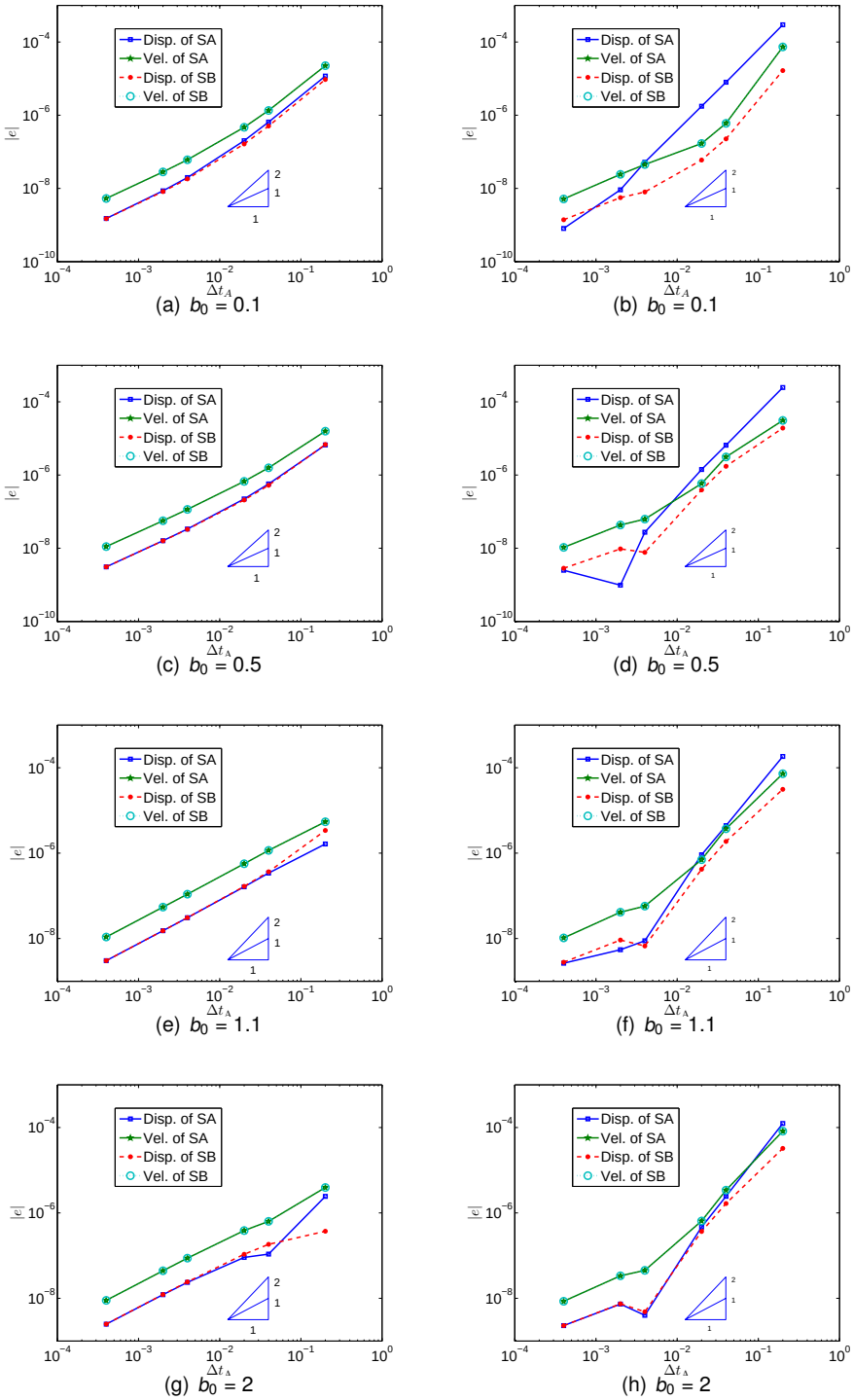

Figure 7.11: Global error of the algorithm on the Single-DOF split mass system with: (a), (c), (e) and (g) $\gamma_A = \gamma_B = 1 - \sqrt{2}/2$; (b), (d), (f) and (h) $\gamma_A = \gamma_B = 1 + \sqrt{2}/2$.

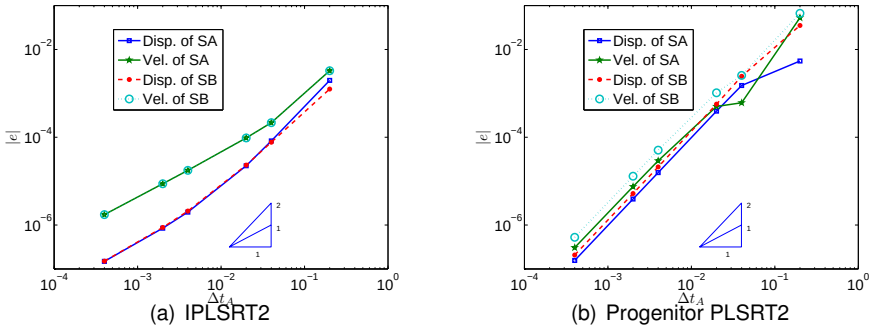

(a) IPLSRT2 (b) Progenitor PLSRT2

Figure 7.12: Global error of the IPLSRT2 and progenitor PLSRT2 on the Single-DOF split mass system with $k_A + k_B = (2\pi)^2$.

tortion; (2) the velocity projection successfully reduce the displacement drift and the velocity amplitude error. However, the phase distortions are observed; (3) the Jacobian modification further improves the response accuracy by reducing the amplitude and phase distortions. Then simulations are repeated under the same conditions except $b_0 = 2$, as shown in Figure 7.14. One can see that (1) as expected, the displacement drift is reduced in the developed method; (2) the velocity response of the PLSRT2 seems to be accurate in terms of amplitude errors and phase shifts. In fact, as shown in Figure 7.15, the PLSRT2 is not stable. It indicates that the developed method exhibits better stability in this case. Moreover, it is more robust considering the algorithm dissipation introduced by the velocity projection.

7.8.2 Numerical simulations on 2DOF split mass system

The 2DOF emulated structure and split system, used in the real tests as well, are shown in Figure 7.16. In simulations, structural properties are listed in Table 7.1. In addition, the structure is excited by sinusoidal waves in two directions with the frequencies 2Hz and 1.5Hz. Figure 7.17 depicts the time histories simulated with two algorithms. The velocity histories are not presented here, since the velocity drifts are very small or eliminated for both methods, respectively. In the figure, both displacements provided by the developed method exhibit favourable accuracy while the drifts of the PLSRT2 are apparent. These simulations re-confirm that for the common appli-

cations the developed method is superior to the PLSRT2 in terms of the displacement drift.

7.8.3 Numerical simulations on 4DOF split mass system

All DOFs are split in the two simulations above and therefore in this simulation the structure of four-DOF is analyzed to consider more general cases. The structure model is shown in Figure 7.18. For brevity, the following characteristics are endowed to the model

$$m_1^{\mathrm{A}} = m_2^{\mathrm{A}} = m_1^{\mathrm{B}} = m_2^{\mathrm{A}} + m_3^{\mathrm{B}} = 1\mathrm{kg},\ \frac{\mathrm{m}_3^{\mathrm{B}}}{\mathrm{m}_2^{\mathrm{A}}} = \mathrm{b_m}, \mathrm{k}_1^{\mathrm{A}} = \mathrm{k}_2^{\mathrm{A}} = \mathrm{k}_3^{\mathrm{A}} = \mathrm{k}_1^{\mathrm{B}} = \mathrm{k}_2^{\mathrm{B}} = 100\mathrm{m/s}. \quad (7.45)$$

which result in the natural frequencies of the structures

$$f_1 = 0.98\mathrm{Hz}\ f_2 = 1.87\mathrm{Hz}\ f_3 = 2.58\mathrm{Hz}\ f_4 = 3.03\mathrm{Hz} \quad (7.46)$$

In the simulations, $b_m = 0.5$, the initial displacement condition $u_1^{\mathrm{B}}(0) = 0.01\mathrm{m}$ and the time step $\Delta t = 0.004\mathrm{s}$ were adopted. Figure 7.19 depicts the displacement time histories of the interface DOF. For the purpose of comparison, the results provided by the PLSRT2 are also presented. As expected, the results re-confirm the effectiveness of the developed method to reduce the displacement drift.

7.9 Test validations

RHS on the 2DOF system as shown in Figure 7.16, were conducted to verify the performance of the two algorithms. Although the TT1 test rig is so flexible that specimens endowed with different characteristics can be configured with springs, dampers and masses, herein we just take into account two combined springs as the specimen for two reasons: (1) the internal forces of the physical substructure are required and therefore it is convenient if the specimen includes only springs and dampers; (2) generally speaking, physical dampers facilitate the tests and in our case we want to

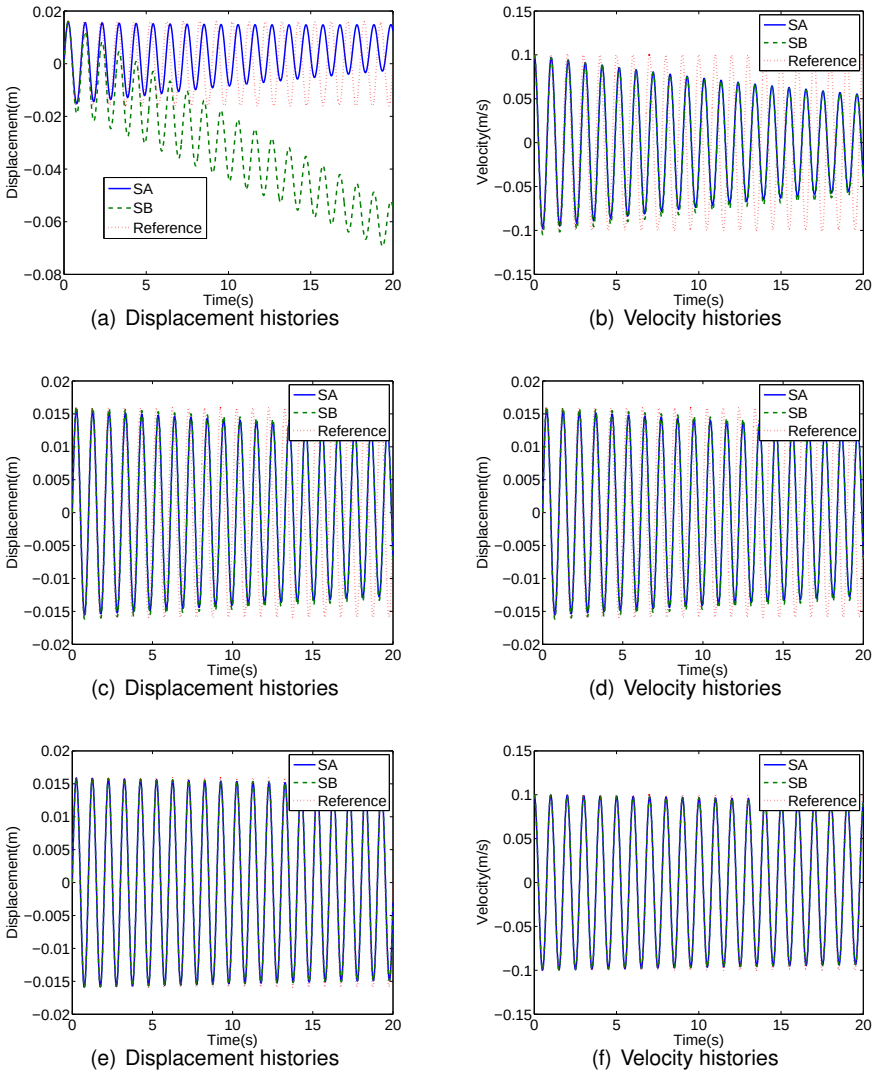

Figure 7.13: Comparisons between two methods with b=0.1: (a) and (b) displacement and velocity histories obtained with the PLSRT2; (c) and (b) displacement and velocity histories obtained with the IPLSRT2 method but without modified Jacobian;(e) and (f) displacement and velocity histories obtained with the IPLSRT2 method.

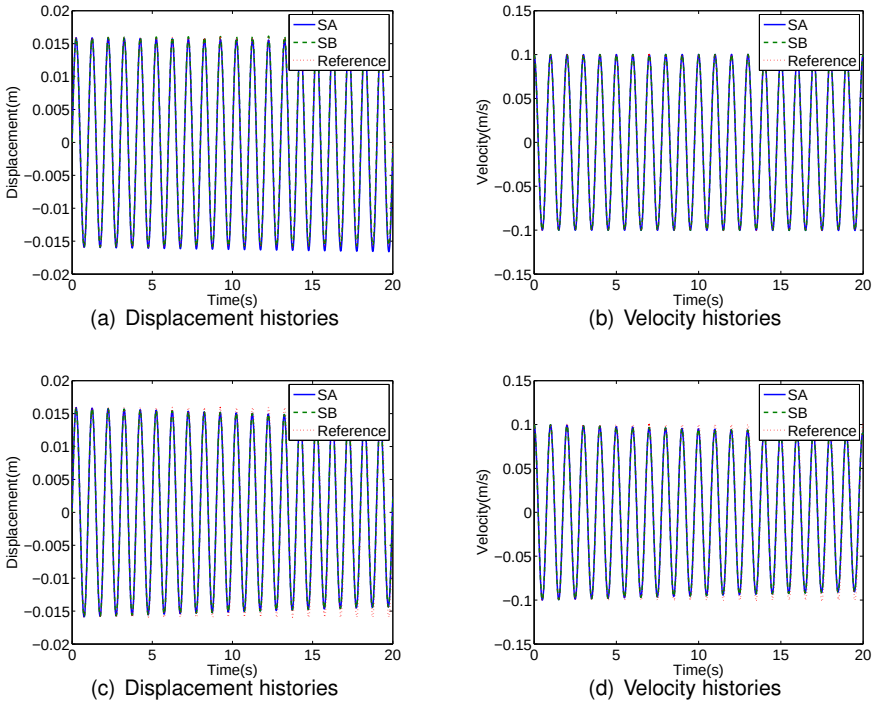

Figure 7.14: Comparisons between two methods with b=2: (a) and (b) displacement and velocity histories obtained with the PLSRT2; (c) and (b) displacement and velocity histories obtained with the IPLSRT2 method.

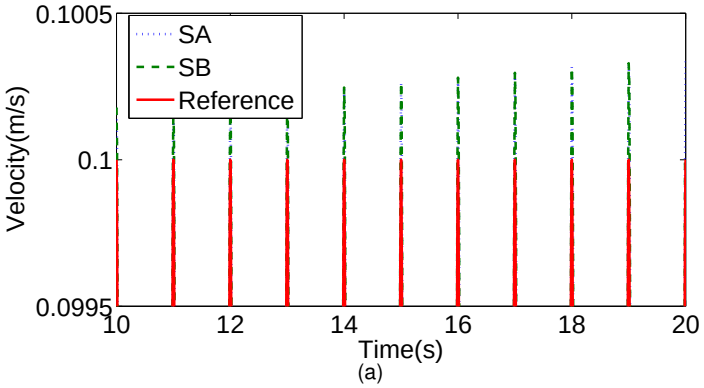

Figure 7.15: Close-up view of the velocity history obtained with the PLSRT2.

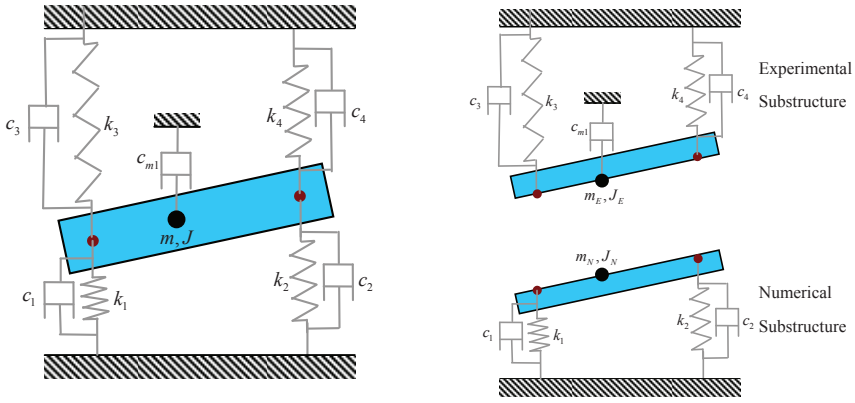

(a) 2DOF emulated structure (b) The split system

Figure 7.16: The 2DOF model.

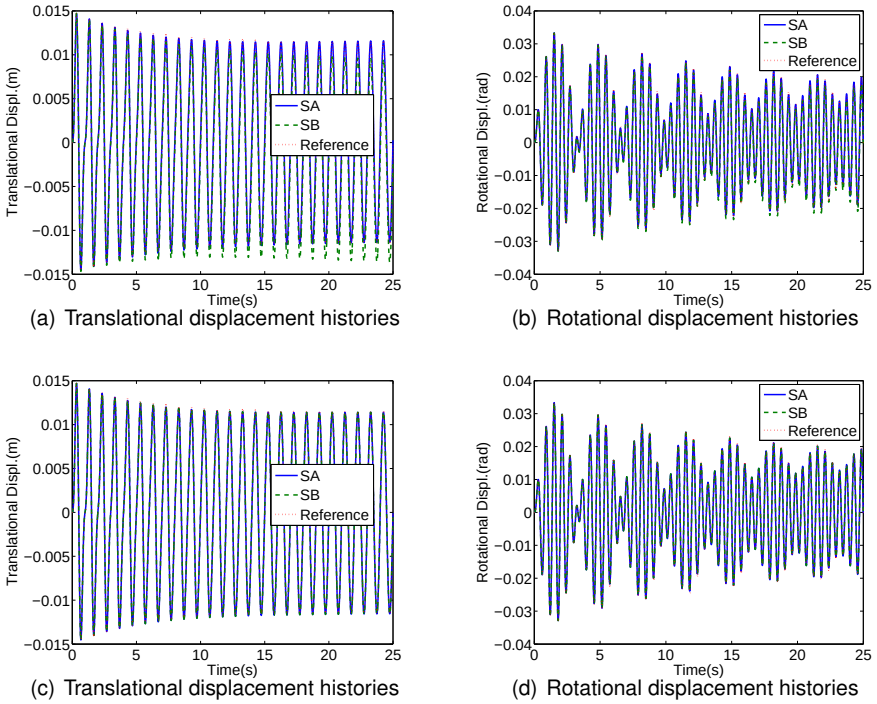

(a) Translational displacement histories (b) Rotational displacement histories

(c) Translational displacement histories (d) Rotational displacement histories

Figure 7.17: Comparisons between two methods of a 2DOF split mass system: (a) and (b) displacement histories obtained with the PLSRT2; (c) and (b) displacement histories obtained with the IPLSRT2 method.

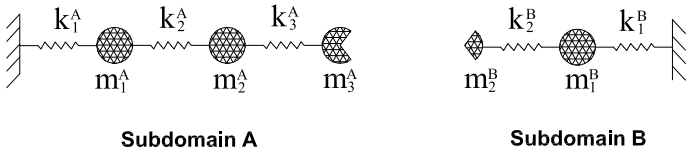

Figure 7.18: The emulated 4DOF structure.

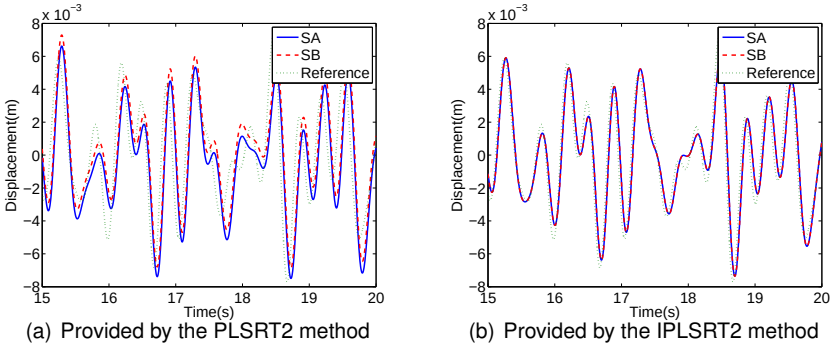

(a) Provided by the PLSRT2 method (b) Provided by the IPLSRT2 method

Figure 7.19: Displacement time histories of the interface DOF provided by two algorithms.

validate the robustness. Structural parameters are presented in Table 7.1, which is attached at the end of this chapter. Furthermore, the two actuators are separately operated in displacement by the strategy of internal model control devised in Chapter 3. The time step Δt for integration and the substep number were 4ms and 2, respectively, and therefore, Δt_A = 16ms and Δt_B = 2ms. The sampling time for control was set to 1ms, the same as the first stage size of integration in Subdomain A and stage sizes in Subdomain B. As a consequence, programs of two tasks, sampling times equal to 1ms and 4ms, were designed in Matlab/Simulink. The process of making the program demonstrated one advantage of the algorithm, it is to say, the ease of implementation, since the starting procedure of the IPLSRT2 method can be conducted in advance and therefore the information exchange is simplified.

The delay compensation effects in the test with the IPLSRT2 method are presented in Figure 7.20. The compensation method proposed by Lamarche et al. (2010) was applied for its better robustness to compensate for the system delay, which is about 23ms and estimated in advance. Figure 7.20(a) shows the unintended loops due to the actuator delay while Figure 7.20 (b) indicates that the delay is effectively reduced

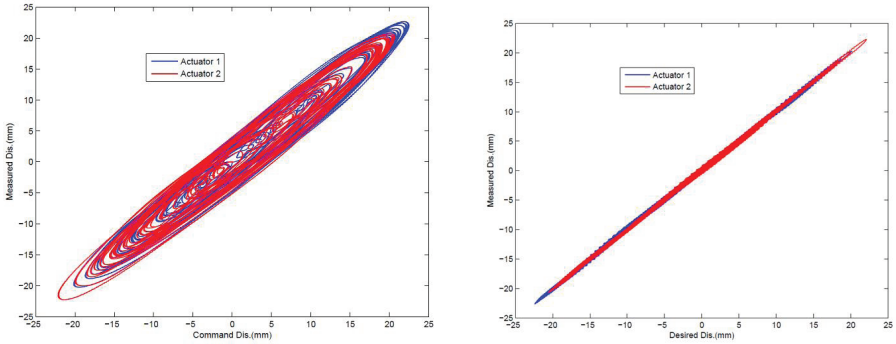

(a) Command v.s. measured displacements (b) Desired v.s. measured displacements

Figure 7.20: Delay compensation: (a) command and measured displacements; (b) desired and measured displacements.

by the compensation.

For the brevity, here we just present displacement comparisons of the RHS using two algorithms, as shown in Figure 7.21. Obviously, the displacement drifts are reduced to the acceptable level. It is worthy mentioning that the errors between the tested and simulated results are due to the friction existing in the test but not modeled in the numerical simulation. Moreover, even though it is not presented here, one test with the IPLSRT2 method continued for more than 10 minutes. This is impossible for the PLSRT2 method owing to the displacement drift and noise in tests.

7.10 Discussions on the accuracy reduction

Clearly, the accuracy order of the proposed method is reduced compared with the progenitor algorithms - the LSRT2 method and the PLSRT2 method. In this section, we are to discuss the reason of this reduction. First of all we have the lemma: the velocity projection based on the mass provides results of the lower accuracy order of the original data. This can be briefly proved as follows: Suppose that the original

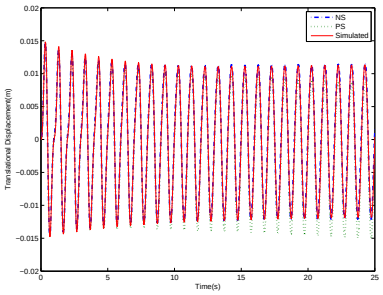

(a) Translational displacement histories

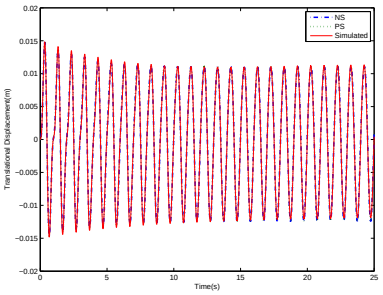

(b) Translational displacement histories

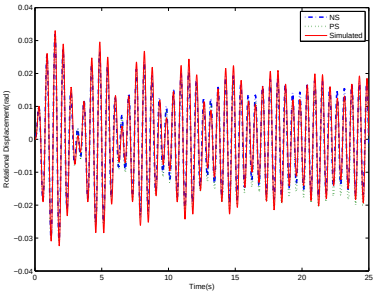

(c) Rotational displacement histories

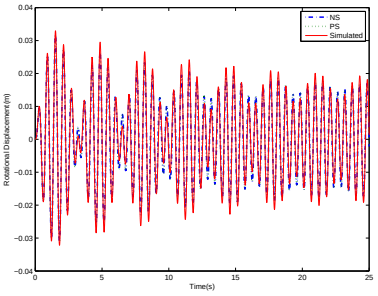

(d) Rotational displacement histories

Figure 7.21: Displacement comparisons: (a) and (c) provided by the PLSRT2; (b) and (d) provided by the proposed algorithm.

velocities are p-th and q-th order accurate, i.e.

$$\begin{cases} \tilde{\dot{u}}^A = \dot{u}(t) + o(\Delta t^p) \\ \tilde{\dot{u}}^B = \dot{u}(t) + o(\Delta t^q) \end{cases} \tag{7.47}$$

The minimization problem can be recast into

$$\begin{cases} m^A \dot{u}^A + \mu = m^A \tilde{\dot{u}}^A \\ m^B \dot{u}^B - \mu = m^B \tilde{\dot{u}}^B \\ \dot{u}^A = \dot{u}^B \end{cases} \tag{7.48}$$

which yields the solution

$$\dot{u}^A = \dot{u}^B = \frac{m^A}{m^A + m^B} \tilde{\dot{u}}^A + \frac{m^B}{m^A + m^B} \tilde{\dot{u}}^B \tag{7.49}$$

Substituting Eq. (7.47) into this solution gives

$$\dot{u}^A = \dot{u}^B = \dot{u}(t) + \frac{m^A}{m^A + m^B} o(\Delta t^p) + \frac{m^B}{m^A + m^B} o(\Delta t^q) \tag{7.50}$$

Therefore the projected results are endowed with the lower accuracy order of the original data. On the other hand, the linear interpolation employed at the odd steps to generate the velocity for projection results in the first order accurate results even though the original data is higher-order accurate. With this in mind, the velocity projection at the odd steps just offer first-order accurate velocity for Subdomain B. For Subdomain A, it does not immediately influence the results, in that the projected velocity is not utilized in the following steps. The only effect of the velocity projection to Subdomain A is originated from the projection at the even steps and the error propagation of the odd step projections. From this analysis we can conclude that the method is second order accurate if the projections are performed at only even steps, rather than all steps. This is validated by accuracy analysis shown in Figure 7.22.

However, the accuracy order is one of the crucial problems involved in RHS. The actual accuracy for a specific problem and the stability are significant as well. The stability of the algorithm with the even-step projection is examined and the eigenvalues are plotted in Figure 7.23, where a limited stability range is observed. Taking into account stability and accuracy, we applied the projection at all steps.

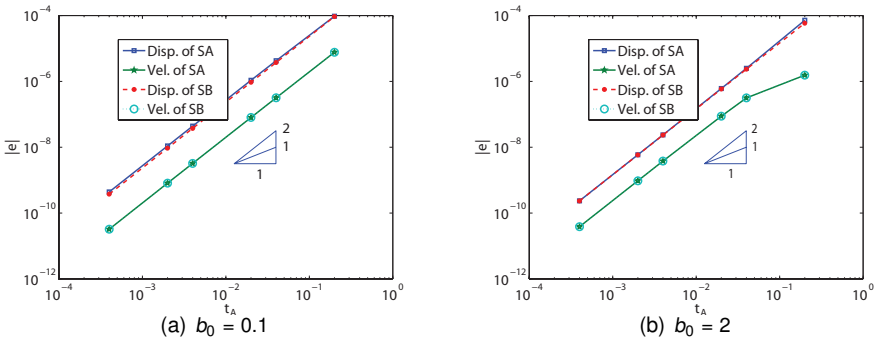

(a) $b_0 = 0.1$ (b) $b_0 = 2$

Figure 7.22: Accuracy analysis with: (a) and (b) projections at even steps.

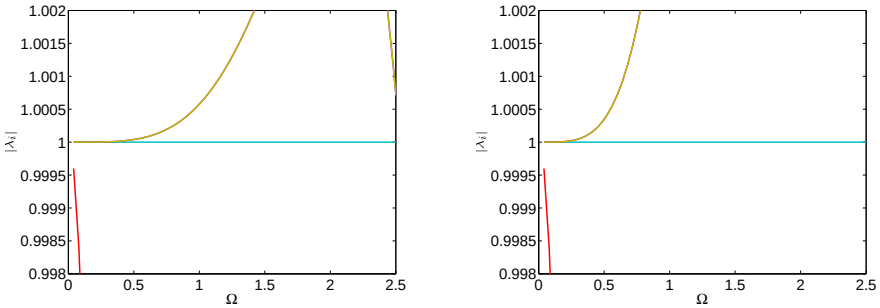

(a) $b_0 = 0.1$ (b) $b_0 = 2$

Figure 7.23: Stability analysis with: (a) and (b) projections at even steps.

7.11 Conclusions and discussions

An inter-field parallel algorithm for RHS in earthquake engineering is developed and analyzed. This method is based on the monolithic integrator - the Rosenbrock method - and the inter-field parallel integrator - the PLSRT2 by Jia (Jia, 2010; Jia et al., 2011). The LSRT2 with different stage sizes, velocity projection and modified Jacobian are introduced to the algorithm in order to avoid and/or weaken the disadvantages of the PLSRT2, such as inefficient computation, displacement and velocity drifts and complicated starting procedure. Compared with the PLSRT2, this method exhibits pros and cons. In detail, the method loses the accuracy order due to velocity projection. However, it can provide more accurate displacement and velocity results for common applications. In some cases, the proposed method exhibits smaller phase shifts and dissipation. Moreover, computation efficiency is improved and its implementation in real-time applications is simplified.

Other two shortcomings of the PLSRT2 and the IPLSRT2 method are that: (1) movement quantities are interpolated instead of internal forces; (2) responses of all DOFs are required to calculate the Lagrange multiplier rather than only the responses at the interface. The first problem leads to many evaluations of the internal force of Subdomain A and the storage of the parameters of Subdomain A in the computer for Subdomain B. This problem can be catered for by conducting force interpolation. In fact, the stability and accuracy analysis are also valid when force interpolation are exploited because the problem is linear. The second problem is related to the Lagrange multiplier calculation and it is hard to solve. This may be the topic of future work.

Table 7.1: Properties of the emulated and split system for RHS

Structural type	Emulated system			NS - Subdodomain A			PS - Subdomain B		
Physical quantity	M	K	C	M_N	K_N	C_N	M_P	K_P	C_P
Translational	2210.9	346310	555.66	1658.2	306640	555.66	552.7	39670	0
Rotational	157.2	138524	22.226	117.9	12265	22.226	39.3	1711	0
Note: all values are expressed in International Units.									

CHAPTER 8

SUMMARIES, CONCLUSIONS AND FUTURE PERSPECTIVES

8.1 Summaries and conclusions

The main objective of this thesis is to develop Real-time Hybrid Simulation (RHS) in terms of transfer system control and integration algorithms. In detail, the thesis deals with i) a practical model-based control strategy - Internal Model Control (IMC), ii) online delay estimation based on a simplified actuator model, iii) new delay compensation schemes, iv) the EFC method for split-mass systems as well as v) an improved parallel partitioned algorithm based on the Rosenbrock method. Main contributions can be summarized as follows:

- Implementation of IMC on a novel test system, i.e. the TT1 test system;
- Proposition of an online delay estimation based on a simplified actuator model, resulting in an adaptive delay compensation scheme;
- Development of two types of delay compensation schemes. One aims at applying explicit displacement and velocity targets provided by some lately proposed integration algorithms while the other constitutes of overcompensation and optimal force feedback, resulting in control error reduction and possible stability improvement;
- Analysis of the advantages of the EFC method and to propose a correction taking into account both displacement and acceleration for RHS on a split mass as well as the displacement correction;

- To propose a new parallel partitioned integration for RHS based on the Rosenbrock method.

The forthcoming portion of this subsection summarizes the main works and conclusions of each chapter in the thesis.

Chapter 2 has provided the context of this thesis research. First of all, various seismic experimental methods were introduced and remarked, including the well-established methods, i.e., quasi-static testing, pseudo-dynamic testing and shaking table testing, as well as the methods under development, i.e., the effective force method and real-time hybrid simulation. Successively main crucial issues in RHS were discussed, which were concerned with integration methods, delay estimation and compensation, transfer system control and applications of RHS.

The implementation of IMC and comparison with the classic PID/PI control on the lately developed high performance test system - the TT1 test system - were presented in Chapter 3. In detail, advantages and the design procedure of IMC were firstly introduced. Then Parker software from the manufacturer of actuators was configured for speed loop of the electromagnetic motors and the inner displacement loop in the TT1 test system were designed with proportional control and identified. Then IMC and PID (sometimes as well as PI control) for the outer displacement loop were implemented and compared in the frequency domain with swept sinusoidal waves and in the time domain with a step change. In addition, real-time hybrid tests on a split mass system were conducted with the TT1 test system regulated by IMC. Analysis showed that the IMC is preferable for its performance considering robustness and its ease of implementation. Numerical simulations of the real-time hybrid simulations confirmed that the test results are reliable and the system worked well.

The fourth chapter is devoted to adaptive delay compensation based on a simplified actuator model - a pure delay multiplied by a gain representing amplitude errors. Two classic techniques, namely Newton's method and Taylor series, were employed for identifying the system delay, resulting in two kinds of estimation schemes or adaptive laws in the framework of adaptive control. The latter one was developed further by introducing the recursive least square algorithm with a forgetting factor to treat the influence of measurement noise and other application problems. Successively, numerical simulations and realistic RHS with a stiffness specimen were carried out

in order to examine the ability of the method to estimate and compensate for delay. At last, it was identified that the proposed method is satisfactory in terms of its convergence speed and accuracy.

With the insight relevant to explicit velocity targets in mind, two polynomial delay compensation formulae considering the latest displacement and velocity targets were proposed in Chapter 5. Assessment and comparisons of the formulae by means of Bode plots and stability analysis were carried out. In order to loosen the assumption on control in RHS, another novel compensation scheme characterized by overcompensation and optimal feedback was conceived. Numerical simulations and real RHS were performed to examine the proposed overcompensation scheme. The analysis revealed that the proposed polynomial formulae exhibit smaller prediction errors and the second-order scheme with the LSRT2 algorithm was endowed with a somewhat larger stability range. On the other hand, the overcompensation scheme was concluded to have the ability of error reduction and sometimes stability improvement.

Although most algorithms applied in RHS are explicit for displacement or both displacement and velocity, Chapter 6 deals with the split-mass RHS with an implicit algorithm in the framework of the EFC method for its favourable algorithmic properties. In detail, the EFC method was initially compared with the conventional iteration and advantages of the method was then concluded. Then the difficulty of control in a split-mass RHS was discussed, which are mass ratio limits and control errors. In view of displacement incompatibility between two substructures, a displacement correction scheme was devised considering loading overshoot and undershoot. A correction for both displacement and acceleration was also presented, followed by stability analysis and simulations to investigate its properties and effectiveness. Spectral stability analysis and numerical simulations demonstrated that: (1) the correction can remove the constraint of zero-stability to the method and reduce algorithmic dissipation; (2) it also works well for MDOF.

An inter-field parallel algorithm for RHS in earthquake engineering was developed and analysed in Chapter 7. This method was based on the monolithic integrator - the Rosenbrock method - and the interfiled parallel integrator - the PLSRT2 method conceived by Jia (Jia, 2010). The LSRT2 method with different stage sizes, velocity projection and modified Jacobian were introduced to the algorithm in order to avoid

and/or reduce the disadvantages of the PLSRT2 method, such as inefficient computation, displacement and velocity drifts and complicated starting procedure. Accuracy analysis, spectral stability analysis, pure numerical simulations and realistic RHS were performed to investigate the properties of the method. Compared with the PLSRT2 method, this method exhibits pros and cons. For instance, the method loses the accuracy order due to velocity projection. However, it can provide more accurate displacement and velocity results for common applications. In some cases, the proposed method exhibits smaller phase shifts and dissipation and more robustness. Moreover, computation efficiency is improved and its implementation in real-time applications is simplified.

8.2 Future perspectives

With reference to this thesis, a lot of research work for RHS remains to be performed. Some of them are very significant and urgent.

IMC is preferable due to its tracing performance and robustness. More tests considering stronger coupling between the actuator and specimens, between actuators are required to be carried out for evaluation of the IMC method. This work will be also beneficial for complex tests of other kinds of hybrid simulations.

The tests in Chapter 4 has shown that the delay changes greatly at the beginning of tests and then varies little. The reason of this phenomenon needs to be analysed and verified by more tests in other laboratories.

Displacement correction was applied in pseudo-dynamic testing with implicit time integration algorithms. This thesis extends this to RHS. However, more investigations should be carried out to extend the technique to RHS with an explicit integrator.

Merits of most partitioned methods are appealing. However, their algorithmic properties are not satisfactory. More research work needs to be conducted to improve these properties for RHS as well as distributed hybrid simulations.

In addition, this dissertation often applies the proposed methods to SDOF system.

For the purpose of validating the effectiveness of these methods, realistic tests with a more general emulated model should be carried out. Shaking table tests can be utilized to examine these methods as well.

APPENDIX A

PROOF OF SUFFICIENT CONDITION FOR CONVERGENCE OF REAL-TIME ITERATION

Most iterative methods for solving a fixed point problem

$$f(x) = 0 \tag{A.1}$$

can be rearranged into this form (called as Picard iteration)

$$x_{i+1} = \varphi(x_i). \tag{A.2}$$

There is a corollary related to convergence of this iteration:

Corollary(Isaacson and Keller, 1994, Page 90): If $x = \varphi(x)$ has a root at $x = x^*$ and in the interval

$$|x - x^*| < \rho \tag{A.3}$$

$\varphi(x)$ satisfies

$$|\varphi'(x)| \leq L < 1 \tag{A.4}$$

then for any x_0 in the interval

① all the iterates $x_i$lie in the interval,

② the iterates x_i converge to x^*

③ the root x^* is unique in this interval.

Similarly, we conclude this theorem related to convergence of a real-time iteration

$$x_{i+1} = \varphi(t_i, x_i) \tag{A.5}$$

for solving

$$f(t, x) = 0 \tag{A.6}$$

where x is a time-invariant unknown:

Theorem: If $x = \varphi(t, x)$ has a root at $x = x^*$ and in the interval:

$$|x - x^*| < \rho \tag{A.7}$$

$\varphi(x)$ satisfies

$$\begin{aligned} &\left|\frac{\partial \varphi}{\partial x}\right| \leq L(t) < 1 \\ &L_{\sup} = \sup\{L(t), t > 0\} < 1 \end{aligned} \tag{A.8}$$

then for any x_0 in the interval

① all the iterates $x_{i+1} = \varphi(t_i, x_i)$lie in the interval,

② the iterates $x_{i+1} = \varphi(t_i, x_i)$ converge to x^*

③ the root x^* is unique in this interval.

Proof. Part (i) is proved by induction. By hypothesis x_0 is in the interval and we assume iteratesx_1,x_2,x_3,$\cdots$,x_{i-1} are also. Then since $x^* = \varphi(t, x^*)$, we have

$$|x^* - x_i| = |\varphi(t, x^*) - \varphi(t_{i-1}, x_{i-1})| = |\varphi(t_{i-1}, x^*) - \varphi(t_{i-1}, x_{i-1})| \tag{A.9}$$

According to the mean value theorem, one obtains

$$\varphi(t_{i-1}, x^*) - \varphi(t_{i-1}, x_{i-1}) = \left.\frac{\partial \varphi}{\partial x}\right|_{(t_{i-1}, \xi_{i-1})} (x^* - x_{i-1}) \tag{A.10}$$

Inserting Eq. (A.2) into Eq. (A.10) gives

$$|x^* - x_i| = \left|\left.\frac{\partial \varphi}{\partial x}\right|_{(t_{i-1}, \xi_{i-1})}\right| \times |x^* - x_{i-1}| < L_{\sup} |x^* - x_{i-1}| \tag{A.11}$$

$L_{\sup} < 1$ causes

$$|x^* - x_i| < \rho \tag{A.12}$$

Therefore Part (i) is concluded.

From the proof of Part (i), we have

$$\begin{aligned} |x^* - x_i| &< L_{\sup} |x^* - x_{i-1}| \\ &< L_{\sup}^2 |x^* - x_{i-2}| \\ &..... \\ &< L_{\sup}^i |x^* - x_0| \end{aligned} \tag{A.13}$$

By letting $i \to \infty$, $x_i \to x^*$, then Part (ii) is proved.

For Part (iii), let x^{**}be another root in the interval. Then we have

$$|x^* - x^{**}| = |\varphi(t, x^*) - \varphi(t, x^{**})| < L_{\sup} |x^* - x^{**}| \tag{A.14}$$

Therefore, $x^* = x^{**}$ since $0 < L_{\sup}$, which completes the proof.

This theorem shows that real-time iteration may not converge to the fixed point if $L_{\sup} = 1$. As an example, we set $L(t_i) = \frac{i^2}{i^2+1}$, then $L(t_i)L(t_{i-1}) \cdots L(t_0)$does not approach zero when$i \to \infty$.

With regard to the convergence speed, we define convergence order for the real-time iteration following the definition of that of Picard iteration (Isaacson and Keller, 1994, Page 95):

Definition: The iteration method is called a p-th order procedure if

$$\begin{cases} \left.\frac{\partial \varphi}{\partial x}\right|_{(t,x^*)} = \left.\frac{\partial^2 \varphi}{\partial x^2}\right|_{(t,x^*)} = \cdots = \left.\frac{\partial^{(p-1)} \varphi}{\partial x^{(p-1)}}\right|_{(t,x^*)} = 0, \\ \left.\frac{\partial^{(p)} \varphi}{\partial x^{(p)}}\right|_{(t_i,x^*)} \neq 0, \left|\left.\frac{\partial^{(p)} \varphi}{\partial x^{(p)}}\right|_{(t_i,x^*)}\right| \leq n! \times M \end{cases} \tag{A.15}$$

Now let's move on to the real-time iteration originating from Newton's method, i.e.,

$$\varphi(t, x) = x - \frac{f(t, x)}{\left.\frac{\partial f}{\partial x}\right|_{(t,x)}} \tag{A.16}$$

Obviously, if $\left.\frac{\partial f}{\partial x}\right|_{(t,x^*)} \neq 0$, then

$$\left.\frac{\partial \varphi}{\partial x}\right|_{(t,x^*)} = \left[1 - \frac{\left(\frac{\partial f}{\partial x}\right)^2 - f\frac{\partial^2 f}{\partial x^2}}{\left(\frac{\partial f}{\partial x}\right)^2}\right]\Bigg|_{(t,x^*)} = \left.\frac{f\frac{\partial^2 f}{\partial x^2}}{\left(\frac{\partial f}{\partial x}\right)^2}\right|_{(t,x^*)} = 0 \tag{A.17}$$

which means that the iteration is second-order convergent. If $\left.\frac{\partial f}{\partial x}\right|_{(t,x^*)} = 0$, we set

$$f(t, x) = (x - x^*)^p h(x), p > 1 \tag{A.18}$$

then

$$\left.\frac{\partial \varphi}{\partial x}\right|_{(t,x^*)} = 1 - \frac{1}{p} \tag{A.19}$$

which implies the iteration is first-order convergent.

APPENDIX B

STABILITY INVESTIGATION OF RHS WITH COMPENSATION SCHEMES FOR SMALL Ω

B.1 Introduction

In the stability analysis of RHS with the linear acceleration compensation scheme and the third-order Hermite scheme in Chapter 5, both cases are found to be unstable for a small non-dimensional frequency. In order to validate the results, we conduct theoretical analysis herein for both cases, including zero-stability analysis and stability analysis for a small non-dimensional frequency.

B.2 Stability analysis for RHS with the linear acceleration compensation scheme

B.2.1 Zero-stability analysis

Zero-stability is the stability of an integrator when the time step approaches zero, which is a necessary condition of convergence of an integrator. Therefore, eigenvalues of a method with Δt approaching to zero, i.e. $\lambda(\Delta t \rightarrow 0)$, can be exploited to examine zero-stability. In addition, $\lambda(\Delta t \rightarrow 0)$ is equal to $\lambda(\Delta t = 0)$ provided that λ are

continuous with respect to Δt. Therefore, we set $\Delta t = 0$ in the amplification matrix, i.e. Eq. (5.13), and obtain

$$\mathbf{A}(\Delta t \to 0) = \begin{bmatrix} 1 & 1 & 1/2 & 0 & 0 \\ 0 & 1 & 1/2 & 0 & 0 \\ 0 & 0 & 0 & 0 & 0 \\ 0 & 0 & 1 & 0 & 0 \\ 1 & 2 & 10/3 & -4/3 & 0 \end{bmatrix}. \tag{B.1}$$

Evidently, this matrix has eigenvalues $\lambda_{1,2} = 1$ and $\lambda_{3,4,5} = 0$. Moreover, there is only one linearly independent eigenvector related to the eigenvalues $\lambda_{1,2} = 1$. Thus when the amplification matrix is expressed in the Jordan form, there exists a Jordan block

$$\mathbf{J} = \begin{bmatrix} 1 & 1 \\ 0 & 1 \end{bmatrix}. \tag{B.2}$$

Clearly, this block will render the response unbounded as the analytical time tends to infinity. Therefore, the method is not zero stable.

B.2.2 Stability analysis for a small non-dimensional frequency

Generally speaking, an integrator which is not zero-stable is not stable for a non-dimensional frequency close enough to zero. However, the method under discussion is not zero-stable due to weak instability and this conclusion is not necessarily true. Therefore, we investigate the stability of the method for a small non-dimensional frequency with the Routh-Hurwitz criterion, which is well-known for its ability of analysing absolute stability of a system in control theory. The criterion states that the number of roots of a polynomial in the Laplace variable s with positive real parts is equal to the number of changes in sign of the coefficients of the first column of the array obtained according to a specific rule. Therefore, only signs of the coefficients in the first column are required in order to investigate stability. For the purpose of applying this criterion, the characteristic polynomial associated with the integrator is firstly converted to $s-$plane by replacing the eigenvalue variable λ with $(1+s)/(1-s)$. This process maps the unit circle, $|\lambda| = 1$, into the imaginary axis $s = a \times i$, and the interior part of the circle into the left half-planeHughes (1983). Henceforth, the sufficient condition of

Table B.1: The array associated with the Routh-Hurwitz criterion

a_5	a_3	a_1
a_4	a_2	a_0
b_1	b_2	0
c_1	c_2	0
d_1	0	
e_1		

stability is that all first column coefficients have negative real part.

The characteristic equation related to the amplification matrix in Eq. (5.13) is

$$3\lambda^5 + (3\Omega_n^2 - 6)\lambda^4 + (3 + 13\Omega_e^2)\lambda^3 - 21\lambda^2\Omega_e^2 + 15\Omega_e^2\lambda - 4\Omega_e^2 = 0 \tag{B.3}$$

Substituting $\lambda = (1 + s)/(1 - s)$ into Eq. (B.3) and then multiplying $(1 - s)^5$ yield

$$\begin{aligned}(-3\Omega_n^2 + 53\Omega_e^2 + 12)s^5 + (-9\Omega_n^2 + 36 - 73\Omega_e^2)s^4 + (-6\Omega_n^2 + 2\Omega_e^2 + 36)s^3 \\ +(6\Omega_e^2 + 12 + 6\Omega_n^2)s^2 + (9\Omega_n^2 + 9\Omega_e^2)s + 3\Omega_e^2 + 3\Omega_n^2 = 0\end{aligned} \tag{B.4}$$

Then the array associated with the Routh-Hurwitz criterion is obtained and tabulated in Table B.1, with

$$\begin{aligned} b_1 &= \frac{a_4 a_3 - a_2 a_5}{a_4} & b_2 &= \frac{a_4 a_1 - a_0 a_5}{a_4} & c_1 &= \frac{b_1 a_2 - b_2 a_4}{b_1} \\ c_2 &= b_1 & d_1 &= \frac{c_1 b_2 - c_2 b_1}{c_1} & e_1 &= c_2 \end{aligned} \tag{B.5}$$

Here $a_i (i = 1, 2, ..., 5)$ is the coefficient of the i-th order term in Eq. (B.3). In addition, d_1 is expressed as

$$d_1 = \frac{128(\Omega_e^2 + \Omega_n^2)(224\Omega_e^4 - 102\Omega_e^2 + 264\Omega_n^2\Omega_e^2 + 9 - 81\Omega_n^2 + 36\Omega_n^4)\Omega_e^2}{\left[\begin{array}{l} -576 - 1416\Omega_n^2\Omega_e^2 + 1776\Omega_e^2 - 108\Omega_n^4 - 1052\Omega_e^4 \\ +9\Omega_n^6 + 432\Omega_n^2 + 504\Omega_n^4\Omega_e^2 + 3093\Omega_n^2\Omega_e^4 + 2598\Omega_e^6 \end{array}\right]} \tag{B.6}$$

Clearly, it is negative when Ω_e and Ω_n are small, which implies that there are at least two eignvalues with positive real parts and the integration is not stable. This is consistent with that in Section 5.2.

B.3 Stability investigation of RHSs with the third-order compensation scheme considering latest velocity

Eigenvalues in Figure 5.4(d) reveal that this method is always unstable. Here we just prove its zero instability and its instability when Ω is small with similar techniques in the previous appendix.

B.3.1 Zero stability analysis

By conducting the same technique in Section B.2.1, we can attain the amplification matrix

$$\mathbf{A}(\Delta t \to 0) = \begin{bmatrix} 1 & 1 & 0 & 0 & 0 & 0 & 0 & 0 \\ 0 & 1 & 0 & 0 & 0 & 0 & 0 & 0 \\ 1 & 3/2 & 0 & 0 & 0 & 0 & 0 & 0 \\ 0 & 0 & 0 & 0 & 0 & 0 & 0 & 0 \\ 0 & 0 & 0 & 0 & 0 & 0 & 1 & 0 \\ 0 & 0 & 0 & 0 & 0 & 0 & 0 & 1 \\ 1 & 2 & 0 & 0 & 0 & 0 & 0 & 0 \\ 0 & 0 & 0 & 0 & 0 & 0 & 0 & 0 \end{bmatrix} \tag{B.7}$$

and its eigenvalues and eigenvectors. In fact, there are also two eigenvalues which are unity and only one linearly independent eigenvector is related to them. Therefore, analogous to that in Section B.2.1, this method is not zero stable, either.

B.3.2 Stability analysis for a small non-dimensional frequency

In this case, the amplification matrix is 8×8. Fortunately, there are three eigenvalues which are zero; thus we just focus on the other five eigenvalues. The characteristic

equation reads

$$0 = \left[\begin{array}{l} (4+8\gamma^2\Omega_n^2+8\gamma^2\Omega_e^2+4\gamma^4\Omega_n^4+4\gamma^4\Omega_e^4+8\gamma^4\Omega_n^2\Omega_e^2)\lambda^5+(-16\gamma^2\Omega_n^2-4\Omega_n^4 \\ \gamma^2-8\gamma^4\Omega_n^4-16\gamma^4\Omega_n^2\Omega_e^2-8-2\Omega_e^4\gamma^2+16\Omega_n^4\gamma^3-4\Omega_e^2\gamma^2\Omega_n^2+24\Omega_n^2\gamma^3\Omega_e^2+ \\ 8\gamma^3\Omega_e^4+4\Omega_n^2-16\gamma^2\Omega_e^2-8\gamma^4\Omega_e^4)\lambda^4+(4\gamma^4\Omega_n^4-16\Omega_n^4\gamma^3+146\Omega_e^4\gamma^2-8\Omega_n^4\gamma \\ -76\Omega_n^2\gamma\Omega_e^2-36\Omega_e^2-72\Omega_n^2\gamma^3\Omega_e^2+272\Omega_e^2\gamma^2\Omega_n^2+4+8\gamma^2\Omega_e^2+4\gamma^4\Omega_e^4+20\Omega_n^4 \\ \gamma^2+8\gamma^4\Omega_n^2\Omega_e^2-36\Omega_e^4\gamma+168\gamma\Omega_e^2-56\gamma^3\Omega_e^4+8\gamma^2\Omega_n^2+\Omega_n^4)\lambda^3+(104\Omega_n^2\gamma^3\Omega_e^2 \\ +276\Omega_n^2\gamma\Omega_e^2-162\Omega_e^4-54\Omega_n^2\Omega_e^2+84\Omega_e^2-312\Omega_e^2\gamma^2\Omega_n^2-1662\Omega_e^4\gamma^2-336\gamma\Omega_e^2 \\ +104\gamma^3\Omega_e^4+1020\Omega_e^4\gamma)\lambda^2+(-1576\Omega_e^4\gamma+168\gamma\Omega_e^2+76\Omega_e^2\gamma^2\Omega_n^2-56\Omega_n^2\gamma^3\Omega_e^2 \\ -44\Omega_e^2-6\Omega_n^2\Omega_e^2+8\Omega_n^2\gamma\Omega_e^2+207\Omega_e^4-56\gamma^3\Omega_e^4+3102\Omega_e^4\gamma^2)\lambda-1568\Omega_e^4\gamma^2+ \\ 808\Omega_e^4\gamma-106\Omega_e^4 \end{array}\right] \tag{B.8}$$

The technique in Section B.2.2 carried out here yields the array similar to Table B.1. In fact, d_1 has the form

$$d_1 = \frac{num(\Omega_e)}{den(\Omega_e)}\Omega_e^4 \tag{B.9}$$

where *num* and *den* are two polynomials with respect to Ω_e. In addition, as $\Delta t \to 0$, $num(\Omega_e) \to 17408 - 83968\gamma + 63488\gamma^2 + 16384\gamma^3$ and $den(\Omega_e) \to 128$. Clearly, if $\gamma = 1 - \sqrt{2}/2$, $17408 - 83968\gamma + 63488\gamma^2 + 16384\gamma^3 = -1.3276 \times 10^3 < 0$, and thus the method is not stable. This result matches well with that in Figure 5.4.

APPENDIX C

ACKNOWLEDGEMENT

This dissertation was completed with elaborate conception and diligent supervision of Prof. Bin WU and Prof. Oreste S. BURSI. Your serious attitude to research and keen insight are my good examples to follow. The tremendous help provided by Prof. Bin WU and Prof. Oreste S. BURSI during my study will be in my mind for ever. At the moment of thesis completion, I gratefully acknowledge your continuing guidance, patience and encouragement.

Many thanks to all professors, teachers and classmates in School of Civil Engineering, Harbin Institute of Technology, China and the Faculty of Engineering, University of Trento, Italy for their help and assistance. Thanks also go to staff in laboratories and computer centres in two schools. Especially to Dr. Marco Molinari in the Faculty of Engineering, whose smile is as sunny as the Sun in the Spring.

I would like to express my sincere thanks to colleagues in Prof WUs group in the past seven years. Thanks to all friends in Prof. BURSIs group as well.

I am very grateful to my parents for their supports, understanding throughout this entire journey.

Finally, financial supports from National Natural Science Foundation of China (Grant number: 90715036), from European Union through the SERIES project (Grant number: 227887) and from China government through other related projects are acknowledged.

APPENDIX D

RESUME

Zhen WANG

- 3rd April, 1983

  Born in Linquan County, Anhui Province, China.

- September, 2001- July, 2005

  Study Civil Engineering at China University of Mining and Technology in the city of Xuzhou, China

- June, 2009- April, 2011

  Do research in the University of Trento, Italy supervised by Prof. BURSI.

- August, 2005- July, 2012

  Study Disaster Prevention and Reduction Engineering and Protective Engineering for masters and doctoral degrees at Harbin Institute of Technology in the city of Harbin, China supervised by Prof. WU.

BIBLIOGRAPHY

Carlos A., K.C. Park, and Charbel Farhat. Partitioned analysis of coupled mechanical systems. *Computer Methods in Applied Mechanics and Engineering*, 190(24-25): 3247 – 3270, 2001. ISSN 0045-7825. ¡ce:title¿Advances in Computational Methods for Fluid-Structure Interaction¡/ce:title¿.

M. Ahmadizadeh, G. Mosqueda, and A.M. Reinhorn. Compensation of actuator delay and dynamics for real-time hybrid structural simulation. *Earthquake Engineering & Structural Dynamics*, 37(1):21–42, 2008. ISSN 1096-9845.

K. J. Åström and T. Hägglund. *PID Controllers: Theory, Design, and Tuning*. Research Triangle Park, N.C. Instrument Society of America, 2nd edition, 1995.

D. Balageas, C.P. Fritzen, and A. Güemes, editors. *Structural Health Monitoring*. ISTE USA, 2006.

O.A. Bauchau and André L. Review of contemporary approaches for constraint enforcement in multibody systems. *Journal of Computational and Nonlinear Dynamics*, 3(1):011005, 2008.

V. Bayer, U.E. Dorka, U. Füllekrug, and J. Gschwilm. On real-time pseudo-dynamic sub-structure testing: algorithm, numerical and experimental results. *Aerospace Science and Technology*, 9(3):223 – 232, 2005. ISSN 1270-9638.

A. Bonelli, O.S. Bursi, L. He, G. Magonette, and P. Pegon. Convergence analysis of a parallel interfield method for heterogeneous simulations with dynamic substructuring. *International Journal for Numerical Methods in Engineering*, 75(7):800–825, 2008. ISSN 1097-0207.

P.A. Bonnet. *The Development of Multi-axis Real-time Substructure Testing*. PhD thesis, University of Oxford, 2006.

P.A. Bonnet, C.N. Lim, M.S. Williams, A. Blakeborough, S.A. Neild, D.P. Stoten, and C.A. Taylor. Real-time hybrid experiments with newmark integration, MCSmd outer-loop control and multi-tasking strategies. *Earthquake Engineering & Structural Dynamics*, 36(1):119–141, 2007. ISSN 1096-9845.

P.A. Bonnet, M.S. Williams, and A. Blakeborough. Evaluation of numerical time-integration schemes for real-time hybrid testing. *Earthquake Engineering & Structural Dynamics*, 37(13):1467–1490, 2008. ISSN 1096-9845.

C. Brosilow and B. Joseph. *Techniques of Model-Based Control*. Prentice Hall PTR, 2002.

B. Burgermeister, M. Arnold, and B. Esterl. DAE time integration for real-time applications in multi-body dynamics. *ZAMM - Journal of Applied Mathematics and Mechanics*, 86(10):759–771, 2006. ISSN 1521-4001.

R.S. Burns. *Advanced Control Engineering*. Butterworth-Heinemann, 2001.

O.S. Bursi and D. Wagg, editors. *Modern Testing Techniques for Structural Systems: Dynamics and Control*. Springer Wien, 2008.

O.S. Bursi, A. Gonzalez-Buelga, L. Vulcan, S.A. Neild, and D.J. Wagg. Novel coupling Rosenbrock-based algorithms for real-time dynamic substructure testing. *Earthquake Engineering & Structural Dynamics*, 37(3):339–360, 2008. ISSN 1096-9845.

O.S. Bursi, L. He, A. Bonelli, and P. Pegon. Novel generalized-α methods for interfield parallel integration of heterogeneous structural dynamic systems. *Journal of Computational and Applied Mathematics*, 234(7):2250 – 2258, 2010. ISSN 0377-0427. Fourth International Conference on Advanced COmputational Methods in ENgineering (ACOMEN 2008).

O.S. Bursi, C. Jia, L. Vulcan, S.A. Neild, and D.J. Wagg. Rosenbrock-based algorithms and subcycling strategies for real-time nonlinear substructure testing. *Earthquake Engineering & Structural Dynamics*, 40(1):1–19, 2011. ISSN 1096-9845.

Fang C. and Xiao D. *Process Identificatioin*. Tsinghua University Press, 1988.

J. Carrion, B. Spencer, and B. Phillips. Real-time hybrid simulation for structural control performance assessment. *Earthquake Engineering and Engineering Vibration*, 8:481–492, 2009. ISSN 1671-3664. 10.1007/s11803-009-9122-4.

S.Y. Chang. Explicit pseudodynamic algorithm with unconditional stability. *Journal of Engineering Mechanics*, 128(9):935–947, 2002. ISSN 07339399.

C. Chen. *Development and Numerical Simulation of Hybrid Effective Force Testing Method*. PhD thesis, Lehigh University, MN, 2007.

C. Chen and J.M. Ricles. Development of direct integration algorithms for structural dynamics using discrete control theory. *Journal of Engineering Mechanics*, 134(8): 676–683, 2008a. ISSN 07339399.

C. Chen and J.M. Ricles. Stability analysis of sdof real-time hybrid testing systems with explicit integration algorithms and actuator delay. *Earthquake Engineering & Structural Dynamics*, 37(4):597–613, 2008b. ISSN 1096-9845.

C. Chen and J.M. Ricles. Improving the inverse compensation method for real-time hybrid simulation through a dual compensation scheme. *Earthquake Engineering and Structural Dynamics*, 38(10):1237–1255, 2009.

C. Chen and J.M. Ricles. Analysis of implicit HHT-α integration algorithm for real-time hybrid simulation. *Earthquake Engineering & Structural Dynamics*, pages n/a–n/a, 2011. ISSN 1096-9845.

C. Chen, J.M. Ricles, T.M. Marullo, and O. Mercan. Real-time hybrid testing using the unconditionally stable explicit CR integration algorithm. *Earthquake Engineering & Structural Dynamics*, 38(1):23–44, 2009. ISSN 1096-9845.

F. Chi, J. Wang, and F. Jin. Delay-dependent stability and added damping of SDOF real-time dynamic hybrid testing. *Earthquake Engineering and Engineering Vibration*, 9(3):425–438, 2010.

R. Christenson and Y.Z. Lin. Real-time hybrid simulation of a seismically excited structure with large-scale magneto-rheological fluid dampers. In Victor Saouma and M.V. Sivaselvan, editors, *Hybrid Simulation: Theory, Implementation and Applications*, pages 169–180. Taylor & Francis, 2008.

J. Chung and G.M. Hulbert. A time integration algorithm for structural dynamics with improved numerical dissipation: The generalized-alpha method. *Journal of Applied Mechanics*, 60(2):371–375, 1993.

MTS System Corporation. *Model 793.10 Multipurpose Testware: User Information and Software Reference*, 2001.

A.P. Darby, M.S. Williams, and A. Blakeborough. Stability and delay compensation for real-time substructure testing. *Journal of Engineering Mechanics*, 128(12):1276–1284, 2002.

L. Deng. *Numerical Stability Analysis of Substructure Testing*. PhD thesis, Harbin institute of technology, 2011.

M. Diehl, H.G. Bock, and J.P. Schloder. A real-time iteration scheme for nonlinear optimization in optimal feedback control. *SIAM Journal on Control and Optimization*, 43(5):1714–1736, 2005.

J. Dimig, C. Shield, C. French, F. Bailey, and A. Clark. Effective force testing: A method of seismic simulation for structural testing. *Journal of Structural Engineering*, 125(9):1028–1037, 1999. ISSN 07339445.

Parker SSD Drives. *890 Quickstart Munual*, ha471072u000 issue 4 edition, 2007.

Parker SSD Drives. *AC890 Engineering Reference*, ha468445u003 issue 4 edition, 2008.

S.J. Dyke, B.F. Spencer, P. Quast, and M.K. Sain. Role of control-structure interaction in protective system design. *Journal of Engineering Mechanics*, 121(2):322–338, 1995. ISSN 07339399.

L.C.A. Enrique. Modeling and simulation of permanent magnet synchronous motor drive system. Master's thesis, UNIVERSITY OF PUERTO RICO MAYAGEZ CAMPUS, 2006.

C.E. Garcia and M. Morari. Internal model control. 1. A unifying review and some new results. *Industrial & Engineering Chemistry Process Design and Development*, 21 (2):308–323, 1982.

A. Gonzalez-Buelga, D. Wagg, S. Neild, and O.S. Bursi. A comparison of runge kutta and novel l-stable methods for real-time integration methods for dynamic substructuring. Chicago, Illinois, USA, November 2006. ASME International Mechanical Engineering Congress and Exposition.

A. Gravouil and A. Combescure. Multi-time-step explicitcimplicit method for non-linear structural dynamics. *International Journal for Numerical Methods in Engineering*, 50(1):199–225, 2001. ISSN 1097-0207.

M. Hakuno, M. Shidawara, and T. Hara. Dynamic destructive test of a cantilever beam, controlled by an analog-computer. *Transactions of the Japan Society of Civil Engineers*, 171(1):1–9, 1969.

Parker Hannifin. *ET manual: ET Electro-thrust cylinders - metrical*. Electromechanical Automation Europe [EME], Robert-Bosch-Strasse 22 Offenburg, Germany, 192-550013 n6 edition, July 2008.

S. Hashimoto, Y. Fujii, M. Kigure, and T. Ishikawa. High-precision control of linear actuators based on internal model control. In *Proc. of 2nd IEEE Conf. on Industrial Electronics and Applications (ICIEA2007)*, 2007.

L. He. *Development of Partitioned Time Integration Scheme for Parallel Simulation of Heterogeneous System*. PhD thesis, University of Trento, 2008.

H.M. Hilber, T.J.R. Hughes, and R.L. Taylor. Improved numerical dissipation for time integration algorithms in structural dynamics. *Earthquake Engineering & Structural Dynamics*, 5(3):283–292, 1977. ISSN 1096-9845.

T. Horiuchi and T. Konno. A new method for compensating actuator delay in real-time hybrid experiments. *Philosophical Transactions of the Royal Society of London. Series A: Mathematical, Physical and Engineering Sciences*, 359(1786):1893–1909, 2001.

T. Horiuchi, M. Inoue, T. Konno, and Y. Namita. Real-time hybrid experimental system with actuator delay compensation and its application to a piping system with energy absorber. *Earthquake Engineering & Structural Dynamics*, 28(10):1121–1141, 1999. ISSN 1096-9845.

T. Horiuchi, M. Inoue, and T. Konno. Development of a real-time hybrid experimental system using a shaking table. 12th Word Conference on Eathquake Engineering, 2000.

T.J.R. Hughes. *Computational Methods for Transient Analysis*, chapter Analysis of Transient Algorithms with Particular Reference to Stability Behavior, pages 67–155. North Holland, 1983.

H. Iemura. Principles of TMD and TLD: Basic principles and design procedure. In T.T. Soong and M.C. Costantinou, editors, *Passive and Active Structural Vibration Control in Civil Engineering*, pages 241–253. Springer-Verlag, Italy, 1994.

E. Isaacson and H.B. Keller. *Analysis of Numerical Methods*. Dover Publications, INC., New York., 1994.

C. Jia. *Monolithic and partitioned Rosenbrock-based time integration methods for dynamic substructure tests*. PhD thesis, University of Trento, 2010.

C. Jia, O.S. Bursi, A. Bonelli, and Z. Wang. Novel partitioned time integration methods for DAE systems based on L-stable linearly implicit algorithms. *International Journal for Numerical Methods in Engineering*, 87(12):1148–1182, 2011. ISSN 1097-0207.

R.Y. Jung and P.B. Shing. Performance evaluation of a real-time pseudodynamic test system. *Earthquake Engineering & Structural Dynamics*, 35(7):789–810, 2006. ISSN 1096-9845.

R.Y. Jung, P.B. Shing, E. Stauffer, and B. Thoen. Performance of a real-time pseudodynamic test system considering nonlinear structural response. *Earthquake Engineering & Structural Dynamics*, 36(12):1785–1809, 2007. ISSN 1096-9845.

Min-Seok Kim and Sung-Chong Chung. A systematic approach to design high-performance feed drive systems. *International Journal of Machine Tools and Manufacture*, 45(12-13):1421 – 1435, 2005. ISSN 0890-6955.

S. Krenk and J. R. Hgsberg. Properties of time integration with first order filter damping. *International Journal for Numerical Methods in Engineering*, 64(4):547–566, 2005. ISSN 1097-0207.

C.P. Lamarche, A. Bonelli, O.S. Bursi, and R. Tremblay. A Rosenbrock-W method for real-time dynamic substructuring and pseudo-dynamic testing. *Earthquake Engineering & Structural Dynamics*, 38(9):1071–1092, 2009. ISSN 1096-9845.

C.P. Lamarche, R. Tremblay, P. Léger, M. Leclerc, and O.S. Bursi. Comparison between real-time dynamic substructuring and shake table testing techniques for nonlinear seismic applications. *Earthquake Engineering & Structural Dynamics*, 39 (12):1299–1320, 2010. ISSN 1096-9845.

S.K. Lee, E.C. Park, K.W. Min, and J.H. Park. Real-time substructuring technique for the shaking table test of upper substructures. *Engineering Structures*, 29(9):2219 – 2232, 2007. ISSN 0141-0296.

D. Li, F. Zeng, Q. Jin, and L. Pan. Applications of an IMC based PID controller tuning strategy in atmospheric and vacuum distillation units. *Nonlinear Analysis: Real World Applications*, 10(5):2729–2739, October 2009. ISSN 14681218.

H. Li and S.K. Tso. Higher order fuzzy control structure for higher order or time-delay systems. *Fuzzy Systems, IEEE Transactions on*, 7(5):540 –552, oct 1999. ISSN 1063-6706.

Y. Li. *Seismic Performance of Buckling-restrained Braces and Substructure Testing Methods*. PhD thesis, Harbin institute of technology, 2007.

F.J. Lin, R.J. Wai, and H.P. Chen. A PM synchronous servo motor drive with an online trained fuzzy neural network controller. *Energy Conversion, IEEE Transactions on*, 13(4):319 –325, dec 1998. ISSN 0885-8969.

P. Ioannou and B. Fidan. *Adaptive Control Tutorial*. Society for Industrial and Applied Mathematics: Philadelphia, 2006.

S.A. Mahin and P.B. Shing. Pseudodynamic method for seismic testing. *Journal of Structural Engineering*, 111(7):1482–1503, 1985. ISSN 07339445.

S.A. Mahin, P.B. Shing, C.R. Thewalt, and R.D. Hanson. Pseudodynamic test method: Current status and future directions. *Journal of Structural Engineering*, 115(8): 2113–2128, 1989. ISSN 07339445.

S. Mitra. *Digital Signal Processing: A Computer-Based Approach*. McGraw-Hill Science/Engineering/Math, 3rd edition, 2005.

M. Morari and E Zariou. *Robust Process Control*. Prentice Hall, 1989.

G. Mosqueda. *Continuous Hybrid Simulation with Geographically Distributed Substructures*. PhD thesis, UNIVERSITY of CALIFORNIA, BERKELEY, 2003.

G. Mosqueda and M. Ahmadizadeh. Combined implicit or explicit integration steps for hybrid simulation. *Earthquake Engineering & Structural Dynamics*, 36(15):2325–2343, 2007. ISSN 1096-9845.

G. Mosqueda, B. Stojadinovic, and S.A. Mahin. Real-time error monitoring for hybrid simulation. Part I: Methodology and experimental verification. *Journal of Structural Engineering*, 133(8):1100–1108, 2007.

M. Nakashima and N. Masaoka. Real-time on-line test for MDOF systems. *Earthquake Engineering & Structural Dynamics*, 28(4):393–420, 1999. ISSN 1096-9845.

M. Nakashima, H. Kato, and E. Takaoka. Development of real-time pseudo dynamic testing. *Earthquake Engineering & Structural Dynamics*, 21(1):79–92, 1992. ISSN 1096-9845.

S.A. Neild, D.P. Stoten, D. Drury, and D.J. Wagg. Control issues relating to real-time substructuring experiments using a shaking table. *Earthquake Engineering & Structural Dynamics*, 34(9):1171–1192, 2005. ISSN 1096-9845.

J. Orden and R. Aguilera. Energy considerations for the stabilization of constrained mechanical systems with velocity projection. In K. Arczewski, W. Blajer, J. Fraczek, and M. Wojtyra, editors, *Multibody Dynamics*, volume 23 of *Computational Methods in Applied Sciences*, pages 153–171. Springer Netherlands, 2011. ISBN 978-90-481-9971-6.

P. Pan, M. Nakashima, and H. Tomofuji. Online test using displacementcforce mixed control. *Earthquake Engineering & Structural Dynamics*, 34(8):869–888, 2005. ISSN 1096-9845.

R. Peek and W.H. Yi. Error analysis for pseudodynamic test method. I: Analysis. *Journal of Engineering Mechanics*, 116(7):1618–1637, 1990a. ISSN 07339399.

R. Peek and W.H. Yi. Error analysis for pseudodynamic test method. II: Application. *Journal of Engineering Mechanics*, 116(7):1638–1658, 1990b. ISSN 07339399.

P. Pegon. Continuous psd testing with substructuring. In Oreste S. Bursi and David Wagg, editors, *Modern Testing Techniques for Structural Systems*, volume 502 of *CISM Courses and Lectures*, pages 197–257. Springer Vienna, 2008. ISBN 978-3-211-09445-7.

P. Pegon and G. Magonette. Continuous PSD testing with non-linear substructuring: Presentation of a stable parallel inter-field procedure. Technical Report I.02.167, E.C., JRC, ELSA, Ispra, Italy, 2002.

L. Petzold. Differential/algebraic equations are not ODE's. *SIAM Journal on Scientific and Statistical Computing*, 3(3):367–384, 1982.

A. Prakash. *Multi-time-step Domain Decomposition and Coupling Methods for Non-linear Structural Dynamics*. PhD thesis, University of Illinois at Urbana-Champaign, 2007.

M.J.N. Priestley, G.M. Calvi, and M.J. Kowalsky. *Displacement-Based Seismic Design of Structures*. IUSS Press, Istituto Universitario di Studi Superiori di Pavia, 2007.

J.C. Quéval, A.L. Maoult, U.E. Dorka, and V.T. Nguyen. Real-time substructure testing on distributed shaking tables in CEA Saclay. In V. Saouma and M.V. Sivaselvan, editors, *Hybrid Simulation: Theory, Implementation and Applications*, pages 123–132. Taylor & Francis, 2008.

H.H. Rosenbrock. Some general implicit processes for the numerical solution of differential equations. *The Computer Journal*, 5(4):329–330, 1963.

V. Saouma and M.V. Sivaselvan, editors. *Hybrid Simulation: Theory, Implementation and Applications*. Taylor & Francis, 2008.

Divisione S.B.C. *Motors SMB-MB: User's manual*. Parker, Cinisello Balsamo (MI), Italy, rev.1.3 edition, Dec 09 2009.

P. Shi. *Pseudo-negative Stiffness Control and Real-time Hybrid Testing of MR Dampers*. PhD thesis, Harbin institute of technology, 2011.

P.B. Shing and T. Manivannan. On the accuracy of an implicit algorithm for pseudodynamic tests. *Earthquake Engineering & Structural Dynamics*, 19(5):631–651, 1990. ISSN 1096-9845.

P.B. Shing and M.T. Vannan. Implicit time integration for pseudodynamic tests: Convergence and energy dissipation. *Earthquake Engineering & Structural Dynamics*, 20(9):809–819, 1991. ISSN 1096-9845.

P.B. Shing, M.T. Vannan, and E. Cater. Implicit time integration for pseudodynamic tests. *Earthquake Engineering & Structural Dynamics*, 20(6):551–576, 1991. ISSN 1096-9845.

M.V. Sivaselvan, A.M. Reinhorn, X. Shao, and S. Weinreber. Dynamic force control with hydraulic actuators using added compliance and displacement compensation. *Earthquake Engineering & Structural Dynamics*, 37(15):1785–1800, 2008. ISSN 1096-9845.

T. Söderström and P. Stoica. *System Identification*. Prentice Hall International, Hemel Hempstead, UK., 1989.

T.T. Soong and M.C. Costantinou, editors. *Passive and Active Structural Vibration Control in Civil Engineering*. Springer-Verlag, Italy, 1994.

D.P. Stoten and E.G. Gómez. Adaptive control of shaking tables using the minimal control synthesis algorithm. *Philosophical Transactions of the Royal Society of London. Series A: Mathematical, Physical and Engineering Sciences*, 359(1786): 1697–1723, 2001.

S. Vijaya, T.K. Radhakrishnan, and S. Sundaram. Model based IMC controller for processes with dead time. *Instrumentation Science & Technology*, 34(4):463–474, 2006.

M.I. Wallace, J. Sieber, S.A. Neild, D.J. Wagg, and B. Krauskopf. Stability analysis of real-time dynamic substructuring using delay differential equation models. *Earthquake Engineering & Structural Dynamics*, 34(15):1817–1832, 2005a. ISSN 1096-9845.

M.I. Wallace, D.J. Wagg, and S.A. Neild. An adaptive polynomial based forward prediction algorithm for multi-actuator real-time dynamic substructuring. *Proceedings of the Royal Society A: Mathematical, Physical and Engineering Science*, 461 (2064):3807–3826, 2005b.

Z. Wang and B. Wu. Real-time substructure testing considering specimen mass with equivalent force control method(in chinese). In Li Hongnan and Yin Tinghua, editors, *Proceedings of the Second International Forum on Advances in Structural Engineering*, pages 1110–1116. China Architecture and Building Press, 2008.

Z. Wang and B. Wu. Stability analysis for implicit dynamic substructure experiment. *Journal of Hunan University (Natural Science Edition)(in Chinese)*, 36(10):23–28, 2009.

B. Widrow and E. Walach. *Adaptive Inverse Control: A Signal Processing Approach*. Wiley, Hoboken, NJ, reissue edition, 2008.

S.L. William, editor. *The Control Handbook(2nd Edition): Control System Fundamentals*. CRC Press, Taylor & Francis Group, 2011.

M. S. Williams and A. Blakeborough. Laboratory testing of structures under dynamic loads: an introductory review. *Philosophical Transactions of the Royal Society of London. Series A: Mathematical, Physical and Engineering Sciences*, 359(1786): 1651–1669, 2001.

B. Wu, H. Bao, J. Ou, and S. Tian. Stability and accuracy analysis of the central difference method for real-time substructure testing. *Earthquake Engineering & Structural Dynamics*, 34(7):705–718, 2005. ISSN 1096-9845.

B. Wu, G. Xu, Q. Wang, and M.S. Williams. Operator-splitting method for real-time substructure testing. *Earthquake Engineering & Structural Dynamics*, 35(3):293–314, 2006. ISSN 1096-9845.

B. Wu, P.B. Wang, Q. andShing, and J. Ou. Equivalent force control method for generalized real-time substructure testing with implicit integration. *Earthquake Engineering & Structural Dynamics*, 36(9):1127–1149, 2007. ISSN 1096-9845.

B. Wu, L. Deng, and X. Yang. Stability of central difference method for dynamic real-time substructure testing. *Earthquake Engineering & Structural Dynamics*, 38(14): 1649–1663, 2009. ISSN 1096-9845.

B. Wu, P. Shi, Q. Wang, X. Guan, and J. Ou. Performance of an offshore platform with MR dampers subjected to ice and earthquake. *Structural Control and Health Monitoring*, 18(6):682–697, 2011a. ISSN 1545-2263.

B. Wu, G. Xu, and P.B. Shing. Equivalent force control method for real-time testing of nonlinear structures. *Journal of Earthquake Engineering*, 15(1):143–164, 2011b.

G. Xu. *EQUIVALENT FORCE CONTROL METHOD FOR REAL-TIME SUBSTRUCTURE TESTING*. PhD thesis, Harbin institute of technology, 2009.

J. Zhao. *Development of EFT for Nonlinear SDOF Systems*. PhD thesis, University of Minnesota, MN, 2003.

J. Zhao, C. French, C. Shield, and T. Posbergh. Considerations for the development of real-time dynamic testing using servo-hydraulic actuation. *Earthquake Engineering & Structural Dynamics*, 32(11):1773–1794, 2003. ISSN 1096-9845.